Land cover change from National to global scales: A spatiotemporal assessment of trajectories, transitions and drivers

By

Taher Mohamed Ali Radwan (B.Sc.; M.Sc.)

Lancaster Environment Centre, Faculty of Science and Technology

Lancaster University, United Kingdom

This thesis is submitted in partial fulfilment of the requirements for the award of the degree of

Doctor of Philosophy

2021

Abstract

Changes in global land cover (LC) have significant consequences for global environmental change, impacting the sustainability of biogeochemical cycles, ecosystem services, biodiversity, and food security. Different forms of LC change have taken place across the world in recent decades due to a combination of natural and anthropogenic drivers, however, the types of change and rates of change have traditionally been hard to quantify. This thesis exploits the properties of the recently released ESA-CCI-LC product – an internally consistent, high-resolution annual time-series of global LC extending from 1992 to 2018. Specifically, this thesis uses a combination of trajectories and transition maps to quantify LC changes over time at national, continental and global scales, in order to develop a deeper understanding of what, where and when significant changes in LC have taken place and relates these to natural and anthropogenic drivers. This thesis presents three analytical chapters that contribute to achieving the objectives and the overarching aim of the thesis. The first analytical chapter initially focuses on the Nile Delta region of Egypt, one of the most densely populated and rapidly urbanising regions globally, to quantify historic rates of urbanisation across the fertile agricultural land, before modelling a series of alternative futures in which these lands are largely protected from future urban expansion. The results show that 74,600 hectares of fertile agricultural land in the Nile Delta (Old Lands) was lost to urban expansion between 1992 and 2015. Furthermore, a scenario that encouraged urban expansion into the desert and adjacent to areas of existing high population density could be achieved, hence preserving large areas of fertile agricultural land within the Nile Delta. The second analytical chapter goes on to examine LC changes across sub-Saharan Africa (SSA), a complex and diverse environment, through the joint lenses of political regions and ecoregions, differentiating between natural and anthropogenic signals of change and relating to likely drivers. The results reveal key LC change processes at a range of spatial scales, and identify hotspots of LC change. The major five key LC change processes were: (i) “gain of dry forests” covered the largest extent and was distributed across the whole of SSA; (ii) “greening of deserts” found adjacent to desert areas (e.g., the Sahel belt); (iii) “loss of tree-dominated savanna” extending mainly across South-eastern Africa; (iv) “loss of shrub-dominated savanna” stretching across West Africa, and “loss of tropical rainforests” unexpectedly covering the smallest extent, mainly in the DRC, West Africa and Madagascar. The final analytical chapter considers LC change at the global scale, providing a comprehensive assessment of LC gains and losses, trajectories and transitions, including a complete assessment of associated uncertainties. This chapter highlights variability between continents and identifies locations of high LC dynamism, recognising global hotspots for sustainability challenges. At the national scale, the chapter identifies the top 10 countries with the largest percentages of forest loss and urban expansion globally. The results show that the majority of these countries have stabilised their forest losses, however, urban expansion was consistently on the rise in all countries. The thesis concludes with recommendations for future research as global LC products become more refined (spatially, temporally and thematically) allowing deeper insights into the causes and consequences of global LC change to be determined.

Table of Contents

Declaration

I declare that this thesis has not been submitted in support for any previous application or award for a higher education degree at any other university. The submitted thesis presents my own work and does not include any work done in collaboration with others except where specifically indicated. Some chapters of this thesis, in collaboration with my academic supervisors, have been published in scientific journals as follows:

Radwan, T.M., Blackburn, G.A., Whyatt, J.D. and Atkinson, P.M. (2019) Dramatic loss of agricultural land due to urban expansion threatens food security in the Nile Delta, Egypt. Remote Sensing. 11 (3), 332.

Radwan, T.M., Blackburn, G.A., Whyatt, J.D. and Atkinson, P.M. (2021) Global land cover trajectories and transitions. Scientific Reports. 11, 12814.

Taher Mohamed Ali Radwan

Lancaster, UK.

October 2021.

Acknowledgements

Foremost, I would like to express my sincere gratitude to my PhD academic supervisors, Alan Blackburn, Duncan Whyatt and Peter Atkinson. Many thanks for all the invaluable and constant support, guidance, advice and encouragement that you have provided me throughout my PhD journey at Lancaster Environment Centre (LEC). I would also like to express my deepest appreciation for allowing me to be part of your esteemed research group, it was an honour and great privilege. Thank you for helping me feel at home in a welcoming environment away from my home country and family.

I would like to thank the Egyptian Cultural Affairs and Missions sector, the Egyptian Ministry of Higher Education and Scientific Research, the British Council (Egypt) and the Egyptian Cultural and Educational Bureau (London) for funding my PhD scholarship at Lancaster University, UK. I was truly privileged to be selected among a few Egyptian researchers to be awarded a Newton-Mosharafa PhD scholarship, hence, giving me the opportunity to pursue my PhD degree at one of the prestigious UK universities. Many thanks, I am immensely grateful!

I would like to express my sincere gratitude to staff members of the postgraduate research programme at LEC. I am thankful that I acted as one of the department PGR Reps during my PhD journey. Many thanks for all the constant help and support you have provided to me and all fellow PhD students at LEC. Special thanks go to Gemma Davies (GIS Office) for her technical support and advice, and Amanda Faulconbridge (LEC Finance Office) for her friendly and approachable attitude and for taking care of my demonstration timesheets at LEC.

I was privileged to be a member of the International Student Ambassadors at Lancaster University. Therefore, I would like to thank the members of staff at the Global Recruitment Office (GRO) of Lancaster University for allowing me to be part of such a wonderful team. Special thanks go to my student ambassador friends whom I met and interacted with throughout my stay at Lancaster, I learned a lot of invaluable experiences from the amazing and diversely cultured conversations which allowed to enhance the social aspect of my lifestyle to regenerate my energy, particularly during the hard moments that I have encountered whilst studying my PhD.

Finally but most importantly, I am thankful to my beloved family for their support during studying my PhD degree despite being far away from home, special thanks to my mother, father and sister. I am also deeply grateful to my wife for her encouragement, sacrifice and holding everything together with constant patience and understanding while studying my PhD degree far away from home. Thank you for taking the sole responsibility to raise and take care of our beloved daughter. I am eternally grateful to my little princess Malak for all the joy and happiness she brought whenever we video chat together throughout my time away from her. I love you!

List of Figures

List of Tables

List of Acronyms

ANN --- Artificial Neural Network

ARD --- Analysis Ready Data

AVHRR --- Advanced Very High-Resolution Radiometer

AWS --- Amazon Web Services

BAU --- Business as Usual

BFAST --- Breaks for Additive Season and Trend

BU --- Boston University

CA --- Cellular Automata

CA-MC --- Cellular Automata-Markov Chain

CCI --- Climate Change Initiative

CDRs --- Climate Data Records

CEH --- Centre for Ecology and Hydrology

CFS --- Canadian Forest Service

CLC --- CORINE Land Cover

CLUE --- Conversion of Land Use and its Effects

CLUE-S --- Conversion of Land Use and its Effects at Small regional extent

CNES --- National Centre for Space Studies

CONUS --- Conterminous USA

CORINE --- Coordination of Information on the Environment

CSA --- Canadian Space Agency

DDO --- Desert Development Only

DLCD --- Dynamic Land Cover Dataset

DPE --- Desert and Population Expansion

DRC --- Democratic Republic of the Congo

EC-JRC --- European Commission's Joint Research Centre

EO --- Earth Observation

EOSD --- Canadian Earth Observation for Sustainable Development of Forests

EROS --- Earth Resources Observation and Science Data Centre

ESA --- European Space Agency

ETM+ --- Enhanced Thematic Mapper

EVI --- Enhanced Vegetation Index

FAO --- Food and Agriculture Organisation

FAOSTAT --- Food and Agriculture Organisation Corporate Statistics Database

FLUS --- Future Land Use Simulation

FROM-GC --- Finer Resolution Observation and Monitoring-Global Cropland

FROM-GLC --- Finer Resolution Observation and Monitoring of Global Land Cover

G3WBM --- Global Water Bodies Map

GAIA --- Global Artificial Impervious Area

GDP --- Gross Domestic Product

GEE --- Google Earth Engine

GFSAD30 --- Global Food Security Analysis Data

GIS --- Geographic Information System

GLAD --- Global Land Analysis and Discovery

GLASS --- Global Land Surface Satellite

GLC2000 --- Global Land Cover 2000

GLCF --- Global Land Cover Facility

GLC-FCS --- Global Land Cover-Fine Classification Scheme

GLCF-GIW --- Global Land Cover Facility-Global Inland Water

GLCNMO --- Global Land Cover by National Mapping Organizations

GLS --- Global Land Survey

GMP --- Global Mapping Project

GERD --- Grand Ethiopian Renaissance Dam

GVI --- Global Vegetation Index

IGBP --- International Geosphere-Biosphere Programme

IGBP-DISCover --- International Geosphere-Biosphere Programme, Data and Information Systems

IIASA-IFPRI --- International Institute for Applied Systems Analysis-International Food Policy Research Institute

ISODATA --- Iterative Self-Organizing Data Analysis Technique

LAC --- Latin America and the Caribbean

LC --- Land Cover

LCCS --- Land Cover Classification System

LCM --- Land Change Modeler

LCS --- Land change science

LST --- Land Surface Temperature

LULC --- Land use/Land cover

MC --- Markov Chain

MENA --- Middle East and North Africa

MERIS --- Medium Resolution Imaging Spectrometer

MLC --- Maximum Likelihood Classification

MLCT --- MODIS Land Cover Type

MMU --- Minimum Mappable Unit

MOA --- Mosaic of Antarctica

MODIS --- Moderate Resolution Imaging Spectroradiometer

MRLC --- Multi-Resolution Land Characteristics

MSI --- Multispectral Instrument

NALCD --- North American Land Cover Database

NALCMS --- North American Land Cover Monitoring System

NASA --- National Aeronautics and Space Administration

NBAR --- Nadir BRDF-Adjusted Reflectance

NDBI --- Normalised Difference Built-up Index

NDVI --- Normalised Difference Vegetation Index

NDWI --- Normalised Difference Water Index

NLCD --- National Land Cover Database

NOAA --- National Oceanic and Atmospheric Administration

NPP --- Net Primary Productivity

NTL --- Night-time Lights

NUACI --- Normalised Urban Areas Composite Index

OLI --- Operational Land Imager

PAL --- Pathfinder Land

PDE --- Population-Driven Expansion

PFTs --- Plant Functional Types

POK --- Pixel-Object-Knowledge

PROBA-V --- Project for On-Board Autonomy-Vegetation

RF --- Random Forest

RS --- Remote Sensing

SAGE --- Centre for Sustainability and the Global Environment

SAR --- Synthetic-Aperture Radar

SDC --- Seamless Data Cubes

SDGs --- Sustainable Development Goals

SPOT --- Satellite Pour l'Observation de la Terre

SRTM --- Shuttle Radar Topography Mission

SSA --- Sub-Saharan Africa

SVM --- Support Vector Machine

SWBD --- SRTM Water Body Dataset

TM --- Thematic Mapper

TMF --- Tropical Moist Forests

TOA --- Top of Atmosphere

UCL --- Unified Cropland Layer

UKCEH-LCM --- UK Centre for Ecology and Hydrology Land Cover Map

UMd --- University of Maryland

UN --- United Nations

UNDP --- United Nations Development Programme

UNL --- University of Nebraska-Lincoln

USA --- United States of America

USGS --- United States Geological Survey

UW-M --- University of Wisconsin-Madison

VI --- Vegetation Indices

VIIRS --- Visible Infrared Imaging Radiometer Suite

WELD --- Web-Enabled Landsat Data

Chapter 1. Introduction

1.1. Research rationale

Land cover (LC) is the physical material that covers the Earth's surface (e.g., vegetation, urban land, bare land, water bodies) and is the product of natural processes (e.g., climatic, hydrologic, geologic) and anthropogenic processes that occur over a variety of spatiotemporal scales (Turner *et al.*, 2007; Foley *et al.*, 2005; Lambin *et al.*, 2001). LC is the most crucial biophysical component of the terrestrial ecosystem and, therefore, it contributes to our understanding of global ecosystem services (Turner *et al.*, 2007; Foley *et al.*, 2005; Lambin *et al.*, 2001). Changes in LC at the global scale have considerable implications for the environmental conditions, hence, LC change has been recognised as the cause and consequence of global environmental change (Turner *et al.*, 2007; Foley *et al.*, 2005; Lambin *et al.*, 2001). LC change is a widespread phenomenon, and irrespective of whether it is naturally or anthropogenically driven, it can stimulate climate change and cause alterations in the sustainability of biogeochemical cycles, ecosystem services, biodiversity and food security. It is, therefore, important to study global LC change in order to better understand the complex interactions between natural and anthropogenic processes and their impacts from national to global scales (Turner *et al.*, 2007; Feddema *et al.*, 2005; Rindfuss *et al.*, 2004).

Considerable LC change has occurred over the Earth's surface in recent decades, due to both natural and anthropogenic drivers including urban expansion (see section 2.2.2.3) (Gong *et al.*, 2020) and the associated loss of fertile cropland (see section 2.2.2.1) (D'Amour *et al.*, 2017), deforestation (see section 2.2.2.2) (Hansen *et al.*, 2013) and the associated cropland expansion (see section 2.2.2.1) (Chaplin-Kramer *et al.*, 2015). Satellite-derived Earth Observation (EO) LC data can contribute towards our knowledge of what, where, when and ultimately why LC changes have taken place across a variety of spatial scales, providing valuable information for decision-makers and policy-legislators tasked with the responsibility of promoting sustainable natural resource management to preserve the environment (Turner *et al.*, 2007; Foley *et al.*, 2005). Frequent, systematic and rigorous analyses of satellite-derived LC data are, therefore, essential given the changing state of our planet (Chen *et al.*, 2015; Turner *et al.*, 2007).

Historically, a variety of LC datasets have been produced using a wide range of satellite sensors with different spatial and temporal resolutions (Grekousis *et al.*, 2015; Pérez-Hoyos

et al., 2017). For example, the International Geosphere-Biosphere Programme, Data and Information Systems (IGBP-DISCover) (Loveland *et al.*, 2000), the University of Maryland (UMd) (Hansen *et al.*, 2000), and the Global Land Cover 2000 (GLC2000) (Bartholomé and Belward, 2005) global LC products were all produced at a spatial resolution of 1 km (during the early 2000s) and released for a single year. The release of the Moderate Resolution Imaging Spectroradiometer (MODIS) Land Cover Type (MLCT) Collection-5 and Collection-6 (Friedl *et al.*, 2010; Sulla-Menashe *et al.*, 2019) at 500 m spatial resolution was a major step-forward in mapping global LC since these products are available at higher spatial resolution than earlier LC products. The MODIS MLCT was the first global LC product, to be released on an annual basis, from 2001.

The Finer Resolution Observation and Monitoring of Global Land Cover (FROM-GLC) (Gong *et al.*, 2013) and GlobeLand30 (Chen *et al.*, 2015) global LC products were generated at a spatial resolution of 30 m based on Landsat data. Recently, the FROM-GLC10 product (Gong *et al.*, 2019) was the first global LC product to be released at a spatial resolution of 10 m based on Sentinel-2 Multispectral Instrument (MSI) data. The vast majority of global LC products to date share one or more of the following characteristics: single year coverage (Hansen *et al.*, 2000; Gong *et al.*, 2013), coarse spatial resolution (Song *et al.*, 2018; Liu *et al.*, 2020a), low thematic resolution (Song *et al.*, 2018), different classification techniques, and/or different classification systems. Hence, they cannot be directly compared (Grekousis *et al.*, 2015; Ban *et al.*, 2015). High-resolution annual time series-based global LC studies do exist, however, they mostly focus on mapping and/or quantifying change of a single LC type, such as forest cover (Vancutsem *et al.*, 2021; Hansen *et al.*, 2013), urban land (Gong *et al.*, 2020) or surface water (Pekel *et al.*, 2016).

The capabilities of satellite remote sensing (RS) for EO continue to advance rapidly, allowing users to produce higher quality global LC maps more than ever before (Zhang *et al.*, 2021; Gong *et al.*, 2019). However, the production of global LC datasets is challenging, with each global LC product lacking in one or more of the following: spatial coverage, spatial resolution, temporal coverage, thematic resolution, and accuracy assessment (Grekousis *et al.*, 2015; Ban *et al.*, 2015). Hence, there is a pressing need for spatiotemporally consistent satellite-derived global LC datasets with annual time-series to be used to accurately analyse and quantify changes in LC that take place over a variety of spatial scales (Ban *et al.*, 2015; Chen *et al.*, 2015; Turner *et al.*, 2007).

This research, therefore, utilises the recently-released and spatiotemporally consistent European Space Agency Climate Change Initiative Land Cover (ESA-CCI-LC) product. This global LC product comprises 27 annual time-series LC maps at relatively high spatial resolution (300 m) and high thematic resolution, and was used to develop an understanding of the characteristics and drivers of LC change at multiple spatial scales over an extended period of time.

1.2. Thesis structure

The thesis is presented over six chapters: chapter 1 (Introduction), chapter 2 (Literature Review), followed by three independent yet related analytical chapters that address the aims and objectives of the thesis. The final chapter provides a synthesis of the key findings of the thesis and opportunities for future research. This is followed by a unified reference section. Brief summaries of individual chapters are as follows:

Chapter 1. Introduction

This chapter explains the research rationale of this thesis by providing insights into the importance of studying global LC change, the nature of the major LC changes and the associated implications for the environment, and a brief review of historical and recent global LC mapping efforts.

Chapter 2. Literature Review

This chapter reviews the historic timeline of satellite-derived global LC datasets and products, and the major LC changes that occurred with their recognised drivers at continental, regional and national scales. This chapter also reviews different models and techniques for monitoring and simulating LC changes as well as cloud computing platforms for geospatial applications before providing a thorough description of the ESA-CCI-LC dataset that has been used throughout this thesis. Lastly, the comprehensive literature review presented in chapter 2 leads to the main aims and objectives of the thesis, which are provided at the end of the chapter.

Chapter 3. Dramatic loss of agricultural land due to urban expansion threatens food security in the Nile Delta, Egypt

This chapter quantifies historical LC changes between 1992 and 2015 in the Nile Delta of Egypt. This densely populated, rapidly urbanising region is considered a global hotspot for urban expansion at the expense of fertile agricultural land, posing crucial threats to national

food security. The main LC trajectories and transitions (e.g., gains in urban land at the expense of fertile agricultural land) are quantified. This chapter also simulates future LC change (see section 2.5) in the region to 2030 using a series of different scenarios designed to minimise the loss of productive agricultural land to urban expansion. This chapter was published in the journal Remote Sensing (Radwan *et al.,* 2019).

Chapter 4. Satellite data reveal extensive land cover changes due to anthropogenic and climatic drivers across sub-Saharan Africa

This chapter characterises, quantifies, and interprets spatial and temporal changes in the distribution of LC across the diverse environment of sub-Saharan Africa (SSA) over the past 27 years at the SSA, national and ecoregional scales, and explores their drivers. The ESA-CCI-LC data were used in conjunction with political and ecological boundaries (ecoregions) to analyse the dynamics of LC changes that have occurred across the most impacted countries as well as the most vulnerable ecoregions for biodiversity loss. This chapter also reveals the key LC change transitions and processes at the SSA and ecoregional scales, hence improving our understanding of hotspot locations of LC change and their potential anthropogenic and climatic drivers.

Chapter 5. Global land cover trajectories and transitions

This chapter characterises, quantifies, and interprets LC changes that have occurred across the globe over the last three decades, providing a comprehensive assessment of LC gains and losses, trajectories and transitions at global, continental and national scales. Countries experiencing the largest percentage gains in urban land or forest loss are selected for national-scale analysis. This chapter demonstrates variability in LC change between and within the continents and includes a full assessment of uncertainties in the global LC dataset. This chapter was published in the journal Scientific Reports (Radwan *et al.,* 2021).

Chapter 6. Synthesis and conclusions

This chapter presents a summary of the main findings and key contributions of the thesis before acknowledging some limitations of the research and opportunities for future work.

Chapter 2. Literature Review

This chapter discusses: (a) the historic timeline of the advancements in satellite-derived global, continental and regional LC products; (b) the geospatial techniques used in deriving these LC products; (c) the major LC changes that occurred with their recognised drivers across the globe; (d) a description of the ESA-CCI-LC product that has been used throughout this thesis; (e) different models and techniques for monitoring and modelling LC change; (f) cloud computing platforms for geospatial applications; (g) accuracy assessment of LC change, and (h) aims and objectives of the thesis.

2.1. Global LC datasets

Table 2.1. presents global LC products listed in chronological order. During the late 1980s and the early 1990s after the launch of the Advanced Very High-Resolution Radiometer (AVHRR) sensor, a small number of studies were carried out to explore LC changes at the continental scale, such as Tucker *et al.* (1985), who classified LC types in Africa based on multi-temporal Normalised Difference Vegetation Index (NDVI) data, and Townshend *et al.* (1987) who utilised the Global Vegetation Index (GVI) of National Oceanic and Atmospheric Administration (NOAA), AVHRR and NDVI data to investigate the seasonal changes in LC in South America. Nevertheless, until the early 1990s, there was no global LC dataset available.

2.1.1. UMd LC product (Defries and Townshend, 1994)

The first effort to map global LC using satellite remote sensing (RS) data, was performed by a research team from the University of Maryland (UMd) of the United States of America (USA) (Defries and Townshend, 1994). This global LC product was produced at a coarse spatial resolution of 1°x 1° (approx. 111 km), using monthly composites of NDVI-based AVHRR data for the year 1987. The product was essentially developed using the 8 km spatial resolution AVHRR data but then aggregated to 1°x 1° spatial resolution. A Maximum Likelihood supervised classification (MLC) algorithm was used to distinguish 11 major LC classes that represent the main global biomes, based on their individual NDVI spectral signatures and seasonal phasing. Identifying representative training samples and validation sites was significantly challenging at that time, with no available global LC data to validate against. Hence, the product was not validated systematically, merely promoted to demonstrate the feasibility of utilising satellite RS data to obtain phenological change information at the global scale (Defries and Townshend, 1994).

Table 2.1. Global LC products listed in chronological order

Satellite Sensor	Spatial Resolution	Year of Mapping (Dataset Name)	Classification Method	Classification Scheme	Overall Accuracy (%)	Reference
AVHRR-NDVI monthly composite	111 km	1987	Supervised Maximum Likelihood (MLC)	11 LC classes	N/A	DeFries and Townshend (1994)
NASA-NOAA-PAL AVHRR 10-day	8 km	1984	Supervised Decision Tree (DTC)	IGBP (13 LC classes)	81.4	DeFries *et al.* (1998)
AVHRR-NDVI 10-day composites	1 km	1992 (IGBP-DISCover)	Unsupervised K-means Clustering	IGBP (17 LC classes)	66.9	Loveland *et al.* (2000)
AVHRR 10-day composited data	1 km	1992 (UMd LC)	Supervised Decision Tree (DTC)	IGBP (13 LC classes)	65.0 - 82.0	Hansen *et al.* (2000)
SPOT-4 VGT	1 km	2000 (GLC2000)	Unsupervised ISODATA	FAO LCCS (22 LC classes)	68.6	Bartholomé and Belward (2005)
MODIS MLCT (MCD12Q1)	500 m	2001 - onwards MLCT Collection-5	Supervised Algorithm	IGBP (17 LC classes)	74.8	Friedl *et al.* (2010)
MODIS NBAR 16-day (MOD43B4)	1 km	2003 (GLCNMO v.1)	Supervised Maximum Likelihood (MLC)	FAO LCCS (20 LC classes)	76.5	Tateishi *et al.* (2011)
Landsat-5 TM Landsat-7 ETM+	30 m	2010 (FROM-GLC)	Supervised (MLC-RF-SVM-DT J4.8)	Hybrid FAO-IGBP (10 LC classes)	53.9 - 64.9	Gong *et al.* (2013)
MODIS NBAR 16-day (MCD43A4)	500 m	2008 (GLCNMO v.2)	Supervised Maximum Likelihood (MLC)	FAO LCCS (20 LC classes)	77.9	Tateishi *et al.* (2014)
Landsat-5, 7 Chinese HJ-1	30 m	2000 - 2010 (GlobeLand30)	Supervised (MLC-SVM-DT)	10 LC classes	78.6 - 80.3	Chen *et al.* (2015)
MODIS MLCT (MCD12Q1)	500 m	2001 - onwards MLCT Collection-6	Supervised RF Algorithm	8 schemes including (FAO & IGBP)	73.6	Sulla-Menashe *et al.* (2019)
Sentinel-2 MSI	10 m	2017 (FROM-GLC10)	Supervised RF Algorithm	Hybrid FAO-IGBP (10 LC classes)	72.8	Gong *et al.* (2019)
AVHRR 8-day composites	5 km	1982 - 2015 (GLASS-CDRs)	Supervised RF Algorithm	Hybrid FAO-IGBP (7 LC classes)	82.8	Liu *et al.* (2020)
Landsat-8 OLI	30 m	2015 (GLC-FCS30-2015)	Supervised RF Algorithm	FAO LCCS (9, 16, 24 LC classes)	68.7 - 82.5	Zhang *et al.* (2021)

2.1.2. UMd LC product (DeFries *et al.*, 1998)

One of the early efforts to map global LC for the year 1984, at a spatial resolution of 8 km was performed by DeFries *et al.* (1998). The global LC dataset was produced using the National Aeronautics and Space Administration-NOAA (NASA-NOAA) Pathfinder Land (PAL), and 10-day composited AVHRR data. The product was generated using a decision-tree (DT) supervised classification technique and multiple NDVI-based and surface temperature metrics, generating 13 major LC types according to the International Geosphere-Biosphere Programme (IGBP) LC classification scheme (LCCS). The product achieved an overall accuracy of 81.4%. Comparisons were made between the output product in this study and the product developed by (Defries and Townshend, 1994) at a much coarser spatial resolution of 1°x 1° (approx. 111 km at the equator), with an overall good agreement in depicting the major LC types.

2.1.3. IGBP-DISCover LC product

A collaborative project between researchers from the United States Geological Survey (USGS), University of Nebraska-Lincoln (UNL) and the European Commission's Joint Research Centre (EC-JRC) resulted in the production of the International Geosphere-Biosphere Programme, Data and Information Systems (IGBP-DISCover) global LC dataset in 2000 (Loveland *et al.*, 2000). The IGBP-DISCover global LC dataset was generated at a spatial resolution of 1 km using monthly AVHRR 10-day NDVI composites, collected between April 1992 and March 1993. The LC classification process was performed through a continent-by-continent approach using a K-Means clustered unsupervised classification resulting in a product with 17 main LC classes based on the IGBP LCCS. This LC product revealed that forests and woodlands covered 28% of the global terrestrial surface and non-vegetated land (e.g., bare land and ice/snow) covered 24% of the global terrestrial surface, mostly in the major deserts (e.g., Sahara), Antarctica and Greenland. Croplands and mosaics of cropland/natural vegetation accounted for 19% of the global terrestrial surface, whilst shrublands (14%) and grasslands (14%) accounted for 28%, collectively. The overall accuracy of the IGBP-DISCover LC product was reported as 66.9%.

2.1.4. UMd LC product (Hansen *et al.*, 2000)

In 2000, a team of researchers from the UMd of the USA developed and produced a global LC dataset at a spatial resolution of 1 km (Hansen *et al.*, 2000). The global product was generated following a previous effort to map global LC at 8 km spatial resolution (DeFries *et al.*, 1998), using AVHRR 10-day composited data, acquired between April 1992 and March

1993. A DT supervised classification algorithm and NDVI-based metrics were used to obtain the 13 main LC classes based on the IGBP LC classification system. The primary methodology utilised a total of 156 Landsat MSS images and was based on the research performed by DeFries *et al.* (1998). Comparisons between the output dataset (UMd) and other higher-resolution LC datasets such as CORINE (Coordination of Information on the Environment) and national forest statistics, such as the Food and Agriculture Organisation Corporate Statistics Database (FAOSTAT), revealed overall good agreement in depicting LC classes, such as woodlands and forests. However, other LC classes such as croplands and pastures showed relatively poor agreement. Africa was found to be the continent with the largest disagreement between the UMd dataset and the FAOSTAT data. The key findings showed that the overall accuracy ranged from 65% to 82%. Moreover, more than 50% of the global LC was distributed between bare land (23.3%), wooded grassland (15.8%) and open shrubland (12.5%).

2.1.5. MODIS MLCT Collection 4

The release of the Boston's University (BU) Moderate Resolution Imaging Spectroradiometer (MODIS) Land Cover Type (MLCT) product in 2004 (Friedl *et al.*, 2002) marked a significant advance in the field of global LC mapping. This LC product had substantially improved spatial, spectral, radiometric and geometric characteristics in comparison to existing global LC datasets. The MLCT Collection 4 product was generated at 16-day temporal resolution and 1 km spatial resolution using a supervised classification algorithm and includes 17 major LC classes based on the IGBP LC classification system.

2.1.6. GLC-2000 LC product

The Global Land Cover 2000 (GLC2000) product was released in 2005 (Bartholomé and Belward, 2005), based on global daily scenes collected from the Satellite Pour l'Observation de la Terre (SPOT-4) VEGETATION (VGT) sensor between November 1999 and December 2000. The product was generated at a spatial resolution of 1 km using an ISODATA unsupervised classification algorithm, with 22 major LC classes, based on the Food and Agriculture Organisation (FAO) of the United Nations (UN) classification system FAO-LCCS. The GLC2000 product was developed and produced by the EC-JRC through an international collaboration involving 30 global research teams. The product achieved an overall accuracy of 68.6%. It was developed using a geographic region-specific processing approach, with 18 global regions. The main findings demonstrated that 25% of the Earth's terrestrial surface is made up of bare land, ice and snow and urban land. Forest extent covered 28%, whilst

shrublands and grasslands covered 27.5%. Lastly, cropland and pastures accounted for 11%, while areas of mosaic cropland/natural vegetation accounted for 6%.

2.1.7. MODIS MLCT Collection 5

In 2010, MODIS MLCT Collection 5 (MCD12Q1) was released based on an ensemble, DT supervised classification technique (Friedl *et al.*, 2010), with annual coverage from 2001 onwards, and substantial improvements and refinements to the past generation of the MLCT product (Collection 4), resulting in improved overall accuracy of the product. MLCT Collection 5 represented a major step forward for global LC mapping, with a spatial resolution of 500 m, relatively higher than other 1 km global LC products (e.g., IGBP-DISCover, UMd LC and GLC2000). Additional input features were included in the production of the MLCT Collection 5, including the Enhanced Vegetation Index (EVI), MODIS Land Surface Temperature (LST) and MODIS Nadir BRDF-Adjusted Reflectance (NBAR) 500 m data. The overall accuracy of the MLCT Collection 5 product was 74.8%.

2.1.8. GLCNMO LC products

The Global Land Cover by National Mapping Organizations (GLCNMO v.1 and GLCNMO v.2) datasets were released in 2011 and 2014 (Tateishi *et al.*, 2011, 2014), respectively, by the Global Mapping Project (GMP). The datasets were produced at a spatial resolution of 1 km for the year 2003 (GLCNMO v.1) and 500 m for the year 2008 (GLCNMO v.2), using an MLC algorithm. The primary data sources were the MODIS NBAR 16-day 1 km (MOD43B4) product for GLCNMO v.1 and MODIS NBAR 16-day 500 m (MCD43A4) for GLCNMO v.2. Both iterations of the GLCNMO product have 20 main LC classes based on the FAO-LCCS - 14 were classified using the MLC algorithm using a continent-by-continent approach, whilst 6 LC classes (urban, open tree, wetland, mangrove, ice/snow, and water bodies) were classified independently as it proved too challenging to classify them using the MLC technique. The achieved overall accuracy was 76.5% (GLCNMO v.1) and 77.9% (GLCNMO v.2).

2.1.9. FROM-GLC LC product

The Finer Resolution Observation and Monitoring of Global Land Cover (FROM-GLC) product was released in 2013 with the first global LC map for the year 2010 at a relatively high spatial resolution of 30 m, using Landsat Thematic Mapper (TM) and Enhanced Thematic Mapper (ETM+) images (Gong *et al.*, 2013). Four automated supervised classifiers were utilised in the global LC mapping process, including MLC, Random Forest (RF), Support Vector Machine (SVM) and J4.8 DT algorithms. A newly proposed LC classification system based on both the

FAO and IGBP LC classification schemes, was used to classify the global LC into 10 major LC types in a Level-1 classification scheme. The SVM classifier achieved the highest overall accuracy of 64.9% followed by the RF classifier (59.8%), J4.8 DT classifier (57.9%) and the MLC (53.9%). The FROM-GLC product revealed that forest cover occupied the largest global LC extent (28.4%), followed by bare land (16.5%), grasslands (13.4%), snow/ice cover (12.8%), croplands (11.5%), shrublands (11.5%), inland water bodies (3.6%) and urban land (0.7%). Interestingly, whilst Africa achieved the highest overall classification accuracy across the four classifiers, 14 countries within sub-Saharan Africa (SSA) achieved sub-50% classification accuracy.

2.1.10. GlobeLand30 LC product

With recent advancements in satellite RS data and the availability of the freely-accessible, long-term Landsat archive, the development and production of a relatively finer-resolution global LC product has become feasible. China initiated a global LC mapping project in 2010, with the main aim of producing a 30 m global LC product (GlobeLand30) for the nominal years 2000 and 2010. In 2014, a reliable LC product (GlobeLand30) with global coverage was released with a spatial resolution of 30 m (Chen *et al.*, 2015), depicting 10 major LC classes. The GlobeLand30 LC product is considered superior to older coarser-resolution global LC products (e.g., IGBP-DISCover, GLC2000 and MODIS MCD12Q1). Over 10,000 Landsat TM and ETM+ (30 m) scenes within the growing season for the years 2000 and 2010 were the primary data source for the global LC mapping process, along with images from the Chinese Environmental and Disaster satellite (HJ-1; 30 m) for the year 2010. An integrated Pixel-Object-Knowledge (POK) based approach was developed and employed to generate the 10-LC class global product. The overall classification accuracy was 80.3% and 78.6% for the years 2010 and 2000, respectively. It was reported that the overall quality of the GlobeLand30 product was comparable to the Europe-based CORINE dataset in 2000. However, when compared with a similar spatial resolution (30 m) LC dataset (FROM-GLC), it was clear that the overall quality of the classification results for GlobeLand30 was superior (Chen *et al.*, 2015).

2.1.11. MODIS MLCT Collection 6

Recently, MODIS MLCT Collection 6 was released in 2019 (Sulla-Menashe *et al.*, 2019), exploiting recent advancements in geospatial techniques and computational storage and processing capabilities that were not possible previously. The MLCT product has a global extent and annual coverage with the inclusion of eight different LC classification schemes.

The MLCT Collection 6 was generated using a RF supervised classification algorithm within the R environment and a hierarchical classification model. The 500 m MODIS NBAR MC43A4 and MC43A2, the terrestrial ecozones of the Earth (Olson *et al.*, 2001), MODIS water land mask (MCD44W) (Carroll *et al.*, 2009), MODIS VCF (MCD44B) (Hansen *et al.*, 2003), and a global cropland intensity map (Ramankutty *et al.*, 2008), were the main inputs to generate the MLCT Collection 6 product. This product achieved an overall classification accuracy of 73.6%. In addition to the five legacy classification systems from Collection 5, Collection 6 includes three new hierarchical classification schemes based on the FAO-LCCS, with 23 primary LC classes.

2.1.12. FROM-GLC10 LC product

After the successful release of FROM-GLC (Gong *et al.*, 2013) in 2013, a novel first attempt was made to produce a global LC map at a spatial resolution of 10 m (FROM-GLC10) using multispectral Sentinel-2 data in 2017 (Gong *et al.*, 2019). The FROM-GLC10 product was generated using a RF classification technique within the environment of Google Earth Engine (GEE). The training samples were collected from Li *et al.* (2017). The output product contains 10 major LC classes using the Level-1 classification system from Gong *et al.* (2013), achieving an overall accuracy of 72.8%. Comparisons with the FROM-GLC 30m Landsat-based product demonstrate that the FROM-GLC10 product has greater spatial detail and can better distinguish LC features. Pertinently, the overall accuracy of the product decreased by less than 1% when only 40% of the global training sample was utilised.

2.1.13. GLASS CDRs LC product

The Global Land Surface Satellite (GLASS) Climate Data Records (CDRs) product is one of the most recent attempts to map global LC dynamics annually from 1982 to 2015, with long temporal coverage and 5 km spatial resolution (Liu *et al.*, 2020a). The production process was performed within the GEE geospatial cloud computing platform. The main source of data was the 0.05° (approx. 5 km) 8-day AVHRR-based GLASS CDRs, with the utilisation of a RF classification algorithm using an adjusted classification system derived from the FROM-GLC product. Since GLASS CDRs is a land surface product, surface water was masked out. Furthermore, at this coarse spatial resolution of 5 km, identifying small patches of other LC types (e.g., wetlands and urban land) was a challenging task. Therefore, water bodies, wetlands and urban land were not included in this study. The GLASS CDRs presents seven major LC types namely, cropland, forest, shrubland, grassland, tundra, bare land and ice/snow, with an overall accuracy of 82.8%. Large LC changes at multiple spatial scales were

reported, including cropland gain, forest loss and bare land loss in the tropics, forest increases in the Northern Hemisphere, and grassland declines in Asia.

2.1.14. iMap World v1.0 LC product

A novel global LC mapping framework based on the intelligent mapping (iMap) of LC using a number of cutting-edge technologies, including artificial intelligence, machine learning, virtual constellations, cloud computing and spatiotemporal fusion and construction was developed by Liu *et al.* (2021). They built an automated, cloud-based and serverless data repository and simultaneous LC mapping scheme using the Amazon Web Services (AWS), establishing the first global daily Seamless Data Cubes (SDC) and annual/seasonal global LC maps for 1985-2020 (iMap World v1.0), at 30 m spatial resolution. The 36-year long global dataset was produced using multi-sensor spatiotemporal data including Landsat, MODIS and AVHRR, based on fusion and reconstruction techniques. The overall accuracy of the annual global LC maps was 80% for Level-1 classification (29 LC classes) and 73% for Level-2 classification (33 LC classes). Furthermore, the accuracy of the iMap World v1.0 dataset was higher than their GlobeLand30 counterpart by 10%. The main key findings revealed that global forest cover declined by 1.47 million km^2, cropland experienced a net gain of 0.84 million km^2 and urban land increased by 0.48 million km^2, between 1985 and 2020.

2.1.15. GLC-FCS30-2015 LC product

Zhang *et al.* (2021) produced a global LC product with 30 major LC types for the year 2015 using a fine classification scheme, at a spatial resolution of 30 m (GLC-FCS30-2015). The GLC-FCS30-2015 product was generated using a RF classifier within the GEE cloud computing platform, using all the available Landsat-8 Operational Land Imager (OLI) surface reflectance scenes between 2014 and 2016, for the nominal year 2015. The main results showed that the overall accuracy of the GLC-FCS30-2015 product was 82.5% for Level-1 classification system with nine main LC types, an overall accuracy of 71.4% for the Level-2 FAO-LCCS with 16 LC types, whilst achieving an overall accuracy of only 68.7% for the FAO-LCCS Level-3 classification system with 24 LC types. The GLC-FCS30-2015 product was compared with other global-coverage LC products including FROM-GLC, GlobeLand30, the European Space Agency Climate Change Initiative Land Cover (ESA-CCI-LC) and MODIS MCD12Q1. The product captured more spatial detail than the ESA-CCI-LC and MODIS MCD12Q1 products, and greater thematic detail than either FROM-GLC and GlobeLand30, achieving much higher overall accuracy (82.5%) in comparison to GlobeLand30 (75.9%) and FROM-GLC (59.1%).

2.2. Global LC mapping

2.2.1. Mapping of multiple LC types

Global LC types were mapped (Wang *et al.*, 2015) for the years 2001 and 2010 at a spatial resolution of 250 m, using MODIS collection-5 (MOD13Q1) 16-day data. Each map (2001 and 2010) was produced using data acquired from the exact, previous and subsequent years. A RF classifier was utilised to classify the global LC types into seven main LC classes including croplands, forest, grasslands, shrublands, barren land, water bodies and snow/ice. The adopted classification system was generated from the FROM-GLC product (Gong *et al.*, 2013). The reported overall accuracy was 74.9% and 75.2% for the years 2001 and 2010, respectively. Global LC mapping (e.g., multiple and individual LC types) efforts listed in chronological order are shown in Table 2.2.

Global LC change was mapped and quantified (Song *et al.*, 2018) between 1982 and 2016 annually, at a spatial resolution of 5 km using a combination of satellite data obtained from multiple sensors including AVHRR, MODIS and Landsat ETM+. The final LC product provides a comprehensive account of major LC change dynamics at a global scale over the 35-year period. The LC change-product classifies global LC using a supervised regression tree algorithm into three main LC classes; tree canopy, short vegetation and bare ground. The key findings revealed, interestingly, and perhaps in stark contrast with most recent global LC change based studies, a net gain in tree canopy cover by 2.24 million km^2 (+7.1%). Short vegetation cover witnessed a net decline of 0.88 million km^2 (-1.4%). Lastly, bare ground cover also declined by 1.16 million km^2 (-3.1%), between 1982 and 2016. The data demonstrate that of all global LC changes, 60% were associated with anthropogenic drivers (e.g., deforestation and agricultural expansion) and 40% with natural drivers (e.g., climate change), suggesting that the Earth's terrestrial ecosystems are dominated and altered by anthropogenic activities.

Table 2.2. Global LC mapping efforts listed in chronological order

Mapped LC Type	Satellite Sensor	Spatial Resolution	Year of Mapping (Dataset Name)	Classification Method	Classification Scheme	Overall Accuracy (%)	Reference
Forest cover	AVHRR	1 km	1992 - 1993	Supervised Decision Tree	IGBP (12 tree/ Non-tree classes)	N/A	DeFries *et al.* (2000)
Forest cover	MODIS	500 m	2000 - 2001	Supervised Regression Tree	Forest/non-forest	N/A	Hansen *et al.* (2003)
Cropland	BU-MODIS 1 km SPOT-4 VGT 1km	10 km	2000	Supervised/ Unsupervised	Cropland/non-cropland	N/A	Ramankutty *et al.* (2008)
Cropland	MODIS MOD09	250 m	2000 - 2008	Supervised Decision Tree	Cropland/non-cropland	63.0	Pittman *et al.* (2010)
Cropland	Landsat-5 TM Landsat-7 ETM+	30 m	2010 (FROM-GC)	Supervised SVM Algorithm	Cropland/non-cropland	N/A	Yu *et al.* (2013)
Forest cover	Landsat-7 ETM+	30 m	2000 - 2012 (GFW)	Supervised Decision Tree	Forest/non-forest	99.6 - 99.7	Hansen *et al.* (2013)
Multiple LC types	MODIS VI MOD13Q1	250 m	2001 2010	Supervised RF Algorithm	Hybrid FAO-IGBP (7 LC classes)	74.9 - 75.2	Wang *et al.* (2015)
Cropland	Global, regional, national data	1 km	2005 (IIASA-IFPRI)	Supervised/ Unsupervised	Cropland/non-cropland	82.0	Fritz *et al.* (2015)
Cropland	Global, regional, national data	250 m	2014 (UCL)	Supervised/ Unsupervised	Cropland/non-cropland	82.0 - 94.0	Waldner *et al.* (2015)
Forest cover	Landsat-5 TM Landsat-7 ETM+	30 m	1990 2000 2005 (GLCF)	Supervised Decision Tree	Forest/non-forest	88.0 - 91.0	Feng *et al.* (2016c)
Surface water bodies	Landsat-5/7/8 TM/ETM+/OLI	30 m	1984 - 2015	Supervised Decision Tree	3 classes (water, land, null)	N/A	Pekel *et al.* (2016)
Multiple LC types	AVHRR, MODIS, Landsat-7 ETM+	5 km	1982 - 2016	Supervised Regression Tree	3 LC classes	90.1 - 95.6	Song *et al.* (2018)
Urban land	Landsat-5/7/8 TM/ETM+/OLI	30 m	1985 - 2018 (GAIA)	Automated GEE	Urban/non-urban	90.0	Gong *et al.* (2020)
Urban land	Landsat-8 OLI Sentinel-1 SAR	30 m	2015	Automated GEE	Urban/non-urban	95.0	Zhang *et al.* (2020)

The Global Land Analysis and Discovery team (GLAD) at the UMd, USA, developed and created a global-coverage, fine resolution (30 m), free-access and spatiotemporally consistent Landsat Analysis Ready Data (ARD) for multi-spatial (local to global) scale LC mapping and change detection purposes (Potapov *et al.*, 2020). The GLAD ARD employed the full archive of 16-day, 1 X 1 geographic degree tiled Landsat Level-1 (L1T) TM, ETM+ and OLI imageries, acquired from the USGS Earth Resources Observation and Science (EROS) Data Centre website from 1997 to present, and updated annually. Nearly three million images (2.985 million) covering the period from January 1997 to October 2019, were selected and subjected to a number of image processing steps. The GLAD ARD product was developed using multi-spatiotemporal data processing tools (e.g., machine learning) provided via the GLAD servers.

2.2.2. Mapping of individual LC types

2.2.2.1. Cropland

A global croplands and pastures dataset for the year 2000 was developed by the Centre for Sustainability and the Global Environment (SAGE) of the University of Wisconsin-Madison (UW-M), USA (Ramankutty *et al.*, 2008). The dataset was generated at a spatial resolution of 5' (approx. 10 km at the equator) using satellite EO data including the BU-MODIS 1 km global LC product (Friedl *et al.*, 2002) and the 1 km GLC2000 product based on the SPOT-4 VGT sensor (Bartholomé and Belward, 2005). Furthermore, for the first time in such global-scale LC studies, statistical uncertainty estimates were quantified and included. The study revealed that croplands occupied 15 million km^2 (12.2-17.1, with 90% confidence level), accounting for 12% of the Earth's land surface. Pastures occupied 28 million km^2 (23.6-30, with 90% confidence level), accounting for 22% of the total global land surface area, in the year 2000. The key findings were compared against their corresponding total areas reported by the FAOSTAT database. FAOSTAT reported that global croplands and pastures occupied 15.3 and 34.4 million km^2, respectively. This suggests that there was an overall good agreement for croplands between the two data sources; however, pasture extent found to be considerably lower than reported in the FAOSTAT database.

The global cropland extent map at 250 m spatial resolution covering the period 2000-2008 (Pittman *et al.*, 2010) was one of the first attempts to solely map global cropland extent. MODIS surface reflectance 250 m data obtained from the MOD09 Collection-5 product and associated NDVI data were used in combination with a supervised classification tree algorithm to produce the global cropland map. In order to evaluate the spatial accuracy of

the global cropland map, it was compared against five global LC products (SAGE, UMd, IGBP DISCover, GLC2000 and MLCT MOD12Q1), achieving an overall accuracy of 63%. The global cropland map was assessed with reference data for 4 main field crops - wheat, rice, corn and soybeans. The results show that the MODIS-based cropland map best characterises intensive broadleaf crops such as corn and soybeans far better than areas cultivated with wheat or rice. Moreover, regions with little to no cropland intensified agriculture (e.g., Africa) were poorly represented irrespective of the crop type.

Yu *et al.* (2013) produced a global croplands (FROM-GC, Finer Resolution Observation and Monitoring-Global Cropland) product at a spatial resolution of 30 m. Multiple datasets were used to generate the final cultivated/non-cultivated map including (i) the FROM-GLC product (Gong *et al.*, 2013), (ii) a global cropland map at a spatial resolution of 250 m generated by Pittman *et al.* (2010) and (iii) FAOSTAT data, which provides a country-level area of croplands. The global cropland area was estimated at 15.34 million km^2 in 2010 and showed overall strong correspondence with the FAOSTAT data since it was reported at 15.41 million km^2 for the same year, and this was based on a country-by-country comparison approach. It was found that the largest discrepancies between the generated map and the FAOSTAT data were found in developing regions including Africa, South-eastern Asia, South America, which may be explained by the lack of sufficient statistics reported in these regions which led to experiencing inconsistencies between the census-based data and the remotely-sensed dataset.

Waldner *et al.* (2015) evaluated the availability of cropland datasets at multiple spatial scales in order to provide strategic plans for mapping the distribution of future cropland. This was achieved by performing a multi-criteria analysis at the national scale to identify priority locations for future cropland mapping. Identified countries and regions included West Africa, Ethiopia, Mozambique, Madagascar, Myanmar, Vietnam, Indonesia and Brazil, suggesting these countries/regions should receive higher priority for future cropland mapping. Based on the outcomes obtained following the multi-criteria analysis, they produced a Unified Cropland Layer (UCL) at a spatial resolution of 250 m with global coverage for the year 2014. The UCL product yielded an overall accuracy ranging from 82%-94%.

The International Institute for Applied Systems Analysis-International Food Policy Research Institute (IIASA-IFPRI) generated a global cropland percentage map for the year 2005 (Fritz *et al.*, 2015) at a spatial resolution of 1 km. This was developed via the integration of multiple

cropland maps at global, regional and country scales (e.g., GLC2000, MLCT collection 5 and CORINE). The final cropland percentage map achieved an overall accuracy of 82%. The IIASA-IFPRI LC product was also compared with the UW-M SAGE cropland dataset demonstrating an overall good agreement in several locations across the world including in Europe, North and Central America, India, China and Southeast Asia. However, considerable disagreements were found in other locations including in Northern and Central Africa, the Middle East, Brazil and Papua New Guinea.

Cropland area in China and Australia, two of the largest and most diverse countries of the world, was mapped (Teluguntla *et al.*, 2018) at a spatial resolution of 30 m. Landsat-8 OLI 16-day Top of Atmosphere (TOA) scenes for the years 2013-2015 were utilised. The main aim was to generate an accurate, high-resolution (30 m) map of croplands/non-croplands across China and Australia for the year 2015 using a pixel-based RF machine learning supervised classification algorithm which was executed using the GEE platform. The final map achieved an overall accuracy of 94% and 97% over China and Australia, respectively. The total area of cropland was estimated at 1.65 million km^2 in China and 0.35 million km^2 in Australia in 2015. The reported cropland areas in both countries were slightly higher when compared with the corresponding areas reported by the national-based statistics (e.g., FAOSTAT database).

As part of the NASA led project to generate high-resolution global cropland maps through the Global Food Security Analysis Data project at 30 m (GFSAD30), thus contributing towards the understanding of the global food security status. Phalke *et al.* (2020) mapped cropland areas in Europe, Russia, the Middle East and Central Asia at 30 m spatial resolution. Landsat-8 OLI and Landsat-7 ETM+ images covering 64 countries in total and acquired between 2014 and 2016 were the primary input data source. A pixel-based RF machine learning supervised classification algorithm was used within the GEE platform to produce a binary map demonstrating cropland/non-cropland extent for the year 2015. The output map was compared with other global (GlobeLand30), Continental (CORINE) and regional (Central Asia LC map at 250 m spatial resolution by Klein *et al.* 2012)) LC products. The overall accuracy of the generated map was 94%, suggesting that cropland area totalled 5.46 million km^2 in 2015 within the investigated regions.

2.2.2.2. Forest cover

A prototype global map of tree cover percentage and its respective proportions of trees with different leaf types (e.g., broadleaf and needleleaf) and leaf longevity (e.g., evergreen and deciduous) was produced by DeFries *et al.* (2000) at 1 km spatial resolution. It was developed to help evaluate tree cover change in the context of the Kyoto protocol and was derived from the AVHRR sensor. It covers the year 1992-1993 and was intended for the use in modelling terrestrial carbon cycle and quantifying associated carbon stocks at the global scale. Proportional tree cover for three vegetation characteristics were developed to include leaf longevity (percentage evergreen and percentage deciduous), leaf type (percentage broadleaf and percentage needleleaf) and leaf form (percentage woody vegetation, percentage herbaceous vegetation and percentage bare land). A DT supervised classification algorithm was utilised to identify 12 tree/non-tree classes based on the IGBP-LCCS.

The first global percent forest cover map (2000-2001) was presented by Hansen *et al.* (2003) at a spatial resolution of 500 m and was derived from the MODIS sensor on board NASA's Terra spacecraft. The methodology was based on using a nonlinear supervised regression tree technique and multi-band MODIS data starting from October 2000 and December 2001. The results illustrated that the final percent tree cover map demonstrated greater spatial accuracy in comparison to previous attempts to map global forest cover using coarser spatial resolution, such as AVHRR data (1 km).

Global forest cover extent was mapped and quantified by Hansen *et al.* (2013) between 2000 and 2012 using 30 m Landsat images. They analysed more than 654,000 Landsat-7 ETM+ scenes during the growing season using a DT algorithm. Image analysis was performed within the GEE cloud platform to facilitate large-scale computational processing and reduce the time and effort required for such an onerous and time-consuming task. The key findings revealed 1.5 million km^2 of net global forest loss with 2.3 million km^2 of gross forest loss and 0.8 million km^2 of gross forest gain between 2000 and 2012. Of all the four major climatic regions (tropical, subtropical, temperate and boreal), the tropical region experienced the largest declines in forest cover with an annual loss rate of 2,100 km^2. Not only this dataset provides detailed information on global forest cover changes based on 30 m spatial resolution, but also it is updated annually with current coverage up to 2020, providing reliable and consistent monitoring of historical global forest extent changes.

Global forest cover between 1990 and 2000 was mapped (Kim *et al.*, 2014) at a spatial resolution of 30 m based on the analysis of about 30,000 Landsat scenes. The Global Land Survey (GLS) 1990 (covering 1987-1997) was used as the main source of images for the 1990 epoch. DT classification and change-detection techniques were used to produce a 30 m global extent map of forest cover for 1990 and a global forest cover-change map between 1990 and 2000. The product yielded an overall accuracy of 93% and 84% for the 1990 forest cover map and the forest cover-change map (1990-2000), respectively. The final global forest cover-change map demonstrates the gross gains, gross losses and net change in forest cover. The key findings show expansive forest cover-change within the tropics followed by the boreal region where wildfires were widespread. Regions that witnessed large net forest losses (e.g., Amazon Basin) were linked to large-scale agricultural expansion.

Global forest dynamics, including forest cover and the associated changes in its extent, were mapped and quantified for the nominal epochs of 1990, 2000 and 2005 at a spatial resolution of 30 m by the Global Land Cover Facility (GLCF) research team (Feng *et al.*, 2016c). Using pixel-based estimates of tree cover-extent and associated uncertainties, they produced a global binary forest map for each epoch and quantified the temporal gains and losses in forest extent using Landsat TM and ETM+ images. The overall accuracy was 91% for the binary forest-extent maps and 88% for the forest change maps. These achieved accuracies are among the highest reported in recent global forest cover mapping products. The study revealed that the global gross gain in forest cover was 0.73± 0.38 million km^2 and the global gross loss in forest cover was 0.28± 0.26 million km^2, between 2000 and 2005. Moreover, the gross gains and losses in forest extent between 1990 and 2000 were 1.08± 0.53 and 0.53± 0.47 million km^2, respectively.

Vancutsem *et al.* (2021) mapped global Tropical Moist Forests (TMF) extent with associated anthropogenic/natural historical changes (deforestation, degradation, disturbance, and post-deforestation regrowth) annually from January 1990 to December 2019. Landsat imagery (30 m) was the primary source of the TMF mapping process. They employed a sequential DT classification algorithm (Pekel *et al.*, 2016) that is operated within the environment of the GEE cloud computing platform. The main findings revealed that 17% (2.19 million km^2) of the global TMF cover was lost, whilst 1.07 million km^2 was found in a degraded/disturbed state between 1990 and 2019, with a remaining TMF extent of 10.7 million km^2 in 2019. Most degraded TMF were found in Asia (41%), Latin America (37%) and Africa (22%), respectively. Furthermore, the expansion of palm oil and rubber

plantations in Indonesia and Malaysia was the main cause for the consistent deforestation in the region, contributing 81% of the global TMF conversion to plantations. Assuming no reduction of the ongoing disturbance rates, undisturbed TMF will completely disappear from the large humid tropical regions by the year 2050.

2.2.2.3. Urban land

Global urban land was mapped at a spatial resolution of 500 m using MODIS data over one year (2001-2002). Schneider *et al.* (2009, 2010) used 8-day MODIS images along with an ensemble DT supervised classification algorithm. The results showed an overall accuracy of 93% with a high level of agreement based on comparisons with finer resolution Landsat-generated maps over 140 cities. Global urban land was estimated at approximately 670,000 km^2. Furthermore, 53% of the global urban land was reported to be in the USA, Canada, Australia, China, Japan, South Korea and the Middle East.

Liu *et al.* (2018) mapped global urban area using multi-temporal Landsat images with a spatial resolution of 30 m (e.g., Landsat-5 TM calibrated TOA reflectance data) via the GEE platform, between 1990 and 2010 at 5-year intervals. They proposed a Normalised Urban Areas Composite Index (NUACI) based method and used GEE to facilitate the Landsat image classification process, achieving an overall accuracy of 81%-84% for their global urban mapping results. The NUACI is largely based on the integration of other indices including the Normalised Difference Built-up Index (NDBI), the Normalised Difference Water Index (NDWI) and the NDVI. They found that global urban area has increased by 296,000 km^2 between 1990 and 2010, with China, the USA and India contributing 43% towards this total gain.

Global urban expansion was mapped between 1992 and 2016 at a spatial resolution of 1 km by He *et al.* (2019) using a fully convolutional network. They found that global urban area increased by 346,000 km^2 (126%) between 1992 and 2016. At the continental scale, Asia experienced the largest areal increase in urban land, contributing 42% of the global increase. At the country scale, a number of countries with large areal contributions to the global and corresponding continental urban gain were reported, including China, Vietnam, Indonesia and Malaysia in Asia; USA, Mexico, Brazil and Argentina in the Americas, and Russia, France, Spain and Italy in Europe.

Global Artificial Impervious Area (GAIA) was mapped annually between 1985 and 2018 using all available images in the Landsat archive with 30 m spatial resolution, within the GEE

cloud computing platform (Gong *et al.*, 2020). GAIA was mapped at 5-years intervals with an overall accuracy in excess of 90%. At the global scale, the results demonstrate that global urban areas totalled 797,000 km^2 in 2018, which is 150% higher than their corresponding areas in 1990. At the national scale, China and the USA had a substantial areal amount of urban land, accounting for 50% of the globe's total GAIA in 2018. Furthermore, other countries across most continents were found to have large gains in urban area including India and Japan in Asia; Brazil in South America; Canada in North America, and Russia, Italy, France and Germany in Europe.

A global impervious surface map was developed and generated by Zhang *et al.* (2020) with a spatial resolution of 30 m for the year 2015. This was achieved by using Landsat-8 OLI images, Synthetic-Aperture Radar (SAR) Sentinel-1 images and Visible Infrared Imaging Radiometer Suite (VIIRS) Night-time Lights (NTL) images on the GEE platform. They reported an overall accuracy of 95% and kappa coefficient of 0.90. This study achieved the highest overall accuracy among other global urban mapping studies that have been used for comparison purposes (e.g., He *et al.* (2019), Liu *et al.* (2018a)). The results show the top 20 countries with the largest area of the impervious surface area including the USA, China and Russia, contributing 41% of the total global impervious surface area in 2015.

2.2.2.4. Surface water bodies

The global surface water extent was mapped and quantified (Pekel *et al.*, 2016) between 1984 and 2015 using the entire orthorectified multi-temporal L1T Landsat satellite imagery archive (e.g., TM, ETM+ and OLI) at 30 m spatial resolution. A sequential DT classification algorithm was used on GEE. The main findings demonstrate that between 1984 and 2015, the global surface water experienced a net areal gain of about 94,000 km^2, with 184,000 km^2 and 90,000 km^2 for the gross gain and loss, respectively. Furthermore, all continents showed net gains in permanent water, except Oceania which was the only continent to witness a slight decline (1%). Most of the gains in global permanent surface water came from dam reservoirs filling. However, over 70% of the global net permanent surface water loss was in Central Asia (e.g., Kazakhstan and Uzbekistan) and in the Middle East (e.g., Iran, Iraq and Afghanistan) due to climate change (e.g., droughts) and human-induced actions (e.g., damming and river diversion). These losses in global water bodies raise serious concerns over global water security and the management of transboundary water bodies.

Feng *et al.* (2016a) generated a global-scale inland surface water bodies product (Global Land Cover Facility-Global Inland Water (GLCF-GIW)) at a spatial resolution of 30 m for the

year 2000. An automated parameterised classification-tree algorithm was applied to the GLS collection of Landsat imagery. The GLS 2000 epoch comprising Landsat-7 ETM+ scenes obtained between 1999 and 2002 was used. The output GIW product was also compared with global datasets (e.g., MODIS 250 m water mask) and national datasets including the U.S. National Land Cover Database (NLCD) and the Canadian Earth Observation for Sustainable Development of Forests (EOSD) LC datasets. The results show that the GIW dataset mapped approximately 3.65 million km^2 of global inland surface water bodies, with the majority located in North America and Asia, together contributing over 73% of global inland water extent. A strong linear correlation between the GIW dataset and the MODIS water mask was reported. Moreover, a high agreement was also reported with the U.S. NLCD and EOSD LC datasets, albeit to a lesser extent with the EOSD LC product.

A global water bodies map (G3WBM) at 90 m spatial resolution was generated (Yamazaki *et al.*, 2015) using multi-temporal Landsat images retrieved from the GLS database along with an automated classification-tree algorithm. The Landsat TM and ETM+ scenes were obtained from four GLS epochs (1990, 2000, 2005 and 2010) to produce a seamless global water bodies map. One of the main objectives of this study was to distinguish between permanent and temporal water bodies. Therefore, more effort was placed on delineating river channels and smaller water bodies than in previous coarser-resolution studies. The G3WBM dataset mapped approximately 3.25 million km^2 of global permanent water bodies. The G3WBM product showed an overall good agreement with other datasets, however, there were also minor disagreements in the total reported area of water bodies and within the smaller water bodies where it was challenging to distinguish the shoreline pixels. Generally, the global area of water bodies was found to increase when using finer resolution datasets since detecting and mapping smaller water bodies becomes more feasible at finer spatial resolutions.

Carroll *et al.* (2009) produced a global water surface mask product (2000-2001) at a spatial resolution of 250 m using MODIS data in combination with the 30 m Shuttle Radar Topography Mission (SRTM) Water Body Dataset (SWBD) and the 125 m Mosaic of Antarctica (MOA) dataset. The binary water product was generated using an automated regression tree classification. The advantages of using the SWBD include the fine spatial resolution of 30 m, the relatively short temporal resolution of 11-days, and the superior performance of using radar data over multispectral and optical data, when it comes to cloud penetration efficiency in cloudy regions. The MODIS 250 m 16-day (MOD44C) was used mainly to map the 250 m water/land global mask but also to fill the gaps where the SWBD

was not available. The results demonstrate that the 250 m water mask showed strong agreement with the NLCD dataset since 98% of the surface water areas intersected between both datasets. Nevertheless, the water surface area was overestimated by 18% in the 250 m water mask in comparison with the NLCD product. This overestimation was attributed to the coarser spatial resolution of MODIS compared with the NLCD 30 m, as small shore areas can be difficult to delineate using coarse spatial resolutions.

2.3. Mapping and quantifying continental LC change

2.3.1. Asia

Asia is the largest and most populous continent globally with a total land area of 44.6 million km^2, covering more than one-third of the total iceless land area of the planet (Dong *et al.*, 2012). In recent decades, the Asian continent has witnessed major anthropogenic and climatic driven LC changes including urban expansion with large losses in neighbouring agricultural land (Shi *et al.*, 2016), unprecedented deforestation rates with associated commodity crops expansion (Stibig *et al.*, 2014), cropland abandonment (Chen *et al.*, 2013), land degradation (Kaplan *et al.*, 2014) and shrinkage of inland water bodies (Shen *et al.*, 2019). Table 2.3 summarises continental, regional and national LC mapping attempts in Asia, listed in chronological order.

2.3.1.1. LC mapping efforts across South and Southeast Asia

One of the earliest attempts to map LC extent in Asia was by Stibig *et al.* (2007). They mapped LC types of South and Southeast Asia at 1 km spatial resolution for the year 2000. Researchers continued to give considerable attention to mapping LC over Southeast Asia, particularly after rising rates of deforestation were reported during the late 1990s and the early 2000s (Miettinen *et al.*, 2012, 2016). The extent of LC in Southeast Asia was mapped in 2010 (Miettinen *et al.*, 2012) and 2015 (Miettinen *et al.*, 2016) at a spatial resolution of 250m, achieving an overall accuracy of more than 85%. Klein *et al.* (2012) mapped the LC types of Central Asia for the years 2001 and 2009 at a spatial resolution of 250 m whilst Li *et al.* (2014) and Qin *et al.* (2015) mapped forest cover in China for the year 2010 at spatial resolutions of 30 m and 50 m, respectively. Moreover, with recent advancements in EO and image processing, national LC mapping attempts have started taking place at relatively fine spatial resolutions (e.g., Japan (Sharma *et al.*, 2016), Vietnam (Hoang *et al.*, 2020)).

Table 2.3. Continental, regional and national LC mapping attempts in Asia listed in chronological order

Study Coverage	Mapped LC Type	Satellite Sensor	Spatial Resolution	Year of Mapping	Classification Method	Classification Scheme	Overall Accuracy (%)	Reference
South and Southeast Asia	Multiple LC types	SPOT-VGT (GLC2000)	1 km	2000	Unsupervised ISODATA	FAO LCCS (26 LC classes)	72.0	Stibig *et al.* (2007)
Insular Southeast Asia	Multiple LC types	MODIS ALOS-PALSAR	250 m	2010	Unsupervised ISODATA	(13 LC classes)	85.3	Miettinen *et al.* (2012)
Central Asia	Multiple LC types	MODIS-NDVI	250 m	2001 2009	Supervised DT C5.0 algorithm	FAO LCCS (13 LC classes)	91.2	Klein *et al.* (2012)
China	Forest cover	Landsat TM MODIS-EVI	30 m	2010	Supervised (RF-MLA)	IGBP (6 forest classes)	72.7	Li *et al.* (2014)
East and Southeast Asia	Urban land	MODIS-NBAR MODIS-EVI	250 m	2010	Supervised DT C4.5 algorithm	Urban/non-urban	84.0	Mertes *et al.* (2015)
China	Forest cover	ALOS-PALSAR MODIS-NDVI	50 m	2010	Supervised DT algorithm	Forest/non-forest	96.2	Qin *et al.* (2015)
Southeast Asia	Multiple LC types	MODIS Sentinel-1	250 m	2015	Unsupervised ISODATA	18 LC classes	82.0 - 86.0	Miettinen *et al.* (2016)
Japan	Multiple LC types	Landsat-8 OLI	30 m	2013 - 2015	Supervised (RF-MLA)	7 LC classes	88.6	Sharma *et al.* (2016)
Central Asia	Forest cover	Landsat-5/7 MODIS-VI	250 m	2010	Supervised (RF-MLA)	IGBP (3 forest classes)	83.0	Yin *et al.* (2017)
Central Asia, China	Cropland	Landsat-5/7/8	30 m	2001 – 2016	Supervised (RF-MLA)	Cropland/non-cropland	92.6 - 97.9	Hao *et al.* (2018)
Southeast-Northeast Asia	Cropland	Landsat-7/8 ETM+/OLI	30 m	2013 - 2016	Supervised (RF-MLA)	Cropland/non-cropland	88.6	Oliphant *et al.* (2019)
Vietnam	Forest cover	PALSAR-2 MODIS-NDVI	50 m	2015 - 2018	Probabilistic KDEC-MLA	Forest/non-forest	86.6	Truong *et al.* (2019)
South Asia	Cropland	Landsat-8 OLI	30 m	2015	Supervised (RF-MLA)	Cropland/non-cropland	88.7	Gumma *et al.* (2020)
Vietnam	Multiple LC types	PALSAR-2 Sentinel-1/2	50 m	2016	Probabilistic KDEC-MLA	FAO LCCS (12 LC classes)	85.6	Hoang *et al.* (2020)

Southeast Asia contains the third-largest (only after the Amazon and the Congo basin) global area of tropical humid rainforests (Dong *et al.*, 2012), with one of the most diverse humid-forest ecosystems in the world, providing habitats for millions of indigenous people and thousands of mammal and plant species. The alarming rates of deforestation in Southeast Asia and the substantial amount of tropical forest cleared and converted to commodity crops (e.g., palm oil plantations), have received considerable attention from leading global researchers (Miettinen *et al.*, 2016; Dong *et al.*, 2012). These persistent losses in tropical rainforests cause crucial threats to the ecosystem services and major implications for the sustainability of the global carbon sink (Stibig *et al.*, 2007).

Between 1990 and 1997, Southeast Asia lost the world's second-largest area of tropical rainforest (130,000 km^2) and experienced the highest annual deforestation rate globally (Achard *et al.*, 2002). Similarly, more recent studies (Achard *et al.*, 2014; Stibig *et al.*, 2014), report tropical forest losses of 317,000 km^2 to 329,000 km^2 between 1990 and 2010. The expansion of commodity plantations (e.g., palm oil and timber) via large-scale industrial logging, was the main driver of deforestation in Southeast Asia (Stibig *et al.*, 2014), with 78% of the deforestation being attributed to the expansion of commodity crops between 2001 and 2015 (Curtis *et al.*, 2018).

Miettinen *et al.* (2011) analysed and quantified deforestation rates in insular Southeast Asia between 2000 and 2010, estimating an overall loss of 110,000 km^2 with an annual decline of 1%, suggesting that 10% of the tropical forest extent in 2000 was lost by the year 2010. Borneo is the largest island in Asia and the third largest globally with an area equivalent to the size of Zambia or Chile. It includes large parts from Indonesia, Malaysia and Brunei. Gaveau *et al.* (2014) quantified historical rates of deforestation in Borneo between 1973 and 2010 revealing that the island had lost 168,500 km^2 of its tropical rainforest by the year 2010, due to the expansion of palm oil, timber and rubber plantations. Indonesia contains about 40% of the tropical rainforest extent in Southeast Asia and is one of the major global agricultural producers (Achard *et al.*, 2002).

Indonesia is the largest global producer of palm oil, second for rubber plantations, third for rice and cocoa and fourth for coffee. The country witnessed a significant amount of deforestation over recent decades, with rates twice and three times higher than corresponding rates for DR Congo and Brazil, respectively (Turubanova *et al.*, 2018). Sumatra, is the second largest island in Asia and the sixth largest globally, with an area equivalent to the size of Uzbekistan. The island, similar to Borneo, has experienced extensive

deforestation (99,000 km^2) due to the expansion of commodity crop plantations (e.g., palm oil, rubber and timber) between 1990 and 2010, suggesting that 70% of the tropical forest extent in Sumatra was lost in two decades (Margono *et al.*, 2012).

Despite recently implemented global policies of "Zero Deforestation", palm oil plantations have expanded significantly in the Indonesian islands of Sumatra, Kalimantan (i.e., the Indonesian part of Borneo) and Papua (Austin *et al.*, 2017). Between 1995 and 2015, palm oil plantations expanded by 90,000 km^2 with associated losses (23,000 km^2) in humid natural forests (Austin *et al.*, 2017). Austin *et al.* (2019) quantified the major drivers of deforestation across the main islands of Indonesia, concluding that palm oil plantations accounted for the largest contribution to deforestation (23%), followed by small-scale agriculture (15%), timber plantations (14%) and large-scale plantations of other crops such as coffee and cocoa (7%) between 2001 and 2016.

Annual maps of palm oil extent in Indonesia and Malaysia between 2001 and 2016 were produced by Xu *et al.* (2020). The maps were generated at a spatial resolution of 100 m using ALOS-PALSAR and MODIS NDVI data. Palm oil plantations witnessed a net expansion of 96,600 km^2 (322%) in Indonesia and 38,000 km^2 (147%) in Malaysia, between 2001 and 2016 (Xu *et al.*, 2020). Palm oil is one of the most rapidly expanding commodity crops being grown across the tropics at the expense of natural forests and numerous adverse implications for ecosystem services and biodiversity have been reported (Fitzherbert *et al.*, 2008). Elsewhere in Southeast Asia, in Malaysia, a recent report revealed that the tropical forest extent has decreased by 21%, whilst agricultural land increased by 56% (33,500 km^2), between 1990 and 2017 (Yan *et al.*, 2020). Somewhat similar to Indonesia, the expansion of palm oil and natural rubber plantations was the main cause of deforestation in Malaysia. Malaysia is the second and sixth largest global producer for palm oil and natural rubber, respectively (Yan *et al.*, 2020).

Vietnam is also one of the major global agricultural producers since it is the second largest for coffee, third for natural rubber and fifth for rice and tea. A report on the status of deforestation in the Central Highlands of Vietnam showed that net deforestation in the region has accounted for 3% of the total areal extent between 2000 and 2010 (Meyfroidt *et al.*, 2013). Shifting cultivation was the main direct driver of deforestation, whereas the expansion of commodity crops (e.g., coffee) was the main indirect driver. A more recent report revealed that between 2000 and 2010 a total of 17,700 km^2 of natural forest were removed due to economic and societal factors including commodity crop expansions,

population increase and poverty (Khuc *et al.*, 2018). Myanmar is the sixth largest global producer for rice and the tenth for rubber. Hence, cropland plantations have greatly expanded in the country at the expense of natural forests.

Between 2001 and 2010, a total of 21,200 km^2 of natural forest were lost in Myanmar (Wang and Myint, 2016). Moreover, between 2002 and 2014, the net deforestation in Myanmar totalled 20,700 km^2, whereas cropland plantations increased by 5,400 km^2 (Bhagwat *et al.*, 2017). Recently, between 1988 and 2017, the net natural forest extent declined by 100,000 km^2, whilst cropland plantations saw a net gain of 69,000 km^2 (Yang *et al.*, 2019). The expansion of rubber, sugarcane and palm oil plantations was the major deforestation driver in Myanmar (Bhagwat *et al.*, 2017). Paddy rice is an essential crop in Cambodia, although the national paddy rice yields are the lowest in Southeast Asia and are much lower than the corresponding yields in Thailand and Vietnam (Poffenberger, 2009). Therefore, due to low yields from existing rice farmland, large areas of natural forest have been cleared to expand paddy rice cultivations. Between 2000 and 2016, the net deforestation was estimated at 16,100 km^2, equalling 22% of the total natural forest extent in Cambodia (Magliocca *et al.*, 2020).

2.3.1.2. Urban expansion over China and elsewhere in Asia

Asia witnessed the largest area of agricultural land loss due to urban expansion globally, particularly in China (Shi *et al.*, 2016). Due to the rapid population growth and economic development in China starting from the early 1990s, urban area has expanded substantially at the expense of arable land, with rising concerns for national food security (Cai *et al.*, 2013; Shi *et al.*, 2016). Between 1990 and 2000, urban area has increased by 71% in Beijing, Tianjin and Hebei. Of the new urban land in 2000, 74% had been converted from former agricultural land (Tan *et al.*, 2005). In Beijing, urban land increased from 5% of the total land area in 1978 to 16% of the total land area in 2010, whereas agricultural land declined from 41% of the total land area in 1978 to only 25% of the total land area in 2010 (Tian *et al.*, 2014).

In Shanghai, urban land has increased by 2,700 km^2 between 1979 and 2009, an increase of 1,064%, whilst agricultural land has decreased by 2,535 km^2 (47%), suggesting that 93% of land that was converted to urban was originally arable land (Yin *et al.*, 2011). In China as a whole, between 1990 and 2010, a total of 41,800 km^2 of agricultural land has been converted to urban land, this loss equalling 2.3% of the national area for agricultural land (Cai *et al.*, 2013). The amount of agricultural land converted to urban areas between 2000 and 2010 was almost twofold of the converted area between 1990 and 2000. Furthermore, across the

whole of China, between 2001 and 2013, a total of 33,100 km^2 of arable land was lost due to urban expansion, with urban areas increasing by 49,800 km^2, suggesting that 66% of the new urban land in 2013 was converted from agricultural land (Shi *et al.*, 2016).

Elsewhere in Asia, urban land continued to expand at the expense of cropland. In India as a whole, a total of 7,000 km^2 of agricultural land were converted to built-up land between 2001 and 2010, an area five times the size of Delhi (Pandey and Seto, 2015). In Bangladesh, urban land expanded in Greater Dhaka by 106 km^2, representing a 90% growth in urban areas between 1975 and 2003, whilst cultivated land declined by 30% (Dewan and Yamaguchi, 2009). In Nepal, built-up land increased from 221 km^2 in 1989 to 930 km^2 in 2016 (320%), with former agricultural land accounting for 93% of the new urban areas in 2016 (Rimal *et al.*, 2018b). In Japan, urban land has increased in Tokyo to cover 24% of the total city land area in 2011 having covered only 10% in 1972, whereas agricultural land declined from 41% to 29% over the same period (Bagan and Yamagata, 2012). Urban expansion was also pronounced in other Asian nations including Iran (Jokar Arsanjani *et al.*, 2013), Pakistan (Bhatti *et al.*, 2015), Uzbekistan (Conrad *et al.*, 2015), Thailand (Estoque and Murayama, 2015) and Vietnam (Nong *et al.*, 2018).

2.3.1.3. LC mapping efforts across Central Asia

Other large-scale LC changes were reported in Asia, one of which is cropland abandonment, particularly in Central Asia with former Soviet Union nations (Chen *et al.*, 2013). In Central Asia, between 1990 and 2009, large areas of cropland were abandoned and converted to natural vegetation, particularly after the Soviet Union collapsed in 1991 (Chen *et al.*, 2013). Nevertheless, increases in cropland were reported (Hu and Hu, 2019) from the beginning of the 2000s onwards. Cropland has declined dramatically by 489,000 km^2, a 48% decrease in cropland in one decade between 1990 and 2000. Conversely, between 2000 and 2009, cropland extent increased by 162,000 km^2, suggesting that between 1990 and 2009, cropland area has decreased by 32% (Chen *et al.*, 2013). Desertification and natural vegetation degradation were reported in arid Turkmenistan between 1974 and 2003, mainly due to anthropogenic drivers including livestock overgrazing (Kaplan *et al.*, 2014).

The Aral Sea used to be the world's fourth largest lake but started to shrink from the early 1960s onwards (Shen *et al.*, 2019). This was due to anthropogenic drivers including extensive agricultural activities and diversions of the feeding rivers by former Soviet Union-led agricultural projects in Central Asia (Kazakhstan and Uzbekistan) in addition to climate change. This has led to vast salt-covered areas with implications for the surrounding habitats

and ecosystems. The disappearance of the Aral Sea is widely recognised as one of the world's worst environmental disasters in modern human history (Shen *et al.*, 2019). A recent report revealed that, between 1977 and 2015, the area of the Aral Sea declined by 82% with the water being replaced by bare land with salty soils (Shen *et al.*, 2019). The shrinkage of Lake Urmia in Iran is another example of the adverse implications of LULC change (AghaKouchak *et al.*, 2015). It used to be the world's sixth largest saltwater lake; however, it started shrinking in the 1970s due to anthropogenic drivers (e.g., damming, and intensive agricultural practices) and climatic factors (e.g., droughts). The lake's area has declined by 88% between 1972 and 2014 (AghaKouchak *et al.*, 2015).

2.3.2. Africa

Africa is the second largest continent globally with a total land area of 30.3 million km^2. It is recognised as a region of extensive societal, demographic, economic, climatic and ecological diversity (Serdeczny *et al.*, 2017; Brink and Eva, 2009). Historically, it has been reported that Africa was the most challenging continent globally to map during the process of generating a global LC product (Hansen *et al.*, 2000; Gong *et al.*, 2013). This is due to the vast disparities in the nature and characteristics of vegetation cover across the continent, ranging from the grasslands and shrublands of the Sahel belt to the savanna woodlands of the *Miombo*, the xeric sparse vegetation of the Namib and Kalahari Deserts, and the tropical rainforests of the Congo basin (Brink and Eva, 2009; Fenta *et al.*, 2020). Table 2.4 summarises continental, regional and national LC mapping attempts in Africa, listed in chronological order.

2.3.2.1. Major LC changes and their causes across Africa

In recent decades, Africa has experienced substantial LC changes including agricultural expansion at the expense of tropical rainforests (Mayaux *et al.*, 2013; Malhi *et al.*, 2013), dry forests (Jew *et al.*, 2017; Bodart *et al.*, 2013), natural vegetation and biodiversity (Searchinger *et al.*, 2015; Kehoe *et al.*, 2017), land degradation (Symeonakis and Drake, 2004) and greening of the Sahel (Brandt *et al.*, 2015). This has occurred in response to a variety of anthropogenic and climatic drivers (Brink and Eva, 2009), including population growth (Defries *et al.*, 2010), armed conflicts and civil wars (Nackoney *et al.*, 2014), mining (Wegenast *et al.*, 2019), urbanisation (Forget *et al.*, 2021), smallholder and industrial loggings (Rudel, 2013), migrations (Salerno *et al.*, 2017), increasing rainfall, droughts, and rising temperatures (Serdeczny *et al.*, 2017).

Table 2.4. Continental, regional and national LC mapping attempts in Africa listed in chronological order

Study Coverage	Mapped LC Type	Satellite Sensor	Spatial Resolution	Year of Mapping	Classification Method	Classification Scheme	Overall Accuracy (%)	Reference
Entire Africa	Multiple LC types	NOAA-AVHRR	4 km	1982 - 1983	Principal component	7 vegetation classes	N/A	Tucker *et al.* (1985)
Entire Africa	Multiple LC types	SPOT-VGT (GLC2000)	1 km	2000	Unsupervised ISODATA	FAO LCCS (27 LC classes)	N/A	Mayaux *et al.* (2004)
Sub-Saharan Africa	Rainforest cover	MODIS	250 m	2005	Unsupervised ISODATA	3 forest classes	84.0	Mayaux et *al.* (2013)
West Africa	Multiple LC types	MODIS VI ASAR-TDX/TSX	250 m	2006	Supervised (RF, DT-MLA)	IGBP (14 LC classes)	73.0	Gessner *et al.* (2015)
Entire Africa FROM-GLC v.1	Multiple LC types	Landsat-8 OLI Landsat-5, 7	30 m	2014	Supervised (RF-MLA)	FROM-GLC (10 LC classes)	71.0	Feng et *al.* (2016a)
Entire Africa	Cropland	MODIS NDVI	250 m	2003 - 2014	Supervised DT algorithm	3 cropland classes	89.0	Xiong *et al.* (2017a)
West Africa Sud. Savanna	Cropland	Landsat-8 OLI MODIS VI, LC	250 m	2013	Supervised (RF-MLA)	4 LC classes	81.0	Forkuor *et al.* (2017)
Entire Africa	Multiple LC types	Landsat-7 ETM+	30 m	2000 - 2015	Supervised (RF, DT-MLA)	7 LC classes	88.0	Midekisa *et al.* (2017)
Entire Africa	Cropland	Sentinel-2 MSI Landsat-8 OLI	30 m	2015	Supervised (RF, SVM-ML)	Cropland/non-cropland	94.5	Xiong *et al.* (2017b)
Entire Africa FROM-GLC v.2	Multiple LC types	Landsat-8 OLI MODIS NDVI	30 m	2015	Supervised (RF-MLA)	FROM-GLC (10 LC classes)	75.8	Feng *et al.* (2018)
Southern Africa	Savanna Woody cover	Landsat-5, 7 ALOS-PALSAR	30 m	2008	Supervised (RF-MLA)	FAO LCCS (4 LC classes)	73.7 - 91.1	Symeonakis *et al.* (2018)
Liberia and Gabon	Multiple LC types	Landsat-8 OLI	30 m	2015	Supervised (RF-MLA)	10 LC classes	81.0 - 83.0	De Sousa *et al.* (2020)
West African Sahel	Cropland	Landsat-8 OLI	30 m	2015	Supervised (RF-MLA)	Rainfed, Irrigated, non	90.1	Samasse *et al.* (2020)

Agricultural expansion (e.g., subsistence farming and commodity crops) across Africa is a major driver of LC change (Brink and Eva, 2009; Ordway *et al.*, 2017a), particularly in Eastern and South-eastern Africa where cropland areas (e.g., tobacco) expand at the expense of woodlands (e.g., *Miombo* woodlands). This has been widely supported by a number of recent studies (Bullock *et al.*, 2021; Jew *et al.*, 2017; Ryan *et al.*, 2016). Growing concerns have risen recently in relation to the expansion of commercial agriculture for export markets, with cocoa being the fastest growing cash crop across SSA (Ordway *et al.*, 2017a).

2.3.2.2. LC mapping efforts across Africa

The earliest attempt to map LC types in Africa was performed by Tucker *et al.* (1985) during 1982-1983 at a spatial resolution of 4 km using AVHRR data. In 2004, the LC types of Africa were mapped (Mayaux *et al.*, 2004) for the year 2000 at a spatial resolution of 1 km based on the SPOT-VGT GLC2000 product. However, during these early days of generating continental-scale LC products, reporting uncertainty estimates was not a common approach. Rainforest cover at the SSA scale was mapped (Mayaux *et al.*, 2013) for the year 2005 at a relatively higher spatial resolution compared to previous studies using MODIS data, reporting an overall accuracy of 84%.

Feng *et al.* (2016a) mapped all major LC types for the whole of Africa (FROM-GLC Africa v.1) using Landsat data (30 m) for the year 2014, achieving an overall accuracy of 71%. This study is one of the first studies that used Landsat data to map LC extent across Africa. More recently, and also using Landsat data, Midekisa *et al.* (2017) mapped all main LC types for Africa were mapped annually between 2000 and 2015, achieving an overall accuracy of 88%. Cropland extent across the continent was mapped at a spatial resolution of 30 m using Landsat-8 OLI and Sentinel-2 MSI on GEE for the year 2015, reporting an overall accuracy of 94.5% (Xiong *et al.*, 2017b). The same 10 LC classes across Africa from Feng *et al.* (2016a) were mapped using 30 m spatial resolution of Landsat-8 OLI. However, this time, the mapping process was performed for the year 2015 (FROM-GLC Africa v.2), achieving a higher overall accuracy of 75.8% (Feng *et al.*, 2018).

2.3.3. Latin America and the Caribbean (LAC)

Latin America and the Caribbean (LAC) contains the largest area of tropical rainforests in the world with the richest biodiversity including thousands of plants, birds, and mammal species (Aide *et al.*, 2013; Eva *et al.*, 2004). LAC also harbours the largest aboveground carbon stock globally, hence, helping the Earth in combatting global climate change by reducing carbon emissions (Baccini *et al.*, 2012; Aide *et al.*, 2013). Agricultural expansion (e.g., cropland,

pastureland) at the expense of tropical forests (e.g., humid, dry) continues to contribute greatly to LC change in LAC, and is considered a major driver of environmental change not only in LAC but also globally (Hansen *et al.*, 2013; Aide *et al.*, 2013). As a consequence, deforestation across LAC causes losses in the continental and global biodiversity (Kehoe *et al.*, 2017), alterations in the global carbon cycle with increases in carbon emissions (Baccini *et al.*, 2012) and disturbances for the terrestrial ecosystem services (Foley *et al.*, 2005).

2.3.3.1. LC mapping efforts across the LAC region

Early attempts to map LC in South America (Townshend *et al.*, 1987; Stone *et al.*, 1994; Eva *et al.*, 2004) were based on coarse spatial resolution data (e.g., 4 km, 1 km, and 500 m). The entirety of LAC was mapped (Clark *et al.*, 2012; Aide *et al.*, 2013) annually from 2001 to 2010 at a spatial resolution of 250 m using MODIS NDVI and EVI data (MOD13Q1). These two studies were among the first to map LC changes across the whole region at a relatively high spatial resolution, and achieved better overall classification accuracies than previous coarser resolution-based studies (Townshend *et al.*, 1987; Stone *et al.*, 1994; Eva *et al.*, 2004). Forest cover in LAC exhibited a net loss of 180,000 km^2 between 2001 and 2010 with 540,000 km^2 from gross deforestation and 362,000 km^2 from gross reforestation via forest regeneration/tree plantation (Aide *et al.*, 2013). Deforestation was most prevalent in South America, in Brazil, Argentina, Bolivia, and Paraguay, which collectively account for 80% of the total amount of deforested area in the whole of LAC. In contrast, Venezuela and Colombia experienced the largest net gains in forest cover in South America (Aide *et al.*, 2013). Table 2.5 summarises continental, regional and national LC mapping attempts in LAC, listed in chronological order.

The Caribbean region, conversely, witnessed an overall net gain in forest cover, mainly in Cuba whilst Jamaica and Trinidad and Tobago exhibited the largest net losses. Mexico and Central America have also, interestingly, experienced an overall net gain in forest cover, primarily in Mexico, Honduras and Cost Rica. However, in Central America, Guatemala and Nicaragua experienced the largest net forest losses in the region (Aide *et al.*, 2013; Clark *et al.*, 2012). Furthermore, a study performed by Eva *et al.* (2012) within the tropical region of LAC estimated that the net deforestation was 480,000 km^2 between 1990 and 2005, largely due to cropland and pasture expansions. The most recent attempt to map LC in the entirety of South America (Giri and Long, 2014), has managed to map 6 LC types in 2010 at a spatial resolution of 30 m, using Landsat-based observations with an overall accuracy of 89%.

Table 2.5. Continental, regional and national LC mapping attempts in LAC listed in chronological order

Study Coverage	Mapped LC Type	Satellite Sensor	Spatial Resolution	Year of Mapping	Classification Method	Classification Scheme	Overall Accuracy (%)	Reference
Entire South America	Multiple LC types	NOAA-AVHRR	4 km	1982 - 1983	Supervised MLC	16 LC classes	N/A	Townshend *et al.* (1987)
Entire South America	Multiple LC types	NOAA-AVHRR	1 km	1987 - 1991	Unsupervised clustering	39 LC classes	N/A	Stone *et al.* (1994)
Entire South America	Multiple LC types	SPOT-VGT ATSR-2, DMSP	1 km	2000	Unsupervised ISODATA	FAO LCCS (10 LC classes)	N/A	Eva *et al.* (2004)
Mesoamerica	Multiple LC types	MODIS MOD09GA	500 m	2003	Supervised DT C4.5 algorithm	IGBP (9 LC classes)	77.3	Giri and Jenkins (2005)
The Dry Chaco ecoregion	Multiple LC types	MODIS VI MOD13Q1	250 m	2001 - 2007	Supervised (RF, DT-MLA)	8 LC classes	79.3	Clark *et al.* (2010)
Honduras	Multiple LC types	MODIS LCT 500 m	500 m	2009	Supervised DT algorithm	IGBP (11 LC classes)	76.0	Rivera *et al.* (2012)
Mexico	Multiple LC types	MODIS TOA	250 m	2005	Supervised DT C5.0 algorithm	FAO LCCS (15 LC classes)	82.5 - 83.4	Colditz *et al.* (2012)
Entire Latin America (LAC)	Multiple LC types	MODIS VI MOD13Q1	250 m	2001 - 2010	Supervised (RF, DT-MLA)	8 LC classes	80.2 ± 8.1	Clark *et al.* (2012)
Entire Latin America (LAC)	Multiple LC types	MODIS VI MOD13Q1	250 m	2001 - 2010	Supervised (RF, DT-MLA)	8 LC classes	84.6 ± 6.5	Aide *et al.* (2013)
Latin America (SERENA)	Multiple LC types	MODIS MOD09GA	500 m	2008	Supervised DT C5.0 algorithm	FAO LCCS (22 LC classes)	84.2	Blanco *et al.* (2013)
Entire South America	Multiple LC types	Landsat-5/7 TM, ETM+	30 m	2010	Supervised (RF, DT-MLA)	FAO LCCS (6 classes)	89.0	Giri and Long (2014)
Chile	Multiple LC types	Landsat-8 OLI MODIS EVI	30 m	2014	Supervised (RF, DT-MLA)	FROM-GLC (9 LC classes)	80.0	Zhao *et al.* (2016)
Entire South America	Forest cover	MODIS NDVI ALOS PALSAR	50 m	2007 - 2010	N/A	Forest/non-forest classes	98.0 ± 0.12	Qin *et al.* (2017)

2.3.3.2. Drivers of tropical deforestation across South America

Soybean expansion in South America is prevalent and was reported to be a profound driver of LC change in the continent (Fehlenberg *et al.*, 2017). A recent study (Song *et al.*, 2021) used MODIS data and Landsat TM, ETM+ and OLI observations to map the expansion of soybean in the South American continent between 2000 and 2019, annually. The cultivated area of soybean in South America has increased from 264,000 km^2 in 2001 to 551,000 km^2 in 2019, a twofold increase in two decades (Song *et al.*, 2021). Across the continent, the main source for new soybean-land was former pastures (indirectly converting from former forest), whilst only 10% of the forest cover loss was directly converted to new soybean-land by 2019. Half of the deforestation driven by soybean expansion occurred in the Brazilian Cerrado ecoregion, whilst the other half was distributed among other regions including the Argentine and Paraguayan Gran Chaco (Song *et al.*, 2021). In Brazil, the soybean area increased from 134,000 km^2 in 2001 to 342,000 km^2 in 2019 (Brazil is the current second largest global soybean producer). In Argentina, the area of soybean production increased from 114,000 km^2 in 2001 to 163,000 km^2 in 2019 (Argentina is the current third largest global soybean producer).

The Brazilian Amazon has witnessed historical losses of natural tropical rainforests, with accelerating deforestation rates due to the associated dramatic expansions of cropland (e.g., soybean) and pastures (e.g., cattle ranching for beef production; Brazil is the current second global beef producer) (Barona *et al.*, 2010; Morton *et al.*, 2006). This phenomenon is evident across several areas of the Brazilian Amazon including the state of Mato Grosso, a state of similar size to Venezuela and the third largest in Brazil (Barona *et al.*, 2010). Between 2001 and 2004, more than 5,400 km^2 of natural forest were removed due to soybean and pasture expansions within the Brazilian Mato Grosso region (Morton *et al.*, 2006).

Between 2000 and 2010, about 169,000 km^2 of tropical rainforests were lost from the Brazilian Amazon region, with the majority of this area converting to agriculture-based land uses (Souza *et al.*, 2013). Tyukavina *et al.* (2017) quantified the amount of deforestation in the Brazilian Amazon between 2000 and 2013 and discussed the main drivers behind large-scale deforestation in this region. Their study estimated the forest loss in the Brazilian Amazon to reach 187,000 km^2. The main drivers behind forest removals were the agro-industrial clearing for pastures (63%), followed by small-scale clearing (12%), agro-industrial clearing for cropland (9%), wildfires (9%) and selective logging (7%).

De Sy *et al.* (2015) also investigated the main drivers of deforestation, but for the whole of South America. Pasture expansions, mainly for beef production was the dominant driver (71%) of deforestation, followed by commercial crops (14%). The study identified deforestation hotspots due to pasture expansion (e.g., Western Paraguay, Northern Argentina and the Brazilian Amazon), and commercial cropland expansion (e.g., Brazil's Mato Grosso state, Central Bolivia and Northern Argentina). Graesser *et al.* (2015) explored the dynamics between cropland/pasture expansion and deforestation across the entirety of Latin America between 2001 and 2013, revealing cropland and pasture expansions of 443,000 km^2 and 969,000 km^2, respectively. Moreover, former forest cover contributed 17% and 57% of new cropland and pastures, respectively.

More positively, a number of recent studies have reported slowing rates of deforestation within the Brazilian Amazon region (Nepstad *et al.*, 2014; Kastens *et al.*, 2017), particularly from 2004 onwards (Tyukavina *et al.*, 2017). This was attributed to better management by the Brazilian government, to counter exponential deforestation rates during the 1990s and the early 2000s (Nepstad et al., 2014). A "soybean moratorium" was enforced in 2006 by the government after a Greenpeace-led campaign to reduce the expansion of soybean production at the expense of tropical rainforests (Gibbs *et al.*, 2015; Kastens *et al.*, 2017). Deforestation rates prior to the soybean moratorium in 2006 were found to be five times more than the corresponding deforestation rates after enacting the new policy (Kastens *et al.*, 2017).

Elsewhere in South America, soybean and pasture expansions are not the only threat to the indigenous tropical rainforests and their biodiversity. Palm oil and cocoa plantations have also expanded across the South American continent (Furumo and Aide, 2017; Graesser *et al.*, 2015). Colombia, Ecuador and Peru are three of the largest 10 global producers of palm oil (Castiblanco *et al.*, 2013; Gutiérrez-Vélez *et al.*, 2011), whilst Brazil, Ecuador, Peru and Colombia are four of the top 10 global producers of cocoa. A recent study by Furumo and Aide (2017) sampled 342,000 hectares of palm oil plantations within Latin America, in Guatemala, Peru and Brazil and concluded that the vast majority of the new palm oil plantations (79%) came from former pastures and cropland, whilst 21% came from former forests and woodlands.

2.3.3.3. Drivers of dry forest losses across South America

While most studies have given considerable attention to investigating deforestation of the tropical humid forests in South America, alarming rates of deforestation have also been

reported across South America's tropical dry forests in recent decades (Fehlenberg *et al.*, 2017). Deforestation frontiers for South America's dry forests were observed and monitored in the Brazilian Cerrado ecoregion (Espírito-Santo *et al.*, 2016), the Argentine dry Chaco (Gasparri *et al.*, 2013), the Paraguayan dry Chaco (Baumann *et al.*, 2017) and the Bolivian lowlands (Killeen *et al.*, 2007). The expansions of soybean cultivations and pastures for cattle ranching, perhaps not surprisingly, are the major drivers of deforestation within the dry region of the continent (Fehlenberg *et al.*, 2017).

The South American Gran Chaco ecoregion is one of the global deforestation hotspots for dry forests and woodlands. Between 2001 and 2012, the amount of deforestation in the dry Chaco was estimated at 78,000 km^2, whilst areas cultivated with soybean have increased by 126% (Fehlenberg *et al.*, 2017). In the Brazilian Cerrado, between 2000 and 2015, a total of 9,500 km^2 of the tropical dry forests and woodlands were lost. This was due to expansions of soybean cultivations (Brazil is the largest global producer for soybean), cattle ranching (Brazil is the second largest global producer for beef), charcoal production and road networks (Espírito-Santo *et al.*, 2016).

In the Argentine Chaco (Northern Argentina), between 1972 and 2011, a total of 27,000 km^2 of the dry forests in the region were deforested (Gasparri *et al.*, 2013), whilst another report demonstrated that 23% of the Argentine Chaco's dry forests and woodlands were lost between 2000 and 2010 (Piquer-Rodríguez *et al.*, 2015). In the Paraguayan Chaco, between 1987 and 2012, a total of 44,000 km^2 of the region's dry forests and natural vegetation were lost, accounting for 27% of the extent of dry forests in 1987 (Baumann *et al.*, 2017), whilst between 2000 and 2011, a total of 11,400 km^2 were lost (Caldas *et al.*, 2015). Deforestation in Argentina (3rd and 6th largest global producer for soybean and beef) and Paraguay (6th largest global producer for soybean) was attributed to soybean and pasture expansions (Fehlenberg *et al.*, 2017).

However, in Paraguay, pastureland expansion for cattle ranching and beef production was more prevalent than in Argentina. In contrast, soybean cultivation expansion in Argentina was more predominant than in Paraguay (Caldas *et al.*, 2015; Gasparri *et al.*, 2013). In the Bolivian Chaco, between 1976 and 2004, about 45,000 km^2 of tropical forests were lost to soybean cultivations (Bolivia is the 10th largest global producer) and pastureland (Killeen *et al.*, 2007). Moreover, the expansion of coca plantations in Bolivia at the expense of forest was evident (Bagan *et al.*, 2020).

2.3.3.4. Drivers of LC change across Central America

Recent reports have raised crucial concerns about the increasing expansions in illegal cattle ranching activities relating to illegal cocaine trafficking (narcotics trafficking) in Central America, Guatemala (Devine *et al.*, 2020) and Nicaragua (Tobar-López *et al.*, 2019). Traffickers change the land use of a given area by deforesting and establishing pastures for livestock ranching or commercial agricultural plantations, as part of a money-laundering activity (McSweeney *et al.*, 2014; Sesnie *et al.*, 2017). Narcotics trafficking and its related illegal activities in Central America, has become one of the major drivers of forest cover decline in the region since the beginning of the 21st century (McSweeney *et al.*, 2014). A recent study estimated that narcotics trafficking accounted for 15% up to 30% of the annual forest loss in Guatemala, Nicaragua and Honduras, during the last decade (Sesnie *et al.*, 2017).

Shade-grown coffee, also referred to as coffee agroforests, is perhaps the most prominent commodity and profitable grown crop in Central America (Schmitt-Harsh, 2013). Currently, Honduras, Guatemala and Nicaragua are the 6th, 10th and 12th largest global producers of coffee, respectively. Therefore, the increasing of coffee production, and its associated global trade, contributes greatly to the national Gross Domestic Product (GDP) of these Central American countries and is considered one of the main pillars of their economies (Schmitt-Harsh, 2013). Due to the recent expansion of coffee plantations, particularly over the last two decades, substantial areas of natural forests have been lost as a consequence (Aide *et al.*, 2013; Schmitt-Harsh, 2013). Moreover, a recent report has demonstrated that palm oil plantations are also increasing rapidly in Honduras and Guatemala, with both countries being two of the largest 10 global producers of palm oil (Furumo and Aide, 2017).

2.3.4. North America

North America is the third largest continent in the world, with a vast forest cover of approximately 6 million km^2, accounting for 16% of the total global forest extent (Wulder *et al.*, 2008). Here, Mexico is excluded and considered as a Latin American nation. Several LC mapping studies have been conducted at the national scale (e.g., the USA and Canada), but few have considered the continent in its entirety.

2.3.4.1. LC mapping efforts across the USA

The North American Land Cover Monitoring System (NALCMS) joint initiative developed LC maps for the whole of North America, covering the USA, Canada and Mexico for the years

2005 and 2010 (Colditz *et al.*, 2014). The LC product was named the North American Land Cover Database (NALCD) and was generated at a spatial resolution of 250 m using MODIS monthly composites, resulting in a LC map with 19 classes and an overall accuracy of 68.5% (Colditz *et al.*, 2014). Change detection was performed between 2005 and 2010 data which revealed that 3,400 km^2 of cropland had been lost, whilst shrubland had increased by 24,000 km^2, grassland had increased by 39,000 km^2 whilst forest cover had decreased (mostly within the boreal region) by 58,000 km^2 (Colditz *et al.*, 2014). Table 2.6 summarises continental and national LC mapping efforts in chronological order.

The USGS NLCD, a Landsat-based (30 m) LC dataset developed by the Multi-Resolution Land Characteristics (MRLC) collaboration, and covers the conterminous USA (CONUS), was first released for the year 1992 in 2001 (Vogelmann *et al.*, 2001). It has since been released for the years 2001 (Homer *et al.*, 2007), 2006 (Fry *et al.*, 2011), 2011 (Homer *et al.*, 2015) and 2016 (Homer *et al.*, 2020), with overall accuracies that range from 79% to 86% for 2001 and 2016, respectively. Change detection between 2001 and 2016 data revealed that urban land increased by 28,600 km^2, agricultural land increased by 4,800 km^2 and grassland/shrubland also increased by 29,000 km^2. In contrast, forest cover decreased by 63,500 km^2 (Homer *et al.*, 2020).

Sleeter *et al.* (2013) quantified LC change in the CONUS between 1973 and 2000 using Landsat MSS, TM and ETM+ images for the years 1973, 1980, 1986, 1992 and 2000. About 8.6% of the total land area experienced a change between 1973 and 2000. Forest extent saw the largest net decrease (97,000 km^2) of all investigated LC types. Agricultural land also decreased by 90,000 km^2. Conversely, urban land and grassland/shrubland both increased by 78,000 km^2 and 49,000 km^2, respectively between 1973 and 2000. Hansen *et al.* (2014) quantified the decline in forest cover and increase in bare land across the CONUS for the period 2006-2010. This study was the first to use the USGS-EROS Web-Enabled Landsat Data (WELD) at a spatial resolution of 30m to map LC changes in the CONUS. Landsat-7 ETM+ and a DT classifier were utilised during the LC mapping procedure. Gross forest loss was 53,000 km^2 whilst gross bare land gain was 6,000 km^2 between 2006 and 2010.

Table 2.6. Continental, regional and national LC mapping attempts in North America listed in chronological order

Study Coverage	Mapped LC Type	Satellite Sensor	Spatial Resolution	Year of Mapping	Classification Method	Classification Scheme	Overall Accuracy (%)	Reference
Conterminous USA (NLCD)	Multiple LC types	Landsat-5 TM	30 m	1992	Unsupervised clustering	Anderson (21 LC classes)	60.0	Vogelmann *et al.* (2001)
North/Central America (NCA)	Multiple LC types	SPOT-VGT (GLC2000)	1 km	2000	Unsupervised ISODATA	FGDC-NVCS (28 LC classes)	N/A	Latifovic *et al.* (2004)
Canada	Multiple LC types	NOAA-AVHRR	1 km	1985 - 2000	Classification decision rule	12 LC classes	61.5	Latifovic and Pouliot (2005)
Conterminous USA (NLCD)	Multiple LC types	Landsat-5 TM Landsat-7 ETM	30 m	2001	Decision tree classifier	Anderson (16 LC classes)	78.8	Homer *et al.* (2007)
Canada (EOSD LC 2000)	Multiple LC types	Landsat-7 ETM+	30 m	2000	Unsupervised clustering	NFI (23 LC classes)	77.0	Wulder *et al.* (2008)
Northern Canada	Multiple LC types	Landsat-7 ETM SPOT-VGT	30 m	2000	Unsupervised clustering	15 LC classes	81.5	Olthof *et al.* (2009)
Conterminous USA (NLCD)	Multiple LC types	Landsat-5 TM Landsat-7 ETM	30 m	2006	Decision tree classifier	Anderson (16 LC classes)	78.0	Fry *et al.* (2011)
Canada	Multiple LC types	MODIS TOA	250 m	2000 - 2011	Decision tree classifier	FAO LCCS (19 LC classes)	70.0	Pouliot *et al.* (2014)
North America (NALCD)	Multiple LC types	MODIS month. composites	250 m	2005 - 2010	Decision tree classifier	FAO LCCS (19 LC classes)	68.5	Colditz *et al.* (2014)
Conterminous USA (NLCD)	Multiple LC types	Landsat-5 TM	30 m	2011	Decision tree classifier	Anderson (16 LC classes)	82.0	Homer *et al.* (2015)
Entire North America	Multiple LC types	Landsat-5/7 MODIS LCT	30 m	2010	Supervised (RF-MLA)	IGBP (16 LC classes)	N/A	Zhang and Roy (2017)
Canada	Multiple LC types	Landsat-5 TM Landsat-7 ETM	30 m	2010	Supervised (RF-MLA)	FAO LCCS (19 LC classes)	77.6	Latifovic *et al.* (2017)
Canada	Multiple LC types	Landsat-5 TM Landsat-7 ETM	30 m	1984 - 2012	Supervised (RF-MLA)	NFI (12 LC classes)	70.3 ± 2.5	Hermosilla *et al.* (2018)
Conterminous USA (NLCD)	Multiple LC types	Landsat-8 OLI Landsat-5/7	30 m	2016	Decision tree classifier	Anderson (16 LC classes)	86.4	Homer *et al.* (2020)

2.3.4.2. LC mapping efforts across Canada

In Canada, one of the early attempts to map LC in the forested area of Canada, annually between 1985 and 2005 using AVHRR data (1 km) was developed by Latifovic and Pouliot (2005). In 2008, the EOSD LC project was completed (Wulder *et al.*, 2008). The EOSD LC project was initiated as a collaboration between the Canadian Space Agency (CSA) and the Canadian Forest Service (CFS). The EOSD LC dataset uses Landsat-7 ETM+ data (30 m), hence, achieving much higher spatial resolution than previous LC mapping attempts in Canada. An annual LC product from 2000 to 2011 produced using MODIS calibrated radiance TOA data at a spatial resolution of 250 m, was released in 2014 (Pouliot *et al.*, 2014). The data revealed on the one hand, that needleleaf forest extent had decreased, particularly in the northern boreal region where forest regrowth rates are relatively slow. On the other hand, the broadleaf forest extent had increased, particularly in the Southeast of Canada where forest regrowth rates are relatively faster.

The forest decreases in the boreal region were attributed to natural and ecological factors including wildfires and damage caused by the mountain pine beetle infestations, with associated gains in shrubland and grassland (Pouliot *et al.*, 2014). In 2017, the most recent attempt to map the Canadian LC types was released with a main aim of providing a national LC map for the year 2010 at a spatial resolution of 30 m based on the utilisation of Landsat-5 TM and Landsat-7 ETM+ images (Latifovic *et al.*, 2017). Recently, GEE, Artificial Neural Network (ANN), Sentinel-2 and Sentinel-1 data have been used to produce a Canadian cropland map for 2018 at a spatial resolution of 10 m (Amani *et al.*, 2020a). The approach combined multi-temporal optical Sentinel-2 and SAR Sentinel-1 imageries since each satellite can capture different biophysical and spectral signatures of cropland, hence, compensating the potential limitations of utilising one type of imagery alone. The resulting product included 17 crop types at a spatial resolution of 10 m with an overall accuracy of 77%.

2.3.5. Europe

2.3.5.1. Major LC changes across Europe

The most profound LC changes across Europe over the last three decades are urban expansion (Triantakonstantis and Stathakis, 2015; Hennig *et al.*, 2015) and cropland abandonment (Schierhorn *et al.*, 2013; Meyfroidt *et al.*, 2016). Urban expansion at the expense of cropland was evident during the 1990s and early 2000s, leading to large losses in cropland (Hennig *et al.*, 2015). This phenomenon was widespread across most countries

in the European continent including Ukraine, Spain, Romania and Poland. Furthermore, dramatic cropland abandonment has occurred in Eastern Europe following the collapse of the Soviet Union in the early 1990s (Schierhorn *et al.*, 2013). Cropland abandonment was a profound phenomenon in Eastern Europe starting from the early 1990s, occurring in European Russia, Ukraine and Belarus (Schierhorn *et al.*, 2013). Similar patterns of cropland losses to natural vegetation were reported in former Soviet Union nations in Central Asia such as Kazakhstan and Uzbekistan (Meyfroidt *et al.*, 2016; Chen *et al.*, 2013).

2.3.5.2. LC mapping efforts across Europe

The CORINE Land Cover (CLC) product was the first available (launched in 1985) LC product generated specifically for Europe (Grekousis *et al.*, 2015). The CLC dataset was produced for the years 1990, 2000, 2006, 2012 and 2018 at a spatial resolution of 100 m (European Union, 2021), making it efficient in monitoring and analysing the historical LC change in Europe at a relatively fine resolution. It includes 44 LC classes within its Level-3 classification, 15 LC classes within its Level-2 classification and 5 major LC classes within its Level-1 classification, with an overall classification accuracy in excess of 85%, with the exception of CLC1990 (European Union, 2021). The CLC product has been used at the national scale in Europe for monitoring and analysing the status of LC change, including in France (Vizzari *et al.*, 2018), Spain (Martínez-Fernández *et al.*, 2019), Romania (Grigorescu *et al.*, 2021), Norway (Aune-Lundberg and Strand, 2021) and Greece (Gemitzi *et al.*, 2021).

GlobCorine is a LC product that was launched by the ESA in 2005 to cover the whole of Europe and parts of the Middle East and North Africa (MENA) region. The GlobCorine LC product was generated for the years 2005 and 2009 at a spatial resolution of 300 m, based on the observations of the Envisat Medium Resolution Imaging Spectrometer (MERIS) (Defourny *et al.*, 2010; Grekousis *et al.*, 2015). The LC product was generated using a hybrid supervised/unsupervised classification approach, achieving an overall accuracy of 78% and 80% for the years 2009 and 2005, respectively. GlobCorine includes a total of 14 LC classes based on the UN-FAO-LCCS and is compatible with the aggregated typology of the CLC product (Defourny *et al.*, 2010; Grekousis *et al.*, 2015). The most recent attempt to map the LC extent in Europe (ELC10) was generated for the year 2018 (Venter and Sydenham, 2021) at a spatial resolution of 10 m based on the satellite observations of Sentinel-2 MSI (Multispectral Instrument) and Sentinel-1 SAR. The ELC10 product was developed using machine learning algorithms and a RF classification technique, includes 8 major LC classes and has an overall accuracy of 90% (Venter and Sydenham, 2021).

The main LC product used to assess LC change in the United Kingdom (UK) is the UK Centre for Ecology and Hydrology (CEH) Land Cover Map (UKCEH-LCM). The UKCEH dataset is a satellite-derived LC product and is available for the years 1990, 2000, 2007, 2015, 2017, 2018 and 2019. The LCM1990, LCM2015, LCM2017, LCM2018 and LCM2019 were generated using a supervised RF algorithm and include 21 LC classes, whilst the LCM2000 and LCM2007 were produced using a supervised MLC algorithm and include 26 and 23 LC classes, respectively. LCM1990, LCM2000, LCM2007, LCM2015 were produced at a spatial resolution of 25 m based on the observations of Landsat TM, ETM+ and OLI. However, LCM2017, LCM2018 and LCM2019 have recently been generated at a spatial resolution of 20 m based on the observations of Sentinel-2 MSI (Rowland *et al.*, 2017; Morton *et al.*, 2020). Table 2.7 summarises continental and national LC mapping attempts in Europe, listed in chronological order.

2.3.6. Oceania

2.3.6.1. LC mapping efforts over Australia

The Dynamic Land Cover Dataset version 2.1 (DLCD v2.1) provides LC change information across the whole of Australia between 2001 and 2015 and is considered the first nationally consistent LC product (Lymburner *et al.,* 2015). The DLCD v2.1 product includes 22 LC classes and was generated at a spatial resolution of 250 m using information obtained from the MODIS EVI sensor (MOD13Q1). Recently, the first relatively high resolution (30 m), spatiotemporally consistent, time-series LC dataset for Australia was released (Calderón-Loor *et al.*, 2021). This LC dataset covers the period 1985 to 2015 and was derived from satellite images acquired from Landsat TM, ETM+ and OLI, using a supervised RF algorithm and GEE cloud computation approach. This LC product includes 6 major LC classes with an overall accuracy of 93%. Between 1985 and 2015, urban land increased by 19%, expanding primarily at the expense of grasslands. Conversely, both cropland and forest cover decreased by 9% and 8%, respectively (Calderón-Loor *et al.*, 2021). Table 2.8 summarises regional and national LC mapping attempts in Oceania, listed in chronological order.

Table 2.7. Continental and national LC mapping attempts in Europe

Study Coverage	Mapped LC Type	Satellite Sensor	Spatial Resolution	Year of Mapping	Classification Method	Classification Scheme	Overall Accuracy (%)	Reference
Entire Europe (CLC1990)	Multiple LC types	Landsat-5 MSS/TM	100 m	1986 - 1996	Visual Interpretation	44 LC classes Level-3	85.0	European Union (2021)
Entire Europe (CLC2000)	Multiple LC types	Landsat-7 ETM+	100 m	1999 - 2001	Visual Interpretation	44 LC classes Level-3	≥ 85.0	European Union (2021)
Entire Europe (GlobCorine)	Multiple LC types	Envisat MERIS	300 m	2005 2009	Supervised/ Unsupervised	FAO-LCCS (14 LC classes)	78.0 - 79.9	Defourny *et al.* (2010)
Entire Europe (CLC2006)	Multiple LC types	SPOT-4/5 IRS P6 LISS III	100 m	2005 - 2007	Visual Interpretation	44 LC classes Level-3	≥ 85.0	European Union (2021)
Entire Europe (CLC2012)	Multiple LC types	IRS P6 LISS III RapidEye	100 m	2011 - 2012	Visual Interpretation	44 LC classes Level-3	≥ 85.0	European Union (2021)
Entire Europe (CLC2018)	Multiple LC types	Sentinel-2 MSI Landsat-8	100 m	2017 - 2018	Visual Interpretation	44 LC classes Level-3	≥ 85.0	European Union (2021)
Entire Europe (ELC10)	Multiple LC types	Sentinel-2 MSI Sentinel-1 SAR	10 m	2018	Supervised Random Forest	8 LC classes	90.0	Venter and Sydenham, (2021)
UK (UKCEH)	Multiple LC types	Landsat-5, 7, 8 TM/ETM+/OLI	25 m	1990 2000 2007 2015	Supervised RF/MLC	21, 26, 23, 21 LC classes	83.0 (2007)	Rowland *et al.* (2017)
UK (UKCEH)	Multiple LC types	Sentinel-2 MSI	20 m	2017 - 2019	Supervised Random Forest	21 LC classes	78.6 - 79.6	Morton *et al.* (2020)

Table 2.8. Regional and national LC mapping attempts in Oceania listed in chronological order

Study Coverage	Mapped LC Type	Satellite Sensor	Spatial Resolution	Year of Mapping	Classification Method	Classification Scheme	Overall Accuracy (%)	Reference
Australia (CSIRO)	Forest cover	Landsat TM, ETM+	25 m	1989 - 2006	Supervised Decision Tree	Forest/non-forest LC classes	N/A	Lehmann *et al.* (2013)
Australia (DLCD v2.1)	Multiple LC types	MODIS EVI (MOD13Q1)	250 m	2001 - 2015	Support Vector Clustering	ISO 19144-2 (22 LC classes)	65.0	Lymburner *et al.* (2015)
Australia	Multiple LC types	Landsat-5, 7, 8 TM/ETM+/OLI	30 m	1985 - 2015	Supervised Random Forest	DLCD (Agg. 6 LC classes)	93.0	Calderón-Loor *et al.* (2021)

2.4. The ESA-CCI-LC dataset

Based on the provided comprehensive literature review, it is fair to say that the production of global LC products is a challenging task, with each global LC product being limited in one or more of the following: spatial coverage, spatial resolution, temporal coverage, thematic resolution, and accuracy assessment (Grekousis *et al.*, 2015; Ban *et al.*, 2015). Therefore, there is a crucial need for internally consistent satellite-derived global LC datasets with annual time-series to be used to accurately analyse and quantify changes in LC that take place over a range of spatial scales (Ban *et al.*, 2015; Chen *et al.*, 2015; Turner *et al.*, 2007). Hence, the ESA-CCI-LC product was deemed appropriate to fulfil the overarching aim of this thesis and has been used across subsequent analytical chapters.

The ESA-CCI-LC dataset (http://maps.elie.ucl.ac.be/CCI/viewer/) was released in 2017 by the recently launched CCI-LC programme which aimed to deliver reliable and consistent satellite-derived LC data with global coverage for climate modelling purposes (ESA, 2017; Mousivand and Arsanjani, 2019). The dataset provides spatiotemporally consistent global maps with a spatial resolution of 300 m, annually from 1992 to 2018 (ESA, 2017; Li *et al.*, 2018). The ESA-CCI-LC dataset provides the longest annual times-series of global LC to date, extending for 27 years. It is considered the most recent, consistent and up-to-date global LC product with relatively fine spatial resolution and annual time-series extending more than a quarter of a century (ESA, 2017; Li *et al.*, 2018).

The ESA-CCI-LC dataset was produced using global daily surface reflectance data from multiple EO sensors while aiming to deliver high spatiotemporal consistency (ESA, 2017; Li *et al.*, 2018), including the full archive of the 300 m Envisat MERIS from 2003 to 2012, the 300 m time-series of the Project for On-Board Autonomy-Vegetation (PROBA-V) from 2013 to 2015, the 1 km NOAA-AVHRR from 1992 to 1999, the National Centre for Space Studies (CNES) 1 km SPOT-VGT from 1999 to 2013 and the 1 km PROBA-V from 2014 to 2015 (ESA, 2017; Li *et al.*, 2018; Duan and Tan, 2019). This is different to most global LC datasets which are based on a single sensor or produced for a single year (ESA, 2017; Mousivand and Arsanjani, 2019).

ESA completed a series of pre-processing procedures on the derived LC dataset including radiometric calibration, atmospheric and geometric corrections (ESA, 2017; Li *et al.*, 2018). The ESA-CCI-LC dataset was generated using an unsupervised classification fused with machine learning algorithms (ESA, 2017; Li *et al.*, 2018; Mousivand and Arsanjani, 2019). The ESA-CCI-LC product represents all global LC classes and assigns them into a total of 37

LC classes, subdivided into 22 global LC classes (Level-1) and 15 regional LC classes (Level-2) according to the UN-FAO-LCCS (ESA, 2017; Di Gregorio, 2005). The overall accuracy of the ESA-CCI-LC product is estimated at 75.4%, which is considered more than satisfactory for global-coverage LC products (ESA, 2017; Ji *et al.*, 2020). Table 2.9 shows the original LC class codes and their corresponding descriptions.

Table 2.9. The ESA-CCI-LC original codes and LC class descriptions (ESA, 2017).

LC class codes in the ESA-CCI-LC dataset	Description of the LC classes in the ESA-CCI-LC dataset
10, 11, 12	Rainfed cropland
20	Irrigated cropland
30	Mosaic cropland (> 50%)/natural vegetation (tree, shrub, herbaceous cover) (< 50%)
40	Mosaic natural vegetation (tree, shrub, herbaceous cover) (> 50%)/cropland (< 50%)
50	Tree cover, broadleaved, evergreen, closed to open (> 15%)
60, 61, 62	Tree cover, broadleaved, deciduous, closed to open (> 15%)
70, 71, 72	Tree cover, needleleaved, evergreen, closed to open (> 15%)
80, 81, 82	Tree cover, needleleaved, deciduous, closed to open (> 15%)
90	Tree cover, mixed leaf type (broadleaved and needleleaved)
100	Mosaic tree and shrub (> 50%)/herbaceous cover (< 50%)
110	Mosaic herbaceous cover (> 50%)/tree and shrub (< 50%)
120, 121, 122	Shrubland
130	Grassland
140	Lichens and mosses
150, 151, 152, 153	Sparse vegetation (tree, shrub, herbaceous cover) (<15%)
160	Tree cover, flooded, fresh or brakish water
170	Tree cover, flooded, saline water
180	Shrub or herbaceous cover, flooded, fresh-saline or brakish water
190	Urban
200, 201, 202	Bare areas and sparse vegetation
210	Water
220	Permanent ice and snow

A few researchers have used the newly released ESA-CCI-LC dataset to explore the environmental change at various spatial scales. Li *et al.* (2018) investigated gross and net changes in Plant Functional Types (PFTs) at the global scale between 1992 and 2015. The results were compared with other LC datasets. Global forest cover in the year 2000 was estimated at 30.4 million km^2 which was found to be lower than that reported by Hansen *et al.* (2013). The global net forest decline between 1992 and 2015 was 0.6 million km^2. However, this study did not assess the LC change uncertainties (Li *et al.*, 2018). Liu *et al.* (2018b) quantified the LC transitions at the global scale from 1992 and 2015 using a

transition analysis method in order to identify global hotspots of LC change. The total area of LC change was estimated at 5.99 million km^2, equalling 3.4% of the total global land area. Forest cover and cropland exhibited the largest LC change, totalling 32% of all global LC changes. Most LC change that occurred in tropical regions was due to deforestation, with most cropland expansion taking place in tropical subtropical regions (Liu *et al.*, 2018b).

Duan and Tan (2019) investigated the spatiotemporal dynamics of forest cover change within developing countries between 1992 and 2015. Forest cover witnessed a net decline of 0.5 million km^2 over this period with South America experiencing the largest reductions in forest cover, then Asia, whilst Africa saw a slight overall net increase in forest cover. Mousivand and Arsanjani (2019) quantified changes in LC between 1992 and 2015 at the global scale. They revealed large-scale changes in LC across the world which they related to urbanisation, deforestation, afforestation and shrinkage of inland water bodies. Estoque *et al.* (2019) used the ESA-CCI-LC dataset as the main LC data for their study on forecasting the extent of forest cover of Southeast Asia until 2050. They concluded that a total of 52,000 km^2 of the natural forest would be lost by 2050 over southeast Asia.

van Vliet (2019) investigated the indirect and direct natural forest losses by cropland displacement and urban expansion, respectively, at the global scale between 1992 and 2015. He revealed that global urban area increased by 381,000 km^2, resulting in a direct loss in forest cover of 33,000 km^2 and indirect losses of 178,000 km^2 to 324,000 km^2 via the displacement of cropland. Nowosad *et al.* (2019), somewhat similar to Li *et al.* (2018), used the ESA-CCI-LC to quantify global LC change between 1992 and 2015, from a landscape ecology perspective. Lastly, Ji *et al.* (2020) quantified forest cover change in China between 1992 and 2015. The ESA-CCI-LC data was proven reliable, achieving good agreement in comparison with other LC products with finer spatial resolutions such as Hansen *et al.* (2013).

2.5. Modelling of LC change

2.5.1. Modelling of LC change detection

Following the recent advancements in the fields of RS and EO, monitoring global LC changes has become more available than ever before, with the utilisation of LC time-series derived from satellite imagery data (Masiliūnas *et al.*, 2021). An extended LC time-series can provide information about the nature of the distribution of LC in a given monitored location. Hence, allowing the algorithms of LC change detection to locate, identify and quantify the historical

changes that occurred in LC with confidence (Masiliūnas *et al.*, 2021). Several LC change detection algorithms are available and they are increasing over time with the continuous advancements in geospatial techniques. Examples include but are not limited to, LandTrendr (Kennedy *et al.*, 2010), Breaks for Additive Season and Trend (BFAST) (Verbesselt *et al.*, 2010), BFAST Lite (Masiliūnas *et al.*, 2021), BFAST Monitor (Verbesselt *et al.*, 2012) and Continuous Change Detection and Classification (CCDC) (Zhu and Woodcock, 2014). All of which have been proven useful in analysing time-series of satellite imagery (e.g., Landsat) and detecting LC change over an extended period of time (Masiliūnas *et al.*, 2021).

2.5.2. Cloud computing platforms for geospatial applications

In recent years, several RS datasets have become available due to the advancements in satellite sensor capabilities with regard to spatial, temporal, spectral and radiometric resolutions. Therefore, RS datasets are getting larger and larger over time, both in terms of the amount of data and computer storage capacity needed to store them (Amani *et al.*, 2020b). One of the most recognised examples is the historical Landsat archive that extends from 1972 to the current day with 30 m spatial resolution, 16-day temporal resolution and global coverage (Wulder *et al.*, 2019; Roy *et al.*, 2014). Working with huge RS data (i.e. petabytes) is an onerous task, hence, managing, visualising, analysing and interpreting this amount of data using desktop computing resources is not practical and sometimes could be impossible (Ma *et al.*, 2015; Chi *et al.*, 2016). Therefore, there has been a pressing need to develop an advanced, efficient and unconventional solution, namely cloud computing platforms, to analyse large amounts of RS data, overcoming this big challenge without the need to worry about the computational capacity of current-day desktop computers (Ma *et al.*, 2015; Chi *et al.*, 2016).

Cloud computing platforms are effective solutions for storing, accessing and analysing geospatial data "on the cloud" using extremely powerful servers, which utilises a number of supercomputers for the users (Amani *et al.*, 2020b). A few cloud computing platforms have been developed over recent years. For example, AWS, which provides its users with a pay-as-you-go service, where they can pay for the number of hours, they used the platform. AWS has access to several satellite data (e.g., Landsat-8 OLI, Sentinel-1, Sentinel-2 and NOAA), and it also hosts a wide range of machine learning techniques and services (Tamiminia *et al.*, 2020; Ma *et al.*, 2015). Azure is the cloud computing platform introduced by Microsoft, it uses artificial intelligence algorithms and tools to address environmental challenges (e.g., climate, water, agriculture and biodiversity). Similar to the AWS platform, Azure is also

offering pay-as-you-go services, however, it only provides satellite data from Landsat, MODIS and Sentinel-2, starting from 2013 (albeit Sentinel-2 starts from 2017) and covers North America (Pedrayes *et al.*, 2021).

GEE is currently the most popular cloud computing platform, launched in 2010 by Google to facilitate the processing of large amounts of geospatial data (Amani *et al.*, 2020b). This has allowed new horizons to monitor the environment across the globe over extended periods of time. Despite being released in 2010, the geospatial capabilities of GEE have not been fully utilised for RS and EO applications until recent years (Amani *et al.*, 2020a, 2020b). Google has provided its cloud computing platform with the latest computational infrastructure and access to several RS data including the archives of Landsat and Sentinel (Tamiminia *et al.*, 2020; Gorelick *et al.*, 2017). The GEE platform provides access to a wide range of LC classification algorithms as well as simultaneous image processing capabilities in order to overcome the challenges associated with managing big data (Tamiminia *et al.*, 2020; Gorelick *et al.*, 2017). Over recent years, this platform has been utilised to map changes in LC across the globe (Gong *et al.*, 2020; Liu *et al.*, 2020a; Zhang *et al.*, 2020) including in Asia (Gumma *et al.*, 2020; Oliphant *et al.*, 2019; Hu and Hu, 2019); Africa (Xiong *et al.*, 2017a, 2017b; Samasse *et al.*, 2020; Midekisa *et al.*, 2017); South America (Alencar *et al.*, 2020); North America (Amani *et al.*, 2020a); Europe (Venter and Sydenham, 2021; Phalke *et al.*, 2020), and Australia (Calderón-Loor *et al.*, 2021; Teluguntla *et al.*, 2018).

2.5.3. Forecasting LC change

Forecasting LC change using prediction modelling techniques is advancing (Chen *et al.*, 2021). Such studies are profound in developing countries, where the rapid and consistent population increases drive LC change and ultimately, impact the limited land resources (Hou *et al.*, 2019). Predicting future LC change is essential in helping decision-makers and policy-legislators frame and implement more sustainable actions (Hou *et al.*, 2019; Aburas *et al.*, 2017) and can be useful for identifying and analysing the drivers of LC change (Chen *et al.*, 2021), and predicting the future status of the diminishing land resources in relation to population growth pressures. LC simulation models are widely used to assess future urban expansion in developing countries, particularly when this occurs at the expense of fertile agricultural land (Losiri *et al.*, 2016; Hou *et al.*, 2019).

Simulation models of LC change are fundamentally divided into two main categories: quantity prediction models and spatial prediction models (Chen *et al.*, 2021; Hou *et al.*, 2019). Quantity prediction models can effectively simulate the areal extent of LC change over

time, without predicting the relevant spatial distribution for each LC type and include Markov chain (Muller and Middleton, 1994), system dynamics (Geng *et al.*, 2017), regression (Jokar Arsanjani *et al.*, 2013) and ANN models (Thapa and Murayama, 2012). Spatial prediction models, on the other hand, can effectively simulate the spatial distribution of each LC type (Chen *et al.*, 2021; Hou *et al.*, 2019), and include Cellular Automata (CA) (Clarke *et al.*, 1997; Santé *et al.*, 2010), SLEUTH (Dietzel and Clarke, 2007), Land Change Modeler (LCM) (Li *et al.*, 2020), the Conversion of Land Use and its Effects (CLUE) (Veldkamp and Fresco, 1996) and Future Land Use Simulation (FLUS) (Liu *et al.*, 2017) models. Therefore, using an integrated model that combines the characteristics of both the areal extent and spatial configuration of future LC can provide better spatial and statistical results and minimise the drawbacks of using a single model category in isolation (Hou *et al.*, 2019). Examples of the integrated models include the Conversion of Land Use and its Effects at Small regional extent (CLUE-S) (Verburg *et al.*, 2002) and CA-Markov (Guan *et al.*, 2011).

A number of researchers in developing countries have used LC change simulation models to predict the future dynamics of LC change (e.g., urban expansion and its effects on the surrounding environment). Integrated models have also been widely used to improve the overall accuracy of the predicted output and therefore, eliminate the constraints of a solo model (Hou *et al.*, 2019). An ANN model was used to simulate future urban expansion in the Kathmandu valley of Nepal under 3 different scenarios (Thapa and Murayama, 2012). Similarly, a hybrid-integrated model combining logistic regression, MC and CA models was used to predict future patterns of urban sprawl in Tehran, Iran (Jokar Arsanjani *et al.*, 2013). Likewise, a CLUE-S model coupled with a MC model was used to simulate future LC change in Beijing, China, under 3 scenarios (Han *et al.*, 2015).

A hybrid CA-SLEUTH model was used to forecast future urban expansion in Dhaka, the capital of Bangladesh and the most densely populated city in the world (Pramanik and Stathakis, 2016). A FLUS-CA integrated model was used to predict future LC change for the whole of mainland China based on four scenarios (Liu *et al.*, 2017). An integrated LCM model combining logistic regression and CA-Markov was used to simulate future LC change patterns under two different scenarios in Gansu province, China (Li *et al.*, 2020). Recently, an integrated Markov-FLUS model was used to predict the spatiotemporal dynamics of future LC change in Hokkaido, Japan based on three different scenarios (Chen *et al.*, 2021).

2.5.4. Markov Chain model

Markov Chain (MC) is a stochastic, powerful and widely used modelling technique that has been extensively utilised across the world to analyse and explore the dynamics of future LC change at multiple spatial scales (Muller and Middleton, 1994). It can predict and quantify future LC change extent over time efficiently, however, it cannot predict the spatial distribution of future LC change for each LC type (Mishra and Rai, 2016). The MC model is capable of predicting future LC change dynamics based on information from the past via producing transition probability matrices (Rimal *et al.*, 2018a). A transition probability matrix of LC change is generated by using information (e.g., LC maps) from two different dates (earlier and later) to estimate the probability of each pixel of a given LC class transitioning to another LC class or remaining in its existing LC class (Mishra and Rai, 2016).

2.5.5. Cellular Automata model

Cellular Automata (CA) is a discrete, dynamic type of model for predicting the spatial distribution of future LC change (Clarke *et al.*, 1997; Santé *et al.*, 2010). In recent years, it has been widely used with other simulation models to predict future LC change dynamics, particularly in simulating urban sprawl patterns in developing countries (Losiri *et al.*, 2016; Aburas *et al.*, 2017). To overcome the shortcomings of using CA and MC models in isolation (Shafizadeh Moghadam and Helbich, 2013), they can be integrated in CA-Markov models to simulate both the amount and spatial distribution of LC change through time and have been widely used to predict future urban expansion (Rimal *et al.*, 2018a; Shafizadeh Moghadam and Helbich, 2013) and natural vegetation dynamics (Hyandye and Martz, 2017; Kamusoko *et al.*, 2009).

2.5.6. Integrated CA-Markov model

Integrated CA-Markov models have proven to provide effective and robust means of simulating the spatiotemporal dynamics of changes in LC (Guan *et al.*, 2011). The CA-Markov model has been widely used across the world, particularly in developing countries where the limited land resources are pressured by the rapid population increases and the associated urban expansion (Hou *et al.*, 2019). The CA-Markov model has been utilised successfully in Zimbabwe (Kamusoko *et al.*, 2009), Bangladesh (Ahmed and Ahmed, 2012), Malaysia (Memarian *et al.*, 2012; Aburas *et al.*, 2017), India (Shafizadeh Moghadam and Helbich, 2013)(Tang and Di, 2019), Chile (Puertas *et al.*, 2014), Turkey (Ozturk, 2015), Saudi Arabia (Alqurashi *et al.*, 2016), Thailand (Losiri *et al.*, 2016), Tanzania (Hyandye and Martz, 2017), Nigeria (Wang and Maduako, 2018), Iran (Hamad *et al.*, 2018), Nepal (Rimal *et al.*,

2018a), Japan (Wang *et al.*, 2018b; Guan *et al.*, 2011), China (Hou *et al.*, 2019; Wang *et al.*, 2018a), Kazakhstan and Uzbekistan (Shen *et al.*, 2019), Vietnam (Nguyen *et al.*, 2019), Indonesia (Yulianto *et al.*, 2019) and Pakistan (Baqa *et al.*, 2021).

2.5.7. Accuracy assessment of LC change

Quantifying LC changes at national, continental and global scales requires precise information on the extent of LC types and their dynamics over time, and such geospatial information is often acquired from RS data (Hansen *et al.*, 2013). Satellite RS data has the capability to provide such information with high accuracy. However, this does not eliminate the possibility of including geospatial uncertainties within the remotely captured information. Hence, a number of issues may be experienced while processing and analysing this information (Olofsson *et al.*, 2013). Accuracy can be defined as the degree to which the generated map corresponds with the reference data. Common measures used to assess accuracy include (i) overall accuracy; (ii) user's accuracy; (iii) producer's accuracy; and (iv) the kappa coefficient of agreement (Olofsson *et al.*, 2013).

The reported area of LC change that is obtained directly from a difference map could differ substantially from the actual area of change due to underlying errors within the original RS data, uncertainties and sometimes lack of consistency within the reference data and map classification errors (Olofsson *et al.*, 2013). Hence, accurately quantifying changes in LC at large spatial scales over time (e.g., global) while accounting for uncertainties and estimating error margins is an onerous and challenging task and therefore, many studies briefly mention it or completely avoid discussing it (Olofsson *et al.*, 2013). The area of LC change can be directly obtained from difference maps (e.g., initial and final years) acquired from satellite RS data. Satellite image classification analysis is typically carried out to produce such change maps. There are several methods for classifying LC change based on RS data, using a post-classification comparison analysis is one of the most common techniques, where the accuracy of LC change is not validated as only the individual map classifications (e.g., each date) are assessed (Olofsson *et al.*, 2013). Despite achieving high classification accuracies for the produced LC maps (i.e. per each date), there is still a possibility that the computed change area is not sufficiently accurate. Hence, the accuracy of the change map could be much lower than accuracies achieved from the individual classifications (Olofsson *et al.*, 2013).

Olofsson *et al.* (2013) demonstrated that providing uncertainty estimates within LC change studies should be an essential good practice. Hence, they presented a method to quantify

uncertainties within a given area of LC change (e.g., between two different LC types) over time (e.g., between two dates). This was achieved by (i) assessing user's, producer's and overall accuracies; (ii) computing area of LC change using sample data to correct mapped area and account for classification errors; (iii) constructing a confusion matrix; (iv) estimating error margins for the "corrected" areas of change (Olofsson *et al.*, 2013). A few LC change studies have recently followed this good practice to provide more confident figures of LC change globally (Curtis *et al.*, 2018; Vancutsem *et al.*, 2021). Curtis *et al.* (2018) quantified the error intervals to determine the spatial attribution of the drivers of global forest loss between 2001 and 2015, whilst Vancutsem *et al.* (2021) applied it to map the extent and changes (e.g., disturbance, degradation, deforestation, recovery) across the humid tropics between 1990 and 2019.

2.6. Aims and Objectives

The overarching aim of this thesis was to develop an understanding of what, where, when and ultimately why LC changes have taken place over national, continental and global scales. This was achieved using a relatively high spatial resolution annual time-series, which is spatiotemporally consistent with global coverage from 1992 to 2018. The main aim of the thesis was addressed through the following objectives:

1. To investigate spatiotemporal changes in LC by analysing, quantifying and interpreting the gains and losses, trajectories and transitions, as well as the drivers behind these LC changes (Chapters 3, 4 and 5).

2. To simulate future LC change within a rapidly urbanising country with threats to the neighbouring agricultural land and national food security (Chapter 3).

3. To identify and differentiate the drivers of LC change (e.g., natural, anthropogenic) in a diverse continent using political and ecological boundaries (Chapter 4).

4. To provide a comprehensive assessment of global LC gains and losses, trajectories and transitions with respect to the uncertainties in the global LC dataset (Chapter 5).

2.7. Conclusion

After reviewing the current global and regional LC products, the ESA-CCI-LC product was considered appropriate to fulfil the aims and objectives of this thesis. Therefore, it has been used across all subsequent analytical chapters. Using this LC product has several advantages, particularly when studying LC change at different spatial scales from national to global. The long annual time-series provided by the ESA-CCI-LC product was of great importance when monitoring and quantifying the dramatic urban expansion over neighbouring fertile

agricultural land in the Nile Delta of Egypt. This has allowed analysis and quantification of the rates of urban expansion based on the produced LC trajectories (chapter 3). Furthermore, combined with the benefit of the long annual time-series (1992-2018), the high thematic resolution of the ESA-CCI-LC product (22 Level-1 and 15 Level-2 LC classes) was crucial for characterising and quantifying LC changes across SSA at a wide range of spatial scales (continental, national and ecoregional). This has allowed assessment of the key LC change transitions and processes and interpretation of their anthropogenic and climatic drivers (chapter 4). Lastly, in addition to the aforementioned strengths, the global coverage of the ESA-CCI-LC has allowed a comprehensive assessment of LC gains and losses, trajectories and transitions at global, continental and national scales. This demonstrated the variability in LC change between and within continents with the inclusion of uncertainties (margins of error) associated within the ESA-CCI-LC product (chapter 5).

Chapter 3. Dramatic loss of agricultural land due to urban expansion threatens food security in the Nile Delta, Egypt

Taher M. Radwan, G. Alan Blackburn, J. Duncan Whyatt and Peter M. Atkinson.

This chapter has been published as an open access research article in *Remote Sensing*.

Radwan, T.M. *et al.* (2019) Dramatic loss of agricultural land due to urban expansion threatens food security in the Nile Delta, Egypt. Remote Sensing. 11 (3), 332.

Abstract

Egypt has one of the largest and fastest growing populations in the world. However, nearly 96% of the total land area is uninhabited desert and 96% of the population is concentrated around the River Nile valley and the Delta. This unbalanced distribution and dramatically rising population have caused severe socio-economic problems. In this research, 24 land use/land cover (LULC) maps from 1992 to 2015 were used to monitor LULC changes in the Nile Delta and quantify the rates and types of LULC transitions. The results show that 74,600 hectares of fertile agricultural land in the Nile Delta (Old Lands) was lost to urban expansion over the 24 year period at an average rate of 3,108 ha $year^{-1}$, whilst 206,100 hectares of bare land was converted to agricultural land (New Lands) at an average rate of 8,588 ha $year^{-1}$. A Cellular Automata-Markov (CA-Markov) integrated model was used to simulate future alternative LULC change scenarios. Under a Business as Usual scenario, 87,000 hectares of land transitioned from agricultural land to urban areas by 2030, posing a threat to the agricultural sector sustainability and food security in Egypt. Three alternative future scenarios were developed to promote urban development elsewhere, hence, with potential to preserve the fertile soils of the Nile Delta. A scenario which permitted urban expansion into the desert only preserved the largest amount of agricultural land in the Nile Delta. However, a scenario that encouraged urban expansion into the desert and adjacent to areas of existing high population density resulted in almost the same area of agricultural land being preserved. The alternative future scenarios are valuable for supporting policy development and planning decisions in Egypt and demonstrating that continued urban development is possible while minimising the threats to environmental sustainability and national food security.

3.1. Introduction

Egypt, with a population of approximately 100 million people, is the 14th most populated country in the world, the 3rd largest in Africa and the largest Arab country (Worldometers, 2018). It has a total land area of almost 1 million km^2 of which nearly 96% is uninhabited desert. The majority (96%) of the national population is located within the River Nile valley and the Delta (Bakr and Bahnassy, 2019a). The combination of unbalanced distribution and dramatic population growth (around 2% annually) has caused severe socio-economic problems including a reduction in living standards, high levels of unemployment, and increasing crime rates (Bakr and Bahnassy, 2019a; Abd El-Kawy *et al.*, 2011; Shalaby and Tateishi, 2007). The ratio between human resources and land resources is a critical issue in Egypt. Such a high annual rate of increase in population means that considerable attention needs to be given to preserve the limited land resources to optimize agricultural productivity, and to help conserve the highly fertile soil of the Nile Delta which is the primary source of staple cereal crops for the nation (Bratley and Ghoneim, 2018).

The agricultural sector in Egypt is the main source of income for around 60% of the population (CAPMAS, 2018). Agricultural land in Egypt can be divided into two main categories; *Old Lands* and *New Lands* (Bakr and Bahnassy, 2019a). The *Old Lands* are areas of highly fertile clayey soils, which have been cultivated intensively for thousands of years in the Nile Valley and the Delta. Due to the fertile nature of the soil, these areas have traditionally been used to cultivate staple cereal crops such as wheat, maize and rice, maintaining agricultural sustainability and preserving food security for the Egyptian people, with the River Nile being the primary water source for crop irrigation by flooding irrigation. The *New lands* are desert areas outside the eastern and western fringes of the Nile Delta, which have been reclaimed over the last 50 years and cultivated with fruit trees (Orchards), (e.g., oranges, grapes, apples, mangoes and bananas) as well as vegetables (e.g., cherry tomatoes and bell pepper) aimed for lucrative export markets with modern irrigation techniques (e.g., sprinkler and drip irrigation) that use groundwater boreholes (Bakr and Bahnassy, 2019a; Bratley and Ghoneim, 2018; FAO, 2018).

Urban expansion is a widespread process in Egypt due to the economic development and exponential population growth. Rapid urban expansion, mainly at the expense of agricultural land, has critical consequences for agricultural productivity and the condition of the environment. It has already been recognized that in Egypt the mismanagement and overexploitation of land resources have negatively affected national GDP, the agricultural

sector and the sustainability of the economic development of the country (Abd El-Kawy *et al.*, 2011; Shalaby and Tateishi, 2007). Urbanisation is a complicated process which not only negatively impacts sociological, cultural and economic aspects but also creates significant changes in the environmental conditions (Lambin *et al.*, 2001; Dewan and Yamaguchi, 2009; Wu and Zhang, 2012). Widespread urbanisation as a result of rapid population growth is now recognized as a critical phenomenon in many developing counties (Wu *et al.*, 2016).

Remote sensing (RS) and Geographic Information Systems (GIS) are robust, useful and efficient tools for assessing the temporal and spatial dynamics of land use/land cover (LULC) change, analysing and mapping these dynamics and providing valuable historical data for monitoring the condition of the environment (Lambin *et al.*, 2001; Wu *et al.*, 2016; Bakr *et al.*, 2010). LULC change is currently considered one of the most critical environmental issues across the globe (Guan *et al.*, 2011). New tools and techniques for monitoring and detecting changes on the Earth's surface at various scales have been developed in response to increased availability of remotely sensed data and technical advances in spatial, spectral and temporal resolution (Rogan and Chen, 2004; Wu *et al.*, 2006).

LULC change analysis is based on historical LULC data where past land transitions are monitored and assessed (Wu *et al.*, 2006; Pijanowski *et al.*, 2002; Halmy *et al.*, 2015; Van Soesbergen, 2016). Predicting LULC change is useful for understanding, highlighting and quantifying potential alterations that might occur over landscapes in the future. Such predictions are helpful to urban planners, agriculturalists, and land use planners as they try to manage and reduce possible adverse impacts on the environment (Wu *et al.*, 2006; Pijanowski *et al.*, 2002). Recently, different types of models and methods within the fields of RS and GIS have been applied to model trends in urban growth (Eastman, 2016; Aburas *et al.*, 2016). These include studies that have used Cellular Automata (CA) and Markov chain analysis models (Aburas *et al.*, 2016, 2017; Clarke *et al.*, 1997).

Markov chain analysis is a powerful modelling approach that has been widely utilized to investigate the dynamics of LULC change at various scales. It can simulate and quantify future LULC change effectively (Halmy *et al.*, 2015; Baker, 1989; Muller and Middleton, 1994; Kamusoko *et al.*, 2009) and is considered a useful method for modelling LULC change, particularly over large areas (Weng, 2002). The model is built around producing a transition probability matrix of LULC change between two different dates. The transition probability matrix provides an estimate of the probability of each pixel of a specific LULC class being converted to another class or remaining in its current class (Halmy *et al.*, 2015; Van

Soesbergen, 2016; Eastman, 2016). The Markov chain analysis model does not simulate the spatial changes in LULC (Balzter, 2000) but can be used to quantify and predict LULC changes efficiently (Yang *et al.*, 2012; Mishra and Rai, 2016).

CA modelling is dynamic, discrete and may be integrated with other models to project and simulate urban growth patterns (Aburas *et al.*, 2017; Clarke *et al.*, 1997). It has been used extensively to simulate urban sprawl dynamics and predict future LULC change over recent years (Guan *et al.*, 2011; Aburas *et al.*, 2017; Weng, 2002; Santé *et al.*, 2010). CA and Markov Chain analysis models (CA-Markov) may be integrated to quantify and simulate spatiotemporal patterns. This integration can overcome the limitations of Markov chain analysis and provide increased understanding of LULC change dynamics, due to the addition of spatial dimensions by the CA model (Guan *et al.*, 2011; Clarke *et al.*, 1997; Memarian *et al.*, 2012; Nouri *et al.*, 2014). Hence, these integrated models consider the temporal and spatial aspects of LULC change patterns (Houet and Hubert-moy, 2006).

The aim of this paper was to monitor, understand and quantify historical LULC changes in the Nile Delta and predict future changes based on different assumed scenarios. To meet this aim, the following objectives were set:

- Monitor historic changes in LULC in the Nile Delta from 1992 to 2015.
- Quantify the rates and types of LULC transitions that have occurred.
- Evaluate the extent of urban sprawl and its implications for the loss of productive agricultural land in the Nile Delta.
- Simulate LULC changes to 2030 for a series of different scenarios designed to reduce the amount of fertile land lost to urban development in the Nile Delta.

3.2. Materials and Methods

3.2.1. Study area

The Nile Delta in Egypt is considered to be one of the oldest agricultural areas in the world; it has been under continuous cultivation since 3000 B.C (Bakr and Bahnassy, 2019a; Bratley and Ghoneim, 2018; Negm *et al.*, 2016). The River Nile and its associated sediments made the Delta soils fertile and highly productive, forming a visible green triangular area within a vast desert. This area supported the settlement, the prosperity and the expansion of one of the oldest and greatest civilizations in world history (Bakr and Bahnassy, 2019a; Negm *et al.*, 2016). The Nile Delta is located in the north of Egypt and stretches from the Alexandria governorate in the west to the Port Said governorate in the east (Shalaby, 2012).

The study area (Figure 3.1) consists of 12 administrative divisions (governorates). It covers a total area of approximately 40,000 km^2 and is characterized by a Mediterranean semi-arid climate. About 60% of Egypt's population is currently living in the Nile Delta region, occupying 4% of the total land area of the country (CAPMAS, 2018). Recently, this region has experienced significant LULC change due to rapid and continuous urban expansion linked to exponential population growth. Figure 3.2 shows population and urban LULC in Egypt from 1992 to 2015 (Worldometers, 2018).

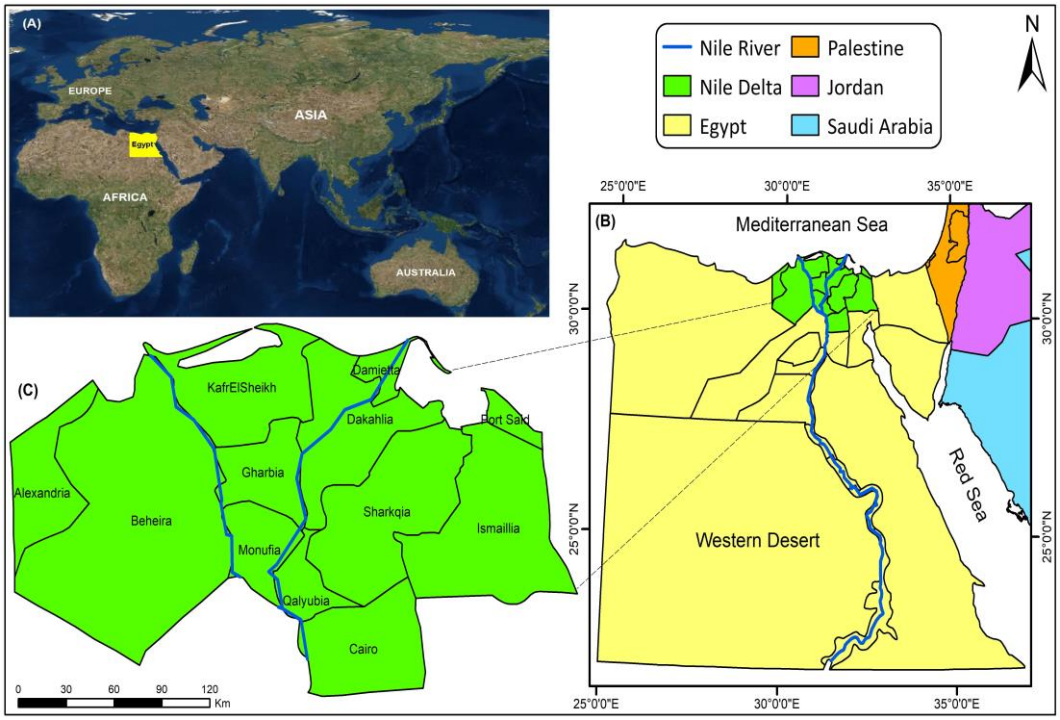

Figure 3.1. Location of the study area: (A) Egypt's location in the North of Africa; (B) The Nile Delta's location in the North of Egypt; (C) the study area (Nile Delta Governorates).

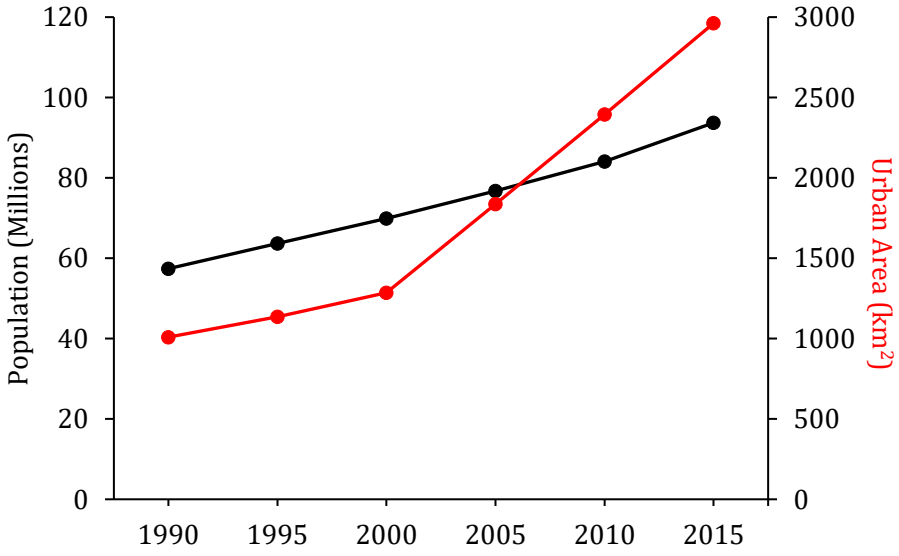

Figure 3.2. Urban land and population growth in Egypt (Worldometers, 2018).

3.2.2. Data collection and processing

3.2.2.1. Land Use/Land Cover (LULC) change analysis

Detailed description of the LC product used in this chapter (ESA-CCI-LC) is provided in section 2.4. The original data were supplied in global coordinates (WGS84) hence they were projected into UTM (Zone 36N) coordinates for the purpose of this analysis using ArcGIS Desktop 10.5 (ESRI, 2016). These maps were analysed to reveal LULC changes for the period 1992 to 2015 inclusive.

A CA-Markov integrated model was used to model likely future LULC dynamics in the Nile Delta. CA-Markov is a change/time series model established within the TerrSet Geospatial Monitoring and Modeling System software (Eastman, 2016; Hyandye and Martz, 2017). In this model, a Markov chain analysis controls the temporal changes in LULC based on transition probabilities, while the spatial changes are controlled by the cell-based rules determined by a CA spatial contiguity filter (Guan *et al.*, 2011; Eastman, 2016; Nouri *et al.*, 2014; Wu, 2002). In order to predict future LULC changes, the first step is to conduct the Markov chain analysis (a Markovian transition estimator), which requires two image data inputs: the first image for an earlier LULC period and the second image for a later LULC period. This generates a transition probability matrix and conditional probability images (Halmy *et al.*, 2015; Eastman, 2016; Hyandye and Martz, 2017; Pontius and Malanson, 2005). The second step is to implement the CA–Markov integrated model using the previously derived transition probability matrix and the later LULC image (Eastman, 2016; Hyandye and Martz, 2017).

In this paper, LULC maps for the years 1999, 2000, 2014 and 2015 were used to derive transition probability matrices of LULC classes between 1999–2000 and 2014–2015 using the Markov model. These transition matrices were then used to simulate LULC changes to future periods. Figure 3.3 illustrates the primary steps carried out within the LULC change analysis using the Markov and CA–Markov models.

To assess the accuracy of a forwards prediction of 15 years (i.e. the length of prediction to be used in this study), we compared the actual LULC map in 2015 with the predicted map generated using a transition probability matrix derived from the 1999 and 2000 maps, with a 5 x 5 cell contiguity filter used to represent the neighbourhood rules for each cell as this technique was the most commonly utilised across previous studies (Hyandye and Martz, 2017; Kityuttachai *et al.*, 2013). The VALIDATE module within TerrSet was used to calculate the overall agreement between actual and predicted LULC maps, using the Kappa index

(Kamusoko *et al.*, 2009; Wang *et al.*, 2012). The importance of model validation prior to simulating future changes in LULC has been emphasized in the literature (Eastman, 2016; Hyandye and Martz, 2017).

Based on the successful validation (see section 3.3) we used the two most recent LULC maps (i.e., 2014 and 2015) to generate the transition probability matrix for the years 2014–2015 within the CA-Markov model to project LULC maps for 2030, simulating up to the sustainable development strategy of Egypt "Egypt's vision 2030". Four scenarios of future urban expansion were used to assess their impact upon the loss of areas of fertile soils within the Nile Delta. These projected scenarios could be useful for aiding policy formulation and planning decisions in the country.

The 1st scenario, Business as Usual (BAU), assumes current patterns of urban growth continuing in the future. The subsequent scenarios were designed to generate the same increase in urban area by 2030 as the BAU, but to spatially distribute this urban expansion in different ways. Hence, the 2nd scenario, Desert Development Only (DDO), was conceived to prevent further urban development within the green zone of the Nile Delta (*Old Lands*), restricting it to the desert only. A binary image of bare land was used to drive this simulation, whilst the agricultural land and waterways binaries were used as spatial constraints for future urban expansion.

The 3rd scenario, Population-Driven Expansion (PDE), assumes that areas of high population act as catalysts for further urban expansion. Population data were obtained from the WorldPop website for Egypt (WorldPop, 2018), at a spatial resolution of 100m, then aggregated to 300m to match the spatial resolution of the LULC data and maintain consistency within the model. The waterways binary then was used as a spatial constraint. This scenario encourages higher levels of urbanisation adjacent to existing areas of higher population in an attempt to minimize the loss of agricultural land in the Delta region.

Finally, the 4th scenario, Desert and Population Expansion (DPE), was constructed using elements of scenarios 2 and 3 (DDO and PDE). The bare land binary and the population layer were used as driving factors for urban expansion. The waterways binary was used as a spatial constraining factor. This hybrid scenario encourages urban expansion in the desert adjacent to existing areas of higher population.

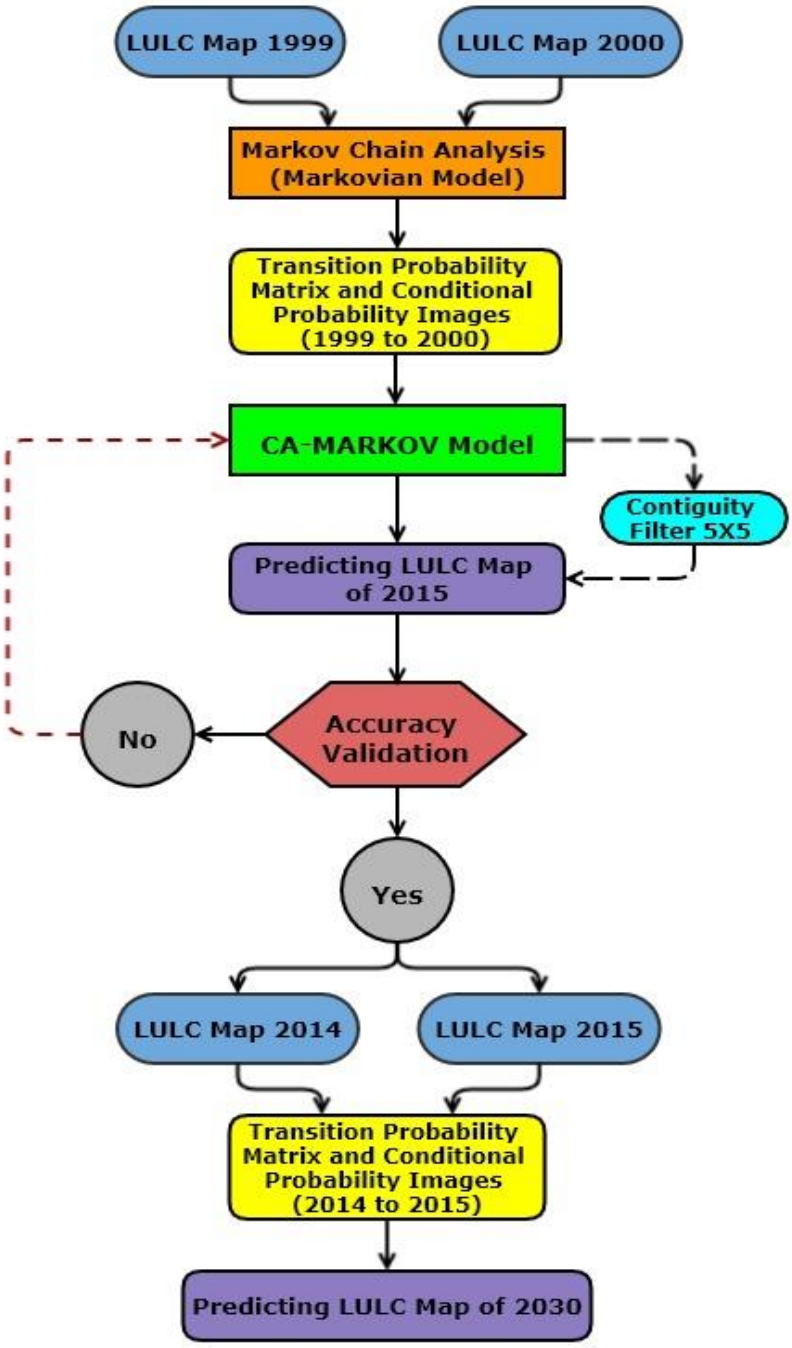

Figure 3.3. Workflow of the methodology used within CA-Markov LULC future analysis.

3.3. Results

3.3.1. LULC change analysis

The original LULC classes in the ESA-CCI-LC dataset were regrouped and simplified into the five major LULC classes found in the Nile Delta namely: agricultural land, aquatic/terrestrial vegetation, urban land, bare land and water bodies (Bakr and Bahnassy, 2019b) as shown in Figure 3.4.

Urban areas increased significantly over the 24 year period in the Nile Delta, from 755 km^2 in 1992 to 1,890 km^2 in 2015 (Table 3.1) at an average rate of 47 km^2 year^{-1}. Agricultural LC increased over this period from 24,053 km^2 in 1992 to 25,576 km^2 in 2015 at an average rate of 63 km^2 year^{-1}. However, all of this additional agricultural land was created in the *New Lands* (formerly desert) through government incentives. Four governorates were selected to explore the process of urban expansion in the Nile Delta in more detail: Dakahlia, Gharbia, Sharkqia and Cairo (Figure 3.1). The first three governorates are considered the largest areas of highly productive soils located in the fertile delta zone (*Old Lands*), and the fourth encompasses the capital city.

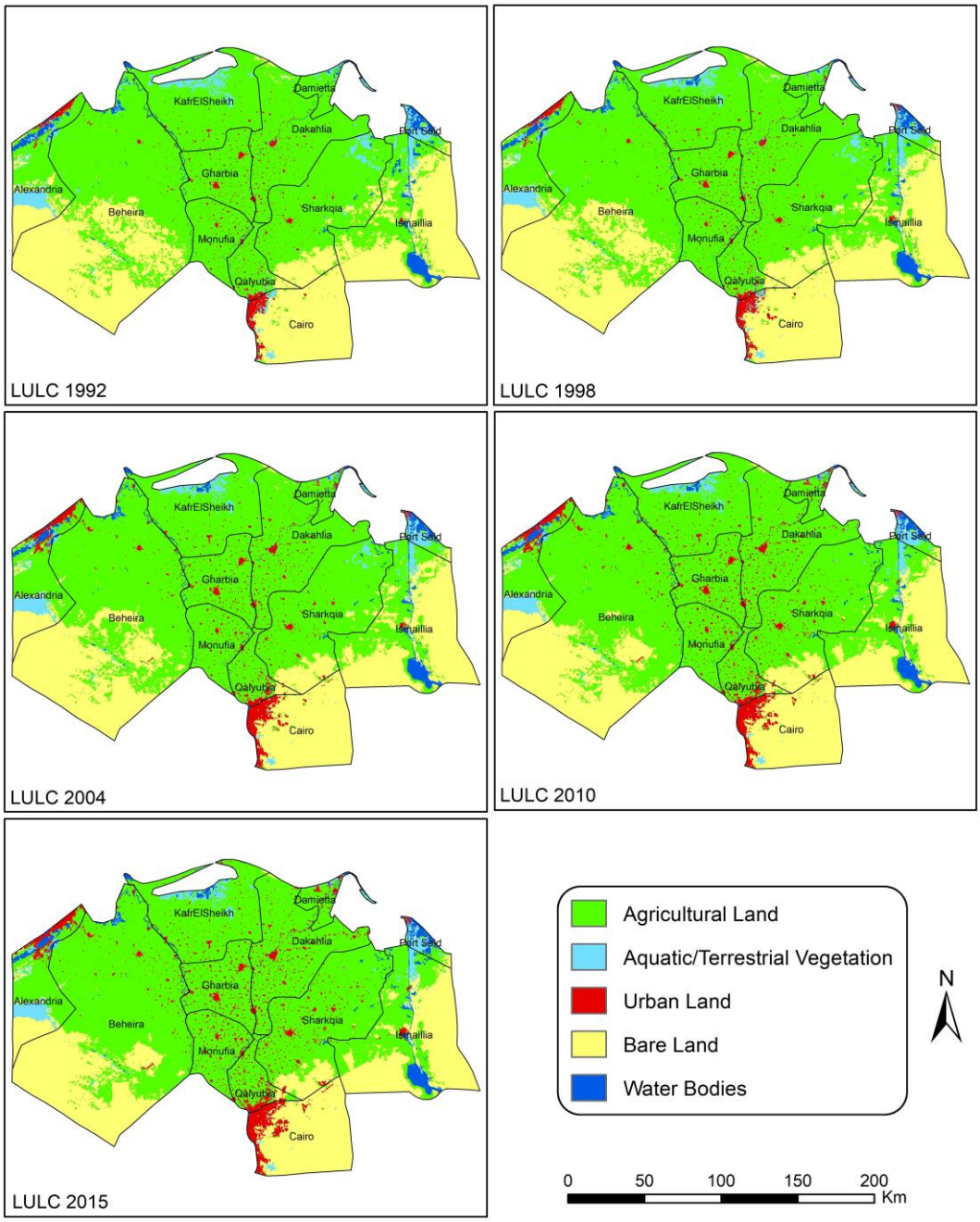

Figure 3.4. The major five LULC classes in the Nile Delta over the study period.

Table 3.1. LULC classes total areas across the Nile Delta over the study period.

LULC class	Area (km²)					Change 1992–2015 (%)
	1992	1998	2004	2010	2015	
Agricultural land	24,053	24,427	24,959	25,430	25,576	6.3
Natural vegetation	1,435	1,301	1,147	1,031	989	-31.1
Urban land	755	873	1,266	1,597	1,890	150.3
Bare land	13,031	12,696	11,947	11,243	10,795	-17.2
Water bodies	841	818	797	815	866	2.9

The amount of urban LC in Dakahlia governorate more than doubled over the 24-year period from 108 km² to 237 km². Similarly, the amount of urban LULC in Gharbia governorate almost doubled over the study period, from 94 km² to 170 km², and more than tripled in Sharkqia governorate, from 59 km² in 1992 to 205 km² in 2015. The most significant urban growth occurred in Cairo governorate over the study period, increasing from 188 km² to 449 km². Urban expansion over the study period from 1992 to 2015 has been plotted for the four selected governorates: Dakahlia, Gharbia, Sharkqia, and Cairo (Figure 3.5). This demonstrates differing trajectories of LULC changes between various governorates. Maps showing different patterns and rates of urbanisation over the productive agricultural land (*Old Lands*) for the four selected governorates are shown in Appendix A.1.

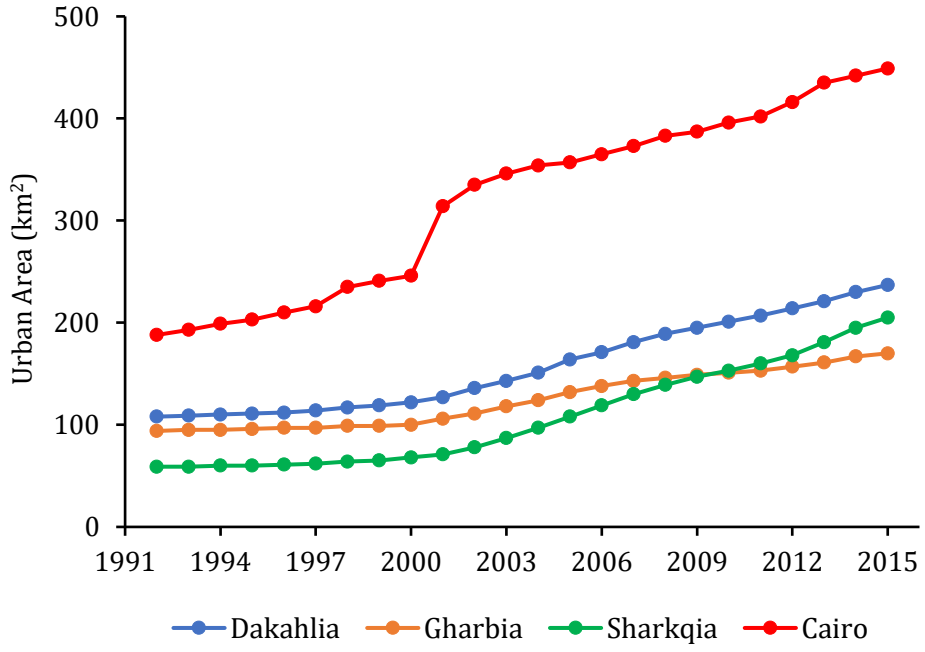

Figure 3.5. Urbanisation in Dakahlia, Gharbia, Sharkqia and Cairo over the study period.

Transitions between different LULC classes in the Nile Delta between 1992 and 2015 are shown in Table 3.2. A change map illustrating the spatial distribution of LULC transitions from 1992 to 2015 is shown in Figure 3.6. Table 3.2 indicates that more than 90% of the total

land area in the Nile Delta did not change over the 24-year period. However, around 2,061 km^2 was converted from bare land to agricultural land, which reflects the government's efforts to reclaim new lands outside the Delta to cater for the exponential population growth, achieve self-sufficiency of food production and maximize national GDP by delivering fruits and vegetables to export markets (Negm et al., 2016; Ghar et al., 2004). Over 900 km^2 of land was converted into urban areas at the expense of fertile agricultural land and natural vegetation in the Nile Delta. This amount of land is 1.16 times the size of New York City, representing a significant loss of crucial natural resources. As Figure 3.6 shows, most of this transition occurs in relatively small patches scattered throughout the Delta. In contrast, 205 km^2 of the desert was converted into urban areas, including New Cairo city, which was established in the year 2000.

Table 3.2. Areas of transition between LULC classes in the Nile Delta from 1992 to 2015.

LULC transition	Area (km^2)	Hectares (ha)
Agriculture to Urban	746	74,600
Vegetation to Urban	170	17,000
No Change	36,352	3,635,200
Vegetation to Agriculture	266	26,600
Bare to Urban	205	20,500
Bare to Agriculture	2,061	206,100
Other LC classes changes	315	31,500

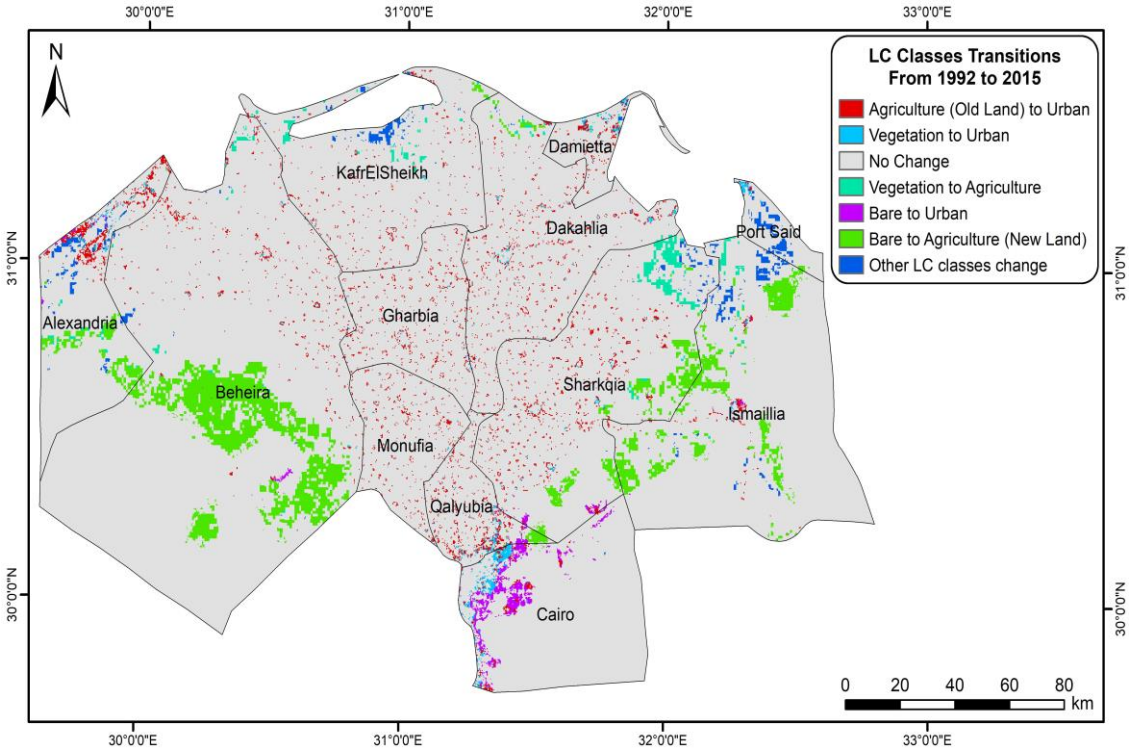

Figure 3.6. Land cover (LC) transitions between 1992 and 2015.

3.3.2. Prediction of future LULC dynamics

3.3.2.1. Application and validation of the CA-Markov integrated model

The Markov model outputs, probability matrix and the conditional probability images were combined using the CA-Markov integrated model to simulate LULC change for 2015. To validate the CA-Markov model, the actual LULC map in 2015 was compared with the predicted map generated using maps from 1999 and 2000 (Figure 3.7). For this forwards prediction of 15 years, the validation results showed a high level of correspondence between the actual and the simulated LULC maps in 2015 where the Kappa index value was 0.94. This Kappa value is significantly higher than the value of 0.80 considered acceptable (Viera and Garrett, 2005) and in line with other studies which have applied the CA-Markov model in LULC change predictions (Guan *et al.*, 2011; Hyandye and Martz, 2017; Kityuttachai *et al.*, 2013; El-Hallaq and Habboub, 2015). Hence, after achieving this level of predictive accuracy, the CA–Markov model was considered suitable for use in simulating future LULC change to 2030. This high K-index value could be attributed to the large amount of land that did not transition at all which was about 90% of the total land area, or the number of LULC classes used in the analyses (five classes). Amini Parsa *et al.* (2016), have previously achieved an overall accuracy of 0.98 based on three LULC classes.

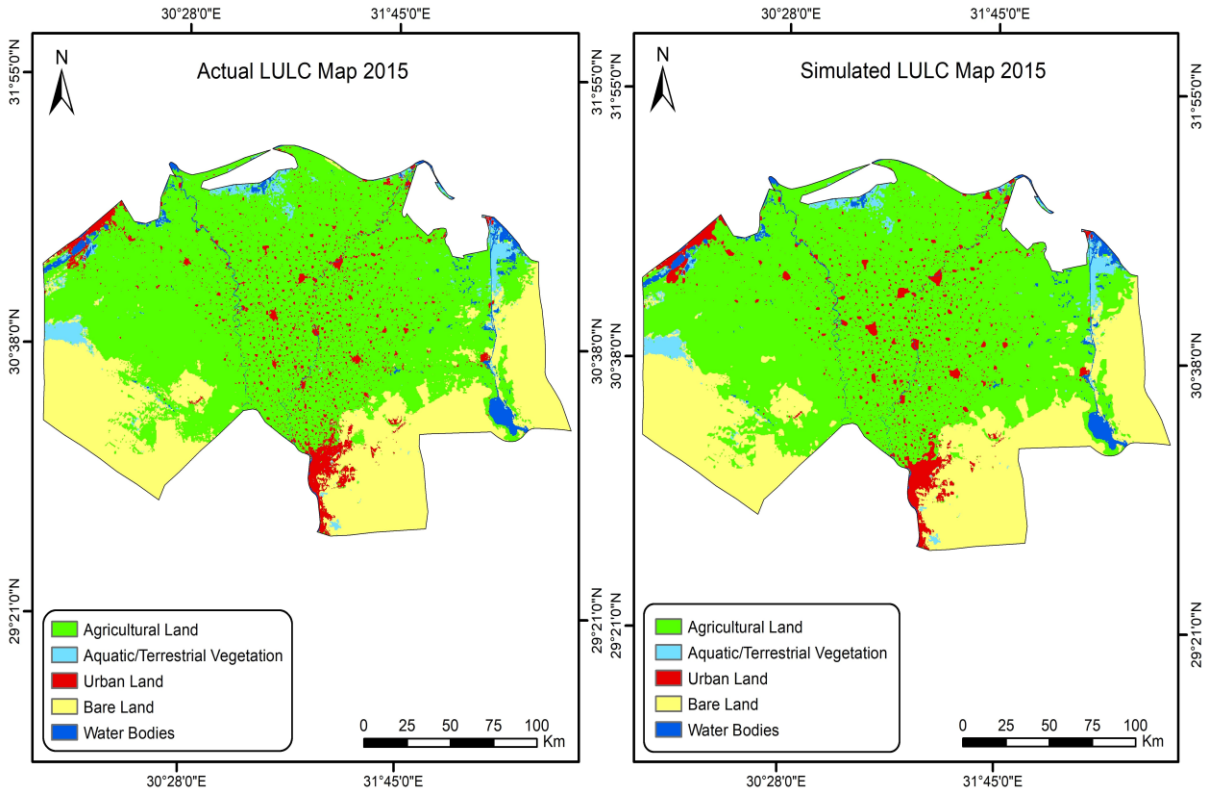

Figure 3.7. Actual (to the left) and simulated (to the right) LULC maps for 2015.

3.3.2.2. Simulation of LULC in 2030 based on different scenarios of urban expansion

Under the BAU scenario, the simulation revealed that there was a significant increase in urban land, from 1890 km^2 in 2015 to 2759 km^2 in 2030 at an average growth rate of 58 km^2 $year^{-1}$. The majority of this increase occurred at the expense of productive agricultural land in the Nile Delta, hence constitutes a significant loss of natural resources (Table 3.3). The BAU simulation results also showed that agricultural land increased by 405 km^2 from 2015 to 2030, at an average rate of 27 km^2 $year^{-1}$. The majority of this growth occurred in the desert (*New Lands*) outside the fertile Delta region (Table 3.3). The amount of bare land decreased from 10,795 km^2 in 2015 to 9,570 km^2 in 2030 at an average rate of 81 km^2 $year^{-1}$. Most of these areas are expected to be converted to agricultural land (*New lands* reclamation). However, some of these areas will change to urban land particularly as Cairo and New Cairo expand over time.

Table 3.3. LULC classes change (gains and losses) over the Nile Delta from 1995 to 2030 (BAU).

LULC Class	Area change (km^2)		
	1995–2005	2005–2015	2015–2030
Agricultural Land	730	595	405
Aquatic/Terrestrial Vegetation	−234	−138	−116
Urban Land	539	556	869
Bare Land	−1,022	−1,083	−1,225
Water Bodies	−14	73	66

Comparing the three alternative future scenarios (Figure 3.8) with the BAU scenario (Table 3.4), we found that agricultural land increased by 410 km^2 in the DDO scenario, with no loss of agricultural land in the Nile Delta, as expected. In contrast, bare land decreased by 325 km^2, as a result of further urbanisation particularly in the zone of Cairo and New Cairo since this scenario restricts urban development to the desert only. In the PDE scenario, agricultural land increased by 254 km^2 compared to BAU. Finally, 346 km^2 of agricultural land is likely to be saved in the DPE scenario. Most of the agricultural land saved in the DDO, PDE and DPE scenarios is located in the (*Old Lands*) zone.

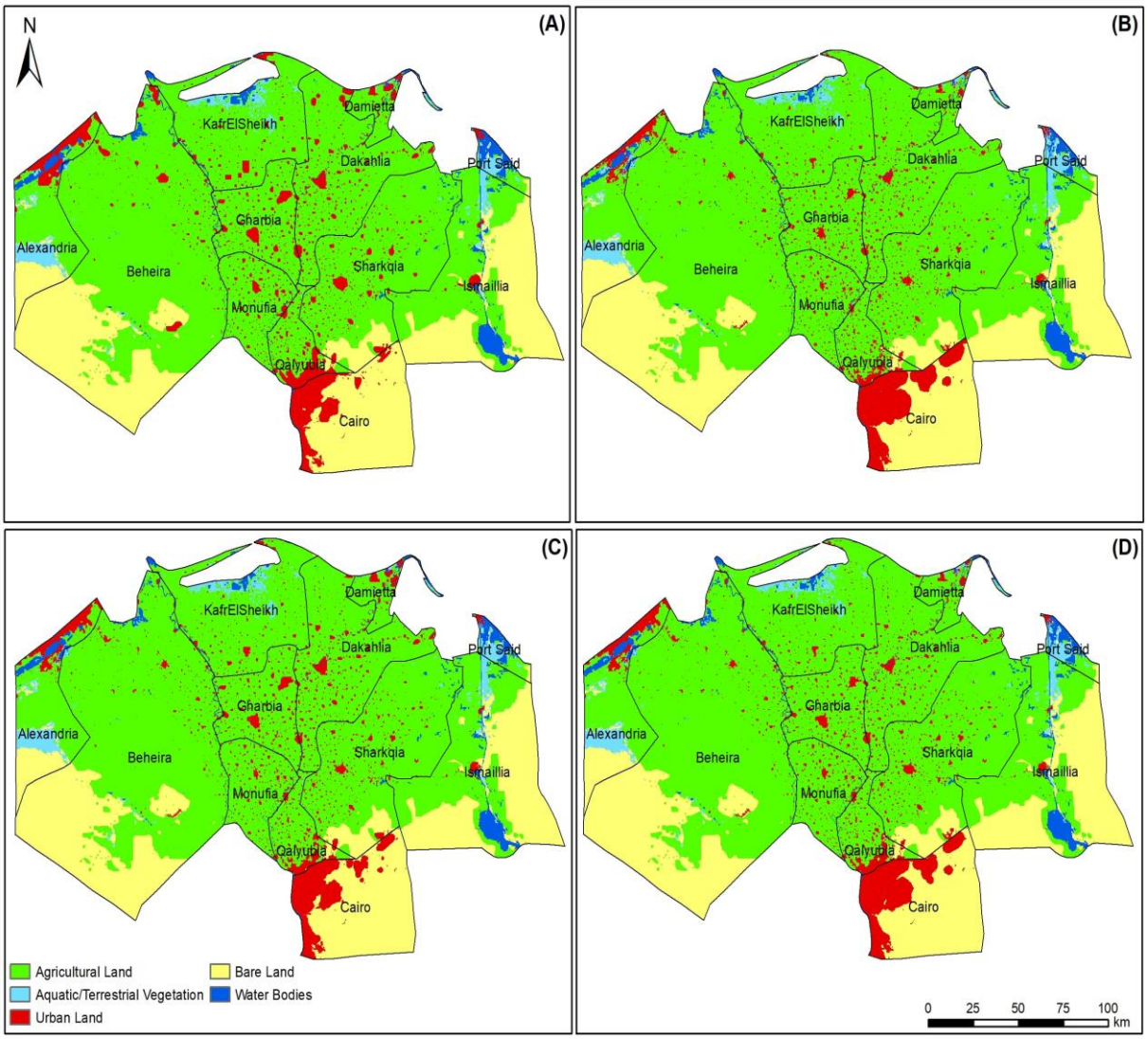

Figure 3.8. Simulated LULC scenarios: (A) BAU, (B) DDO, (C) PDE, (D) DPE.

Table 3.4. The simulated future scenarios LULC total areas over the Nile Delta.

LULC class	Predicted area (km^2)			
	BAU	DDO	PDE	DPE
Agricultural Land	26,078	26,488	26,332	26,424
Aquatic/Terrestrial Vegetation	832	814	806	826
Urban Land	2,683	2,680	2,678	2,681
Bare Land	9,572	9,247	9,403	9,293
Water Bodies	951	887	897	892

Three governorates (Sharkqia, Dakahlia and Gharbia) with the largest amount of fertile agricultural land (*Old Lands*) in the Nile Delta were selected to explore the impacts of the four simulated scenarios in more detail (Figure 3.9). This demonstrates how substantial areas of agricultural land will be lost under BAU, and how the alternative scenarios can preserve significant amounts of agricultural land, particularly under DDO and DPE. Maps

showing the patterns of LULC in the three selected governorates under different urban growth scenarios are shown in Appendix A.2.

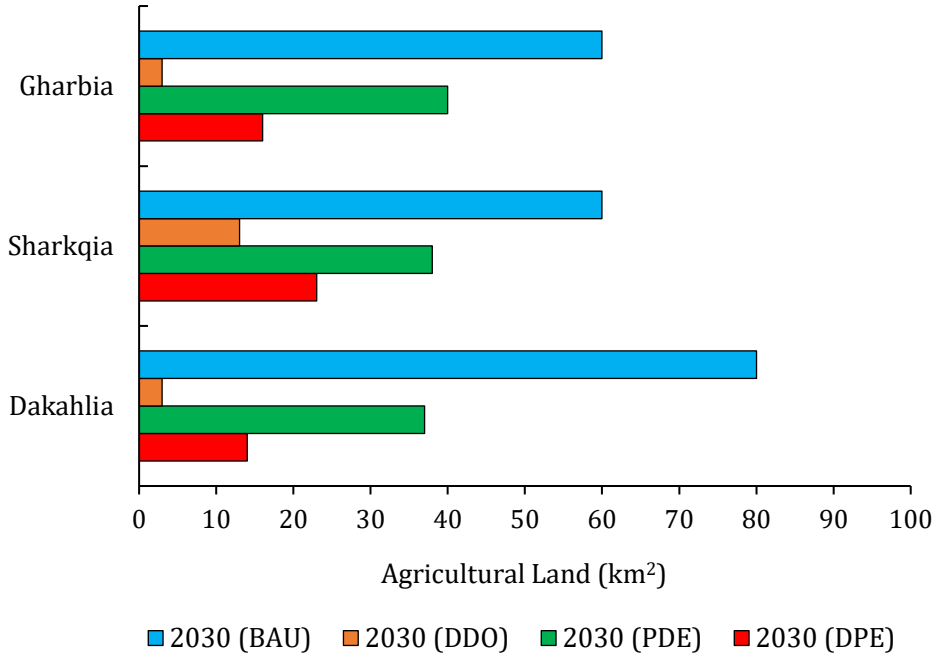

Figure 3.9. Amount of agricultural land lost in three governorates under the different urban growth scenarios between 2015 and 2030.

3.4. Discussion

3.4.1. Previous Nile Delta LULC studies

In Egypt, several smaller-scale LULC studies have focussed on the Nile Delta. Compared to these studies, we found that fertile agricultural land loss due to urban development is a more critical issue than previously suggested. Shalaby *et al.* (2012) assessed the effect of urban expansion on the productive agricultural land in Qalubia governorate between 1992 and 2009 and found that 151 km² of agricultural land had been lost to urban development over this period, accounting for 13% of the total land area of the governorate. Shalaby and Moghanm (2015) assessed the effect of urban sprawl on the fertile agricultural soils of the northern Nile Delta between 1984 and 2006 and found that around 280 km² of productive agricultural land had been lost to urban areas, with urban land expanding by 689 km², 41% of which was at the expense of fertile agricultural land. Megahed *et al.* (2015) mapped, analysed and modelled urban expansion over the Greater Cairo Region from 1984 to 2014, revealing that 357 km² of agricultural land had been lost to urban development.

The results of the present study were in accordance with recent work by Bratley and Ghoneim (2018) who monitored the urban expansion in the Eastern Nile Delta (Sharkqia,

Qalubia and Cairo governorates) from 1988 to 2017 using Landsat imagery. They found that urban land increased by 223% over the 30-year period, mainly at the expense of agricultural land. For a corresponding study area, we found that urban areas increased by 160% from 1992 to 2015. Furthermore, their simulations indicated urban growth of 277 km^2 from 2017 to 2026, and under BAU scenario we predicted an increase of 346 km^2 from 2015 to 2030. Hence, both studies confirm the substantial threats to agricultural land in the Eastern Nile Delta.

3.4.2. Current and possible future alternative land-use strategies

In the present study, we have highlighted a significant loss of agricultural land to urban development across all governorates of the Nile Delta. This will become even more problematic in the future if current land use policies are continued. However, we have also shown that alternative land-use scenarios can potentially accommodate current rates of urban expansion while also preserving valuable agricultural land. The results demonstrate that implementing the DPE scenario, where urban development in desert areas and locations adjacent to existing areas of high population density is likely to save 346 km^2 in the Nile Delta (*Old Lands*) compared to the BAU scenario. This is almost as effective in preserving fertile agricultural land as the more extreme and difficult to implement the DDO scenario. Hence, the DPE scenario is considered the more realistic and achievable scenario.

Rapid urban expansion, mainly at the expense of agricultural land may have critical consequences for agricultural productivity and the condition of the environment. It has already been recognized that in Egypt the mismanagement and overexploitation of land resources has negatively affected national GDP, the agricultural sector and the sustainability of the economic development of the country (Abd El-Kawy *et al.*, 2011; Shalaby and Tateishi, 2007). Recently, the Egyptian government instigated a number of projects to reclaim new desert land (*New Lands*) in response to the rapid national population increase and high demand for food. This resulted in over 12,000 km^2 of bare land being converted to agricultural land (Bratley and Ghoneim, 2018; Barnes, 2012). These efforts could be considered as a potential solution to the current problem. However, this is a very challenging process, and not necessarily a sustainable solution because the soils of these newly reclaimed areas are not only less fertile, but also less effective at holding water than soils in the Nile Delta and have much lower nutrient levels (Bakr and Bahnassy, 2019b; Ghar *et al.*, 2004).

Furthermore, reclaimed areas require substantial resource inputs including water, power and vast amounts of chemical fertilisers to enhance soil fertility, in addition to labour inputs and secure transportation to distant markets (Negm *et al.*, 2016; Bakr and Bahnassy, 2019b). This translates into the requirement for significant financial investment to develop fertile soils with consequences for human health and the surrounding environment due to the utilisation of large amounts of chemical fertilisers. As a result, most of the newly reclaimed areas (*New Lands*) are cultivated with fruit trees and vegetables aimed for lucrative export markets, which undoubtedly do not contribute to agricultural sustainability and self-sufficiency of the country (Bakr and Bahnassy, 2019b; Ghar *et al.*, 2004). Therefore, it is important for the government to consider alternative strategies to tackle both the exponential population growth and rapid urban expansion. These strategies could include:

(1) Preserving current areas of fertile soils in the Nile Delta and constructing new cities, such as New Cairo, outside the delta fringes to accommodate the increasing population, although this is also associated with significant financial and environmental challenges.

(2) Maximizing the agricultural productivity of existing cultivated areas by crop intensification, including the use of higher yielding varieties of cereal crops which are resistant to pathogens and environmental stresses.

3.4.3. LULC change studies beyond Egypt

Urban sprawl is an issue of a global concern, which has severe negative impacts on the sustainability of the environment. Many studies around the world have illustrated the conflict between urban expansion and loss of fertile agricultural land and the related critical consequences for environmental sustainability: In Kenya, Mundia and Aniya (2005) analysed the LULC changes of Nairobi city from 1976 to 2000. They found that the amount of urban area increased substantially from 14 km^2 in 1976 to 61 km^2 in 2000. In contrast, cropland significantly decreased from 100 km^2 to 23 km^2 over the study period. In Bangladesh, Dewan and Yamaguchi (2009) evaluated LULC changes in Greater Dhaka between 1975 and 2003. They found that cultivated land decreased from 120 km^2 in 1975 to 84 km^2 in 2003 and 62 km^2 of cultivated land was lost to urbanisation over the study period.

In India, Sahana *et al.* (2018) analysed the trends of urban growth in Kolkata from 1990 to 2015. They found that agricultural land area decreased from 621 km^2 in 1990 to 405 km^2 in 2015, whilst urban land area increased from 537 km^2 in 1990 to 779 km^2 in 2015, with urban growth accounting for the loss of the productive agricultural land. In China, Shi *et al.* (2016)

studied the conflict between agricultural land loss and urban expansion at the national-level between 2001 and 2013. They found that 33,080 km^2 of agricultural land were lost to urban land and that urban areas had grown substantially from 31,076 km^2 to 80,887 km^2 over the study period, at a growth rate of 13.36% per year. Hence, the present study provides a further example of a process that is significant in many developing countries, and it highlights the seriousness of the threat in Egypt.

3.4.4. Egypt's wider challenges

Egypt faces a number of critical environmental and anthropogenic challenges in relation to both land and water resources. Since 1959, it has received a fixed share of water from the River Nile (equal to 55.5 billion m^3 $year^{-1}$), regardless of the rapid growth in the population. There is limited precipitation in coastal zones in the northern region and there is sea-water intrusion into the Nile Delta (Negm *et al.*, 2016; Bakr and Bahnassy, 2019b). Sea level rise presents a continuing threat in the Nile Delta due to climate warming and recent construction of dams in southern countries of the Nile basin (e.g., the Grand Ethiopian Renaissance Dam (GERD)), present further pressures on the country. In addition, there are multiple anthropogenic challenges, in particular, the exponential increase in the population of the country (Negm *et al.*, 2016; Bakr and Bahnassy, 2019b), which, as this study has demonstrated, has given rise to urban development occurring at the expense of the fertile agricultural land in the Nile Delta.

This is particularly problematic given the geographically constrained nature of fertile agricultural land in the country and the very high rates of LULC transition to urban areas. Hence, there is a pressing need to develop appropriate land-use strategies. The land-use strategies proposed in this paper could inform policy development and planning decisions within the Ministry of Agriculture and Land Reclamation, and the Ministry of Housing, Utilities and Urban Communities in Egypt. These strategies could contribute to long-term sustainability and assure national food security.

3.5. Conclusions

In this research, consistent historical data were used to determine the magnitude and dynamics of LULC changes over the Nile Delta region and to quantify the agricultural and urban land change in different governorates. The results showed that 74,600 hectares of productive agricultural land were lost to urban development between 1992 and 2015. In addition, 206,100 hectares of the desert were converted to high input agriculture (*New*

Lands). These rapid large-scale transitions represent a significant threat to environmental sustainability and food security in Egypt. A CA-Markov integrated model for simulating future LULC changes was validated and used to analyse the implications of a range of different land use scenarios. The simulated distribution of the LULC classes in 2030 under the BAU scenario suggested that, if the current patterns and rates of urban development continue, then 86,900 hectares of fertile agricultural land (*Old Lands*) in the Nile Delta will be lost. Three alternative simulated scenarios were developed to assess the potential impacts of different land-use policies on the loss of fertile agricultural land. The DDO scenario indicated that by restricting urban expansion into the desert only, 41,000 hectares of productive agricultural land could be preserved in the Nile Delta. However, in the more realistic and achievable DPE scenario, urban development in desert areas and locations adjacent to existing areas of high population density could preserve almost as much fertile agricultural land as the DDO scenario. Hence, the simulated scenarios derived from our analysis demonstrate that continued urban development is possible while minimising the threats to the national agricultural sector sustainability and food security, informing a more sustainable land-use strategy for decision makers and appropriate authorities in Egypt.

Chapter 4. Satellite data reveal extensive land cover changes due to anthropogenic and climatic drivers across sub-Saharan Africa

Abstract

Sub-Saharan Africa (SSA) is facing several societal and environmental challenges. Furthermore, SSA has witnessed major land cover (LC) changes over recent decades as a consequence of both anthropogenic disturbances and climatic drivers, and yet we lack a comprehensive understanding of the spatiotemporal distribution and drivers of these changes across SSA. Hence, there is a pressing need for comprehensive quantification and characterisation of the LC changes occurring within SSA. We therefore composited a spatially and temporally consistent LC dataset, the ESA-CCI-LC with an ecoregions-based dataset (Ecoregions2017) to quantify, characterise and interpret the changes in LC that occurred at the whole SSA, national and ecoregional scales between 1992 and 2018. Results showed that the west Sudanian savanna ecoregion witnessed extensive net gains in rainfed cropland (e.g., Nigeria and Mali), deciduous tree cover (i.e. dry forests) (e.g., Nigeria and Ghana), whilst large net losses in shrubland (e.g., Nigeria, South Sudan and Mali) were observed across all ecoregions within SSA. The central Zambezian Miombo woodlands experienced large gains in rainfed cropland and large losses in deciduous tree cover (e.g., Mozambique and Tanzania), whilst the dry Miombo woodlands exhibited both large gains and losses in deciduous tree cover (e.g., Tanzania, Angola and Mozambique). Evergreen tree cover (i.e. tropical rainforests) witnessed large losses in the northeast Congolian lowland forests (e.g., Democratic Republic of the Congo) and western Guinean lowland forests (e.g., Liberia and Côte d'Ivoire), converting mainly to cropland. We associated the major LC transitions that occurred in SSA between 1992 and 2018 into five key LC change processes: (i) "*gain of dry forests*" covered the largest extent and was distributed across the whole of SSA; (ii) "*greening of deserts*" found adjacent to desert areas (e.g., the Sahel belt); (iii) "*loss of tree-dominated savanna*" extending mainly across South-eastern Africa; (iv) "*loss of shrub-dominated savanna*" stretching across West Africa, and "*loss of tropical rainforests*" unexpectedly covering the smallest extent, mainly in the DRC, West Africa and Madagascar. Agricultural expansion at the expense of tropical forests, dry forests and shrubland due to rapid population growth and the increasing demand for food was the main anthropogenic driver behind most LC changes in SSA. Climatic variabilities (e.g., increasing rainfall and atmospheric CO_2 levels) also had a substantial impact on the changes in LC across multiple parts of SSA (e.g., the Sahel). The findings presented in this chapter could inform policy

legislators and decision makers to adopt more sustainable LC strategies, which may contribute to preserving the sustainability of ecosystem services and the wider environment. Our reported highlights provide important information to support progress towards the United Nation's Sustainable Development Goals (UN's SDGs).

4.1. Introduction

The terrestrial ecosystems of our planet have, over the past few decades, witnessed major changes to the land cover (LC) upon which they depend, driven by both anthropogenic and climatic factors, from local to global scales (Rindfuss *et al.*, 2004). These changes in LC have fundamentally impacted the Earth's life support systems and, crucially, threaten the sustainability of the Earth's terrestrial ecosystems (Foley *et al.*, 2005). Such large-scale LC changes include deforestation and biodiversity loss (Gibson *et al.*, 2011), mainly due to agricultural land expansion (Potapov *et al.*, 2017; Curtis *et al.*, 2018), land degradation and desertification (Higginbottom and Symeonakis, 2014; Huang *et al.*, 2020a), and urbanisation at the expense of agricultural land (Radwan *et al.*, 2019). The associated global consequences include climate change, carbon stocks alteration, biodiversity loss and increased food insecurity (Feddema *et al.*, 2005). Hence, it is crucial to monitor, analyse and quantify these LC changes, and enhance our understanding of their consequences (Turner *et al.*, 2007). Specifically, monitoring global LC changes is crucial so that researchers can try to identify the anthropogenic and environmental drivers of change and potential implications (Foley *et al.*, 2005). With recent advancements in, and increasing capabilities of, satellite remote sensing, this has been increasingly feasible, with the ultimate goal of providing evidence to inform national decision-makers and stakeholders to promote environmentally sustainable actions (Foley *et al.*, 2005; Turner *et al.*, 2007).

Sub-Saharan Africa (SSA) covers a total land area of about 24 million km^2. It comprises all African nations which are fully or partially located south of the Sahara Desert (Fenta *et al.*, 2020) and has been recognised as one of the regions most impacted by climate change, globally (Brandt *et al.*, 2015). It is also identified as a region of extensive societal, climatic, and ecological diversity (Serdeczny *et al.*, 2017; Brink and Eva, 2009). The vegetation cover in SSA is diverse, ranging from the grasslands and shrublands of the Sahel belt to the savanna woodlands of the Miombo, the xeric sparse vegetation of the Namib and Kalahari Deserts, and the tropical rainforests of the Congo basin (Brink and Eva, 2009; Fenta *et al.*, 2020). Moreover, the stark variabilities in the demographic, societal, economic, topographic, climatic and ecological factors, underline how greatly diverse is SSA (Linder *et al.*, 2012).

Hence, it is challenging to propose a method that is able to capture all the major LC changes in an equitable fashion (Brink and Eva, 2009). Nigeria, Ethiopia and the Democratic Republic of the Congo (DRC) are the most populous countries, with 206, 115 and 89 million people in 2020 (United Nations, 2019b). About 60% of the inhabitants of SSA live in rural areas, primarily relying on the ecosystem services provided by the forests and natural vegetation to secure their day-to-day life essentials for survival (Geist and Lambin, 2002).

SSA has the world's highest prevalence of food insecurity with 577 million people (55%) experiencing moderate food insecurity and 214 million people (20%) experiencing severe food insecurity (FAO, 2020). The population of SSA has increased from 0.6 billion people in 2000 to 0.8 and 1.1 billion people in 2010 and 2020, respectively, and is expected to reach 1.4 billion by 2030 (United Nations, 2019b). Furthermore, it has been identified as having the world's largest population living below the poverty line (Serdeczny *et al.*, 2017). Such large-scale, rapid population increase requires a corresponding increase in agricultural production to meet the rising demand for food and reduce the region's food insecurity levels (Defries *et al.*, 2010). While this seems like a sensible solution, agriculture expansion in SSA faces several challenges. The increase in agricultural production could be achieved by increasing crop yields on existing agricultural land (i.e., agricultural "intensification"; van Loon *et al.*, 2019) or via land expansion (i.e., agricultural "extensification"; Kehoe *et al.*, 2017). The latter usually comes at the expense of other natural LC classes, such as tropical forests and natural vegetation, with associated threats to the sustainability of carbon stocks and biodiversity (Perrings and Halkos, 2015).

Over the past 30 years, the LC of SSA has been subject to major anthropogenic and climatic disturbances (Brink and Eva, 2009), due to armed conflicts and civil wars (Nackoney *et al.*, 2014), mining (Wegenast *et al.*, 2019), urbanisation (Forget *et al.*, 2021), logging (Rudel, 2013), natural and human-caused fires (Andela and Van Der Werf, 2014), migrations (Salerno *et al.*, 2017), population growth (Defries *et al.*, 2010), famines (Olsson *et al.*, 2005), land degradation (Adenle *et al.*, 2020), increasing rainfall, droughts, and rising temperatures (Serdeczny *et al.*, 2017). Each of these has led to LC changes, with associated implications for the sustainability of ecosystem services, biodiversity, food security and socio-economic welfare (Foley *et al.*, 2005). These impacts are expected to continue with similar trends, if not worsen, if circumstances do not change (Midgley and Bond, 2015; Aleman *et al.*, 2016). Therefore, it is crucial to identify and monitor these changes in LC.

The aim of this paper was to analyse the spatiotemporal distribution of LC changes across SSA over the last three decades at the SSA, national and ecoregional scales, and explore their drivers. Ecoregion-scale assessments of LC change are needed to monitor and characterise the variabilities in LC dynamics across and within countries located in a particular ecological region with mutual natural communities, biodiversity, biophysical and environmental variables (Olson *et al.*, 2001; Bodart *et al.*, 2013). Ecoregions are geographical areas that are delineated based on the distribution of species, natural communities, biodiversity and environmental conditions (e.g., temperature, precipitation and humidity). Assessing LC changes that occur in the ecoregions of a diverse region such as SSA, can provide crucial information to help ecologists, environmental conservationists, landscape planners and policymakers to develop an understanding of the associated impacts on the richness of species and biodiversity within the ecosystems of each ecoregion (Dinerstein *et al.*, 2017; Olson *et al.*, 2001). At the same time, analysing LC change across countries is needed to analyse the different patterns of LC changes arising from the discrepancies in political, economical and societal factors.

To meet the overarching aim, we used a temporally consistent global LC dataset, the European Space Agency Climate Change Initiative Land Cover (ESA-CCI-LC) (ESA, 2017) along with an ecoregions-based dataset, the Ecoregions2017 (Dinerstein *et al.*, 2017) that is spatially-nested within the major terrestrial biomes and covers the entire SSA region. We used these data to quantify, characterise and interpret the LC dynamics that have occurred across the most vulnerable ecoregions for biodiversity loss, as well as the 'worst-case' countries across SSA between 1992 and 2018. Hence, this chapter sheds light on the major LC changes at the continental SSA, national and ecoregional scales, contributing to our understanding of the anthropogenic and climatic drivers behind the significant LC changes occurring in SSA. This can, ultimately, help in making better and more sustainable decisions for the people and the wider environment.

4.2. Materials and Methods

4.2.1. Description of the LC and ecoregions datasets

Detailed description of the LC product used in this chapter (ESA-CCI-LC) is provided in section 2.4.

We used the Ecoregions2017 dataset (Dinerstein *et al.*, 2017; Olson *et al.*, 2001) to characterise and analyse the extent of the expansive ecoregions of SSA. The dataset is widely used for biodiversity conservation planning at regional to global scales. It is a detailed and

the most up-to-date ecoregion-based map, with global coverage of 846 ecoregions nested spatially within 14 terrestrial biomes and eight primary biogeographical realms.

4.2.2. Synthesising the LC and ecoregions datasets

The global LC dataset was clipped to the extent of SSA for each annual LC map from 1992 to 2018. To provide clarity and avoid potential complications in the analysis of LC changes, the 37 original LC classes were reduced to 15 major classes (Table 4.1). Fig. 4.1a depicts the spatial distribution of the 15 main LC classes in 2018. The global ecoregions dataset was also clipped to the extent of SSA. Only 115 of the 846 ecoregions globally were found in SSA. We then selected the largest 24 ecoregions by area for subsequent analysis (Fig. 4.1b). These account for 64% of the total land area of SSA, and 57% of the total land area that underwent a change between 1992 and 2018. Table 4.2 lists the main 24 ecoregions used in this research with their corresponding acronyms.

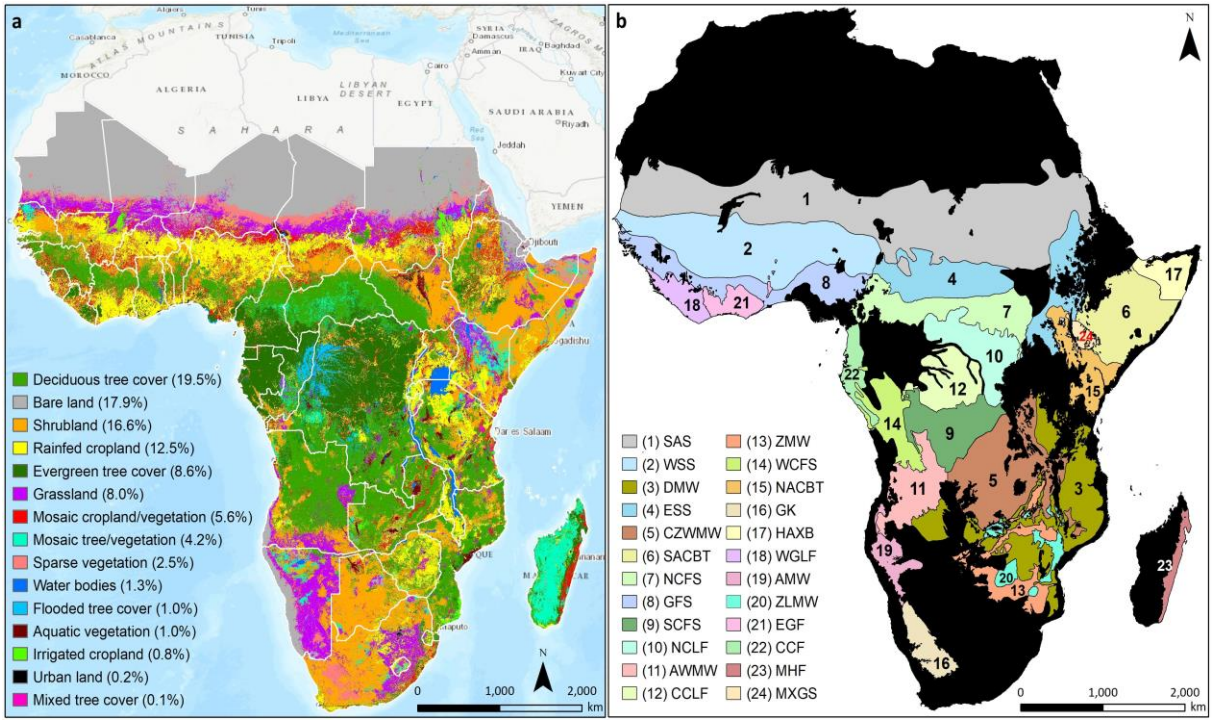

Figure 4.1. Sub-Saharan Africa (SSA): (a) Spatial distribution of the main 15 LC classes in 2018; (b) The selected ecoregions used in this chapter. See Table 4.2 for the acronyms used for ecoregions.

4.2.3. Quantifying LC changes

The 15 class LC data were analysed using the following procedures at three different spatial scales: across the entire SSA, at the national scale for selected individual countries that have witnessed the largest LC changes, and at the ecoregional scale for selected individual ecoregions that have similarly experienced the largest changes. To quantify the gross and net LC gains and losses, a difference map was generated between 1992 and 2018

demonstrating areas gained and lost for each LC class. The total areas of gross gains and losses were calculated by multiplying the total number of pixels representing a gain or loss by pixel area, for each LC class. Net LC changes, however, were quantified by calculating the differences between the gross gains and losses, for each LC class. To analyse the LC trajectories from 1992 to 2018, the total area of each LC class in each individual year was computed, and this was calculated by multiplying the total pixel count by the pixel area.

Finally, the total land area involved in the LC transitions between different combinations of LC classes between 1992 and 2018 was quantified. This was achieved by producing difference maps for each LC class, depicting the areas that had transitioned from that LC class in 1992 (initial year) to each of the other 14 LC classes in 2018 (ending year). Hence, these generated maps showing the areas involved in each of the possible transition types. Then the total area for each transition type was computed by multiplying the total pixel count for that transition type by the pixel area. A spatial aggregation technique was employed to resolve the "salt and pepper" issue at 300 m spatial resolution. Hence, visualising the data appropriately at the continental scale of SSA, and this was based on a 10 x 10 pixel aggregation. Therefore, generating a map depicting the major 12 LC transitions at the SSA scale at a 3 km spatial resolution. We then associated the 12 major LC transitions into five key LC change processes. This allowed us to move from investigating a larger number of LC transitions to a smaller number of key LC change processes to explain and interpret in a simpler manner, namely; gain of dry forests; greening of deserts; loss of tree-dominated savanna; loss of shrub-dominated savanna, and loss of tropical rainforests. Following the same technique that we used to visualise the LC data, a spatial aggregation technique of 10 x 10 pixels was utilised, hence producing a map demonstrating the major five key LC change processes at the SSA scale.

Table 4.1. The LC classes used in this research and the original ESA-CCI-LC classes from which they were generated (ESA-CCI-LC: Product user guide: version 2, available at http://maps.elie.ucl.ac.be/CCI/viewer/download/ESACCI-LC-Ph2-PUGv2_2.0.pdf).

LC classes used in this study	Original LC class codes in the ESA-CCI-LC dataset combined to form the LC classes used in this study	Description of the original LC classes in the ESA-CCI-LC dataset
1. Rainfed cropland	10, 11, 12	Rainfed cropland
2. Irrigated cropland	20	Irrigated cropland
3. Mosaic cropland/ vegetation	30	Mosaic cropland (> 50%)/natural vegetation (tree, shrub, herbaceous cover) (< 50%)
	40	Mosaic natural vegetation (tree, shrub, herbaceous cover) (> 50%)/cropland (< 50%)
4. Evergreen tree cover	50	Tree cover, broadleaved, evergreen, closed to open (> 15%)
	70, 71, 72	Tree cover, needleleaved, evergreen, closed to open (> 15%)
5. Deciduous tree cover	60, 61, 62	Tree cover, broadleaved, deciduous, closed to open (> 15%)
	80, 81, 82	Tree cover, needleleaved, deciduous, closed to open (> 15%)
6. Mixed tree cover	90	Tree cover, mixed leaf type (broadleaved and needleleaved)
7. Mosaic tree/vegetation	100	Mosaic tree and shrub (> 50%)/herbaceous cover (< 50%)
	110	Mosaic herbaceous cover (> 50%)/tree and shrub (< 50%)
8. Shrubland	120, 121, 122	Shrubland
9. Grassland	130	Grassland
	140	Lichens and mosses
10. Sparse vegetation	150, 151, 152, 153	Sparse vegetation
11. Flooded tree cover	160	Tree cover, flooded, fresh or brakish water
	170	Tree cover, flooded, saline water
12. Aquatic vegetation	180	Shrub or herbaceous cover, flooded, fresh-saline or brakish water
13. Urban	190	Urban
14. Bare land	200, 201, 202	Bare land
15. Water bodies	210	Water bodies

Table 4.2. The main ecoregions used with their assigned acronyms. The ecoregions are based on the ecoregions dataset (Ecoregions2017) used in this study, and are listed in a descending order based on the total area of each ecoregion

Ecoregion (acronym)	Ecoregion (acronym)
1. Sahelian Acacia Savanna (SAS)	13. Zambezian Mopane Woodlands (ZMW)
2. West Sudanian Savanna (WSS)	14. Western Congolian Forest Savanna (WCFS)
3. Dry Miombo Woodlands (DMW)	15. Northern Acacia-Commiphora Bushlands and Thickets (NACBT)
4. East Sudanian Savanna (ESS)	16. Gariep Karoo (GK)
5. Central Zambezian Wet Miombo Woodlands (CZWMW)	17. Horn of Africa Xeric Bushlands (HAXB)
6. Somali Acacia-Commiphora Bushlands and Thickets (SACBT)	18. Western Guinean Lowland Forests (WGLF)
7. Northern Congolian Forest Savanna (NCFS)	19. Angolan Mopane Woodlands (AMW)
8. Guinean Forest Savanna (GFS)	20. Zambezian-Limpopo Mixed Woodlands (ZLMW)
9. Southern Congolian Forest Savanna (SCFS)	21. Eastern Guinean Forests (EGF)
10. Northeast Congolian Lowland Forests (NCLF)	22. Congolian Coastal Forests (CCF)
11. Angolan Wet Miombo Woodlands (AWMW)	23. Madagascar Humid Forests (MHF)
12. Central Congolian Lowland Forests (CCLF)	24. Masai Xeric Grasslands and Shrublands (MXGS)

4.3. Results

4.3.1. LC change across Sub-Saharan Africa

Figure 4.2a demonstrates the total gains and losses (gross and net) of the ten major LC classes between 1992 and 2018 at the SSA scale. The LC types are displayed in a descending order based on the net change in area. All LC types, excluding urban, have witnessed considerable gross gains and losses over the timeframe of this study. The largest gross gain was deciduous tree cover followed by rainfed cropland, whilst the largest gross loss was shrubland followed by deciduous tree cover. Six LC types experienced net gains in area, with the largest being associated with rainfed cropland. In contrast, four LC types experienced net losses with the largest being associated with shrubland. The other five LC types (water bodies, flooded tree cover, aquatic vegetation, irrigated cropland and mixed tree cover) are not shown on Figure 4.2a because their respective net changes were considered negligible (less than 10,000 km^2). Therefore, these were excluded from subsequent analysis.

Trajectories of net changes in the total area of each LC type from 1992 to 2018 are illustrated in Fig. 4.2b, and 4.2c for urban land. Six LC types experienced overall gains while the other

four LC types experienced overall reductions. Rainfed cropland was by far the largest net gainer, experiencing the second-largest percentage gain (7.2%) after urban between 1992 and 2018. Rainfed cropland increased rapidly between 1994 and 2012 then stabilised before experiencing declines from 2016 onwards. Deciduous tree cover experienced a slight reduction until 2004 when it started to increase continuously. Mosaic tree/vegetation and sparse vegetation had similar trends to some extent, with both experiencing declines during the early 2000s, but then increasing steadily for the remainder of the time-series. Grassland however, increased from the early 1990s until 2012, before declining.

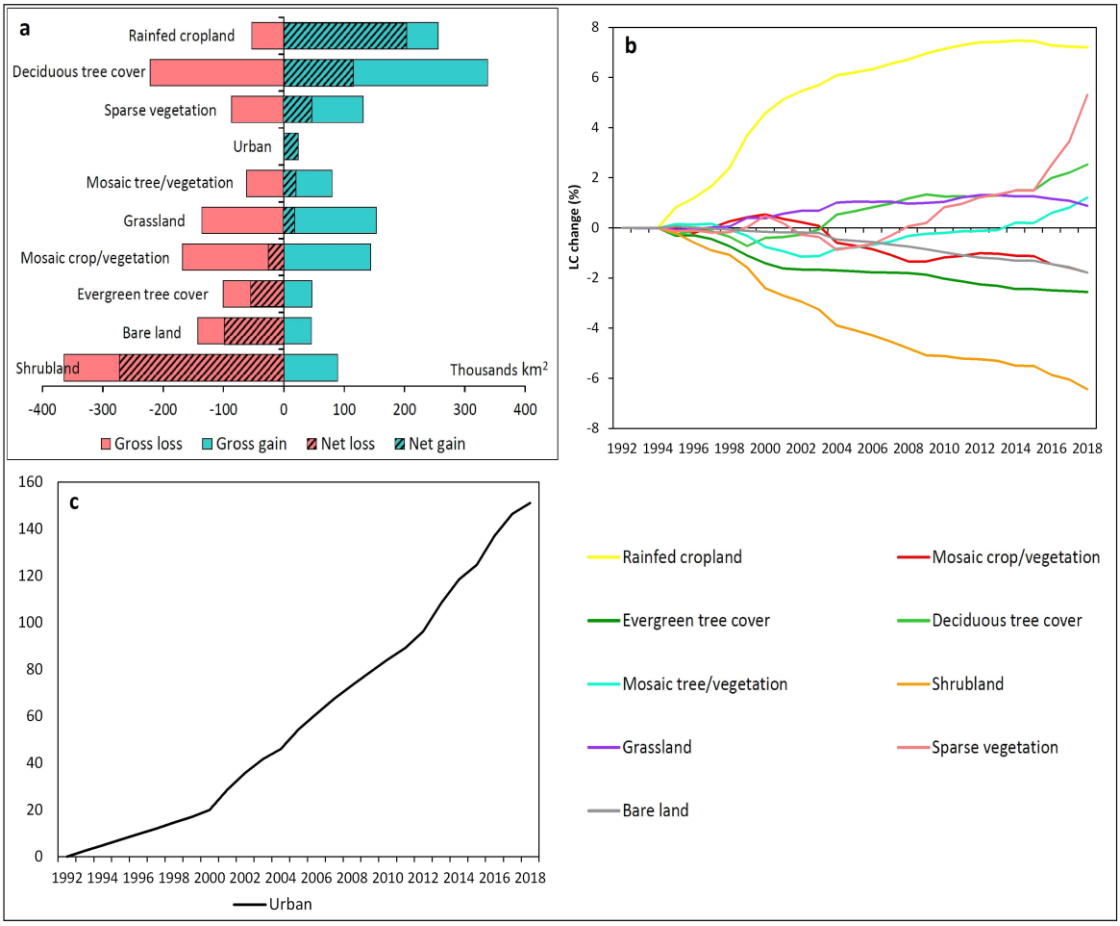

Figure 4.2. Change in the major LC types across SSA: (a) gross and net gains and losses; (b) trajectories of change; (c) trajectories of change for urban land. The colours given to each LC class correspond with the colours used in Figure 4.1a.

Urban area experienced the largest net increase in terms of percentage area (151%) and the fourth largest increase in terms of absolute area. In contrast, the percentage area of mosaic cropland/vegetation increased from 1996 to 2000, but then decreased consistently until 2009 when it started to increase again until 2012, before declining consistently to the end of the time-series. Shrubland, evergreen tree cover and bare land all experienced overall net reductions in area, with shrubland being by far the largest net loser in terms of both absolute

total net area change and percentage area change (-6.43%). The reductions were consistent throughout the three LC types, while for evergreen tree cover, they started to level off towards the end of the time-series.

4.3.2. LC change at the national scale

Here, we identified the 10 countries that experienced the largest LC changes between 1992 and 2018 in SSA, altogether accounting for 56% of the total change that occurred in LC across SSA. Figure 4.3 shows the gains and losses (gross and net) and the trajectories of change for four of the major LC types across SSA including rainfed cropland, mosaic cropland/vegetation, deciduous tree cover and shrubland. The LC types are displayed in descending order based on the net change. The largest increases in rainfed cropland occurred in Nigeria and the DRC, both accounting for 28% of the net gain in rainfed cropland across SSA. Importantly, rainfed cropland was the only LC that experienced net gains only in all investigated nations. The trajectory analysis shows that for the majority of countries rainfed cropland started to level off towards the end of the time-series, with some countries experiencing slight declines including Ethiopia and Tanzania. A larger decline was visible in the case of Nigeria, starting from 2015 onwards.

Mosaic cropland/vegetation is a dynamic LC type that witnessed both net gains and losses across the top 10 countries. The largest net increases occurred in Sudan and Chad, whilst the largest net decreases occurred in Tanzania and the DRC. Some countries showed a consistent increase including Sudan and Chad, whilst the DRC showed a recent increase starting from 2010 onwards after experiencing a consistent decrease starting from the initial year of the time-series. In contrast, some countries experienced a consistent decrease including Tanzania and Ethiopia, with Nigeria showing a reduction in this LC type from 2015, having seen an increase from the start of the time-series. Overall, Tanzania and Ethiopia experienced similar rates of decline in both rainfed and mosaic cropland/vegetation. Nigeria also experienced a similar reduction in both rainfed cropland and mosaic cropland/vegetation, but starting from 2015 onwards only.

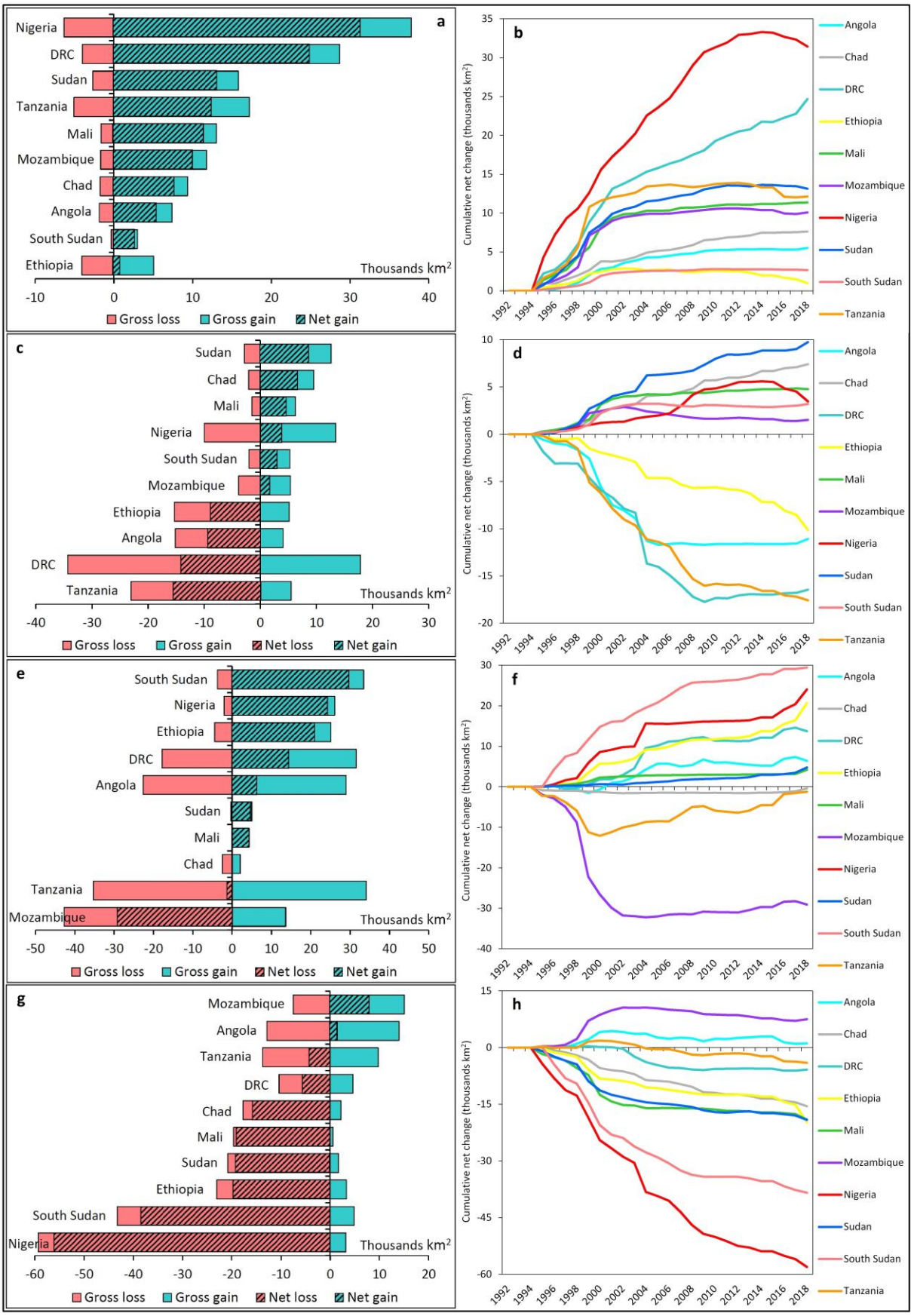

Figure 4.3. LC change at the national scale: (a) and (b) demonstrate the gains and losses and trajectories of change for rainfed cropland; (c) and (d) mosaic cropland/vegetation; (e) and (f) deciduous tree cover, and (g) and (h) shrubland.

Since deciduous tree cover experienced the largest gross gain and second-largest net gain in area across SSA, most countries included in this analysis experienced net gains in deciduous tree cover, with South Sudan, Nigeria and Ethiopia experiencing the largest net gains. However, Mozambique was found to be the largest country that experienced a net decline in deciduous tree cover by far, accounting for 19% of the gross loss across SSA. The trajectory analyses suggests that most countries have seen a relatively steady increase in deciduous tree cover, which was prominent in South Sudan, Nigeria and Ethiopia. In contrast, despite the net losses in Tanzania and Mozambique, there was an increase in the absolute amount of deciduous tree cover in both countries, starting from 2001 and 2004 onwards in Tanzania and Mozambique, respectively. However, this was far more noticeable in Tanzania.

At the scale of SSA, shrubland was the largest gross and net loser by far. Therefore, most countries included in the analysis showed net declines in shrubland, except Mozambique and Angola. The largest losses occurred in Nigeria and South Sudan, both accounting for 34% of the net loss in shrubland across SSA. The trajectory analyses demonstrates that most countries showed steady declines consistently over time and this was far more noticeable and considerable in Nigeria and South Sudan.

Acknowledging the importance of tropical rainforests to the local communities and the sustainability of ecosystem services in SSA, we now identify the top 10 countries with the largest area of tropical rainforests (evergreen tree cover), altogether accounting for 94% of the total area of the tropical rainforests distributed across SSA in 2018. We analysed the amount and trajectories of change in evergreen tree cover throughout the time-series. As shown in Figure 4.2a, evergreen tree cover experienced the third-largest net loss in area across SSA. This is somewhat expected given net declines in evergreen tree cover across most countries. Figure 4.4 shows gross and net gains and losses in area, and trajectories of change in evergreen tree cover between 1992 and 2018 for the top 10 countries with the largest area of evergreen tree cover. Not surprisingly, most countries witnessed net declines, with the DRC and Madagascar experiencing the largest net evergreen tree cover losses across the continent, accounting for 72% of total net loss. In contrast, Ethiopia and Angola both produced net increases in evergreen tree cover.

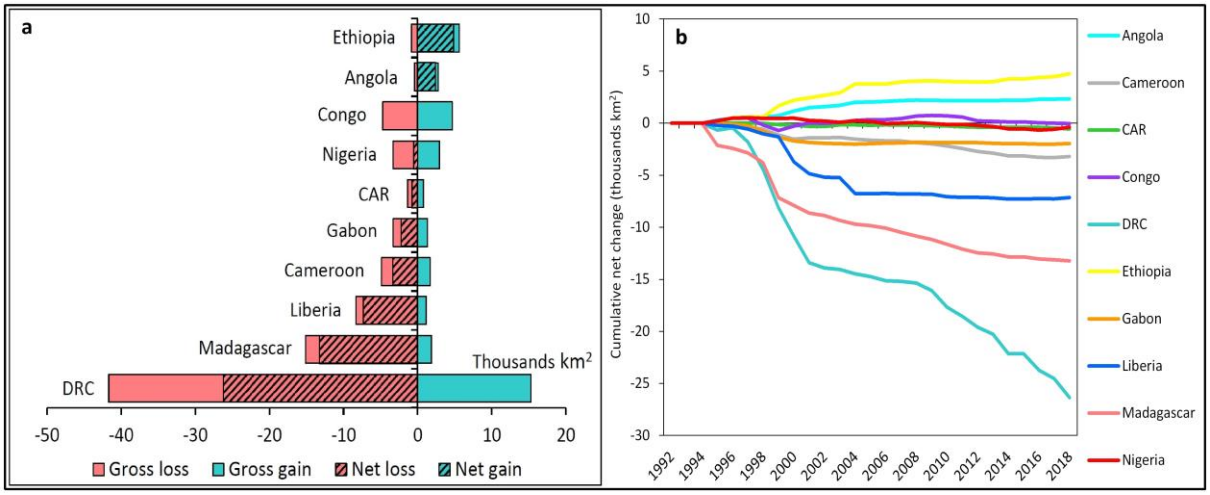

Figure 4.4. Changes in evergreen tree cover (tropical rainforests) at the national scale: (a) gross and net gains and losses; (b) trajectories of change.

The trajectory analysis for evergreen tree cover reveals that the DRC, Madagascar and Liberia experienced the largest declines in area among all countries, alarmingly. This decline started to level off in Liberia in 2004; however, it continues in both the DRC and Madagascar to this day, with a much faster rate in the DRC. In contrast, there was an increase in evergreen tree cover in Ethiopia and Angola. It was interesting to see three groups of countries based on how tropical rainforests changed throughout the study period. Specifically those that experienced (i) large declines; (ii) overall net gains, and (iii) little change or no change, including Congo, the Central African Republic (CAR) and Gabon.

4.3.3. LC change at the ecoregional scale

Due to the importance of understanding the implications of LC change on biodiversity and natural communities within the different terrestrial ecoregions of SSA, we here identify the 10 ecoregions that witnessed the largest LC changes between 1992 and 2018 across SSA, altogether accounting for 67% of the total change that occurred across all ecoregions. Figure 4.5 shows the gross and net gains and losses, and the trajectories of change for the same major LC classes mentioned in section 4.3.2. The LC types are displayed in descending order based on the net change.

The largest net increases in rainfed cropland occurred within the west Sudanian savanna and Dry Miombo woodlands, accounting for 26% of the net gain in rainfed cropland across SSA. Generally, rainfed cropland was the only LC to experience net gains only across all investigated ecoregions. The trajectory analysis shows that the amount of rainfed cropland in most ecoregions started to level off towards the end of the time-series, with some ecoregions experiencing declines including west Sudanian savanna, dry Miombo woodlands

and Guinean forest-savanna, starting from 2014 onwards. Although the overall amount of rainfed cropland gained in the northeast Congolian lowland forests was relatively small, it was the only ecoregion in our analysis that has seen slight, but consistent gains over time.

Most ecoregions experienced net gains in mosaic cropland/vegetation. The largest net gains occurred in the Sahelian Acacia savanna and west Sudanian savanna ecoregions, whilst the largest net losses occurred in the southern Congolian forest savanna and dry Miombo woodlands ecoregions. The trajectory analysis suggests that west Sudanian savanna and Guinean forest-savanna (neighbouring ecoregions) had a similar declining trend starting from 2014 onwards. In Sahelian Acacia savanna, however, the trend rose consistently over time. In contrast, southern Congolian forest savanna, dry Miombo woodlands and central Zambezian wet Miombo woodlands showed overall reductions, and these were found to be levelling-off starting from 2008 in southern Congolian forest savanna and 2009 in central Zambezian wet Miombo woodlands. Dry Miombo woodlands showed a more consistent decreases over time, but with a relatively slower rate starting from 2009.

Since deciduous tree cover experienced the largest gross increase and the second-largest net increase across SSA, expectedly, most ecoregions experienced net gains in deciduous tree cover, with west Sudanian savanna and Guinean forest-savanna being the largest net gainers. In contrast, central Zambezian wet Miombo woodlands experienced the largest net decline in deciduous tree cover across SSA, accounting for 17% of the gross loss across SSA between 1992 and 2018. Most ecoregions showed an increase in deciduous tree cover over time; this was larger and more consistent in some ecoregions (west Sudanian savanna, Guinean forest-savanna and east Sudanian savanna) while levelling off or with relatively modest gains in others (Northern Congolian forest savanna, southern Congolian forest savanna and Sahelian Acacia savanna). In contrast, central Zambezian wet Miombo woodlands and Zambezian mopane woodlands (neighbouring ecoregions) experienced reductions in deciduous tree cover. In Zambezian mopane woodlands, increases in deciduous tree cover were observed starting from 2002 onwards. However, in central Zambezian wet Miombo woodlands, the reductions were far more consistent. Interestingly, after consistent declines in dry Miombo woodlands starting from the initial year of the study period, starting from 2001 onwards, consistent increases were observed until the end year of the time-series.

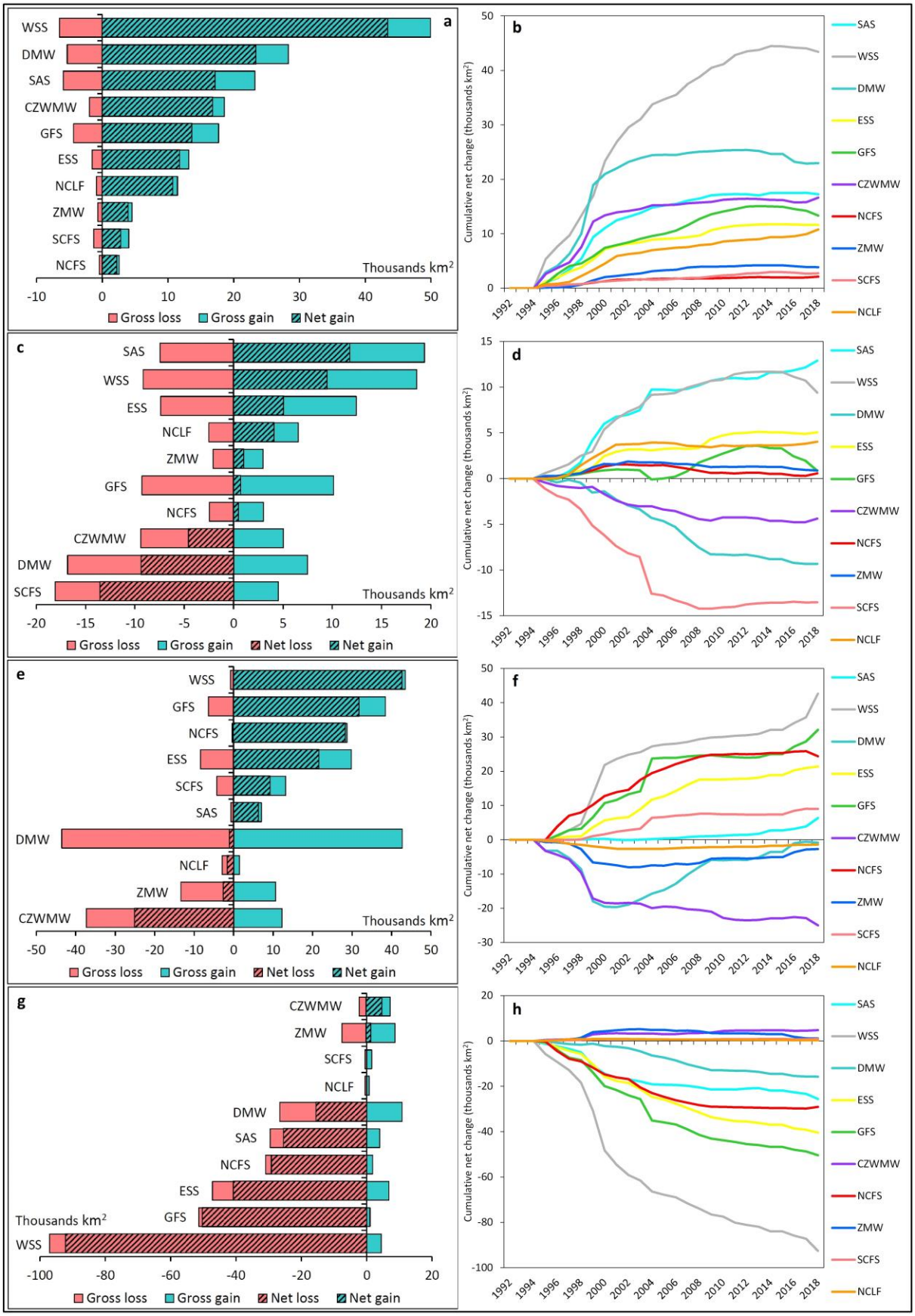

Figure 4.5. LC at the ecoregional scale: (a) and (b) demonstrate the gains and losses and trajectories of change for rainfed cropland; (c) and (d) mosaic cropland/vegetation; (e) and (f) deciduous tree cover, and (g) and (h) shrubland. See Table 4.2 for the acronyms used for ecoregions.

Since shrubland has experienced the largest gross and net loss across SSA, the vast majority of ecoregions showed large net losses, except for central Zambezian wet Miombo woodlands and Zambezian mopane woodlands. The largest net loss occurred in west Sudanian savanna, accounting for 34% and 27% of the net and gross loss, respectively, across SSA. The trajectory analysis demonstrates that most ecoregions showed consistent declines over time, and this was far more noticeable and considerable in west Sudanian savanna. In contrast, starting from 2009 onwards, shrubland started to experience gains in Northern Congolian forest savanna.

4.3.4. LC transitions across sub-Saharan Africa

In this section, we identify and quantify the 12 largest LC transitions based on the area that transitioned between different combinations of LC between 1992 and 2018. They represent the vast majority of the LC transitions that occurred in the region, accounting for 71% of all 182 possible transitions. Figure 4.6 depicts the spatial distribution of the 12 major LC transitions across SSA between 1992 and 2018. The largest transition by far was shrubland converting to deciduous tree cover, accounting for 15.5% of the total changed area. This was widely distributed across the continent with South Sudan, Nigeria and Ghana experiencing the largest areas of shrubland converting to deciduous tree cover. The second-largest LC transition was mosaic cropland/vegetation converting to deciduous tree cover, accounting for 7.8% of all transitions. This was more concentrated around Central and Eastern Africa including in the DRC, Tanzania and Angola. The third-largest LC transition was shrubland converting to rainfed cropland, accounting for 7.3% of the total transitioned area across SSA. This was more focused around the northern part of SSA (south of the Sahara Desert) with most of this transition occurring in western Africa (e.g., Nigeria, Mali and Burkina Faso).

Extensive areas of bare land converted to sparse vegetation (7%) and sparse vegetation to grassland (5.4%) between 1992 and 2018. They were concentrated around and adjacent to desert areas including South of the Sahara Desert (the Sahel region), the Kalahari Desert, the Namib Desert and the Horn of Africa. The largest areas of conversion from bare land to sparse vegetation occurred in Niger, Sudan and Mali, whilst Namibia and Niger experienced the largest areas of sparse vegetation converting to grassland. Transitions from deciduous tree cover to rainfed cropland (6%) and shrubland (5%) were mainly focused around the Eastern and South-Eastern parts of the continent. Deciduous tree cover to rainfed cropland (5.9%) has largely occurred in Tanzania, Malawi and Mozambique, whilst Mozambique,

Angola and Tanzania experienced the largest areas of deciduous tree cover converting to shrubland (5.1%) between 1992 and 2018.

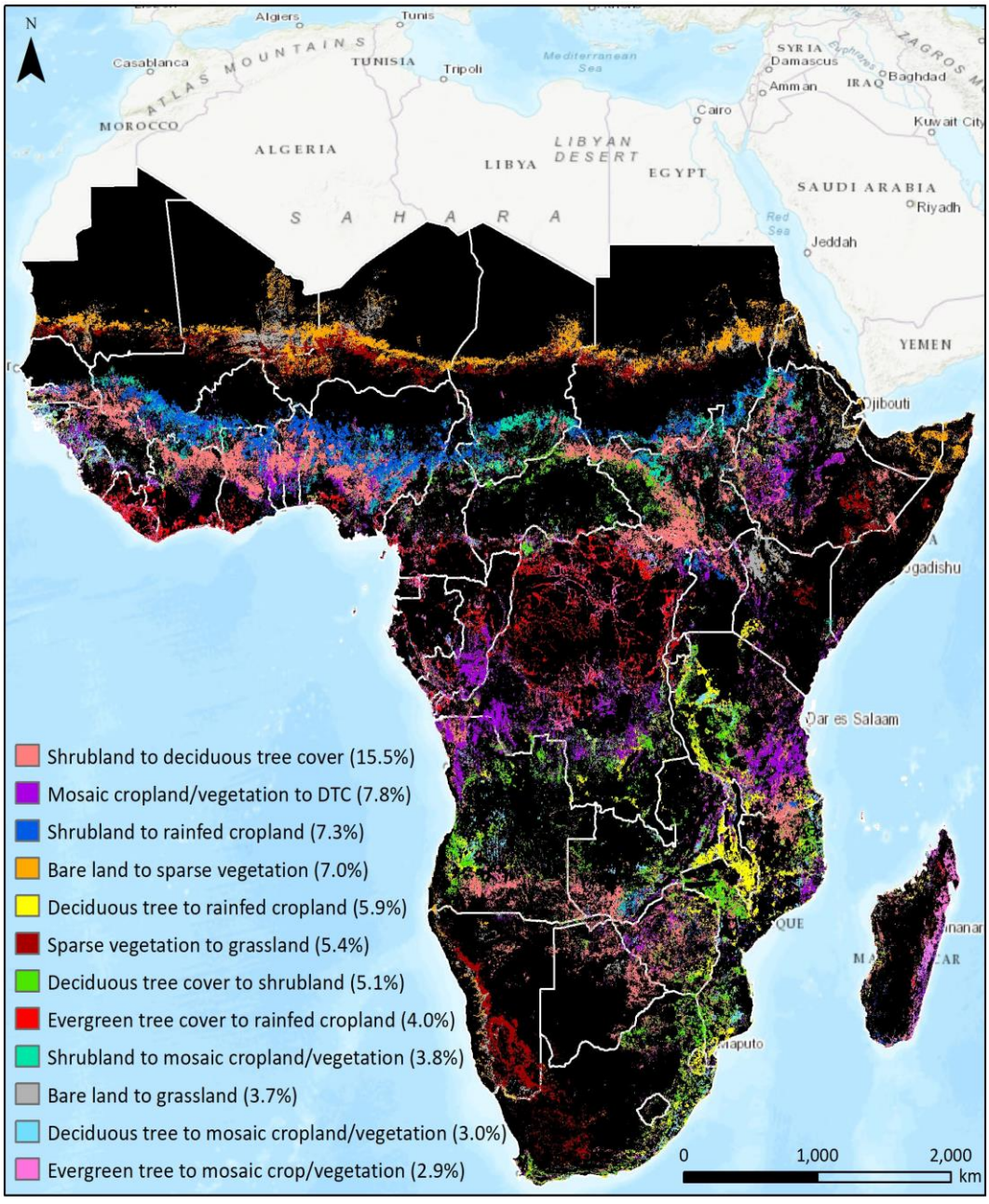

Figure 4.6. The 12 major LC transitions across SSA (1992-2018): The transitions are displayed in descending order based on their areas. The numbers between the brackets indicate the proportion of each LC transition out of the total area changed. The original data were aggregated to a 3 km spatial resolution for visualisation. Black areas are terrestrial zones where there was no change or other LC transitions occurred.

Interestingly, the amount of tropical rainforest lost to agriculture was not as large as anticipated, accounting for 4% and 3% for evergreen tree cover converting to rainfed cropland and mosaic cropland/vegetation, respectively. The DRC, Côte d'Ivoire, and Liberia experienced the largest transitions from evergreen tree cover to rainfed cropland, while the

DRC and Madagascar saw the largest amount of evergreen tree cover converting to mosaic cropland/vegetation between 1992 and 2018.

4.3.5. LC transitions at the Ecoregional scale

We associated the 12 major LC transitions discussed in section 4.3.4 with five key LC change processes namely: woody cover encroachment, greening of deserts, loss of tree-dominated savanna, loss of shrub-dominated savanna and loss of tropical rainforests. The five key LC change processes are listed in descending order based on the total area of each change process. Figure 4.7 shows the spatial distribution of the five key LC change processes across SSA between 1992 and 2018. Table 4.3 lists the 12 major LC transitions used for the association procedure and the corresponding ecoregions in which they occur, from which the five key LC change processes were formed.

The largest key LC change process by far was the *gain of dry forests* and it was widely distributed across SSA. In total, 92 ecoregions experienced this LC change process between 1992 and 2018 across SSA. We identified the largest seven ecoregions that experienced increases in deciduous tree cover, and they were west Sudanian savanna, dry Miombo woodlands, Guinean forest-savanna, east Sudanian savanna, north Congolian forest savanna, western Congolian forest savanna and southern Congolian forest savanna, accounting for 67% of the total area that transitioned into deciduous tree cover across the 92 ecoregions.

The second-largest key LC change process was *greening of deserts*, distributed adjacent to areas including South of the Sahara Desert, Kalahari Desert, Namib Desert and the Horn of Africa. Forty-three ecoregions in total experienced this key process across SSA. We identified the largest seven ecoregions (Sahelian Acacia savanna, Gariep Karoo, Somali Acacia-Commiphora bushlands and thickets, Northern Acacia-Commiphora bushlands and thickets, Angolan Mopane woodlands, Horn of Africa Xeric bushlands and Masai Xeric grasslands and shrublands), accounting for 88% of the total area of this key LC process across the 43 ecoregions.

Loss of tree-dominated savanna was the third-largest key LC change process, covering 88 ecoregions in total across SSA. This LC change process was concentrated around the eastern and South-eastern parts of the continent. We identified the largest seven ecoregions (dry Miombo woodlands, central Zambezian wet Miombo woodlands, Zambezian Mopane woodlands, Zambezian-Limpopo mixed woodlands, Angolan wet Miombo woodlands, east Sudanian savanna and Guinean forest-savanna) that saw the largest area transitioned from woodland-dominated savanna, accounting for 65% of all 88 ecoregions.

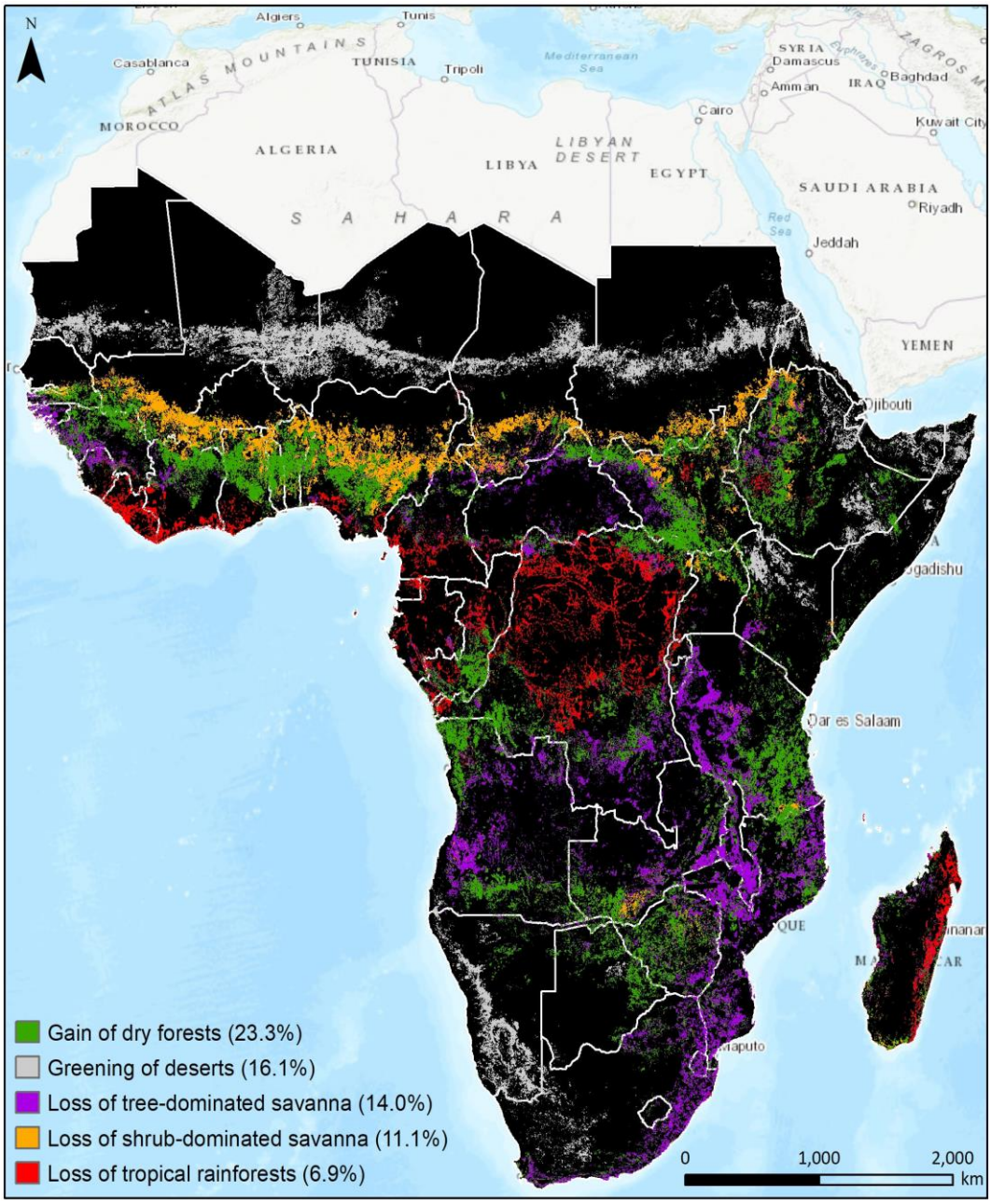

Figure 4.7. The five key LC change processes across SSA (1992-2018): The processes are displayed in descending order based on their areas. The numbers between the brackets indicate the proportion of each LC change process. The original data were aggregated to a 3 km spatial resolution for visualisation. Black areas are terrestrial zones where there was no change or other LC transitions occurred.

The fourth-largest key LC change process was the *loss of shrub-dominated savanna*, spanning 71 ecoregions in total across SSA. It was focused within the northern part of SSA, just south of the Sahara Desert and was found notably in Western Africa. This is the only key process where we have identified only the largest four ecoregions (west Sudanian savanna, east Sudanian savanna, Guinean forest-savanna and Sahelian Acacia savanna), since they were substantially dominant, accounting for 90% of all 71 ecoregions.

Table 4.3. The LC transitions and ecoregions used to analyse and quantify changes across the five key LC change processes, the ecoregions are listed in a descending order based on the size of the area transitioned. See Table 4.2 for the acronyms used for ecoregions.

Key LC process	LC transition	Area and proportion of each LC transition out of all transitions	Ecoregions
1. Gain of dry forests	Shrubland to deciduous tree;	190,110 km² (15.5%)	WSS, DMW, GFS, ESS, NCFS, WCFS, SCFS
	Mosaic cropland/vegetation to deciduous tree cover	95,802 km² (7.8%)	
2. Greening of deserts	Bare land to sparse vegetation;	86,187 km² (7.0%)	SAS, GK, SACBT, NACBT, AMW, HAXB, MXGS
	Sparse vegetation to grassland;	65,761 km² (5.4%)	
	Bare land to grassland	45,751 km² (3.7%)	
3. Loss of tree-dominated savanna	Deciduous tree to rainfed cropland;	72,959 km² (5.9%)	DMW, CZWMW, ZMW, ZLMW, AWMW, ESS, GFS
	Deciduous tree cover to shrubland;	62,595 km² (5.1%)	
	Deciduous tree cover to mosaic cropland/vegetation	36,369 km² (3.0%)	
4. Loss of shrub-dominated savanna	Shrubland to rainfed cropland;	89,313 km² (7.3%)	WSS, ESS, GFS, SAS
	Shrubland to mosaic cropland/vegetation	46,653 km² (3.8%)	
5. Loss of tropical rainforests	Evergreen tree cover to rainfed; cropland	48,773 km² (4.0%)	NCLF, WGLF, MHF, SCFS, EGF, CCLF, CCF
	Evergreen tree cover to mosaic cropland/vegetation	36,104 km² (2.9%)	

Interestingly, the smallest key LC change process in our analysis was the *loss of tropical rainforests*. It was located around areas of Central-Western Africa and Madagascar. In total, 74 ecoregions experienced this LC change process across SSA. The largest seven ecoregions (northeast Congolian lowland forests, western Guinean lowland forests, Madagascar humid forests, southern Congolian forest savanna, eastern Guinean forests, central Congolian

lowland forests and Congolian coastal forests) that we identified, accounted for 70% of all 74 ecoregions between 1992 and 2018.

Figure 4.8 shows the proportional contribution of each ecoregion towards its corresponding key LC change process. In "gain of dry forests", the largest seven ecoregions presented in the analysis accounted for 67% across 92 ecoregions in SSA. The West Sudanian savanna and dry Miombo woodlands were the two largest ecoregions among all, accounting for 28%. In "greening of deserts", the Sahelian Acacia savanna ecoregion which is located adjacent to the Sahara Desert was dominant with 62% of all 43 ecoregions experiencing this key LC change process. In "loss of tree-dominated savanna", the largest seven ecoregions presented in the analysis accounted for 65% across 88 ecoregions across SSA. The Dry Miombo woodlands and central Zambezian wet Miombo woodlands were the two largest ecoregions among all, accounting for 39%. In "loss of shrub-dominated savanna", the west Sudanian savanna was the dominant ecoregion with 44% of all 71 ecoregions experiencing this key LC process. Finally, in "loss of tropical rainforests", the largest seven ecoregions presented in the analysis accounted for 70% across 74 ecoregions in SSA. The Northeast Congolian lowland forests and western Guinean lowland forests were the two largest ecoregions among all, accounting for 35% across SSA between 1992 and 2018.

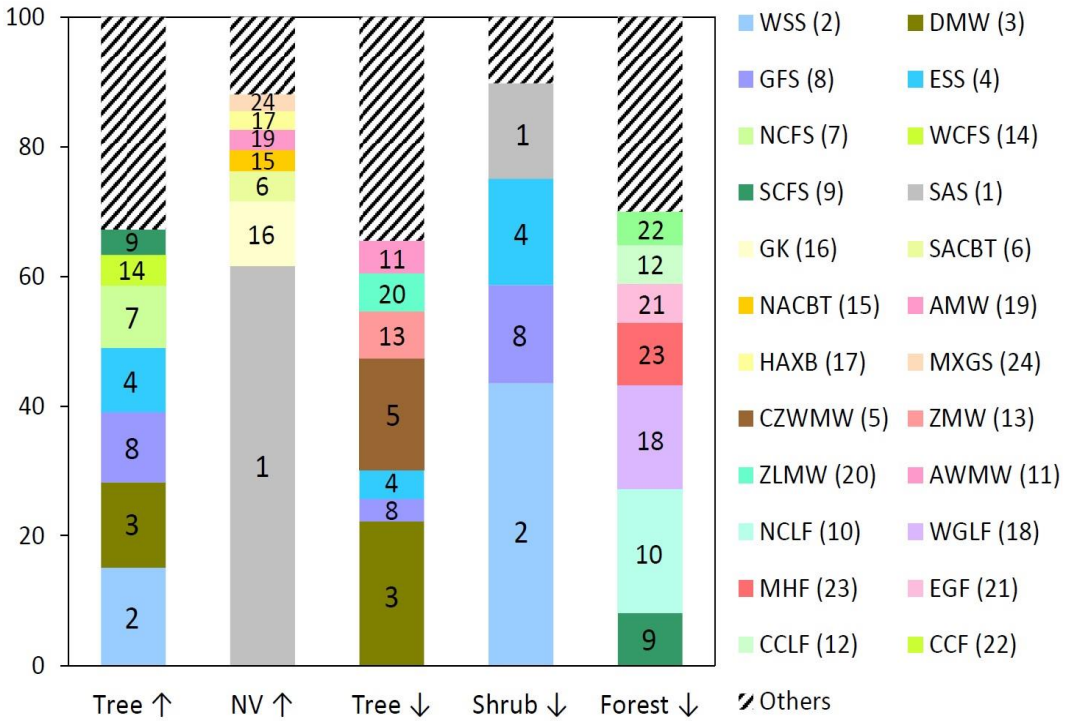

Figure 4.8. The proportional contribution of each ecoregion towards its corresponding key LC change process. The colours given to the ecoregions correspond to their counterparts in Fig. 4.1b.

4.4. Discussion

The largest key LC change process in our analysis, surprisingly, was the "gain of dry forests" over the shrubland dominated savanna. Most forest cover change studies, understandably, are concerned about quantifying the loss in tropical rainforests, with less attention given to other areas where forest cover appears to be increasing (Malhi *et al.*, 2013). Although the dry forests of Africa have suffered large losses over the past few decades due to disturbances via logging, fuelwood extraction, shifting cultivation and cropland expansion (e.g., the case of tobacco in Tanzania, Mozambique and Malawi; Bodart *et al.*, 2013; Mayes *et al.*, 2015; Ryan *et al.*, 2016; Jew *et al.*, 2017), recent studies have reported large increases in tree and woody cover in dry forest territories at the expense of natural vegetation (Mitchard and Flintrop, 2013; Brandt *et al.*, 2017; Venter *et al.*, 2018). Furthermore, such changes have been reported at the global scale, occurring in other locations including South America and Australia. However, Africa was found to be the largest continent exhibiting gains in dry forest regions (Stevens *et al.*, 2017).

Gain of dry forests was attributed to several drivers including: (1) a reduction in the detrimental impacts of human activities (Fenta *et al.*, 2020) via promoting afforestation and local forest management (e.g., South Sudan and Ethiopia), implementing forest protection laws and conservation policies (e.g., shade coffee certification in Ethiopia; Takahashi and Todo, 2013); (2) increasing rainfall due to climate change (Brandt *et al.*, 2015; Tian *et al.*, 2017); (3) increasing atmospheric CO_2 levels favouring the growth of woody cover over grassy vegetation (Midgley and Bond, 2015; Parr *et al.*, 2014; Beerling and Osborne, 2006); (4) the natural recovery of woodlands on abandoned cultivated land (Mayes *et al.*, 2015); (5) alterations in fire regime "fire suppression", as more fires prevent the encroachment of woody shrubs and trees (Roques *et al.*, 2001; Beerling and Osborne, 2006; O'Connor *et al.*, 2014); (6) grass removal and overgrazing by livestock and herbivores (Midgley and Bond, 2015).

We found that the largest increase in tree cover was in South Sudan (Duan and Tan, 2019), Nigeria (Fenta *et al.*, 2020) and Ethiopia (Belay *et al.*, 2013) followed by smaller gains in Southern Africa in Angola, Zambia, Zimbabwe and Botswana (O'Connor *et al.*, 2014). This correlates with our ecoregional analysis since the largest gains were dominant in the West Sudanian savanna, Guinean forest savanna and east Sudanian savanna. It is recognised that the assessment of the spatial and temporal extent of the dry forest of SSA using satellite remote sensing data is challenging and faces many difficulties (Bodart *et al.*, 2013). One of

the main challenges in mapping the dry forests in SSA is the variability in spectral response during the dry and wet seasons, which result in considerable associated uncertainties (Bodart *et al.*, 2013; Mayes *et al.*, 2015).

The second-largest key LC change process in the analysis was found to be, the "*greening of deserts*". This LC change process was found adjacent to desert areas including the South of the Sahara Desert (the Sahel belt), the Kalahari Desert, the Namib Desert and the Horn of Africa. We report that Niger (Nutini *et al.*, 2013), Sudan, Mali (Spiekermann *et al.*, 2015) and Namibia (Wingate *et al.*, 2019) are the largest countries in SSA exhibiting a greening transition, of which three are located within the Sahel belt. The African Sahel has received considerable attention from numerous researchers during the past two decades, as it has been recognised as one of the global hot spots of environmental and climate change (Hickler *et al.*, 2005; Brandt *et al.*, 2015) with fluctuations in both climatic conditions and in human-induced land-use patterns (Herrmann *et al.*, 2005; Anyamba and Tucker, 2005). The region has exhibited major droughts, reductions in rainfall and consequent famines during the 1970s and 1980s (Olsson *et al.*, 2005; Huber *et al.*, 2011). However, starting from the 1990s onwards, precipitation reverted back to pre-Sahelian drought conditions and, thus, rainfall has started to increase again, encouraging the growth of natural vegetation with satellite-measured greening indices increasing accordingly (Brandt *et al.*, 2015; Higginbottom and Symeonakis, 2020).

This phenomenon is widely referred to and known as "greening of the Sahel" with researchers across the globe reporting similar findings demonstrating that the increase in rainfall (Brandt *et al.*, 2015; Herrmann *et al.*, 2005), rise in atmospheric CO_2 concentrations "CO_2 fertilisation" (Helldén and Tottrup, 2008; Brandt *et al.*, 2015), increased temperatures, rural to urban migrations (Olsson *et al.*, 2005; Helldén and Tottrup, 2008) and changes in the management of agricultural land (Herrmann *et al.*, 2005; Olsson *et al.*, 2005) were the main drivers behind this greening pattern in the African Sahel. In addition, it has been reported that a global level of "greenness" was observed in multiple semi-arid locations around the globe between 1981 and 2007, including India, Australia, Turkey and the USA (Fensholt *et al.*, 2012).

Helldén and Tottrup (2008) and Herrmann *et al.* (2005) reported that the Sahel region of Africa had the strongest "greenness" response captured by satellite remote sensing measured indices (e.g., NDVI) at the global level between 1982 and 2003, with subsequent implications for the carbon cycle within the wider region (Ogutu *et al.*, 2021). We find that

the “greening” transitional process usually occurs in a successional manner from bare land to sparse vegetation to grassland, in that order. However, in some areas, a direct transition from bare land to grassland may occur. Hence, we report that the Sahelian Acacia savanna was the largest ecoregion exhibiting the transitions between bare land, sparse vegetation and grassland, by far, and covers the entire Sahel belt.

Our findings demonstrate that the third largest key LC change process was the “*loss of tree-dominated savanna*”, mainly converting to rainfed cropland and shrubland (e.g., dry forest disturbances leading to a degraded dry forest). Although we report a net increase in deciduous tree cover in SSA with the majority of nations exhibiting a similar pattern, we also report large losses in deciduous tree cover in Mozambique (Silva *et al.*, 2019; Sedano *et al.*, 2020), Tanzania (Nzunda and Midtgaard, 2019; Mayes *et al.*, 2015), Angola (Schneibel *et al.*, 2017; Cabral *et al.*, 2011), Malawi (Ngwira and Watanabe, 2019; Gondwe *et al.*, 2019) and Zambia (Phiri *et al.*, 2019). This finding corresponds with those of Bodart *et al.* (2013) and McNicol *et al.* (2018).

It also correlates to our ecoregional analysis suggesting that these large losses were located within the dry Miombo woodlands followed by the central Zambezian wet Miombo woodland territories (neighbouring ecoregions). It is widely recognised that the Miombo woodlands support the livelihoods of more than 100 million residents within local communities (Kalaba *et al.*, 2013), and provide ecosystem services (Ryan *et al.*, 2016) including biodiversity (Jew *et al.*, 2016) and carbon sequestration (McNicol *et al.*, 2018) across an extensive area of SSA since it is considered the largest contiguous area with dry forests and woodlands, globally (Jew *et al.*, 2017; Mayes *et al.*, 2015). It has been reported that the Zambezian Miombo ecoregion is one of the highest for the richness of mammal and bird species, not just at the SSA level, but also globally (Ryan *et al.*, 2016).

We report that the expansion of agriculture is a major driver of LC change in the continental SSA in general (Brink and Eva, 2009; Ordway *et al.*, 2017a) and herein, in Eastern and South-eastern Africa. This is supported widely by other studies investigating the loss of woodland cover in that region, with agricultural expansion being the main driver to the loss of the dry forests of the Miombo woodlands (Bullock *et al.*, 2021; Jew *et al.*, 2017; Ryan *et al.*, 2016; Mayes *et al.*, 2015). It was reported that the savanna woodland of East Africa is one of the top areas with high future potential for cultivation at the global scale (Phalan *et al.*, 2013). With the rapid population increase and the associated implications on urbanisation and

migrations in the region, the demand for the extraction of fuelwood and charcoal has also risen substantially (Mitchard and Flintrop, 2013; Mayes *et al.*, 2015; Jew *et al.*, 2017).

In addition, the expansion of lucrative crops has also increased significantly and perhaps the cases of tobacco and cashew expansions in Tanzania (Jew *et al.*, 2017; Rossi *et al.*, 2009), Mozambique (Jansen *et al.*, 2008; Cramer, 1999) and Malawi (Ngwira and Watanabe, 2019) is one of the most widely recognised in the Miombo woodlands region. It has been reported that the expansion of tobacco cultivation in this region always comes at an expensive environmental cost since 1 kg of cured tobacco requires about 12 kg of firewood (Jew *et al.*, 2017) with evidence of recent shifting cultivation occurring in the Miombo region (McNicol *et al.*, 2015). Furthermore, there is also recent growing evidence regarding a consistent expansion in areas cultivated with soybean (Gasparri *et al.*, 2016) and sugarcane (German *et al.*, 2020) within the savanna ecosystem of South and South-eastern Africa.

As discussed above, the large gains in agriculture in SSA come at the expense of natural vegetation. We report that the "*loss of shrub-dominated savanna*" was the fourth largest key LC change process, converting mainly to rainfed agriculture, with extensive increases in rainfed agriculture across West Africa within the West Sudanian savanna ecoregion and extending across Nigeria (Souverijns *et al.*, 2020), Mali and Burkina Faso (Ruelland *et al.*, 2010; Paré *et al.*, 2008). Since shrubland witnessed the largest decline among all LC classes, it is not surprising to see that most countries and ecoregions exhibited large declines in shrubland. West Sudanian savanna, Guinean forest-savanna and east Sudanian savanna (neighbouring ecoregions) experienced the largest declines in shrubland across all ecoregions in SSA between 1992 and 2018.

Most of the shrubland lost in South Sudan and Ethiopia (Duan and Tan, 2019) converted to deciduous tree cover "*gains of dry forests*", whilst in Mali (Ruelland *et al.*, 2010; Ollenburger *et al.*, 2016) and Burkina Faso (Knauer *et al.*, 2017; Zoungrana *et al.*, 2018), most shrubland lost converted to rainfed cropland. Large-scale cropland expansion in West Africa has been recognised widely as starting from the mid-1970s to the early 2000s (Barnieh *et al.*, 2020; Vittek *et al.*, 2013). Hence, extensive areas of cropland for both subsistence uses and export markets including maize, cotton and cashew were reported in Mali (Ollenburger *et al.*, 2016) and Burkina Faso (Knauer *et al.*, 2017) at the expense of natural vegetation. Moreover, large gains in agriculture were reported in East Africa, particularly in South Sudan, Sudan and Ethiopia between 1990 and 2010 (Brink *et al.*, 2014).

Unexpectedly, the "*loss of tropical rainforests*" was the smallest key LC change process in area across SSA between 1992 and 2018. We report large declines in tropical rainforest across the DRC, Madagascar, Liberia, Ivory Coast and Cameroon, with corresponding losses in the Northeast Congolian lowland forests (Northern DRC), Western Guinean lowland forests (Liberia) and Madagascar humid forests (Madagascar) ecoregions, respectively. Although Africa's tropical rainforests comprise only about 13% of the total continental landmass (Mayaux *et al.*, 2004), they contribute about 90% of the amount of carbon stored within the continent's terrestrial ecosystems (Mayaux *et al.*, 2013).

Furthermore, the rainforests of SSA, which account for about 20% of the global tropical rainforest total area, are primarily located around the Congo basin (Rudel, 2013; Mayaux *et al.*, 2013). The Congo basin is the largest contiguous tropical rainforest area in Africa and the globe's second-largest after the Amazon basin and it has witnessed major civil wars and unrests (Nackoney *et al.*, 2014). It is widely recognised that Africa's tropical rainforests (Rudel, 2013; Mayaux *et al.*, 2013) have experienced large declines due to several anthropogenic-driven causes (Geist and Lambin, 2002; Curtis *et al.*, 2018).

Africa's tropical rainforests play important roles in stabilising carbon storage, reducing carbon emission levels, and combatting climate change, at the global scale (Baccini *et al.*, 2012). At the local scale, they also provide habitat for several mammal and plant species, as well as supporting the livelihood of hundreds of millions of rural people relying on extracting food, medicines, charcoal, fuelwood, timber, fibre, construction materials and food for livestock (Mayaux *et al.*, 2013; Rudel, 2013). At the local scale, the expansion of cropland and forest logging for fuelwood production have been reported as the main causes of the tropical rainforest deforestation in SSA driven by rapid population growth (Geist and Lambin, 2002; Rudel, 2013; Mayaux *et al.*, 2013).

At the global scale, tropical rainforests declines were reported (Davis *et al.*, 2020; Potapov *et al.*, 2017; Achard *et al.*, 2014), with future projections of major agricultural expansion and intensification at the expense of the tropical rainforests in SSA and South America (Laurance *et al.*, 2014). It was reported that the scale of deforestation in Latin America and Southeast Asia was easier to detect by satellites than in SSA due to the diverse nature of the ecosystems in SSA and the unreliable national reporting (Malhi *et al.*, 2013). However, the annual deforestation rates in SSA were found to be lower than their counterparts in Latin America and Southeast Asia (Rudel, 2013; Defries *et al.*, 2010).

The DRC has the second-largest carbon stock after Brazil (Baccini *et al.*, 2012), nevertheless, it was the largest country to exhibit a decline in tropical rainforest area across SSA between 1992 and 2018 (Tyukavina *et al.*, 2018; Zhuravleva *et al.*, 2013; Potapov *et al.*, 2012). However, it has been reported that DRC has one of the lowest global annual deforestation rates (Malhi *et al.*, 2013). Smallholder forest clearing in the DRC between 2000 and 2014, accounted for two-thirds of the total forest loss in the Congo basin (Tyukavina *et al.*, 2018). Several anthropogenic drivers of the tropical rainforest deforestation in the DRC (and across SSA) were reported (Curtis *et al.*, 2018; Tyukavina *et al.*, 2018), including smallholder forest clearing for charcoal and fuelwood production, which is considered the main driver in the DRC; civil wars and mining of "conflict minerals" (e.g., tantalum "coltan"; Bleischwitz *et al.*, 2012); industrial logging (Kranz *et al.*, 2018).

Industrial logging, however, was found to be limited in comparison with other Congo basin countries due to the country's political unrest (Zhuravleva *et al.*, 2013); road expansion (Kleinschroth *et al.*, 2019), and wildfires (Tyukavina *et al.*, 2018). It was also recognised that cropland expansion by shifting cultivation "slash and burn" is a common cultivating approach in west and central Africa, hence, contributing to the removal of large areas of intact tropical forests (Ickowitz, 2006; Curtis *et al.*, 2018). Different patterns, however, were found in other Congo basin countries including Gabon, Congo and Cameroon where industrial selective logging was found evident as a primary driver of deforestation (Tyukavina *et al.*, 2018). Recent concerns regarding the expansion of commercial agriculture for lucrative markets were raised, with cocoa being the fastest growing cash crop across SSA (Ordway *et al.*, 2017a).

In the Congo basin, Cameroon is the 5th and 7th largest global producer of cocoa and palm oil, respectively. Hence, large areas of intact tropical forest were removed due to the expansion of cocoa (Carodenuto, 2019) and palm oil (Ordway *et al.*, 2017b, 2019). Whilst in West Africa, Ivory Coast is the 1st and the 3rd largest global producer of cocoa and cashew, respectively. Ghana is the 2nd and 8th largest global producer of cocoa and palm oil, respectively. Thus, evidence of substantial areas of deforested tropical rainforests was reported in Ivory Coast (Carodenuto, 2019; Barima *et al.*, 2016) and Ghana (Acheampong *et al.*, 2019; Asibey *et al.*, 2020).

Timber and rubber are two of the major commodity crops in Liberia, with large expansions being reported (Christie *et al.*, 2007). Hence, Liberia was reported as one of the top 10 countries with the largest percentage of forest loss with 14% between 1992 and 2018

(Radwan *et al.*, 2021). One-tenth of Liberia's tropical rainforest was found to be lost between 2000 and 2018 (Davis *et al.*, 2020). Large areas of forest were lost in Madagascar due to degradation, disturbances, and upland rice expansion (Zaehringer *et al.*, 2015; Eckert *et al.*, 2011). Furthermore, large areas of cashew have expanded at the expense of tropical forests in Benin and Guinea Bissau since they are the 5th and 7th largest global producers, respectively (Monteiro *et al.*, 2017).

We report that agricultural expansion, either for subsistence and local uses or for export to global markets as cash crops (Ordway *et al.*, 2017a), is the main driver behind most of the LC changes that have occurred across SSA during the study period (Bodart *et al.*, 2013; Jew *et al.*, 2017). Furthermore, agricultural expansion is reported widely as the main contributor to the loss of the tropical dry and humid rainforests at the global scale (Gibbs *et al.*, 2010; Curtis *et al.*, 2018) with subsequent implications for the sustainability of ecosystem services, biodiversity and carbon stocks (Kehoe *et al.*, 2017; Searchinger *et al.*, 2015). It is well recognised that there was a substantial agricultural expansion in SSA starting from the mid-1970s until the late 1990s, particularly in West Africa (Brink and Eva, 2009). Hu *et al.* (2020) reported that Africa has experienced the largest magnitude in cropland increase, globally. To meet the growing demand for food due to rapid and consistent population growth in SSA, cropland expansion mainly at the expense of other natural vegetation LC types (e.g., shrubland, dry and tropical forests) has been an imperative (Brink and Eva, 2009; Fenta *et al.*, 2020), with subsequent implications for the sustainability of ecosystem services and biodiversity (Perrings and Halkos, 2015).

As discussed in the introductory section, the increase in cropland production could be achieved through cropland intensification (van Loon *et al.*, 2019) or via land extensification (Kehoe *et al.*, 2017). While intensifying agriculture (Rudel *et al.*, 2009; Tilman *et al.*, 2011) to produce larger crop yields may seem like a more sustainable approach, it is not realistic to apply in SSA at an extensive scale as most countries simply do not have the capacity to utilise large-scale mechanised-agriculture and modern agricultural techniques due to economic and societal pressures (Chamberlin *et al.*, 2014). Nevertheless, it was recently found that cropland intensification in SSA represents a threat to biodiversity (Zabel *et al.*, 2019). Because of this human intervention, during the last few decades, agricultural land has significantly expanded on former areas of both humid and dry forests (Gibbs *et al.*, 2010; Bodart *et al.*, 2013).

While most agricultural expansion was associated with crop production for domestic markets to meet the local demand for food, there are, however, increasing concerns about the expansion of export-oriented commodity crops aimed for distant markets (Ordway *et al.*, 2017a). Our findings are in accordance with other studies that have been undertaken recently in SSA. We report extensive gains in rainfed cropland in Nigeria, Sudan (Souverijns *et al.*, 2020) and Mali (Phalan *et al.*, 2013) at the expense of shrubland (shrub-dominated savanna), in Tanzania and Mozambique at the expense of dry forests (Bodart *et al.*, 2013) and in the DRC at the expense of tropical rainforest (Mayaux *et al.*, 2013; Rudel, 2013). From the ecoregional scale analysis, we report that the largest gains in rainfed cropland were found in the West Sudanian savanna and dry Miombo woodlands ecoregions which correlate to large parts of Nigeria and Mali, and Tanzania and Mozambique, respectively (Brink and Eva, 2009; Bodart *et al.*, 2013).

4.5. Conclusions

This chapter provides a comprehensive assessment for the major LC changes that have occurred in SSA over the last 30 years, analysed, quantified and interpreted at the continental SSA, national and ecoregional scales. The findings contribute to our understanding of the large changes that have taken place, driven by anthropogenic and climatic drivers, posing threats for environmental sustainability. Using a temporally consistent global LC dataset (ESA-CCI-LC) along with an ecoregions-based dataset (Ecoregions2017) has enabled us to produce a comprehensive assessment of all LC changes (e.g., trajectories, transitions and locations) across a variety of spatial scales within SSA between 1992 and 2018. The majority of the recent studies undertaken in SSA have focused on one major LC change solely (e.g., tropical rainforest loss (Mayaux *et al.*, 2013), dry forest loss (Bodart *et al.*, 2013) and agriculture expansion with the associated impacts on biodiversity (Searchinger *et al.*, 2015)). Hence, a comprehensive quantification, characterisation and understanding of the spatial and temporal distributions, causes and drivers of LC changes across SSA are crucially needed. Therefore, this chapter analysed the full SSA landscape at multiple spatial scales within the context of LC change, highlighting and discussing the extent and drivers of these large LC changes. We explained the major LC transitions that occurred in SSA between 1992 and 2018 by associating them into five key LC change processes. This has enabled us to interpret the major LC changes in a straightforward manner. The key LC change processes were *gains of dry forests*, *greening of deserts*, *loss of tree-dominated savanna*, *loss of shrub-dominated savanna* and *loss of tropical rainforests*, in descending order of importance, based on impacted areas. The main

anthropogenic driver found behind most LC changes in SSA was agricultural expansion, and this was at the expense of the surrounding environment. Climatic factors, including increased rainfall and atmospheric CO_2 levels, have contributed largely to the changes that occurred within the extent of natural vegetation adjacent to desert areas. The highlights reported here may contribute to implementing more sustainable LC management policies and hence, provide crucial information to support progress towards the UN's SDGs.

Chapter 5. Global land cover trajectories and transitions

Taher M. Radwan, G. Alan Blackburn, J. Duncan Whyatt and Peter M. Atkinson.

This chapter has been published as an open access research article in *Scientific Reports*.

Radwan, T.M. *et al.* (2021) Global land cover trajectories and transitions. Scientific Reports. 11, 12814.

Abstract

Global land cover (LC) changes threaten sustainability and yet we lack a comprehensive understanding of the gains and losses of LC types, including the magnitudes, locations and timings of transitions. We used a novel, 300 m spatial resolution and temporally consistent satellite-derived dataset covering the entire Earth annually from 1992 to 2018 to quantify LC changes across a range of scales. At global and continental scales, the observed trajectories of change for most LC types were fairly smooth and consistent in direction through time. We show these observed trajectories in the context of error margins produced by extrapolating previously published accuracy metrics associated with the LC dataset. For many LC classes the observed changes were found to be within the error margins. However, an important exception was the increase in urban land, which was consistently larger than the error margins, and for which the LC transition was unidirectional. An advantage of analysing the global, fine spatial resolution LC time-series dataset is the ability to identify where and when LC changes have taken place on the Earth. We present LC change maps and trajectories that identify locations with high dynamism, and which pose significant sustainability challenges. We focused on forest loss and urban growth at the national scale, identifying the top 10 countries with the largest percentages of forest loss and urban growth globally. Crucially, we found that most of these 'worst-case' countries have stabilized their forest losses, although urban expansion was monotonic in all cases. These findings provide crucial information to support progress towards the UN's SDGs.

5.1. Introduction

In recent decades, the world has been impacted significantly by human-induced environmental changes from local to global scales (Rindfuss *et al.*, 2004). In particular, anthropogenic land cover (LC) changes threaten the sustainability of ecosystem services (Verburg *et al.*, 2011). Major LC changes include urbanisation (Liu *et al.*, 2020b), agricultural land loss (Radwan *et al.*, 2019), agricultural land expansion (Radwan, 2019), deforestation (Nzunda and Midtgaard, 2019), afforestation (Sloan *et al.*, 2019) and desertification (Huang *et al.*, 2020a). Such LC changes can have detrimental impacts on both environmental conditions (Tai *et al.*, 2014) (e.g. by inducing pollution and climate change) and human activities (Feddema *et al.*, 2005) (e.g. by compromising food security and economic development). Therefore, with such a variety of forms of LC change and consequent impacts, there is a pressing need for rigorous and systematic monitoring and analysis of LC dynamics to inform research on the processes involved, and provide evidence to stakeholders and decision-makers across the globe to promote responsible actions (Foley *et al.*, 2005).

Land change science (LCS) plays a pivotal role in monitoring global environmental change and the sustainability of our planet's resources (Ban *et al.*, 2015). The main goal of LCS is to understand both the magnitude and spatial extent of changes in LC over time (Turner *et al.*, 2007). Furthermore, LCS endeavours to identify the drivers of LC change, investigate the possible impacts and potential consequences of LC dynamics, propose better land use planning policies, and inform relevant decision-makers (Rindfuss *et al.*, 2004; Turner *et al.*, 2007). Consequently, this can help address many emerging environmental and societal challenges (Foley *et al.*, 2005; Turner *et al.*, 2007). Within the context of LCS, maps of LC are valuable tools for presenting geospatial information for a wide range of environmental applications (Li *et al.*, 2016; Fuchs *et al.*, 2018). Satellite remote sensing is increasingly capable of generating LC maps at various spatial and temporal resolutions, appropriate for a variety of research objectives to support EO (Grekousis *et al.*, 2015; Pérez-Hoyos *et al.*, 2017).

Over the past two decades, several remote-sensing based LC mapping projects have been established, operating at a variety of scales (Pérez-Hoyos *et al.*, 2017). These projects have generated LC datasets for different time periods and spatial resolutions, with varying classification schemes (Grekousis *et al.*, 2015). Medium-to-fine spatial resolution remotely sensed data are often used at national or regional scales, to develop products such as CORINE Land Cover in Europe (Feranec *et al.*, 2010) and the National Land Cover Database (NLCD)

in the United States of America (Wickham *et al.*, 2017). Coarser spatial resolution remotely sensed data are typically used to generate global LC products (Grekousis *et al.*, 2015) including the International Geosphere-Biosphere Program Data and Information System's LC dataset (IGBP-DISCover) (Loveland *et al.*, 2000), University of Maryland (UMd) Land Cover (Hansen *et al.*, 2000), Global Land Cover (GLC) 2000 (Bartholomé and Belward, 2005), GlobCover 2009 (Arino *et al.*, 2012) and the Moderate Resolution Imaging Spectroradiometer (MODIS) collection 5 land cover type (MCD12Q1) dataset developed by NASA, with a spatial resolution of 500 m and global coverage annually from 2001 onwards (Friedl *et al.*, 2010). The Finer Resolution Observation and Monitoring Global (FROM-GLC) (Gong *et al.*, 2013) and GlobeLand30 (Chen *et al.*, 2015) LC datasets cover the globe based on relatively finer spatial resolution Landsat images. However, the latter is only available for the years 2000 and 2010.

Recently, the European Space Agency's Climate Change Initiative-Land Cover (ESA-CCI-LC) dataset was released (Plummer *et al.*, 2017), which has a spatial resolution of 300 m and global coverage annually from 1992 to 2018. The value of this dataset has been demonstrated in several studies of specific types of environmental change at different scales (Liu *et al.*, 2018b; Xu *et al.*, 2019; Duan and Tan, 2019; Nowosad *et al.*, 2019; Mousivand and Arsanjani, 2019; van Vliet, 2019; Ji *et al.*, 2020; Estoque *et al.*, 2019). However, the full capacity of this dataset to provide a comprehensive assessment of LC change trajectories and transitions at global and continental scales, has yet to be explored. In this study, we characterised and interpreted historical LC changes that have occurred across the entire globe and analysed the variability of LC dynamics between, and within, the Earth's continents over the 27-year timeframe of the ESA-CCI-LC dataset. For each LC type, we quantified the total area that has been gained and lost over the study period and mapped the distribution of these changes. We analysed the trajectories of LC change throughout the study period and quantified the magnitude of the transitions between different combinations of LC types. These LC changes were considered in the context of error margins produced by extrapolating previously published accuracy metrics associated with the LC dataset.

5.2. Methods

5.2.1. The ESA-CCI-LC dataset

Detailed description of the LC product used in this chapter (ESA-CCI-LC) is provided in section 2.4. Being a raster-based product the Minimum Mappable Unit (MMU) of the ESA-

CCI-LC data is effectively equal to the spatial resolution of the data, at 300 × 300 m. It has been argued that in raster-based remotely sensed imagery the smallest observable feature that can be identified reliably is four contiguous pixels in size (i.e. 600 × 600 m). Nevertheless, because the analysis in this paper was based on pixel-by-pixel differences (and not on objects), the MMU of 300 × 300 m is considered valid and the ESA-CCI-LC dataset is appropriate for the objectives of the study.

5.2.2. Reclassification of the ESA-CCI-LC dataset

To provide clarity in the analysis of LC changes, seven main LC types, namely: agriculture, forest, natural vegetation, urban, bare land, water bodies and ice/snow were generated by combining the relevant classes in the original ESA-CCI-LC data, via a reclassification (Table 5.A2). Global data of the seven LC types were generated through the reclassification process for each of the years from 1992 to 2018 and used in the subsequent analysis. For illustrative purposes, Fig. 5.1 shows the global distribution of the main LC types in 2018.

5.2.3. Quantifying LC changes

The seven class LC data were analysed using the procedures described below at three scales: by using the entire global dataset, by extracting data relating to each individual continent, and by using data for selected individual countries that experienced the largest changes of particular LC classes. To quantify the overall LC gains and losses, a map was extracted from the reclassified ESA-CCI-LC data for 1992 and 2018 for each of the five LC types. Then a difference map (between 1992 and 2018) was generated showing areas gained and lost for each LC type. The total areas of gross gains and losses were calculated by multiplying the total number of pixels representing a gain or a loss by the pixel area, for each LC type. Net changes were quantified by calculating the difference between gross gain and gross loss, for each LC type. Furthermore, to map the spatial distribution of the LC gains and losses, the generated difference maps were used. A spatial aggregation technique was used for visualising the data appropriately at the global scale, and this was based on a 10 × 10 pixel aggregation, thereby creating global maps of gains and losses for each LC type at a 3 km spatial resolution.

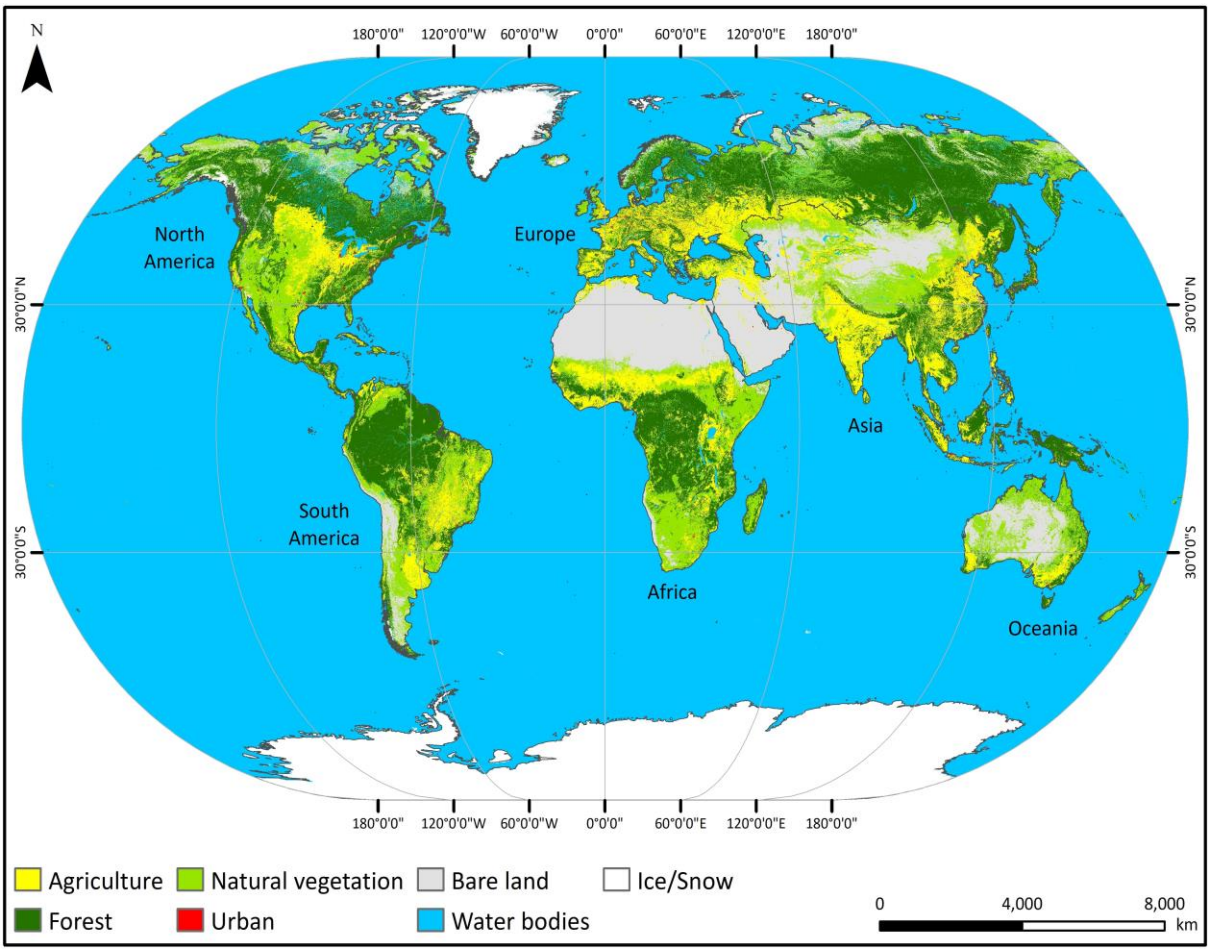

Figure 5.1. Global distribution of LC types in 2018. ArcGIS Desktop 10.5 (ESRI, 2016) was used to generate this figure.

To quantify the LC trajectories from 1992 to 2018, the total area of each LC type in each year was computed, and this was calculated by multiplying the total pixel count by the pixel area. Finally, the area of land involved in transitions between all combinations of LC types from 1992 to 2018 was quantified. This was achieved by generating difference maps for each LC type, showing the areas that had transitioned from that LC type in 1992 to each of the other four LC types in 2018. This has produced maps representing the areas involved in each of the possible transition types. Then the total area for each transition type was computed by multiplying the total pixel count for that transition type by the pixel area. To represent LC transitions in our schematic model, the area of land involved in each transition type was expressed in percentage terms relative to the total area of LC change between 1992 and 2018.

5.2.4. Accuracy assessment and area correction

An accuracy assessment of the ESA-CCI-LC product (ESA, 2017) used a sample of 1,499 locations across the globe to quantify the correspondence between the LC class allocated in

the ESA-CCI-LC product for that location and the LC class as determined from an independent validation dataset. We used the data generated from the accuracy assessment, based on the original 22 global ESA-CCI-LC classes, and combined the data for relevant groups of classes (as in Table 5.A2) to produce a confusion matrix for the seven aggregated classes that were used in this study. A confusion matrix is able to quantify the thematic errors of commission (where pixels are assigned to a particular LC class at locations where there is a different LC in the reference data) and omission (where pixels are not assigned to a particular LC class, but their locations have that LC in the reference data). Using an established method (Olofsson *et al.*, 2013), the errors quantified in the confusion matrix were used to correct the mapped areas (i.e., derived from pixel counts) of each class and express the uncertainty of the estimated area as a margin of error at the 95% confidence interval. The uncertainty in LC change was expressed as the summation in quadrature of the margins of error of the maps of both LC classes that were used to quantify the change. The confusion matrix for the seven classes expressed as the corrected area of each class as a proportion of total area is shown in Table 4.A2, along with accuracy metrics. As explained in the discussion section, this uncertainty analysis can be considered conservative.

5.3. Results

5.3.1. Gains and losses at the global scale

Total global gains and losses (gross and net) of the main LC types between 1992 and 2018 are shown in Figure 5.2. All LC types, apart from urban, showed sizeable gross gains and losses, indicating that many areas of the globe experienced an expansion of these LC types while many other areas experienced a contraction. Most changes were smaller than the error margins associated with the ESA-CCI-LC dataset suggesting that there remains some uncertainty in determining the direction (positive or negative) of the net changes of these LC types at the global scale. The exception was urban, which showed a gross increase larger than the error margin and, in the absence of any gross loss, a sizeable net increase of 1.02 ± 0.78 million km^2.

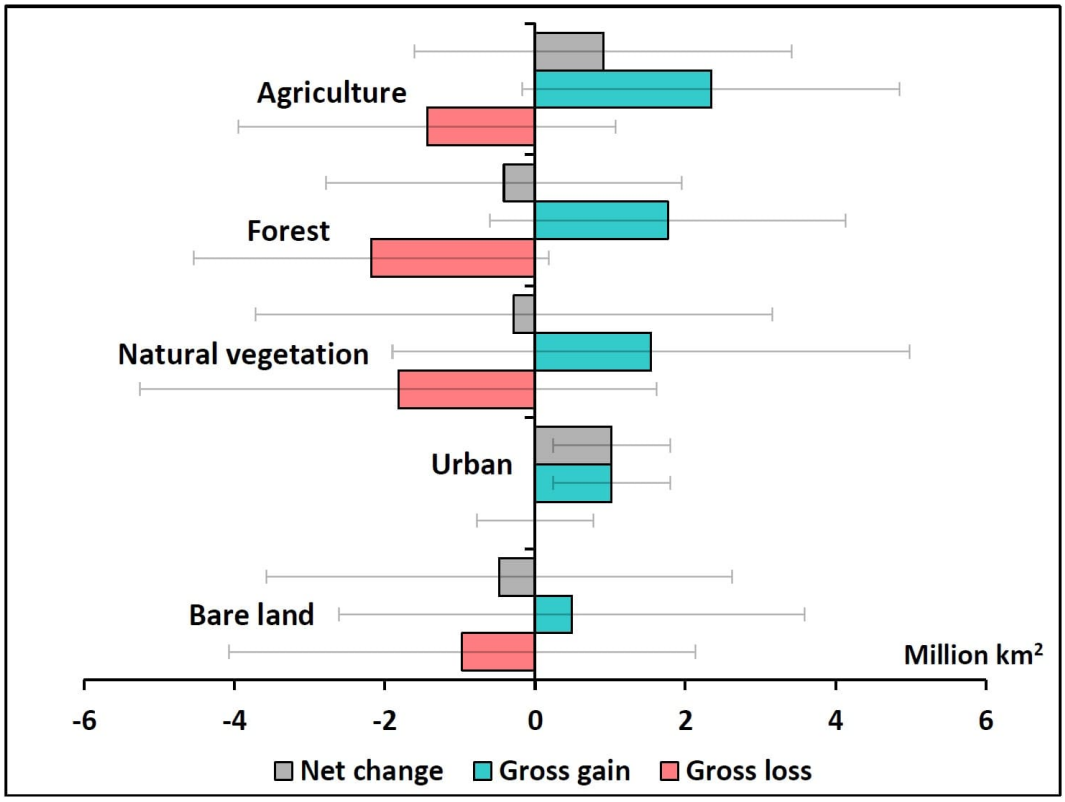

Figure 5.2. Total area of gains and losses of the different LC types across the globe between 1992 and 2018. Error bars represent the margin of error at the 95% confidence interval.

5.3.2. Gains and losses at the continental scale

All continents showed substantial gross gains and losses in most LC types, with the largest changes in Asia, Africa and South America (Fig. 5.3, with data provided in Table 1.A2 for clarity). For most LC types and continents, the changes were smaller than the empirical error margins associated with the ESA-CCI-LC dataset suggesting that it is not possible to determine the direction of the net changes. However, some changes were greater than the error margins. Notably, there was a net increase in urban in all continents, with Asia experiencing the largest net gain, contributing 45% of the global gain in urban area. Also, South America had a large net increase in agriculture and large net loss in forest. Maps of the spatial distribution of LC gains and losses (Fig. 5.4 and Fig. 1.A2) show the variability between and within continents as well as identifying countries with high LC dynamism.

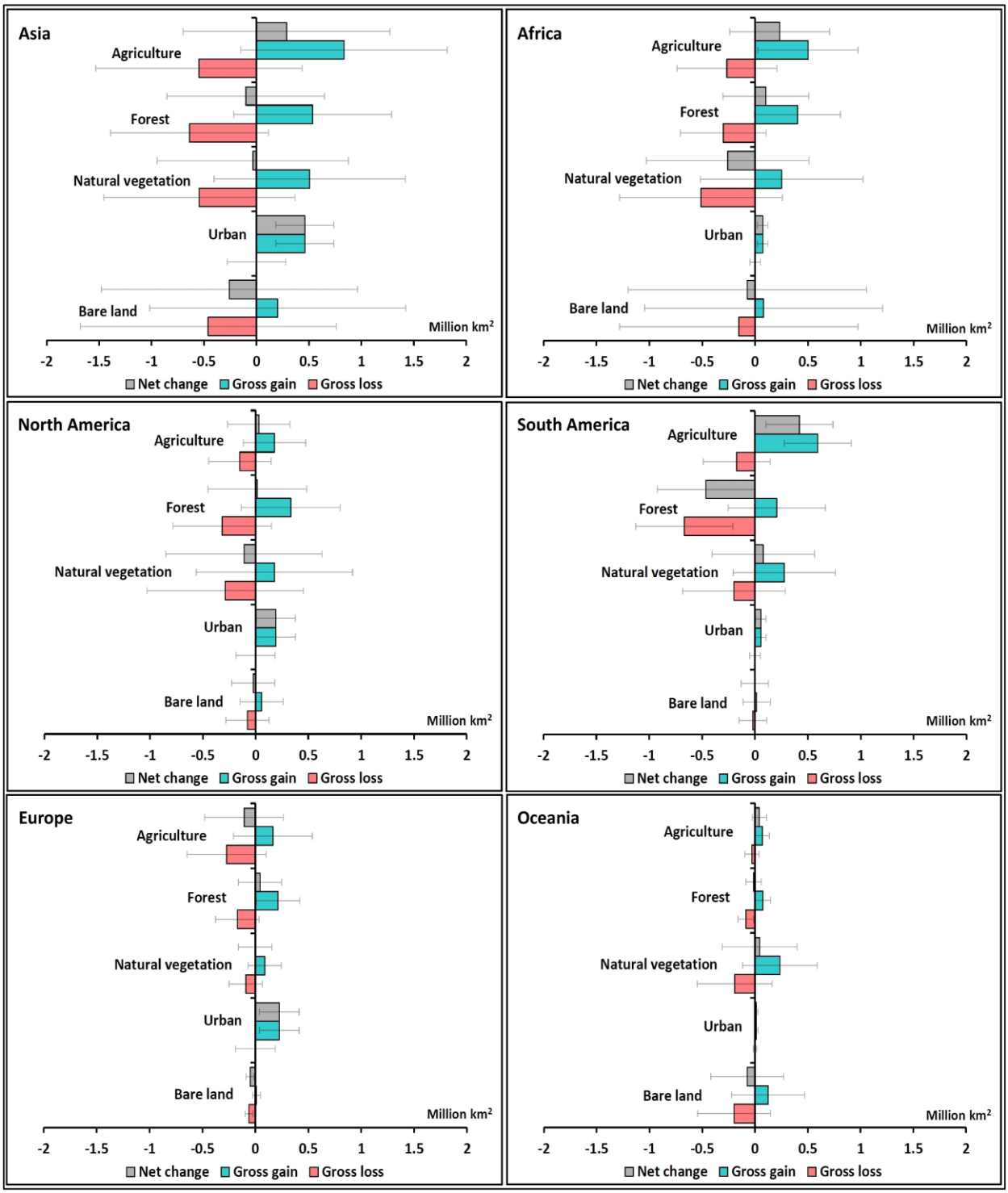

Figure 5.3. Total area of gains and losses of the different LC types in each continent between 1992 and 2018. Error bars represent the margin of error at the 95% confidence interval.

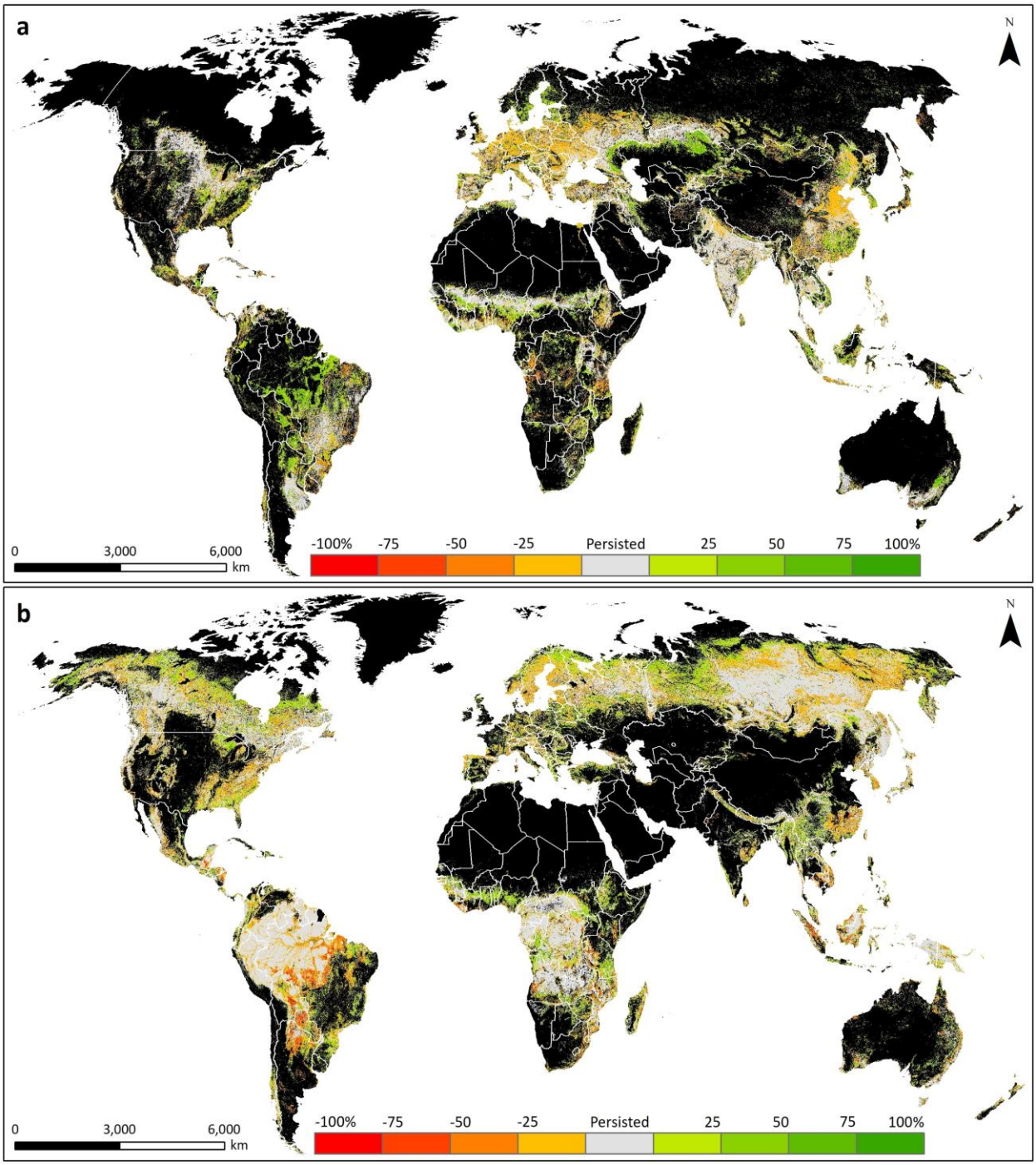

Figure 5.4. Spatial distribution of LC changes between 1992 and 2018. (a) agricultural land and (b) forest cover. The original data were aggregated to a 3 km spatial resolution for visualisation. Black areas are terrestrial zones where the LC type was absent in both 1992 and 2018. ArcGIS Desktop 10.5 (ESRI, 2016) was used to generate this map.

5.3.3. Trajectories of LC types at the global scale

The cumulative net changes in the total global area of each LC type between 1992 and 2018 are shown in Fig. 5.5. As suggested by the analysis of the overall net changes above, for most LC types, the variability in area was within the error margins associated with ESA-CCI-LC

product. However, the trajectories were reasonably smooth and consistent over the annual time-series. Hence, there is some evidence that, globally, forest and natural vegetation decreased more rapidly initially then stabilised, bare land was stable initially then decreased continuously, and agriculture increased more rapidly initially then stabilised. There exists clear evidence that urban increased continuously over time.

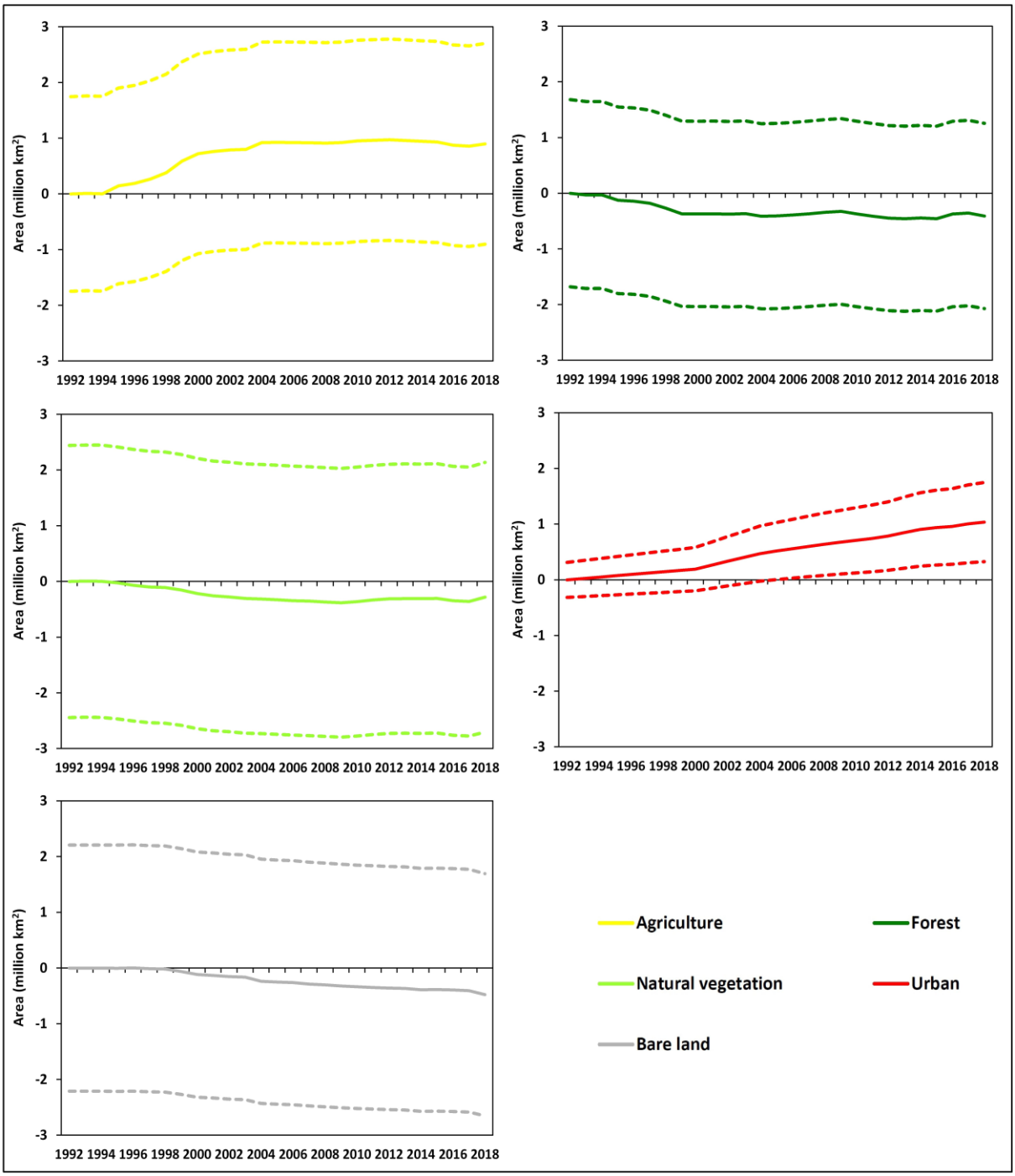

Figure 5.5. Time-series of the cumulative net change in total global area of each LC type between 1992 and 2018. The colours of the lines representing each LC type are consistent with Figs. 5.1 and 5.7. The dashed lines represent the upper and lower bounds of error at the 95% confidence interval.

5.3.4. Trajectories of LC types at the continental scale

The trajectories of LC changes within each continent from 1992 to 2018 are shown in Fig. 5.6, expressed as a percentage (net gain or loss) of the initial area of each LC type in each continent. As suggested by the analysis of the overall net changes above, for most LC types, the variability was within the error margins of the LC product. However, changes for some LC types and continents were larger than the error margin. For example, South America exhibited a large increase for agriculture and a large decrease for forest. The trajectories show that these changes were more rapid initially during the study period and stabilised after approximately 2004. There is some evidence that other continents showed similar trajectories to South America for agriculture, but there was more variability between continents in the forest trajectories.

There is evidence of differences in the continental trajectories of natural vegetation, with divergent patterns in South America and Africa, but these were well within the error margins. Urban showed a consistent and substantial increase in all continents over the study period. Growth rates were similar for all continents until around 2000, after which they differed considerably with the highest rates of urban expansion in Asia and lowest in Oceania. Interestingly, Europe showed a more rapid period of urban growth between 2000 and 2004, with much slower growth before and after this period. For bare land, the trajectories for most continents were within the error margins, but for Europe there was a consistent decrease, with some stability towards the end of the time-series, although the absolute net change was relatively small (− 0.049 ± 0.036 million km^2).

5.3.5. LC transitions at the global scale

The total area of land that transitioned between different LC types between 1992 and 2018 was 6.8 ± 5.8 million km^2, equal to 5% of the total ice-free global land area. Figure 5.7 summarises the transitions that occurred between the five main LC types, where the diameter of the circles represents the area of land that has undergone each transition, expressed in percentage terms relative to the total area of land globally that changed LC type over the study period.

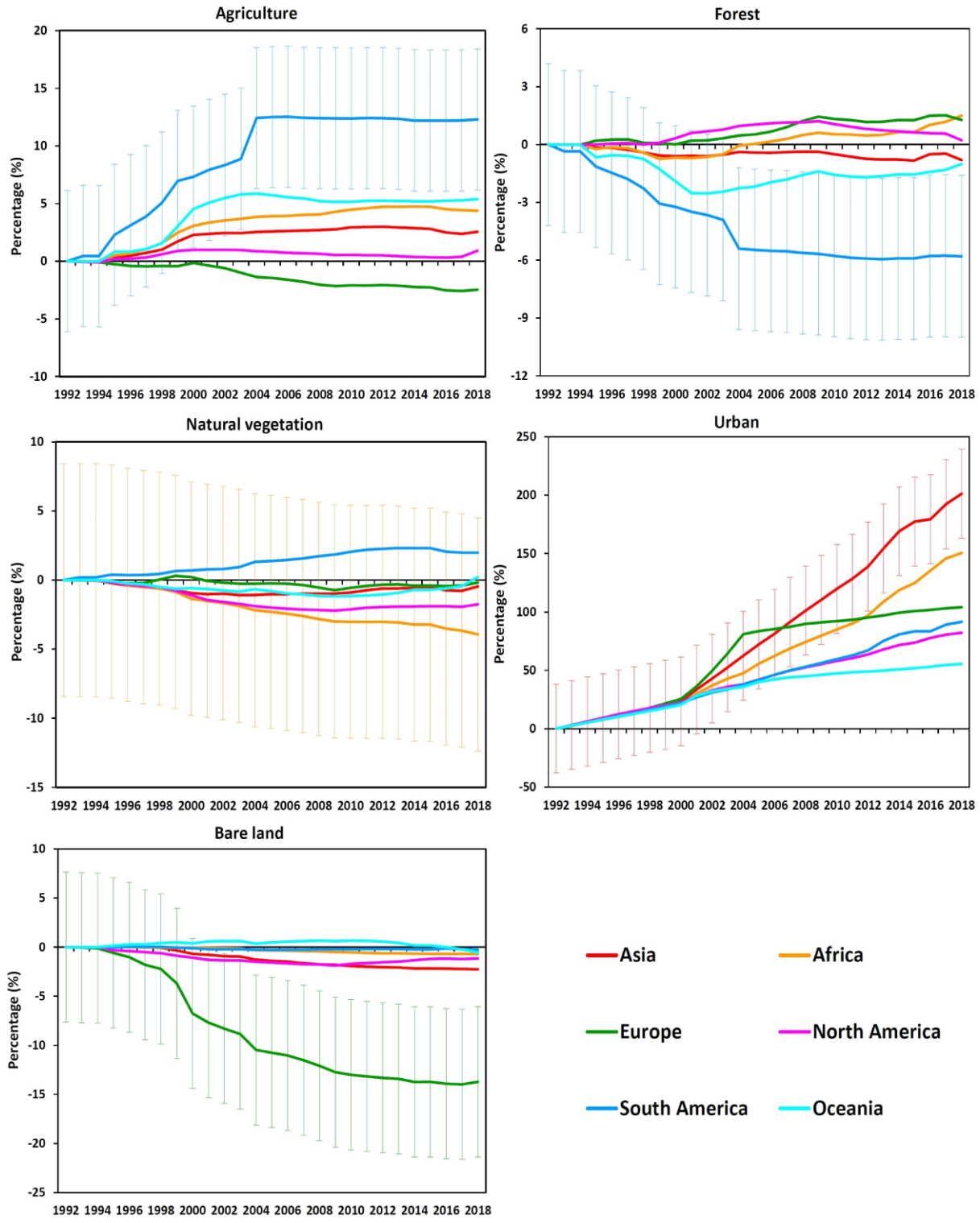

Figure 5.6. Time-series of the area of each LC type in each continent between 1992 and 2018, expressed as a percentage of the initial area of each LC type. To avoid over-complicating the figure, error bars are provided for the continent showing greatest change in each plot, as an example, representing the margin of error at the 95% confidence interval. Note that in these percentage change plots, for each LC type, the error margin is the same as the example shown, for all other continents.

The largest transitions were forest cover converting to agriculture followed by natural vegetation converting to forest cover, together contributing 32% of all global transitions. The next largest transitions were forest cover converting to natural vegetation and agriculture converting to forest cover, together contributing 25% of global transitions. This suggests that the major LC dynamics occurred between forest cover, natural vegetation and agricultural land, representing 57% of all global LC transitions between 1992 and 2018. Figure 5.7 also demonstrates that the transition to urban is unidirectional, as no areas of urban land changed to any other LC class. Hence, we can consider urban development as the endpoint of LC change, which may result from direct conversion from forest, natural vegetation or bare land, or indirectly from these LC types via agriculture. Indeed, the transition from agriculture contributed the greatest amount to urban growth globally (68%).

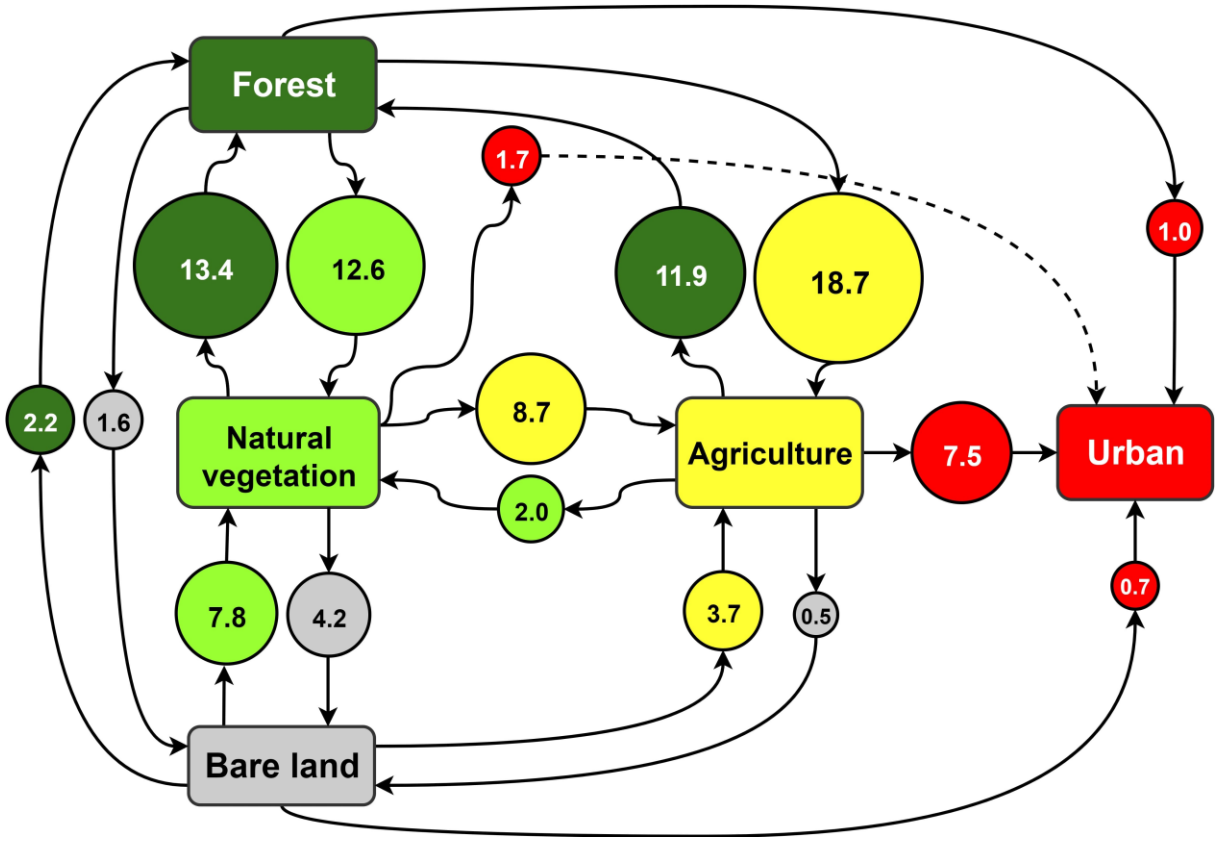

Figure 5.7. Schematic representation of global LC transitions between 1992 and 2018. The transitions are expressed in percentage terms relative to the total global LC area that changed over this period. Note that the sum of the percentages equals 98.2% as the minor LC transitions involving water bodies were not included. For visualisation purposes, the size of each circle is proportional to the magnitude of the LC transition it represents and exact figures are provided within the circle.

5.3.6. LC transitions at the continental scale

The magnitude of transitions between LC types within each continent between 1992 and 2018 are represented schematically in Fig. 2.A2. Asia is the largest continent globally, and so it is not surprising that the largest continental area of LC change was in Asia at 2.36 ± 1.98 million km^2, equal to 5.3% of the total land area of the continent. The largest transitions were forest cover converting to agriculture and natural vegetation converting to forest cover, accounting for 27% of LC transitions in Asia. The area of transition from bare land to agriculture was the largest among all continents, located mainly in Kazakhstan and Iran. In Asia, agriculture transitioning to urban was the second largest among all continents (after Europe), located mainly in China, Asian Russia and India.

The total area of LC change in South America was 1.1 ± 0.75 million km^2, equal to 6.2% of the total continental area. The largest transitions were forest converting to agriculture and forest converting to natural vegetation, collectively accounting for 62% of all continental transitions. The areas of transition from forest to agriculture and forest to natural vegetation were the largest among all continents and were located mainly in Brazil, Argentina, Paraguay and Bolivia. Interestingly, the transition from forest cover to agriculture in South America contributed 36% of the corresponding global transition.

The total area of LC change in Europe was 0.65 ± 0.49 million km^2, equal to 6.5% of the total continental area. The largest transitions were agriculture converting to forest and agriculture converting to urban, collectively accounting for 44% of all continental LC transitions. The areas of transition from agriculture to forest and from agriculture to urban were the largest among all continents, with the latter transition accounting for 79% of urban growth in Europe.

The total area of LC change in Oceania was 0.51 ± 0.50 million km^2, equal to 6% of the total continental area. The largest transitions included bare land converting to natural vegetation and natural vegetation converting to bare land, collectively accounting for 57% of all continental LC transitions. The areas of transition between natural vegetation and bare land were the largest among all continents, located mainly in Australia. Conversely, the transition from agriculture to urban was responsible for the smallest proportion of urban growth in Oceania (23%), the smallest among all continents.

There were two continents where the overall variability in LC was large but within the error margins associated with ESA-CCI-LC product, therefore we refrain from making definitive

statements about these continents. Nevertheless, our results indicate that Africa experienced LC changes covering 1.27 ± 1.50 million km^2, equal to 4.2% of the total continental land area. The largest transitions were natural vegetation converting to forest and natural vegetation converting to agriculture, collectively accounting for 35% of all LC transitions in Africa. It is noted that the area of transition from natural vegetation to agriculture was the largest among all continents. Furthermore, the total area of LC change in North America was 0.88 ± 0.96 million km^2, equal to 4% of the total continental area (excluding Greenland). The largest transitions were natural vegetation converting to forest and forest converting to natural vegetation, collectively accounting for 39% of all LC transitions. The area of transition between forest and bare land was the largest among all continents, focused mainly in Canada.

5.3.7. LC changes at the national scale

Here, we highlight two of the largest LC changes occurring across the globe (i.e., forest loss and urban expansion), by identifying the 10 countries with the largest percentages of these transitions. Figure 5.8a shows the historical trajectories in forest cover between 1992 and 2018 for the top 10 countries with the largest percentages of forest loss. It reveals dramatic deforestation in those countries, with losses in forest area ranging from 7% in Bolivia to 33% in Malawi over the study period (Table 2.A2). The amount of forest lost in the top 10 countries was 308,589 ± 103,316 km^2, accounting for more than 14% of the global total forest loss in 27 years, with Argentina experiencing the largest areal loss of 95,475 ± 24,202 km^2. The main LC type responsible for these substantial forest cover losses was found to be agricultural land. Consequently, agricultural land experienced substantial gains, ranging from 7% in Argentina to 64% in Bolivia (Fig. 5.8b). Forest converting to agriculture was responsible for 25% of forest loss in Argentina and up to 85% in Liberia (Table 2.A2). For visualisation purposes, Fig. 5.9 shows eight of the selected countries in more detail, highlighting the substantial areas of forest cover loss in those countries.

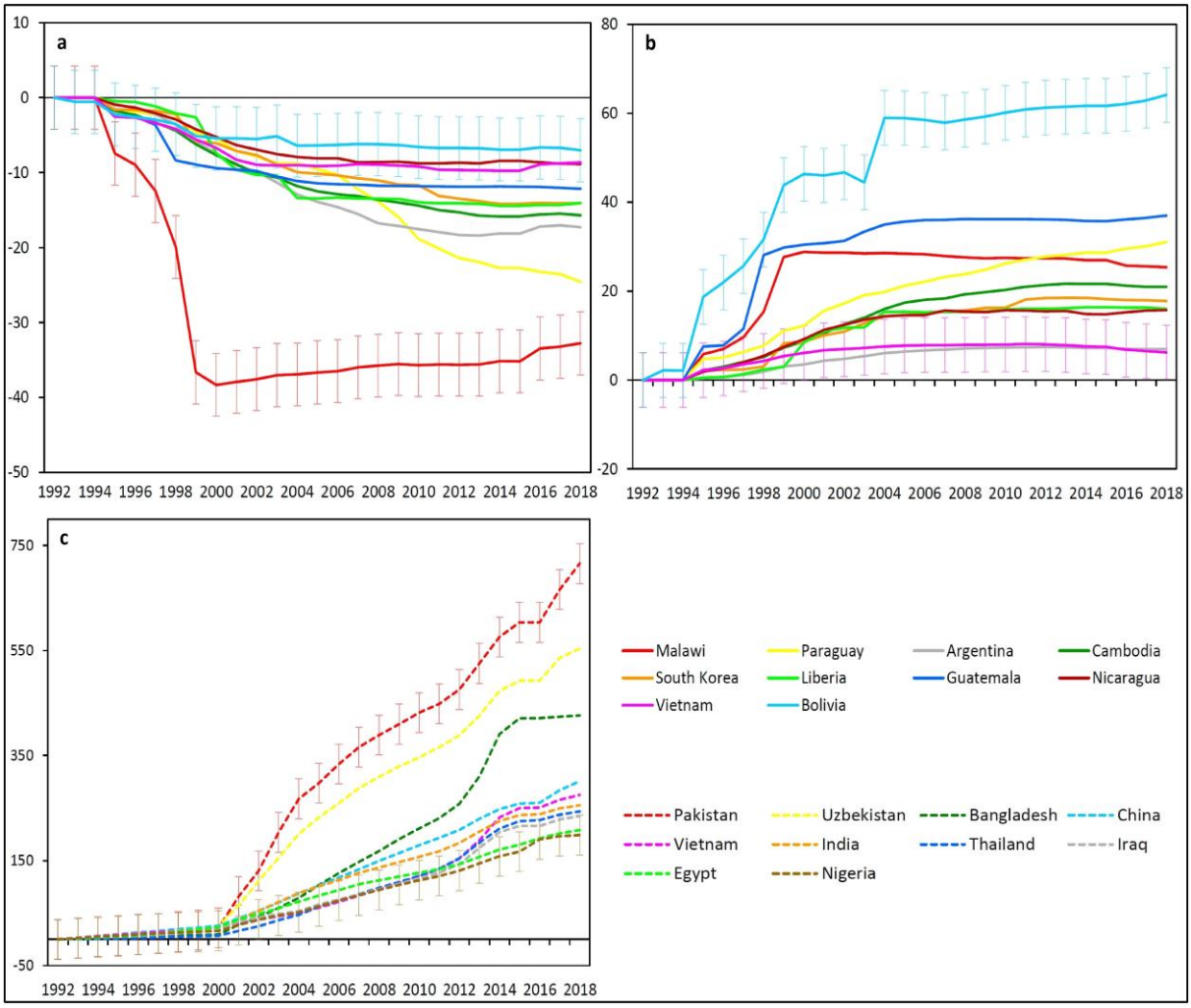

Figure 5.8. Historical trajectories between 1992 and 2018 for the top 10 global countries in (a) forest, (b) agriculture and (c) urban. Values are expressed as a percentage of the initial area of each LC type. To avoid over-complicating the figure, error bars are provided for the top and bottom lines in each plot, as examples, representing the margin of error at the 95% confidence interval. Note that in these percentage change plots, for each LC type, the error margin is the same for all countries.

Figure 5.8c shows the historical trajectories in urban land from 1992 to 2018 within the 10 countries with the largest percentages of urban expansion. It shows the widespread and rapid increases in urban area, with changes over the study period ranging from 199% in Nigeria to 716% in Pakistan (Table 3.A2). The amount of urban land gained in these 10 countries was about 250,968 ± 76,038 km^2, accounting for about 25% of the global urban expansion in 27 years, with China experiencing the largest urban area gained, at 175,802 ± 52,823 km^2. The main LC type lost because of this substantial urban expansion was agriculture. The transition from agriculture to urban accounted for an average of 82% of urban gain and 56% of agriculture loss for the 10 countries (Table 3.A2). This demonstrates the historical and ongoing threats of urban expansion on neighbouring productive

agricultural land. For visualisation purposes, Fig. 5.10 shows selected major urban cities within eight of the top 10 countries, highlighting the dramatic urbanisation in those countries.

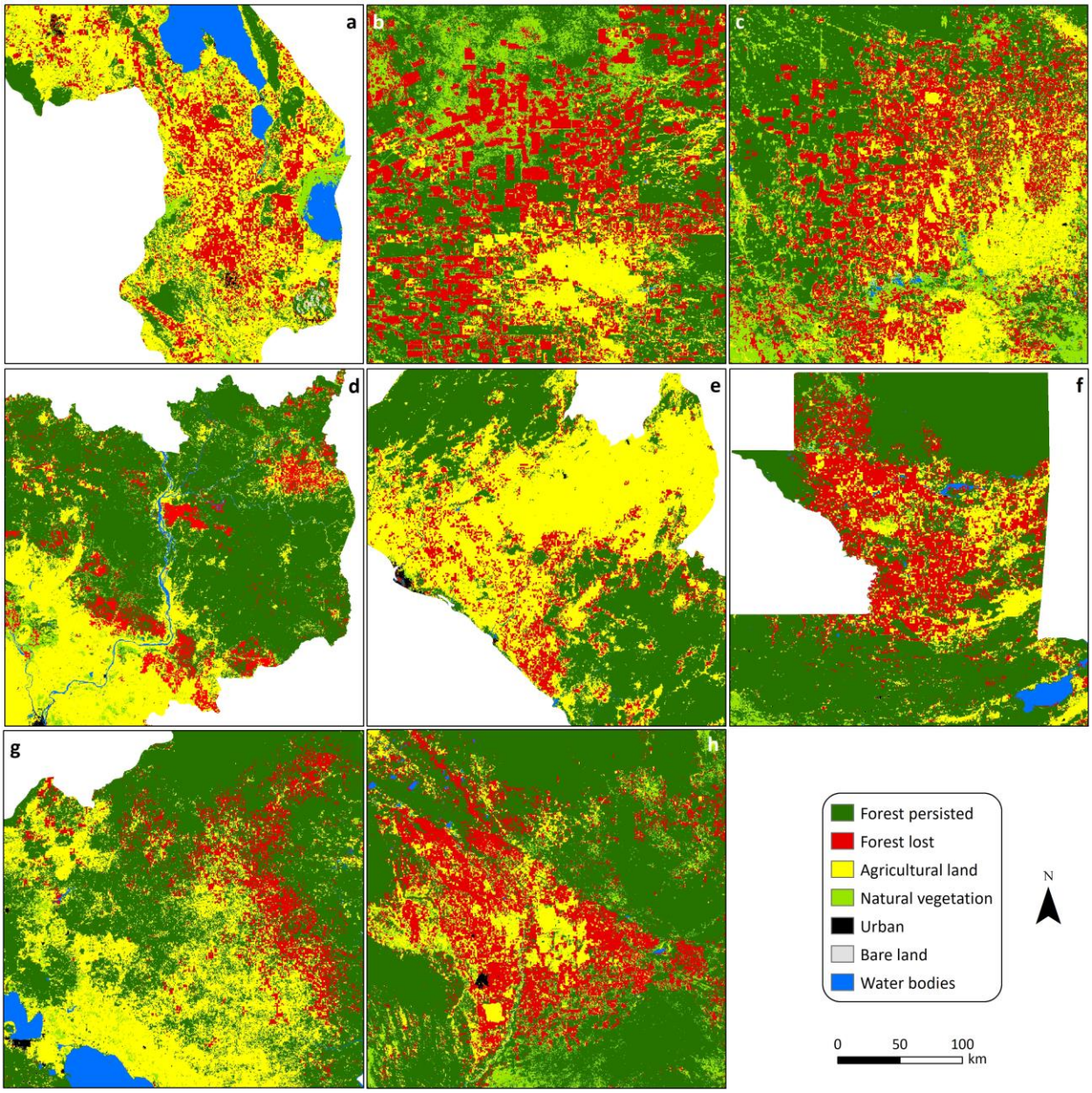

Figure 5.9. Spatial distribution of forest cover in selected countries with the highest percentages of forest loss between 1992 and 2018: (a) Southern Malawi; (b) North-western Paraguay; (c) Northern Argentina; (d) North-eastern Cambodia; (e) Central Liberia; (f) Northern Guatemala; (g) Central Nicaragua; (h) Central Bolivia. Note that a consistent map scale has been adopted across all countries. ArcGIS Desktop 10.5 (ESRI, 2016) was used to generate this figure.

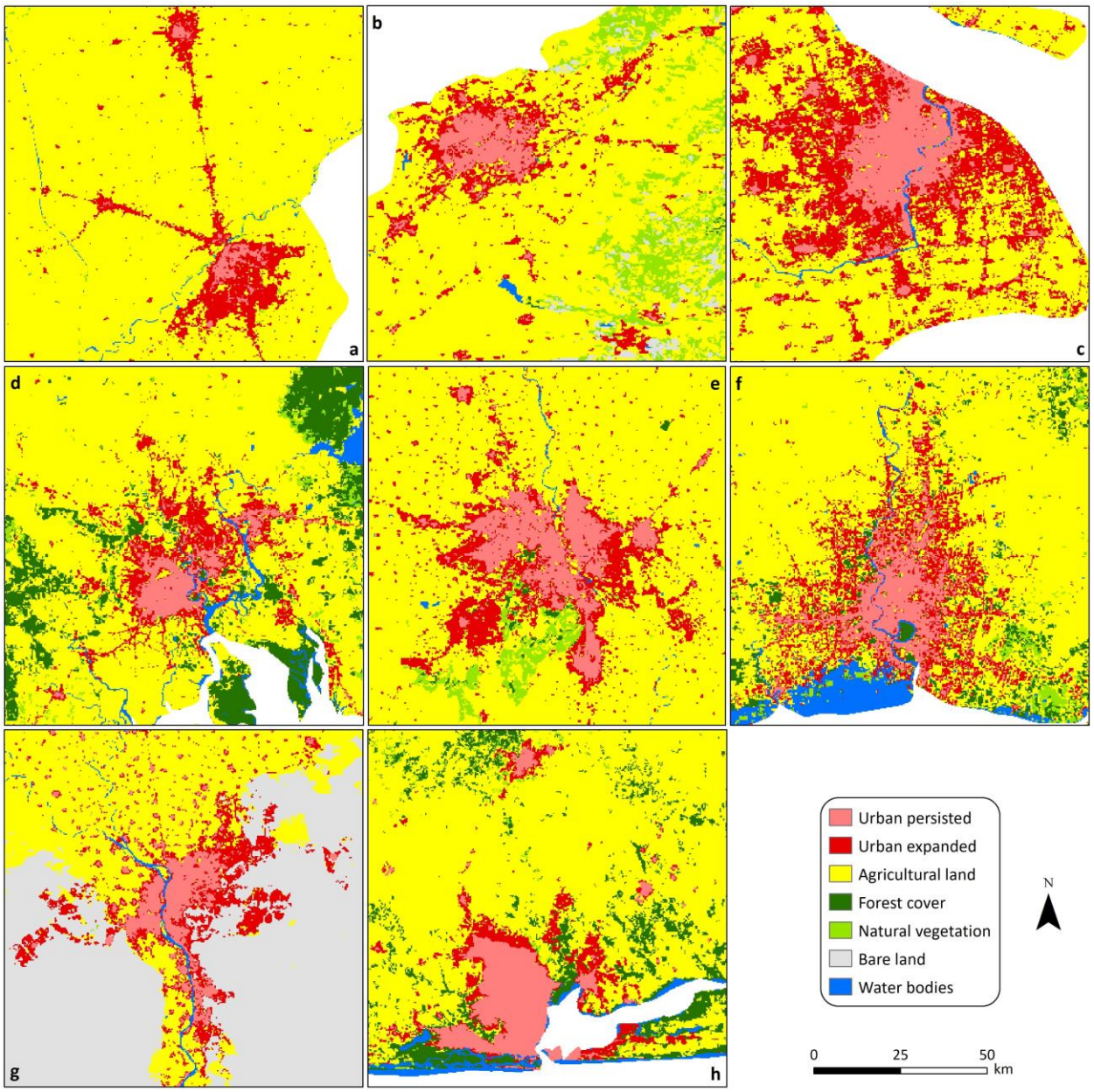

Figure 5.10. Spatial distribution of urban land in selected major urban cities within eight of the 10 countries with the largest percentages of urban expansion between 1992 and 2018: (a) Lahore, Pakistan; (b) Tashkent, Uzbekistan; (c) Shanghai, China; (d) Ho Chi Minh, Vietnam; (e) New Delhi, India; (f) Bangkok, Thailand; (g) Greater Cairo, Egypt; (h) Lagos, Nigeria. Note that a consistent map scale has been adopted across all countries. ArcGIS Desktop 10.5 (ESRI, 2016) was used to generate this figure.

5.4. Discussion and conclusions

The findings of this study provide new insights into the characteristics of LC dynamics across the globe at multiple spatial scales over an extended period of time. To the best of our knowledge, this study is the first to provide a comprehensive analysis of all LC changes across global, continental and national scales between 1992 and 2018 by quantifying LC gains and losses, trajectories and transitions using the ESA-CCI-LC annual time-series at 300 m spatial resolution, and considers the uncertainty in the LC dataset.

While several studies have been undertaken recently to quantify LC changes at the global scale using the ESA-CCI-LC dataset, these have considered global changes from different perspectives including investigating plant functional types (PFTs) (Nowosad *et al.*, 2019) and landscape ecology (Liu *et al.*, 2018b). Huang *et al.* (2020b) analysed the global urban expansion and its associated implications on the Net Primary Productivity (NPP) of cropland. van Vliet (2019) analysed the consequences of global urban expansion on the direct and indirect changes in LC, particularly the neighbouring cropland. Mousivand and Arsanjani (2019) quantified LC changes at the global scale using this dataset. However, they did not consider continental or national-scale LC changes or the magnitude of transitions between different combinations of LC types, and their findings were based on an analysis up to 2015.

Four other studies focused on quantifying related forest cover changes in Southeast Asia (Xu *et al.*, 2019; Estoque *et al.*, 2019), developing countries (Duan and Tan, 2019) and China (Ji *et al.*, 2020). Song *et al.* (2018) developed an annual LC product with global coverage, consisting of three land cover types, namely, tree canopy cover, short vegetation cover and bare ground cover using satellite sensor observations over the period 1982 to 2016. Very few studies have been carried out on a global scale using fine-resolution imagery. Jokar Arsanjani (2019) characterised global LC changes in 2000 and 2010 and reported large changes across all continents using GlobeLand30 LC dataset based on the archive of Landsat imagery.

The comprehensive results produced here using the ESA-CCI-LC dataset are comparable with the findings of other more specific studies that have used finer-resolution data for the analysis of trajectories in, and mapping of cropland (Ramankutty *et al.*, 2008), forest cover change (Hansen *et al.*, 2013) and urbanisation (Gong *et al.*, 2020). This study, thus, demonstrates that the release of the ESA-CCI-LC global dataset has enabled a step-change in understanding global LC changes that have occurred over a period of more than a quarter of

a century, without significant spatial resolution trade-off (Grekousis *et al.*, 2015). Our results also show that the ESA-CCI-LC data can provide valuable insights into LC trajectories, transitions and the locations of changes at continental and national scales, as well as at the global scale (van Vliet, 2019). This is enabled by the high temporal consistency of the ESA-CCI-LC product.

Like any remote sensing based dataset, there are some associated limitations (ESA, 2017) with the ESA-CCI-LC dataset. For example, different sources of input data were used to generate the product, notably the AVHRR sensor from 1992 to 1999 and SPOT-VGT and MERIS from 1999 and 2003 onwards, respectively. The coarser spatial resolution of the AVHRR data was effectively resampled to 300 m to generate the final LC product, but the original 1 km resolution of the data may impose limitations with the data from the earlier years of the LC time series. Likewise, the change in the sources of input data may account for some of the observed changes in LC, such as the notable differences in urban extent after the year 2000.

The confusion matrix (Table 5.A4), which quantifies the correspondence between the ESA-CCI-LC data and independently determined LC reference samples, indicates that the accuracy of the individual LC classes is generally high and typical of a remotely sensed product, although the urban class does have a low producer's accuracy. This meant that when the errors revealed in the confusion matrix were used as the basis to correct the estimated areas of the LC classes, the largest correction was applied to the urban class. While the correction method we used (Olofsson *et al.*, 2013) is well established and logical, it can place a strong emphasis on the specific reference and LC map data used in the accuracy assessment. Furthermore, the accuracy assessment used in this study was derived from the LC map of year 2015 and the confusion matrix derived for that year was used to correct the LC data for all other years. While the accuracy assessment was rigorous and used a large reference dataset, it may be preferable to collect reference data from several other years and derive accuracy assessments from those years of LC data.

Nevertheless, using the confusion matrix (Table 5.A4) as part of the correction method (Olofsson *et al.*, 2013), it was possible to estimate the margin of error at the 95% confidence interval for the LC changes observed. This demonstrated that at the global scale the observed changes for most classes (other than urban) were smaller than the margin of error. This is because at the global scale, despite the absolute areas of change being large (e.g. 0.90 million km^2 for agriculture) these only represented a small percentage of the total global extent of

each LC class (e.g. 3% change for agriculture) which is smaller than the margin of error (e.g. ± 7.4% for the forest to agriculture transition). As we consider smaller spatial extents then LC changes can make up a much larger percentage of the total area of each LC class. If, for example, we considered an area where all of the forest was converted to agriculture, the change would be 100% while the margin of error would remain at ± 7.4%. Hence, as we can see from Tables 5.A1, as we move from global to continental scales, for many LC classes the observed changes become comparable with the margin of error. Furthermore, as we move to the scale of individual countries, the LC changes considerably exceed the margin of error.

While several recent studies have reported the results of their analyses of global LC changes using remotely sensed LC products, few considered the errors associated with such products and the consequent impact on the confidence of the change results. Our findings demonstrate the importance of accounting for errors in the LC product (Stehman and Foody, 2019). For example, the observed global net change in forest was less than the margin of error of the LC product (which is similar to other LC products, as noted above). Therefore, there remains some uncertainty in determining the direction (positive or negative) of the global net change in forest. This may explain the apparently contradictory findings from the Global Forest Resources Assessment 2015 (FAO, 2015) which reported a global net loss in forest of 1.29 million km^2 from 1990 to 2015, and those of Song *et al.* (2018), who reported a global net gain in forest of 2.24 million km^2 from 1982 to 2016. To some extent, our findings (2.42 million km^2) are in line with those of Hansen *et al.* (2013), who reported a global gross forest loss of 2.3 million km^2 between 2000 and 2012.

The observed changes for most other LC types were within the margins of error at global and continental scales, as determined from an accuracy assessment of the LC product. However, such an accuracy assessment evaluates the correspondence between the LC product and reference data and uncertainty in either can lead to lower accuracy (Foody, 2010). A multitude of factors result in error associated with LC reference data collected via techniques such as field surveys or manual interpretation of fine-resolution imagery (McRoberts *et al.*, 2018), as in this study. Hence an accuracy assessment using such reference data can be considered as a measure of the correspondence between two different techniques, rather than a measure of the disparity between a LC product and the 'truth'. Moreover, such an accuracy assessment does not assess the internal consistency of the remote sensing dataset itself, which in many cases, due to the high geometric and measurement precision of the sensing device, is expected to be greater than that of the

reference data. In this sense, the accuracy assessment may be considered as a conservative measure of the value of the ESA-CCI-LC product (Foody, 2008), but does provide some context with which to interpret the LC changes observed.

Our analysis of the global LC dataset allowed identification of when and where changes have taken place, allowing us to focus on hotspots where changes can be observed irrespective of the measurement uncertainty. The maps produced from this analysis provide information on the global distribution of LC changes, and identify locations with high dynamism. These include countries with the highest levels of forest loss and urban growth, for which a more in-depth analysis was undertaken. Such findings provide valuable quantitative insights into the recognised contributions of agricultural expansion to forest cover loss (van Vliet, 2019), particularly via the extensification of cultivation practices in South America (Armenteras *et al.*, 2017) and Southeast Asia (Xu *et al.*, 2019).

In Asia, the amount of land that converted from bare to agriculture was the largest among all continents, particularly in Kazakhstan (Meyfroidt *et al.*, 2016). The area of agricultural land lost in Asia was the largest among all continents, larger than the size of Thailand, which took place mainly through conversion to urban areas in China (Cui *et al.*, 2019) and India (Tang and Di, 2019). Our findings show that over 31% of agricultural land lost in Asia converted to urban areas. Furthermore, Asia experienced the largest gain in urban area worldwide comprising 45% of the global gain, particularly in China (Wu *et al.*, 2015) and India (Sahana *et al.*, 2018), and our findings are in accordance with Dou and Kuang (2020). In addition to China and India, other nations including Pakistan (Bhatti *et al.*, 2015), Uzbekistan (Conrad *et al.*, 2015), Bangladesh (Hassan and Southworth, 2017), Vietnam (Vu *et al.*, 2018), and Thailand (Estoque and Murayama, 2015) have experienced high percentages of urban expansion not only in Asia but also at the global scale.

The amount of forest cover lost in Asia was the second largest of all continents. Large areas have experienced deforestation across Southeast Asia including Indonesia and Malaysia due to agricultural expansion via palm oil and rubber plantations (Zeng *et al.*, 2018; Estoque *et al.*, 2019) and China due to urban expansion (Ji *et al.*, 2020). However, the highest percentages of forest loss were found in Cambodia (Kong *et al.*, 2019) due to the expansion of cassava and rice plantations and Vietnam (Meyfroidt *et al.*, 2013) due to the expansion of commodity crops including coffee and tea. On the other hand, there was a noticeable trend of afforestation recently in China (Piao *et al.*, 2015). Our forest cover findings are in line with those of Duan and Tan (2019).

In Africa, several countries (e.g., Tanzania (Nzunda and Midtgaard, 2019) and Zambia (Phiri *et al.*, 2019)), witnessed a large agricultural expansion, mainly at the expense of forests and natural vegetation. We found that forest cover converting to agriculture was the second largest continental transition. Furthermore, considerable agricultural land was lost due to urban expansion, including in Nigeria (Nkeki, 2016) and Egypt (Radwan *et al.*, 2019), and we found that 51% of the gain in urban area in Africa was at the expense of agriculture (Güneralp *et al.*, 2017). The reduction of natural vegetation cover in Africa was the largest of all continents and the net natural vegetation cover lost in Africa contributed an astonishing 91% of the global net loss. Although the overall net change in forest cover was a net gain, there were considerable high deforestation rates in individual countries including Malawi (Ngwira and Watanabe, 2019) and Liberia (Enaruvbe *et al.*, 2019), mainly due to the expansion of commercial crops such as tobacco in the former and rubber in the latter. Recently, several concerns have been raised regarding the expansion of commodity crops for export to lucrative markets in Sub-Saharan Africa (Ordway *et al.*, 2017a).

In South America, agricultural land saw a significant net gain, equivalent to the size of Japan. Consequently, significant forest cover decline occurred, in which 60% of the gross decline transitioned to agriculture. The net forest cover decline was larger than the size of Paraguay. Our forest cover findings were in line with the FAO (FAO, 2015) and Duan and Tan (2019). This significant area of forest cover lost in South America is clear evidence of the ongoing and continual deforestation processes within one of the most vital places on Earth, the Amazon rainforest (Lu *et al.*, 2013). Soybean production is a major contributor to deforestation processes occurring in South America, with the largest amount of forest cover lost in Brazil (Santos *et al.*, 2020). Furthermore, High percentage rates of deforestation were found in Argentina, Paraguay, and Bolivia due to cattle ranching and pasture expansion as well as soybean plantations (Fehlenberg *et al.*, 2017).

In North America, the transitions between forest cover and bare land were the largest among all continents, and they were located mainly in Canada (Fitzsimmons, 2003). This can be attributed to boreal forest loss due to fires (Hicke *et al.*, 2003), insect infections and logging (Kukavskaya *et al.*, 2013). Furthermore, the areas of forest cover and natural vegetation transitioning to urban were the largest among all continents, and they were located mainly in the USA (Zhang *et al.*, 2012). Guatemala (Devine *et al.*, 2020) and Nicaragua (Tobar-López *et al.*, 2019) experienced high deforestation rates, not only in the Americas but also at the global scale. This could be attributed to the expansion of palm oil plantations in the former

nation and coffee in the latter. Another factor causing this issue in Central America was the illegal cattle ranching expansion in relation to illegal cocaine trafficking (Devine *et al.*, 2020).

In Europe, agricultural abandonment is a common issue, and it is a major contributor to the continental decline observed, particularly in Eastern Europe (Estel *et al.*, 2015). Europe has also witnessed significant agricultural land loss due to urban expansion (Salvati *et al.*, 2018), and we found that this particular LC transition was larger in Europe than all other continents. The amount of agricultural land lost to urban growth was equivalent to the size of the Czech Republic. However, recently, there was a trend in Eastern Europe to recultivate abandoned agricultural land (Smaliychuk *et al.*, 2016). Urban gain in Europe was the second largest of all continents, covering an area equivalent to the size of Portugal. Our observations of the increasing forest cover in Europe were in line with those of the FAO (FAO, 2015).

In Oceania, the transitions between natural vegetation and bare land were the largest among all continents by far, and this may be attributed to climatic variability, particularly in Australia (Long *et al.*, 2019). For example, alternation of extended periods of drought and intermittent rainfall are strong drivers of sporadic growth phases in vegetation in this region in arid and semi-arid zones.

Generally, it is noted that the total areas of LC change in developed regions, including Europe and North America, were much smaller than the corresponding area of changes in developing regions, including Asia and Africa. This can be attributed to the implementation of effective policies and sustainable management strategies in developed regions, and more unrestrained LC management in developing regions (United Nations, 2018).

The world now faces several environmental sustainability challenges, most of which are considered the consequences of recent LC change (Foley *et al.*, 2005), and our results both highlight and quantify the magnitude of these changes. Our results show that the global increase in urban areas between 1992 and 2018 was equivalent to the size of Egypt. Urban was the only LC type that experienced consistent annual gain. This is to be expected since urbanisation is generally considered to be the end-point of a one-way process and, hence, it is very unlikely that it will convert to any other LC type once established (D'Amour *et al.*, 2017). To some extent, our findings (0.43 million km^2) are in line with those of van Vliet (2019) who reported a net gain in urban area of 0.38 million km^2 from 1992 to 2015, and Gong *et al.* (2020) who reported an increase of 0.48 million km^2 from 1990 to 2018. Urban

areas are expected to continue expanding over the coming decades with consequent environmental impacts (Seto *et al.*, 2012).

The sustainable development goals (SDGs) of the United Nations (UN) were introduced in 2015 as a global incentive towards maintaining the sustainability of the Earth's resources and providing better and healthier lives for hundreds of millions of people (United Nations, 2019a). SDG 2 is aimed at ending hunger, achieving food security and promoting sustainable agriculture (United Nations, 2019a). However, it has been recognised that achieving food security for a rapidly growing global population may be hampered due to restrictions in the amount of available arable land (D'Amour *et al.*, 2017). The findings of the present study demonstrate the gravity of this situation and a key issue is the loss of arable land to urban expansion (van Vliet *et al.*, 2017). Our findings further emphasise this problem as the global increase in urban areas by 125% was largely at the expense of agricultural land, a total loss equivalent to the area of Ecuador.

It has been recognised that fulfilling the increasing global demand for food has come at the expense of natural resources, for example, via natural habitat and biodiversity loss (Seto *et al.*, 2012). Our findings confirm the magnitude of these effects, as the expansion of agricultural land has been the major contributor to the loss of natural vegetation and forest across all continents. This highlights the pressing need for alternative solutions to food security such as agricultural intensification (Ceddia *et al.*, 2014) and converting bare land to agricultural land (Radwan *et al.*, 2019), although the latter may itself come at substantial financial costs.

Policy to deliver environmentally sustainable routes to food security must be based on a solid evidence base, with information on global LC changes as a fundamental component, as provided here. Moreover, deep understanding of the human–environment interaction system and, in particular, the magnitude of recent LC changes and the factors driving these changes, is required to address the grand sustainability challenges facing humanity, not least the SDGs of the UNDP. The analysis produced here on the LC changes that have occurred over the last quarter of a century provides crucial information in support of these goals.

Chapter 6. Synthesis and conclusions

Changes in global land cover (LC) have significant consequences for global environmental change (Turner *et al.*, 2007; Foley *et al.*, 2005), impacting the sustainability of biogeochemical cycles, ecosystem services, biodiversity, and food security (Feddema *et al.*, 2005; Rindfuss *et al.*, 2004). Different forms of LC change have taken place globally in recent decades, in response to both anthropogenic and natural drivers (Gong *et al.*, 2020; D'Amour *et al.*, 2017; Chaplin-Kramer *et al.*, 2015; Hansen *et al.*, 2013). With the increasing capabilities of satellite remote sensing for EO and the associated improvements in global LC products, researchers are better placed than ever before to explore patterns, dynamics, and magnitudes of LC change at a variety of spatial scales (Ban *et al.*, 2015; Chen *et al.*, 2015). This in turn provides decision-makers and policy legislators with useful evidence to make informed decisions and frame more sustainable policies to promote sustainable natural resource management and preserve the environment (Turner *et al.*, 2007; Foley *et al.*, 2005).

6.1. Key findings and contributions

This thesis has successfully utilised the ESA-CCI-LC product to characterise, quantify and interpret LC changes and their drivers at a range of spatial scales. This recently-released, spatiotemporally consistent global LC product provides a valuable annual time-series that covers a period of 27 years (1992-2018) at a relatively high spatial resolution of 300 m. Analysis of this LC time-series has led to a consistent and comprehensive understanding of what, where, when and why LC changes have taken place across national, continental and global scales over this 27-year period.

In Chapter 3, historical LC changes from 1992 to 2015 were characterised and quantified in the Nile Delta, a densely populated and rapidly urbanising region of Egypt. This region is considered a global hotspot in terms of urban expansion occurring on fertile agricultural land, posing serious threats to national food security. Other researchers have also investigated LC changes within this region, however, most of them are outdated (Ghar *et al.*, 2004; Shalaby *et al.*, 2012), cover smaller parts of the Delta or show LC changes for a limited number of years (Bratley and Ghoneim, 2018; Shalaby and Moghanm, 2015). This chapter provided the most up-to-date analysis, accounting for LC changes across the whole Nile Delta region based on an annual time-series from 1992 to 2015. Furthermore, this is the first study to simulate future LC change in the region using a series of different scenarios conceived to minimise the loss of productive agricultural land to urban expansion, indicating that further

urban expansion is possible while minimising the losses in fertile agricultural land and preserving national food security (Radwan *et al.*, 2019).

Analysis revealed the rate and magnitude of urban expansion and the associated loss in fertile agricultural land across the Nile Delta as a whole and across four individual Governorates in detail. The results highlight that 74,600 hectares of fertile agricultural land in the *Old Lands* were lost to urban expansion between 1992 and 2015 whilst 206,100 hectares of desert land were converted to agricultural land in the *New Lands* in response to the rapid population growth and increasing demand for food. However, these *New Lands* are mainly used to cultivate high-value commercial fruits for lucrative markets, and hence do not contribute to the national self-sufficiency from staple crops (Radwan *et al.*, 2019).

A Cellular Automata-Markov integrated model was used to simulate future LC change in the region to 2030 based on a set of different scenarios designed to minimise the loss of fertile agricultural land to urban expansion. The Business as Usual scenario revealed that 87,000 hectares of fertile agricultural land would be lost between 2015 and 2030, posing crucial threats to national food security. Three additional scenarios were conceived to encourage future urban development away from the fertile agricultural land of the Nile Delta. The Desert Development Only scenario revealed that 41,000 hectares of fertile agricultural land could be preserved across the whole Nile Delta. However, implementing this scenario may be unrealistic. In contrast, under the Desert and Population Expansion hybrid scenario, 34,600 hectares of fertile agricultural land could be preserved without significant trade-offs (Radwan *et al.*, 2019).

In Chapter 4, the spatiotemporal dynamics of LC across continental sub-Saharan Africa (SSA) were characterised, quantified and interpreted between 1992 and 2018. The analysis was conducted at the SSA, national and ecoregional scales using the ESA-CCI-LC product in conjunction with an ecoregion dataset. SSA is a region of extensive societal, economic, climatic and ecological diversity which has witnessed major LC changes over recent decades as a result of both anthropogenic and climatic drivers (Brink and Eva, 2009). Pertinently, Africa has previously been recognised as one of the most challenging continents to map when producing global LC products, increasing the existing uncertainties associated with generating satellite-derived LC products (Hansen *et al.*, 2000; Gong *et al.*, 2013). Used in conjunction, the ESA-CCI-LC product and the ecoregions dataset provided valuable insights into changes in LC that have occurred across the most impacted countries and the most vulnerable ecoregions for biodiversity loss.

While the majority of the most recent studies undertaken in SSA have focused on one major LC change, for example, tropical rainforest loss (Mayaux *et al.*, 2013) and dry forest loss (Bodart *et al.*, 2013), this research analyses the full SSA landscape using 15 LC classes at a range of spatial scales, highlighting hotspot locations of LC change and interpreting their anthropogenic and climatic drivers. This research also explains the major LC transitions that occurred in SSA between 1992 and 2018 by associating them with five key LC change processes, allowing a more straightforward interpretation of the major LC changes. The largest key LC change process in area across SSA, was the "*gain of dry forests*". Several climatic and anthropogenic drivers have stimulated this LC change process across SSA including increasing rainfall and atmospheric CO_2 levels (Brandt *et al.*, 2017), the natural recovery of woodlands on abandoned cultivated land due to migrations as a consequence of civil wars and conflicts (Mayes *et al.*, 2015) and the promotion of afforestation policies (Fenta *et al.*, 2020).

The "*greening of deserts*" key LC change process followed, mainly located adjacent to desert areas (e.g., the Sahel belt). A mix of climatic and anthropogenic drivers have induced this LC change process including the increases in rainfall, atmospheric CO_2 concentrations (Brandt *et al.*, 2015), rural to urban migrations and changes in the management practices of cultivated land (Olsson *et al.*, 2005). The "*Loss of tree-dominated savanna*" followed, mainly extending across Eastern and South-eastern Africa (e.g., *Miombo* woodlands). Agricultural expansion (e.g., Tobacco) and the increasing demand for extraction of fuelwood were the primary drivers causing this key LC change process (Jew *et al.*, 2017). The "*Loss of shrub-dominated savanna*" followed. Agricultural expansion was the main driver behind this LC change process, with extensive increases in rainfed agriculture across West Africa. Unexpectedly, the "*loss of tropical rainforests*" was the smallest key LC change process in area across SSA, primarily distributed across the DRC, West Africa and Madagascar. The expansion of commodity crops (e.g., cocoa and palm oil), shifting cultivation "*slash and burn*", forest logging (e.g., smallholder and industrial) for fuelwood production, civil wars and mining of "*conflict minerals*" were the dominant drivers causing this tropical rainforest deforestation across SSA, ultimately driven by the rapid population growth (Rudel, 2013; Curtis *et al.*, 2018).

In Chapter 5, LC gains and losses, trajectories and transitions were evaluated at global, continental and national scales between 1992 and 2018. This is the first study to quantify the complete ESA-CCI-LC annual time series and provide a comprehensive assessment of LC changes across a range of spatial scales. It has revealed variability between continents and

identified locations of high LC dynamism, hence, recognising global hotspots for sustainability challenges. Importantly, the comprehensive global LC change analysis presented in this chapter included a full assessment of uncertainties in the global LC dataset. While several studies have utilised satellite-derived global LC products to analyse global LC change, few have considered quantifying the uncertainties associated with such global products. This would make it easier to compare and contrast the findings of other global LC studies, helping to identify the locations where the LC classes and transitions were least or most certain. The uncertainty assessment in this research demonstrates how crucial it is to account for such underlying errors in the LC product (Radwan *et al.*, 2021).

Between 1992 and 2018 at the global scale, agriculture experienced the largest gross gain and urban experienced the largest net gain. In contrast, bare land, forest cover and natural vegetation all experienced net decreases. The largest LC transition across all LC types was forest converting to agriculture. Urbanisation was the endpoint of LC change as transition to urban was unidirectional, with agriculture being the greatest contributor to global urban expansion. At the continental scale, Asia, Africa and South America experienced substantial changes in LC. Asia experienced the largest gross gains in agriculture, forest, natural vegetation, urban and the largest gross losses in agriculture, natural vegetation and bare land. South America experienced the largest net increase in agriculture and net decrease in forest, whilst the largest net decrease in natural vegetation was in Africa, across all continents. Unsurprisingly, urban experienced net increases across all continents. Forest cover converting to agriculture was the largest transition across all LC transitions in Asia and South America. Natural vegetation converting to forest cover was the largest transition across all LC transitions in Africa and North America. In Oceania, the transition from bare land to natural vegetation was the largest across all LC transitions due to climatic variability including droughts and increasing rainfall.

At the national scale, an area of agricultural land equal to the size of Thailand was lost in Asia, the largest across all continents, mainly located in China and India. Cambodia, South Korea and Vietnam were among the top 10 countries with the largest percentages of forest loss globally, whilst eight Asian countries were among the top 10 countries with the largest percentages of urban expansion. In Africa, Malawi and Liberia were among the top 10 nations with the largest percentages of forest loss globally, whilst Egypt and Nigeria were among the top 10 nations with the largest percentages of urban expansion. In Latin America, Paraguay, Argentina and Bolivia were among the top 10 countries with the largest percentages of forest loss globally. An area equal to half the size of Bolivia has been

deforested across South America. Guatemala and Nicaragua were among the top 10 countries with the largest percentages of forest loss globally. The expansion of soybean plantations and pastures for beef production was the main driver of deforestation in South America, whilst the expansion of commodity crop (e.g., palm oil and coffee) plantations was the main driver in Central America. In Europe, the transition from agriculture to urban was the largest across all continents. As a result, agricultural land lost to urban expansion equalled the size of the Czech Republic. In Oceania, Australia experienced the largest area of LC change.

6.2. Research limitations

Although the analytical chapters of this thesis have fulfilled its overarching aim, there are a number of issues that could not be avoided or dealt with within the PhD completion window. The ESA-CCI-LC global LC dataset that has been used throughout this thesis has, like any other satellite-derived remote sensing products, a few associated limitations (ESA, 2017). For example, different types of sensors were used to generate the LC product, including the AVHRR sensor from 1992 to 1999, and SPOT-VGT and Envisat MERIS from 1999 and 2003 onwards, respectively. The coarser spatial resolution (1 km) of the AVHRR data was resampled to 300 m in the final LC dataset, however, the original coarse resolution of these data may impact upon the quality of the LC classification for the early years of the time-series. This, in turn, may have impacted upon the results of the trajectory analysis, for example, when analysing urban expansion in selected countries before and after the year 2000. Although there were increases in urban land across all countries before the year 2000, the trajectories for urban expansion suggested that these increases were negligible, whilst other sources of evidence would suggest there were large increases.

In chapter 3, some of the scenarios that were developed to simulate future LC change to minimise the loss of fertile agricultural land in the Nile delta such as the Desert Development Only (DDO) scenario may be unachievable. The DDO scenario was conceived to prevent any future urban expansion into the fertile *Old Lands*, restricting it to desert areas only. While this, in theory, seems like the best solution to the current urban development problem in the Nile Delta, in practice, it may be extremely difficult to achieve across such a large region. Firstly, not all people will stop building houses on their own agricultural land, particularly if the number of family members continues to rise. Secondly, the government will not be able to immediately establish a number of new desert cities to accommodate the rapidly increasing population. This process will require time and significant financial resources to

establish infrastructure (e.g., roads, rails, electricity and water supply) in such new cities. Nevertheless, this is a possibility. New Cairo, for example, is a live example of a desert city being established from scratch. The city that started to expand in the early 2000s and currently occupies 300 km^2. This is planned to expand to 700 km^2 in the future to accommodate 5-6 million people, helping to reduce the increasing population pressures on the old city of Cairo.

The LC time-series used in chapter 3 extended from 1992 to 2015. However, this was not the case in chapters 4 and 5 where the time-series extended up to 2018 as the ESA-CCI-LC product was initially released to cover the period from 1992 to 2015. Therefore, the LC data from 1992 to 2015 was used to complete the analytical part of chapter 3 in early 2019. However, the LC data covering the period 2016 to 2018 was released solely in late 2019, allowing to use the extended LC time series up to 2018 in chapters 4 and 5 during 2020 and 2021. The author acknowledges that the LC data for the years 2019 and 2020 was recently released by the ESA-CCI in September 2021.

In Chapter 4 this research adopted a higher thematic resolution of 15 classes than in chapters 3 and 5 in order to quantify LC trajectories and transitions in more thematic detail. However, the additional classes added to the complexity of processing the data, with each LC class potentially able to transition into 1 of 14 other classes over the time period under investigation. For this reason, no attempt was made to quantify the uncertainties in LC change in SSA. Furthermore, this chapter did not discuss the ability of the ESA-CCI-LC product to assess natural habitat quality across the ecoregions of SSA, as this requires thorough knowledge and long-term monitoring of the ecological nature and locations of these natural habitats (Spanhove *et al.*, 2012).

One of the main challenges in mapping the dry forests in SSA is the variability in spectral response during the dry and wet seasons, which results in considerable associated uncertainties (Bodart *et al.*, 2013; Mayes *et al.*, 2015). Although the ESA-CCI-LC dataset provides an annual time-series which is useful in analysing the trajectories of LC change over time, this does not account for seasonal variation. This could be particularly problematic in a region like SSA with an extremely diverse environment since the spectral signatures of natural vegetation (e.g., grasslands, shrublands and woodlands) captured by satellite sensors may differ between the various seasons during the same year.

Chapter 5 presented provided a full assessment of uncertainties within the global LC product, hence, accounting for margins of error when reporting global LC changes. However,

the accuracy assessment was generated from LC data for a single year (2015) as this was the only data for accuracy assessment provided by the ESA-CCI team. Therefore, the uncertainty ranges derived from the confusion matrix for the year 2015 were applied across the entire time-series, hence will not be entirely accurate. While the adopted accuracy assessment method was rigorous (Olofsson *et al.*, 2013), it would have been better to utilise reference data from other years (preferably all years) and generate uncertainty estimates for each year, rather than apply uncertainty estimates for one year across all years (as was the case in this study). Furthermore, while the accuracy assessment approach used in this chapter (Olofsson *et al.*, 2013) is well established, it is dependent on the quantity and quality of reference data, which, in the case of the ESA-CCI-LC product was only a sample of 1,499 locations across the globe, making it difficult to truly and fully represent the uncertainties associated with the various LC types. Moreover, the accuracy assessment provided in this chapter did not account for the uncertainty of LC change (i.e. between two different LC types) as there were no available reference data corresponding to the two dates of LC data used in the analysis.

Finally, it is also important to recognise that the uncertainty estimates provided around the LC trajectories suggest, in most cases, that rates of change are negligible, since, with the exception of the urban land class, they fall within the upper and lower bounds of uncertainty. This is most noticeable at the global scale where the reported LC changes are smaller than the margins of error despite the large changes in absolute areas. For example, the global net gain in agriculture was 0.9 million km^2 which represents only a small percentage of the global coverage of agricultural land (3.2%). However, the margin of error for agriculture was ± 9.2% which is larger than the actual LC change. At smaller spatial scales, the reported LC changes across many LC types become comparable with the margins of error, and at the national scale, changes in LC are considerably larger than the margins of error.

6.3. Opportunities for future research

The research conducted in this thesis has successfully fulfilled the overarching aim and objectives, exploring global LC change at a range of spatial scales over the last three decades, and has identified opportunities for future research that could improve our understanding of LC change, particularly in diverse landscapes. With the recent advancements in the field of satellite remote sensing and geospatial data and cloud computation platforms (e.g., GEE), finer spatial resolution LC maps could be generated using multispectral sensors, such as Landsat (30 m) and Sentinel-2 MSI (10-20 m), and these could be utilised in conjunction with

SAR data (e.g., Sentinel-1) particularly in cloudy regions such as the tropics. Hence, producing more robust LC products to provide better information for decision-makers and policy legislators, particularly in hotspot locations for LC change. Nevertheless, it is worth mentioning that using fine-resolution time-series based on Sentinel images (starting 2017), does not match the superior capability of Landsat with its historical image archive dating to the early 1970s.

The accuracy assessment provided for the ESA-CCI-LC product in chapter 5 was generated from LC data for only a single year (2015) as this was the only data for accuracy assessment provided for the ESA-CCI-LC product. Therefore, utilising reference data from across the full LC time-series (preferably all years), and generating uncertainty estimates for each year, could be a possible opportunity for future work. Furthermore, since the accuracy assessment approach used in this chapter (Olofsson *et al.*, 2013) is dependent on the quantity and quality of reference data, which, in the case of the ESA-CCI-LC product was only a sample of 1,499 locations across the globe, hence amplifying the associated uncertainties between and within the various types of LC. Therefore, increasing the number of the reference samples would be of great importance to yield more a comprehensive accuracy assessment and ultimately, reduce the associated uncertainties when accounting for margins of error within the LC product.

This thesis has demonstrated the complexity of the processes of LC change across SSA, the product of both anthropogenic and environmental drivers. Therefore, further research should focus on utilising fine spatial resolution data to distinguish between different patterns of LC change over time in order to determine which are the product of natural and/or anthropogenic processes. For example, sharp transitions in LC in clearly defined parcels would suggest anthropogenic influences, whilst subtle transitions might suggest climatic influences. Higher (spatial and temporal) resolution data could also help explore seasonal changes in LC, resolving the confusion caused by trying to infer processes from a single annual LC map. Other global hotspot locations for LC change that need further research using finer spatial resolution data include Southeast Asia, South and Central America. Furthermore, in food security-threatened regions that are densely populated with limited arable land resources (e.g., Nile Delta), fine spatial resolution images (e.g., 10 m) could be used to map the different types of staple crops, hence monitoring and quantifying the extent of these crops.

The national, continental and global LC transition maps produced in this thesis were based on a single starting point (e.g., 1992) and single endpoint (e.g., 2018) only, whilst the trajectories made use of all available data. This means that the analysis of transitions did not account for any underlying annual changes in LC. It would be beneficial to derive transitions on an annual basis in order to provide a more comprehensive account of LC change over time and provide deeper insights into the drivers through an analysis of gradual and abrupt changes in LC.

Appendices

Appendix 1.A

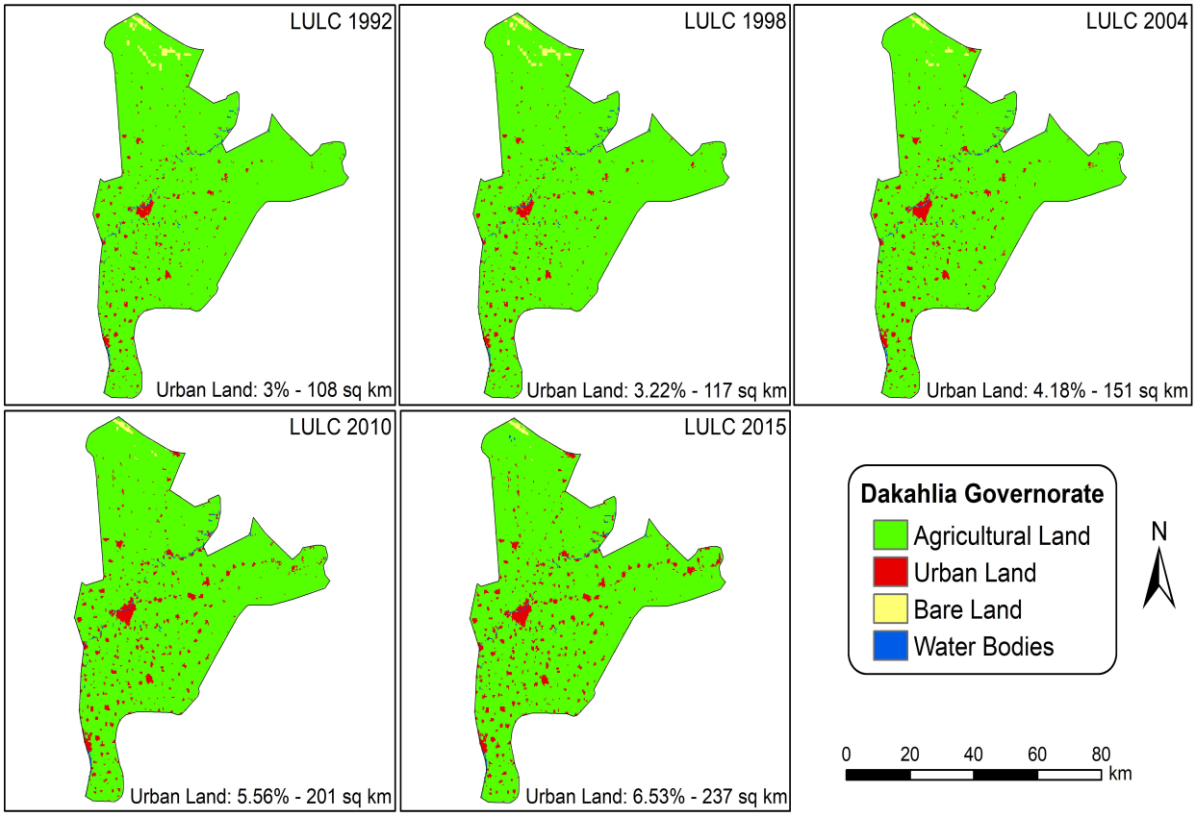

Figure 1.A1. Urban expansion over Dakahlia governorate.

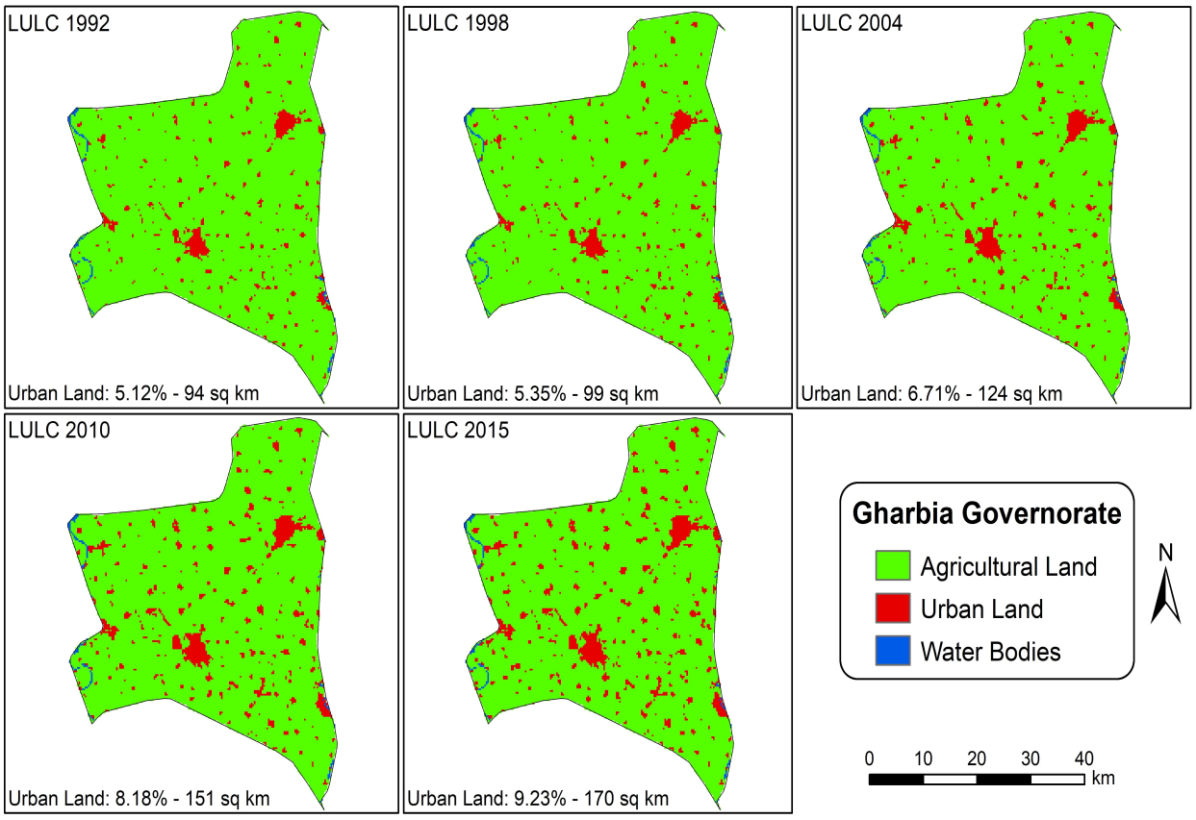

Figure 2.A1. Urban expansion over Gharbia governorate.

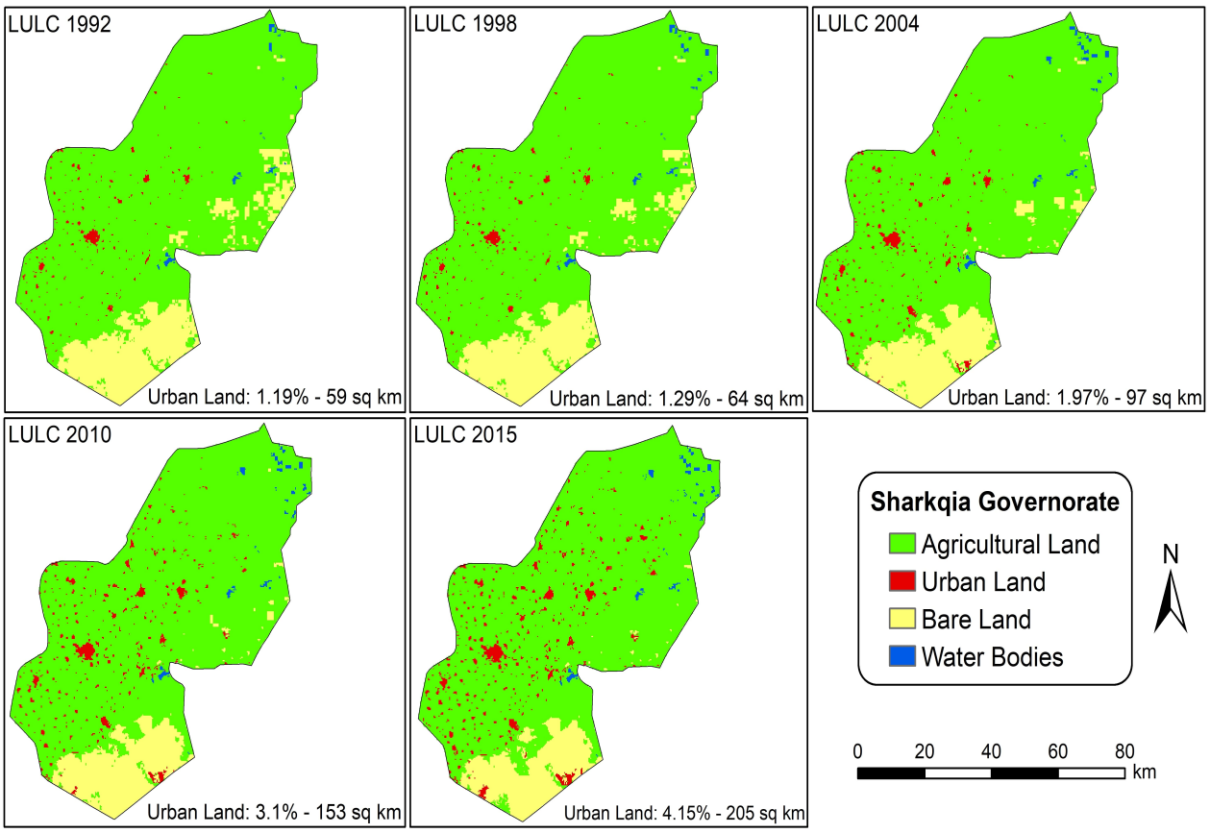

Figure 3.A1. Urban expansion over Sharkqia governorate.

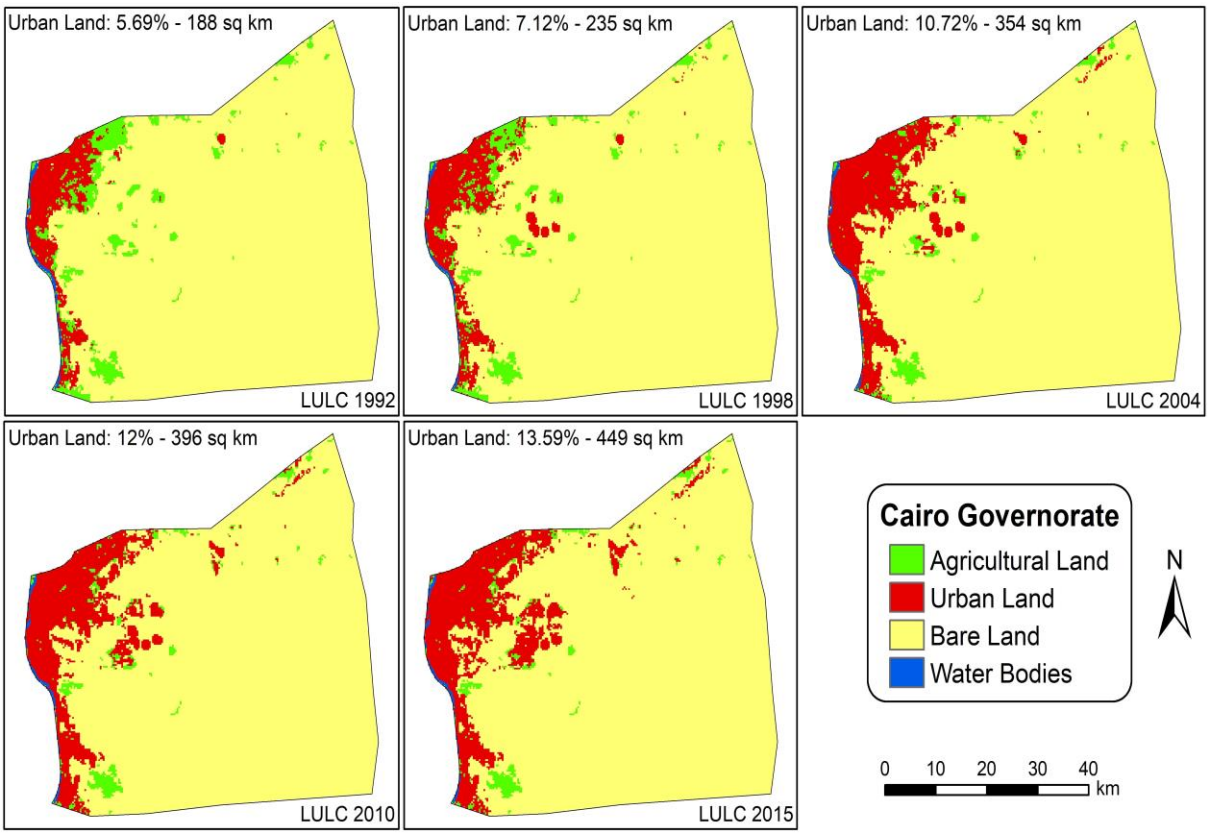

Figure 4.A1. Urban expansion over Cairo governorate.

Appendix 1.B

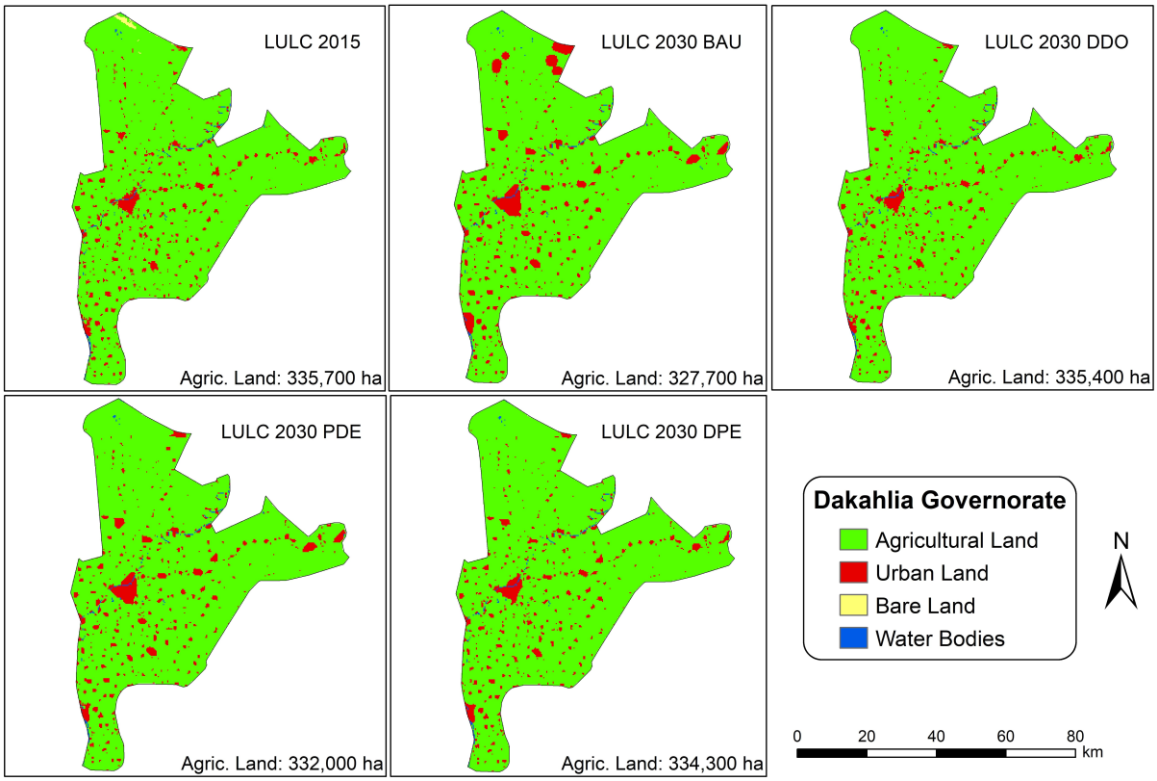

Figure 1.B1. Amount of agricultural land over Dakahlia governorate within the simulated scenarios relative to the state in 2015.

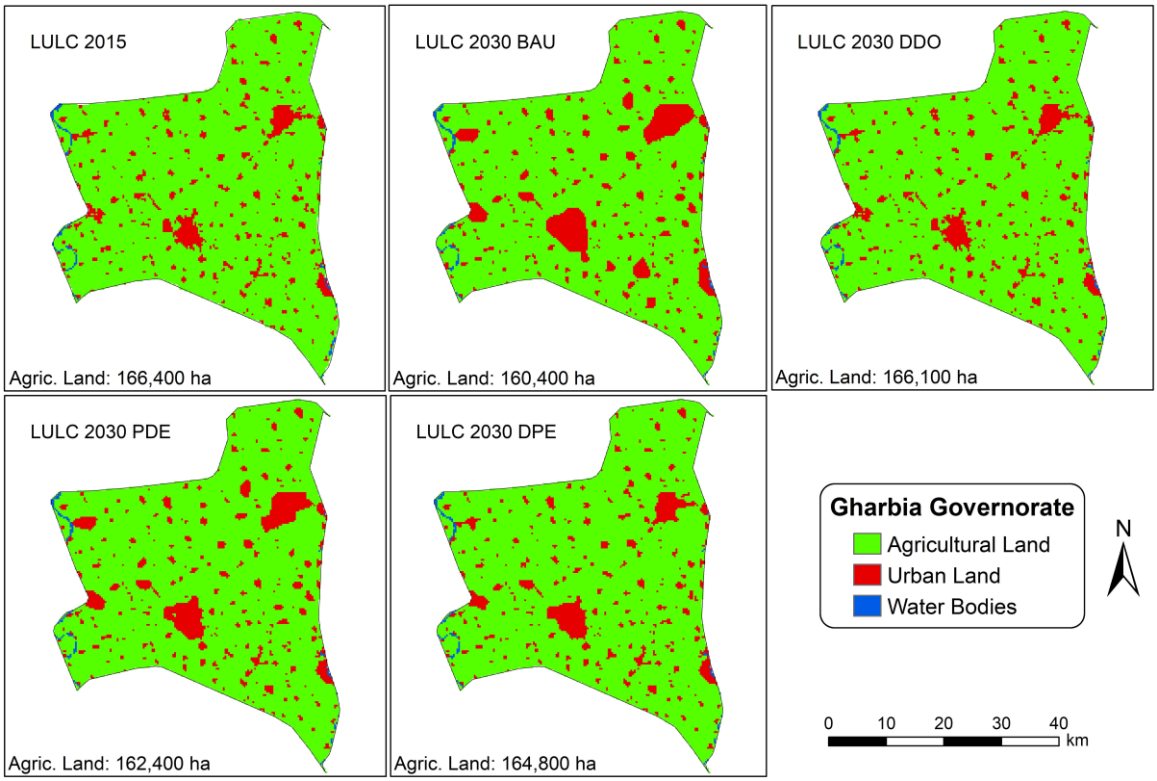

Figure 2.B1. Amount of agricultural land over Gharbia governorate within the simulated scenarios relative to the state in 2015.

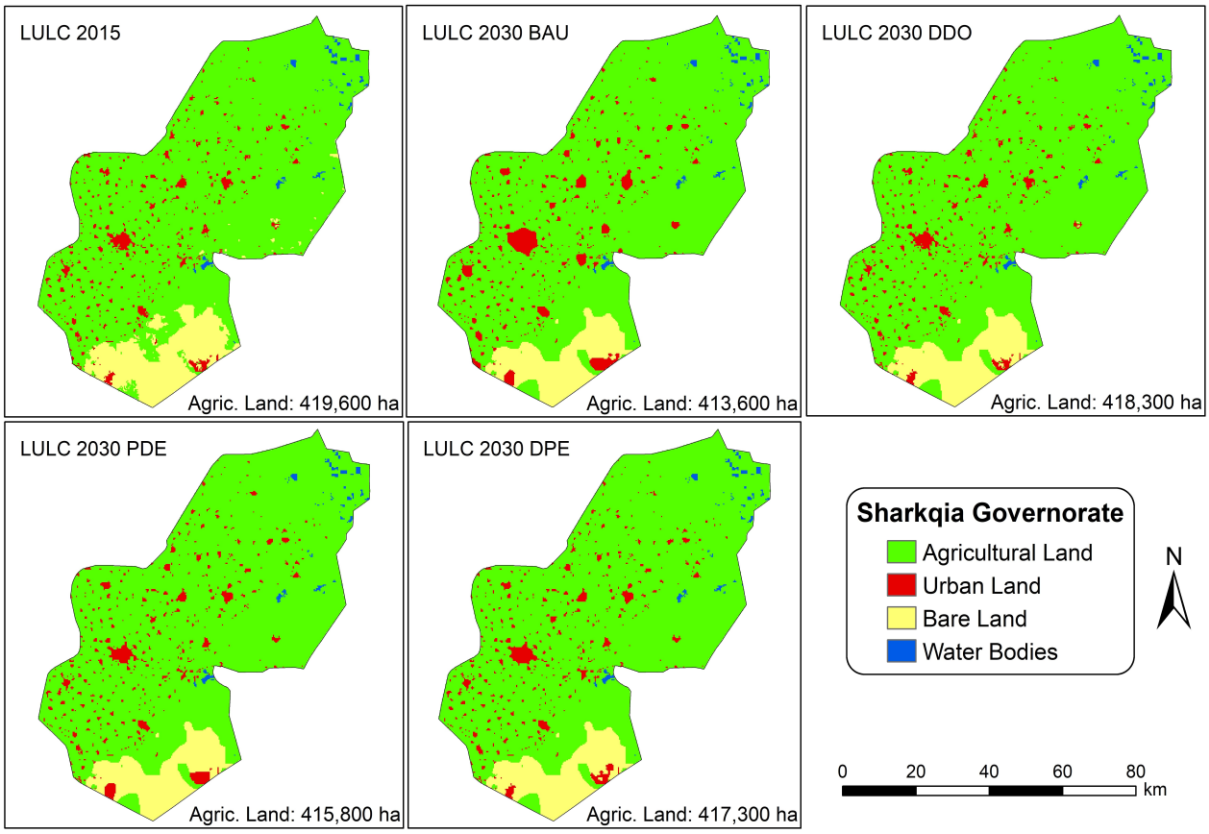

Figure 3.B1. Amount of agricultural land over Sharkqia governorate within the simulated scenarios relative to state in 2015.

Appendix 2

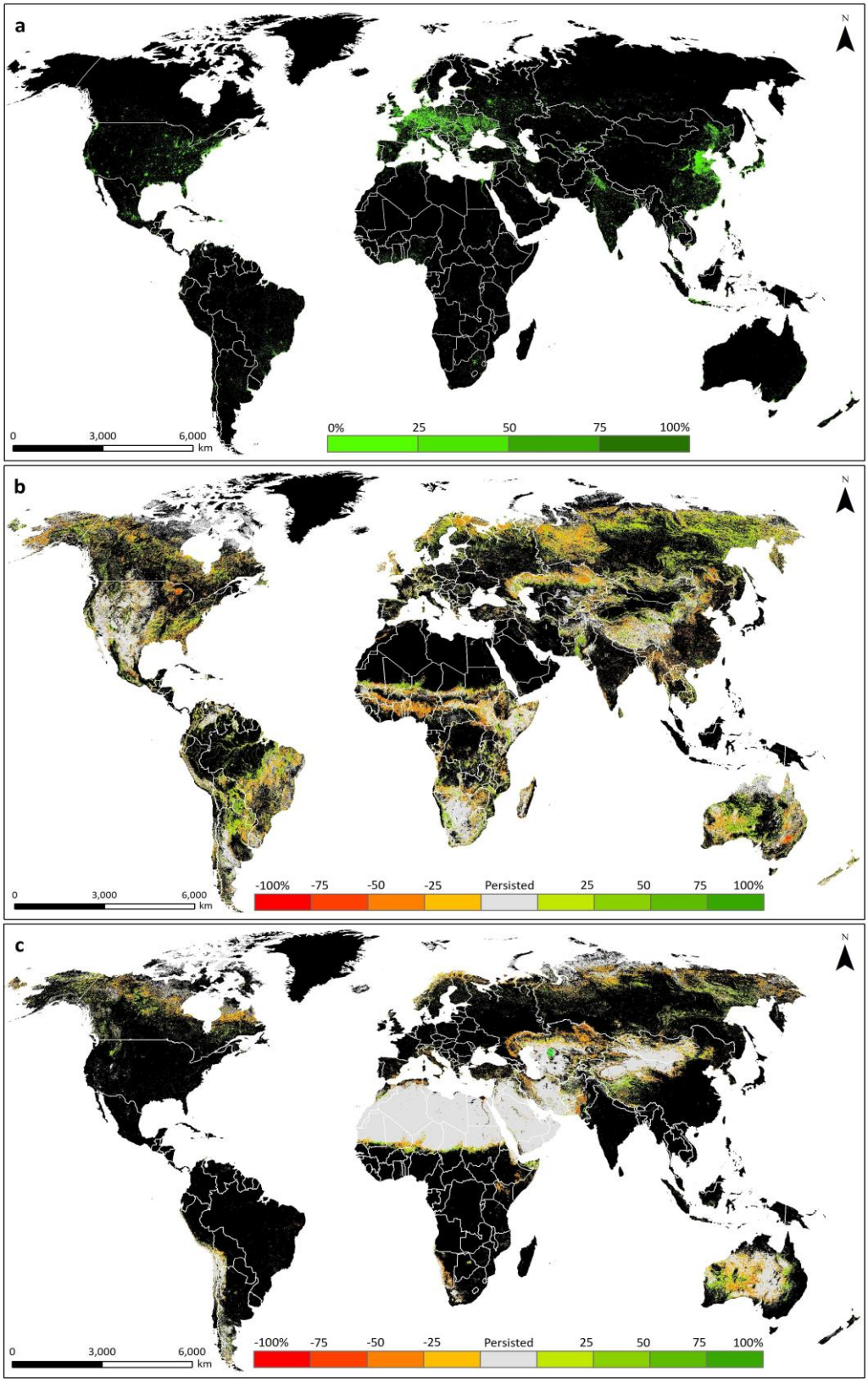

Figure 1.A2. Spatial distribution of LC change between 1992 and 2018. (a) urban; (b) natural vegetation, and (c) bare land. The original data were aggregated to a 3 km spatial resolution for visualisation. Black areas are terrestrial zones where the LC type was absent in both 1992 and 2018. ArcGIS Desktop 10.5 was used to generate this map.

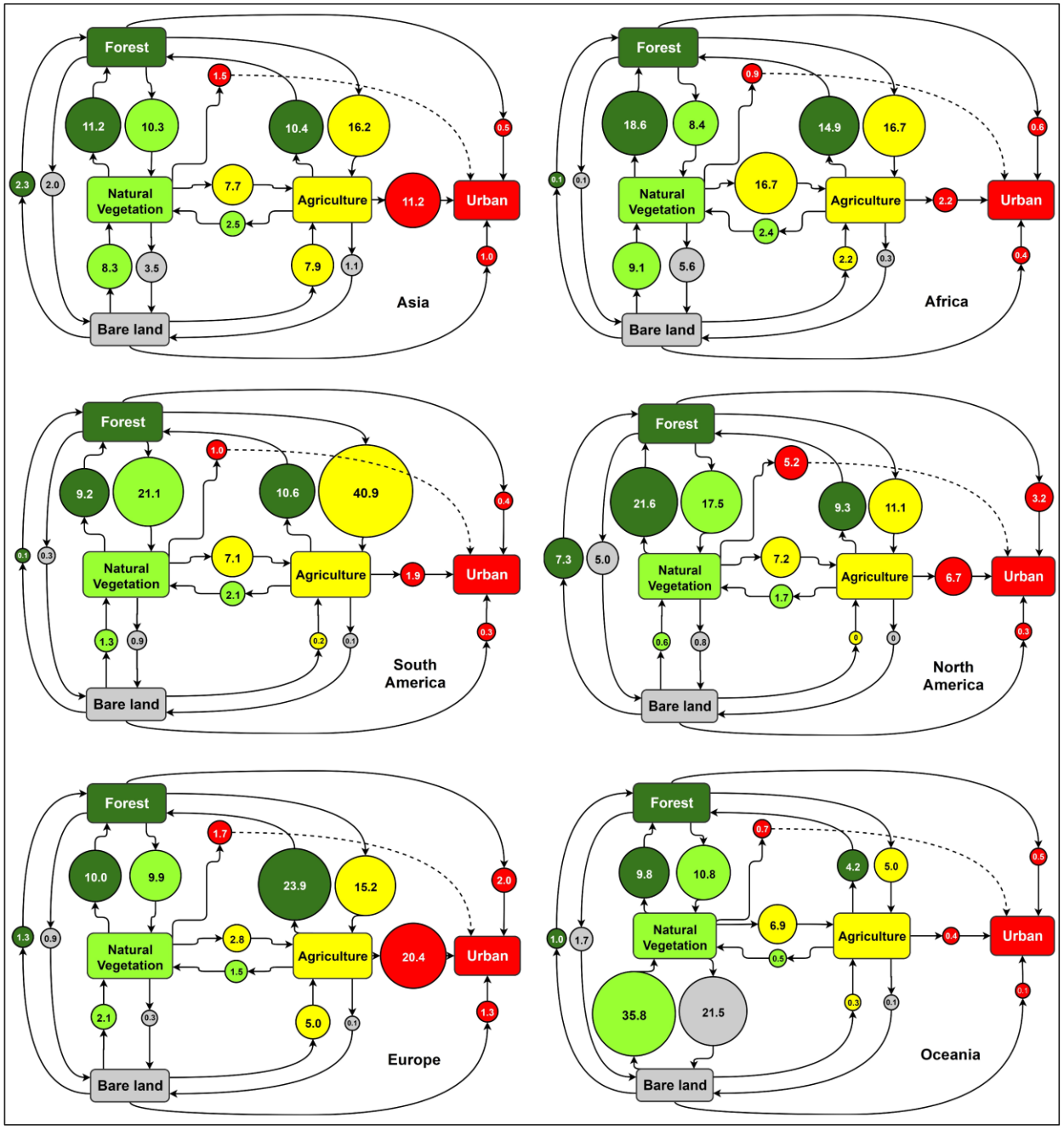

Figure 2.A2. Schematic representation of continental LC transitions between 1992 and 2018. The transitions are expressed in percentage terms relative to the total LC area in each continent that changed over this period. For visualisation purposes, the size of each circle is proportional to the magnitude of the LC transition it represents and exact figures are provided within the circle.

Table 1.A2. Changes in the main five LC classes between 1992 and 2018 at global and continental scales. Areas are expressed in million km² (the minus sign means a loss). The margin of error at the 95% confidence interval is shown for LC changes and transitions.

LC class	Agriculture	Forest	Natural vegetation	Urban	Bare land
Global	0.905 ± 2.510	-0.414 ± 2.364	-0.283 ± 3.437	1.019 ± 0.777	-0.479 ± 3.09
Asia	0.286 ± 0.984	-0.102 ± 0.752	-0.035 ± 0.913	0.462 ± 0.277	-0.258 ± 1.221
Africa	0.233 ± 0.472	0.101 ± 0.406	-0.259 ± 0.769	0.072 ± 0.049	-0.073 ± 1.125
North America	0.031 ± 0.295	0.017 ± 0.467	-0.110 ± 0.739	0.192 ± 0.184	-0.022 ± 0.204
South America	0.422 ± 0.316	-0.462 ± 0.459	0.079 ± 0.483	0.056 ± 0.050	-0.003 ± 0.129
Europe	-0.107 ± 0.372	0.045 ± 0.205	-0.002 ± 0.157	0.226 ± 0.187	-0.049 ± 0.036
Oceania	0.040 ± 0.066	-0.012 ± 0.073	0.044 ± 0.354	0.013 ± 0.016	-0.073 ± 0.345

Table 2.A2. Top 10 countries with the highest percentages of forest loss and the impact on neighbouring agricultural land. The margin of error at the 95% confidence interval is shown for LC changes and transitions.

Country	Forest loss (%)	Forest loss (km²)	Forest to agriculture (km²)	Forest to agriculture (%) of all transitions	Forest to agriculture (%) of total forest loss	Forest to agriculture (%) of total agric. gain
Malawi	32.8	16,502 ±1,982	15,196 ±1,129	74.5	92.1	98.6
Paraguay	24.6	62,015 ±11,997	24,184 ±1,796	32.9	39.0	91.6
Argentina	17.3	95,475 ±24,202	37,539 ±2,788	24.9	39.3	70.2
Cambodia	15.7	16,250 ±5,450	11,791 ±867	56.5	72.6	78.2
South Korea	14.1	9,264 ±3,016	8,671 ±644	62.7	93.6	99.0
Liberia	14.0	8,513 ±2,797	8,423 ±626	85.2	98.9	99.9
Guatemala	12.1	13,398 ±4,464	12,326 ±916	68.4	92.0	99.7
Nicaragua	8.9	9,146 ±4,390	8,193 ±609	70.5	89.6	99.7
Vietnam	8.7	16,451 ±7,309	10,603 ±788	33.3	64.5	68.9
Bolivia	7.0	61,575 ±37,709	36,840 ±2,736	42.8	59.8	96.4

Table 3.A2. Top 10 countries with the highest percentages of urban expansion and the impact on neighbouring agricultural land. The margin of error at the 95% confidence interval is shown for LC changes and transitions.

Country	Urban expansion (%)	Urban expansion (km^2)	Agriculture to urban (km^2)	Agriculture to urban (%) of all transitions	Agriculture to urban (%) of total urban gain	Agriculture to urban (%) of total agric. loss
Pakistan	715.8	6,968 ±1,742	6,243 ±2,407	11.2	89.6	65.7
Uzbekistan	553.7	6,185 ±1,610	5,432 ±2,095	23.6	87.8	61.5
Bangladesh	426.2	1,535 ±418	1,460 ±563	24.7	95.1	45.3
China	301.2	175,802 ±52,823	142,584 ±54,984	23.2	81.1	61.4
Vietnam	275.1	4,457 ±1,365	4,254 ±1,640	13.4	95.5	54.4
India	255.4	35,565 ±11,192	32,257 ±12,439	27.9	90.7	53.7
Thailand	243.6	5,280 ±1,684	5,054 ±1,949	20.0	95.7	50.1
Iraq	234.7	3,062 ±1,008	1,324 ±511	15.2	43.2	44.0
Egypt	208.2	3,860 ±1,318	2,617 ±1,009	30.6	67.8	91.0
Nigeria	198.7	8,254 ±2,878	6,204 ±2,392	6.6	75.2	32.9

Table 4.A2. Confusion matrix for the seven aggregated LC classes used in this study with cell entries expressed as the estimated proportion of area, with user's and producer's accuracies of the individual classes and the overall accuracy of the LC dataset. Mapped classes are the rows and reference classes are the columns.

LC class	Agriculture	Forest	Natural vegetation	Urban	Bare land	Water bodies	Ice/snow	Total	User's	Producer's	Overall
Agriculture	0.1527	0.0063	0.0117	0.0029	0.0015	0.0000	0.0000	0.1751	0.87	0.77	0.82
Forest	0.0094	0.2503	0.0310	0.0006	0.0033	0.0017	0.0006	0.2968	0.84	0.93	
Natural vegetation	0.0325	0.0103	0.1351	0.0022	0.0229	0.0015	0.0022	0.2067	0.65	0.70	
Urban	0.0007	0.0000	0.0000	0.0043	0.0000	0.0000	0.0000	0.0050	0.86	0.36	
Bare land	0.0039	0.0010	0.0157	0.0020	0.1618	0.0010	0.0059	0.1912	0.85	0.84	
Water	0.0003	0.0000	0.0006	0.0000	0.0000	0.0247	0.0000	0.0256	0.96	0.86	
Ice/snow	0.0000	0.0000	0.0000	0.0000	0.0038	0.0000	0.0957	0.0995	0.96	0.92	
Total	0.1995	0.2679	0.1941	0.0120	0.1933	0.0288	0.1044	1.0000			

Table 5.A2. The LC types analysed in this research and the original ESA-CCI-LC classes from which they were derived (ESA-CCI-LC: Product user guide: Version 2, available at http://maps.elie.ucl.ac.be/CCI/viewer/download/ESACCI-LC-Ph2-PUGv2_2.0.pdf).

LC types used in this study	Original LC class codes in the ESA-CCI-LC dataset combined to form the LC types used in this study	Description of the original LC classes in the ESA-CCI-LC dataset
1. Agriculture	10, 11, 12	Rainfed cropland
	20	Irrigated cropland
	30	Mosaic cropland (> 50%)/natural vegetation (tree, shrub, herbaceous cover) (< 50%)
	40	Mosaic natural vegetation (tree, shrub, herbaceous cover) (> 50%)/cropland (< 50%)
2. Forest	50	Tree cover, broadleaved, evergreen, closed to open (> 15%)
	60, 61, 62	Tree cover, broadleaved, deciduous, closed to open (> 15%)
	70, 71, 72	Tree cover, needleleaved, evergreen, closed to open (> 15%)
	80, 81, 82	Tree cover, needleleaved, deciduous, closed to open (> 15%)
	90	Tree cover, mixed leaf type (broadleaved and needleleaved)
	100	Mosaic tree and shrub (> 50%)/herbaceous cover (< 50%)
	160	Tree cover, flooded, fresh or brakish water
	170	Tree cover, flooded, saline water
3. Natural vegetation	110	Mosaic herbaceous cover (> 50%)/tree and shrub (< 50%)
	120, 121, 122	Shrubland
	130	Grassland
	140	Lichens and mosses
	180	Shrub or herbaceous cover, flooded, fresh-saline or brakish water
4. Urban	190	Urban
5. Bare land	150, 152, 153, 200, 201, 202	Bare areas and sparse vegetation
6. Water bodies	210	Water
7. Ice/Snow	220	Permanent ice and snow

References

Abd El-Kawy, O.R. et al. (2011) Land use and land cover change detection in the western Nile delta of Egypt using remote sensing data. *Applied Geography*, 31(2), 483–494.

Aburas, M.M. et al. (2016) The simulation and prediction of spatio-temporal urban growth trends using cellular automata models: A review. *International Journal of Applied Earth Observation and Geoinformation*, 52, 380–389.

Aburas, M.M. et al. (2017) Improving the capability of an integrated CA-Markov model to simulate spatio-temporal urban growth trends using an Analytical Hierarchy Process and Frequency Ratio. *International Journal of Applied Earth Observation and Geoinformation*, 59, 65–78.

Achard, F. et al. (2002) Determination of deforestation rates of the world's humid tropical forests. *Science*, 297(5583), 999–1002.

Achard, F. et al. (2014) Determination of tropical deforestation rates and related carbon losses from 1990 to 2010. *Global Change Biology*, 20(8), 2540–2554.

Acheampong, E.O. et al. (2019) Deforestation is driven by agricultural expansion in Ghana's forest reserves. *Scientific African*, 5, e00146.

Adenle, A.A. et al. (2020) Human-induced land degradation dominance in the Nigerian Guinea Savannah between 2003 – 2018. *Remote Sensing Applications: Society and Environment*, 19, 100360.

AghaKouchak, A. et al. (2015) Aral Sea syndrome desiccates Lake Urmia: Call for action. *Journal of Great Lakes Research*, 41(1), 307–311.

Ahmed, B. & Ahmed, R. (2012) Modeling urban land cover growth dynamics using multioral satellite images: A case study of Dhaka, Bangladesh. *ISPRS International Journal of Geo-Information*, 1(1), 3–31.

Aide, T.M. et al. (2013) Deforestation and Reforestation of Latin America and the Caribbean (2001-2010). *Biotropica*, 45(2), 262–271.

Aleman, J.C. et al. (2016) Land-use change outweighs projected effects of changing rainfall on tree cover in sub-Saharan Africa. *Global change biology*, 22(9), 3013–3025.

Alencar, A. et al. (2020) Mapping three decades of changes in the brazilian savanna native vegetation using landsat data processed in the google earth engine platform. *Remote Sensing*,

12(6), 924.

Alqurashi, A.F. et al. (2016) Urban land cover change modelling using time-series satellite images: A case study of urban growth in five cities of Saudi Arabia. *Remote Sensing*, 8(10), 838.

Amani, M. et al. (2020a) Application of google earth engine cloud computing platform, sentinel imagery, and neural networks for crop mapping in Canada. *Remote Sensing*, 12(21), 1–18.

Amani, M. et al. (2020b) Google Earth Engine Cloud Computing Platform for Remote Sensing Big Data Applications: A Comprehensive Review. *IEEE Journal of Selected Topics in Applied Earth Observations and Remote Sensing*, 13, 5326–5350.

Amini Parsa, V. et al. (2016) Spatio-temporal analysis of land use/land cover pattern changes in Arasbaran Biosphere Reserve: Iran. *Modeling Earth Systems and Environment*, 2(4), 1–13.

Andela, N. & Van Der Werf, G.R. (2014) Recent trends in African fires driven by cropland expansion and El Niño to la Niña transition. *Nature Climate Change*, 4(9), 791–795.

Anyamba, A. & Tucker, C.J. (2005) Analysis of Sahelian vegetation dynamics using NOAA-AVHRR NDVI data from 1981-2003. *Journal of Arid Environments*, 63(3), 596–614.

Arino, O. et al. (2012) Global Land Cover Map for 2009 (GlobCover 2009). *European Space Agency (ESA) & Universite catholique de Louvain (UCL)*. PANGAEA. Available at: doi:10.1594/PANGAEA.787668

Armenteras, D. et al. (2017) Deforestation dynamics and drivers in different forest types in Latin America: Three decades of studies (1980–2010). *Global Environmental Change*, 46, 139–147.

Asibey, M.O. et al. (2020) Patterns of land use, crop and forest cover change in the Ashanti region, Ghana. *Journal of Sustainable Forestry*, 39(1), 35–60.

Aune-Lundberg, L. & Strand, G.-H. (2021) The content and accuracy of the CORINE Land Cover dataset for Norway. *International Journal of Applied Earth Observation and Geoinformation*, 96, 102266.

Austin, K.G. et al. (2017) Shifting patterns of oil palm driven deforestation in Indonesia and implications for zero-deforestation commitments. *Land Use Policy*, 69, 41–48.

Austin, K.G. et al. (2019) What causes deforestation in Indonesia? *Environmental Research*

Letters, 14(2), 024007.

Baccini, A. et al. (2012) Estimated carbon dioxide emissions from tropical deforestation improved by carbon-density maps. *Nature Climate Change*, 2(3), 182–185.

Bagan, H. et al. (2020) Spatiotemporal analysis of deforestation in the Chapare region of Bolivia using LANDSAT images. *Land Degradation and Development*, 31(18), 3024–3039.

Bagan, H. & Yamagata, Y. (2012) Landsat analysis of urban growth: How Tokyo became the world's largest megacity during the last 40years. *Remote Sensing of Environment*, 127, 210–222.

Baker, W.L. (1989) A review of models of landscape change. *Landscape Ecology*, 2(2), 111–133.

Bakr, N. et al. (2010) Monitoring land cover changes in a newly reclaimed area of Egypt using multi-temporal Landsat data. *Applied Geography*, 30(4), 592–605.

Bakr, N. & Bahnassy, M.H. (2019a) Egyptian Natural Resources. In: *The Soils of Egypt; World Soils Book Series; Springer: Cham, Switzerland*. [Online]. Available at: https://doi.org/10.1007/978-3-319-95516-2_3

Bakr, N. & Bahnassy, M.H. (2019b) Land Use/Land Cover and Vegetation Status. In: *The Soils of Egypt; World Soils Book Series; Springer: Cham, Switzerland*. [Online]. Available at: doi:http://link.springer.com/10.1007/978-3-319-95516-2_4

Balzter, H. (2000) Markov chain models for vegetation dynamics. *Ecological Modelling*, 126(2–3), 139–154.

Ban, Y. et al. (2015) Global land cover mapping using Earth observation satellite data: Recent progresses and challenges. *ISPRS Journal of Photogrammetry and Remote Sensing*, 103, 1–6.

Baqa, M.F. et al. (2021) Monitoring and modeling the patterns and trends of urban growth using urban sprawl matrix and CA-Markov model: A case study of Karachi, Pakistan. *Land*, 10(7), 700.

Barima, Y.S.S. et al. (2016) Cocoa crops are destroying the forest reserves of the classified forest of Haut-Sassandra (Ivory Coast). *Global Ecology and Conservation*, 8, 85–98.

Barnes, J. (2012) Pumping possibility: Agricultural expansion through desert reclamation in Egypt. *Social Studies of Science*, 42(4), 517–538.

Barnieh, B.A. et al. (2020) Mapping land use land cover transitions at different spatiotemporal scales in West Africa. *Sustainability (Switzerland)*, 12(20), 1–52.

Barona, E. et al. (2010) The role of pasture and soybean in deforestation of the Brazilian Amazon. *Environmental Research Letters*, 5(2), 024002.

Bartholomé, E. & Belward, A.S. (2005) GLC2000: A new approach to global land cover mapping from earth observation data. *International Journal of Remote Sensing*, 26(9), 1959–1977.

Baumann, M. et al. (2017) Deforestation and cattle expansion in the Paraguayan Chaco 1987–2012. *Regional Environmental Change*, 17(4), 1179–1191.

Beerling, D.J. & Osborne, C.P. (2006) The origin of the savanna biome. *Global Change Biology*, 12(11), 2023–2031.

Belay, T.A. et al. (2013) Woody vegetation dynamics in the rangelands of lower Omo region, southwestern Ethiopia. *Journal of Arid Environments*, 89, 94–102.

Bhagwat, T. et al. (2017) Losing a jewel-Rapid declines in Myanmar's intact forests from 2002-2014. *PLoS ONE*, 12(5), 1–22.

Bhatti, S.S. et al. (2015) A multi-scale modeling approach for simulating urbanization in a metropolitan region. *Habitat International*, 50, 354–365.

Blanco, P.D. et al. (2013) A land cover map of Latin America and the Caribbean in the framework of the SERENA project. *Remote Sensing of Environment*, 132, 13–31.

Bleischwitz, R. et al. (2012) Coltan from Central Africa, international trade and implications for any certification. *Resources Policy*, 37(1), 19–29.

Bodart, C. et al. (2013) Continental estimates of forest cover and forest cover changes in the dry ecosystems of Africa between 1990 and 2000. *Journal of Biogeography*, 40(6), 1036–1047.

Brandt, M. et al. (2015) Ground-and satellite-based evidence of the biophysical mechanisms behind the greening Sahel. *Global Change Biology*, 21(4), 1610–1620.

Brandt, M. et al. (2017) Human population growth offsets climate-driven increase in woody vegetation in sub-Saharan Africa. *Nature Ecology and Evolution*, 1(4), 1–6.

Bratley, K. & Ghoneim, E. (2018) Modeling urban encroachment on the agricultural land of

the Eastern Nile Delta using remote sensing and a GIS-Based Markov Chain Model. *Land*, 7(4), 9–11.

Brink, A.B. et al. (2014) Anthropogenic pressure in East Africa-Monitoring 20 years of land cover changes by means of medium resolution satellite data. *International Journal of Applied Earth Observation and Geoinformation*, 28(1), 60–69.

Brink, A.B. & Eva, H.D. (2009) Monitoring 25 years of land cover change dynamics in Africa: A sample based remote sensing approach. *Applied Geography*, 29(4), 501–512.

Bullock, E.L. et al. (2021) Three decades of land cover change in East Africa. *Land*, 10(2), 1–15.

Cabral, A.I.R. et al. (2011) Spatial dynamics and quantification of deforestation in the central-plateau woodlands of Angola (1990-2009). *Applied Geography*, 31(3), 1185–1193.

Cai, H. et al. (2013) Spatiotemporal Patterns of Urban Encroachment on Cropland and Its Impacts on Potential Agricultural Productivity in China. *Remote Sensing*, 5(12), 6443–6460.

Caldas, M.M. et al. (2015) Land-cover change in the Paraguayan Chaco: 2000–2011. *Journal of Land Use Science*, 10(1), 1–18.

Calderón-Loor, M. et al. (2021) High-resolution wall-to-wall land-cover mapping and land change assessment for Australia from 1985 to 2015. *Remote Sensing of Environment*, 252, 112148.

CAPMAS (2018) *The Central Agency for Public Mobilization and Statistics. The Arab Republic of Egypt*. Available at: http://www.capmas.gov.eg/ [Accessed: 6 June 2018].

Carodenuto, S. (2019) Governance of zero deforestation cocoa in West Africa: New forms of public–private interaction. *Environmental Policy and Governance*, 29(1), 55–66.

Carroll, M.L. et al. (2009) A new global raster water mask at 250 m resolution. *International Journal of Digital Earth*, 2(4), 291–308.

Castiblanco, C. et al. (2013) Oil palm plantations in Colombia: A model of future expansion. *Environmental Science and Policy*, 27, 172–183.

Ceddia, M.G. et al. (2014) Governance, agricultural intensification, and land sparing in tropical South America. *Proceedings of the National Academy of Sciences of the United States of America*, 111(20), 7242–7247.

Chamberlin, J. et al. (2014) Scarcity amidst abundance? Reassessing the potential for cropland expansion in Africa. *Food Policy*, 48, 51–65.

Chaplin-Kramer, R. et al. (2015) Spatial patterns of agricultural expansion determine impacts on biodiversity and carbon storage. *Proceedings of the National Academy of Sciences of the United States of America*, 112(24), 7402–7407.

Chen, J. et al. (2015) Global land cover mapping at 30 m resolution: A POK-based operational approach. *ISPRS Journal of Photogrammetry and Remote Sensing*, 103, 7–27.

Chen, X. et al. (2013) Changes in land use/land cover and ecosystem services in Central Asia during 1990-2009. *Current Opinion in Environmental Sustainability*, 5(1), 116–127.

Chen, Z. et al. (2021) Integrating remote sensing and a Markov-FLUS model to simulate future land use changes in Hokkaido, Japan. *Remote Sensing*, 13(13), 1–23.

Chi, M. et al. (2016) Big Data for Remote Sensing: Challenges and Opportunities. *Proceedings of the IEEE*, 104(11), 2207–2219.

Christie, T. et al. (2007) Fragmentation and clearance of Liberia's forests during 1986-2000. *Oryx*, 41(4), 539–543.

Clark, M.L. et al. (2010) A scalable approach to mapping annual land cover at 250 m using MODIS time series data: A case study in the Dry Chaco ecoregion of South America. *Remote Sensing of Environment*, 114(11), 2816–2832.

Clark, M.L. et al. (2012) Land change for all municipalities in Latin America and the Caribbean assessed from 250-m MODIS imagery (2001-2010). *Remote Sensing of Environment*, 126, 84–103.

Clarke, K.C. et al. (1997) A self-modifying cellular automaton model of historical urbanization in the San Francisco Bay area. *Environment and Planning B: Planning and Design*, 24(2), 247–261.

Colditz, R.R. et al. (2012) Generation and analysis of the 2005 land cover map for Mexico using 250m MODIS data. *Remote Sensing of Environment*, 123, 541–552.

Colditz, R.R. et al. (2014) Detection of North American land cover change between 2005 and 2010 with 250m MODIS Data. *Photogrammetric Engineering and Remote Sensing*, 80(10), 918–924.

Conrad, C. et al. (2015) Measuring rural settlement expansion in Uzbekistan using remote

sensing to support spatial planning. *Applied Geography*, 62, 29–43.

Cramer, C. (1999) Can Africa industrialize by processing primary commodities? The case of Mozambican cashew nuts. *World Development*, 27(7), 1247–1266.

Cui, Y. et al. (2019) Accelerating cities in an unsustainable landscape: Urban expansion and cropland occupation in China, 1990-2030. *Sustainability (Switzerland)*, 11(8), 2283.

Curtis, P.G. et al. (2018) Classifying drivers of global forest loss. *Science*, 361(6407), 1108–1111.

D'Amour, C.B. et al. (2017) Future urban land expansion and implications for global croplands. *Proceedings of the National Academy of Sciences of the United States of America*, 114(34), 8939–8944.

Davis, K.F. et al. (2020) Tropical forest loss enhanced by large-scale land acquisitions. *Nature Geoscience*, 13(7), 482–488.

Defourny, P. et al. (2010) *Globcorine 2009, Description and Validation Report*.

Defries, R.S. et al. (2010) Deforestation driven by urban population growth and agricultural trade in the twenty-first century. *Nature Geoscience*, 3(3), 178–181.

DeFries, R.S. et al. (1998) Global land cover classifications at 8 km spatial resolution: The use of training data derived from Landsat imagery in decision tree classifiers. *International Journal of Remote Sensing*, 19(16), 3141–3168.

DeFries, R.S. et al. (2000) A new global 1-km dataset of percentage tree cover derived from remote sensing. *Global Change Biology*, 6(2), 247–254.

Defries, R.S. & Townshend, J.R. (1994) Ndvi-Derived Land Cover Classifications At a Global Scale. *International Journal of Remote Sensing*, 15(17), 3567–3586.

Devine, J.A. et al. (2020) Drug trafficking, cattle ranching and Land use and Land cover change in Guatemala's Maya Biosphere Reserve. *Land Use Policy*, 95, 104578.

Dewan, A.M. & Yamaguchi, Y. (2009) Land use and land cover change in Greater Dhaka, Bangladesh: Using remote sensing to promote sustainable urbanization. *Applied Geography*, 29(3), 390–401.

Dietzel, C. & Clarke, K.C. (2007) Toward optimal calibration of the SLEUTH land use change model. *Transactions in GIS*, 11(1), 29–45.

Dinerstein, E. et al. (2017) An Ecoregion-Based Approach to Protecting Half the Terrestrial Realm. *BioScience*, 67(6), 534–545.

Dong, J. et al. (2012) A comparison of forest cover maps in Mainland Southeast Asia from multiple sources: PALSAR, MERIS, MODIS and FRA. *Remote Sensing of Environment*, 127, 60–73.

Dou, Y. & Kuang, W. (2020) A comparative analysis of urban impervious surface and green space and their dynamics among 318 different size cities in China in the past 25 years. *Science of the Total Environment*, 706, 135828.

Duan, Q. & Tan, M. (2019) Spatial and temporal variations of forest cover in developing countries. *Sustainability (Switzerland)*, 11(6), 1517.

Eastman, J.. (2016) *TerrSet Geospatial Monitoring and Modeling Software; Clark University: Worcester, MA, USA*. Available at: https://clarklabs.org/terrset/

Eckert, S. et al. (2011) Deforestation and forest degradation monitoring and assessment of biomass and carbon stock of lowland rainforest in the Analanjirofo region, Madagascar. *Forest Ecology and Management*, 262(11), 1996–2007.

El-Hallaq, M.A. & Habboub, M.O. (2015) Using Cellular Automata-Markov Analysis and Multi Criteria Evaluation for Predicting the Shape of the Dead Sea. *Advances in Remote Sensing*, 04(01), 83–95.

Enaruvbe, G.O. et al. (2019) Armed conflict and mining induced land-use transition in northern Nimba County, Liberia. *Global Ecology and Conservation*, 17, e00597.

ESA (2017) *European Space Agency. Land Cover CCI Product User Guide Version 2.0*. Available at: http:%0A//maps.elie.ucl.ac.be/CCI/viewer/download/ESACCI-LC-Ph2-PUGv2_2.0.pdf

Espírito-Santo, M.M. et al. (2016) Understanding patterns of land-cover change in the Brazilian Cerrado from 2000 to 2015. *Philosophical Transactions of the Royal Society B: Biological Sciences*, 371(1703).

ESRI (2016) *Environmental Systems Research Institute. ArcGIS Desktop 10.5; ESRI: Redlands, CA, USA*.

Estel, S. et al. (2015) Mapping farmland abandonment and recultivation across Europe using MODIS NDVI time series. *Remote Sensing of Environment*, 163, 312–325.

Estoque, R.C. et al. (2019) The future of Southeast Asia's forests. *Nature Communications*,

10(1), 1–12.

Estoque, R.C. & Murayama, Y. (2015) Intensity and spatial pattern of urban land changes in the megacities of Southeast Asia. *Land Use Policy*, 48, 213–222.

Eva, H.D. et al. (2004) A land cover map of South America. *Global Change Biology*, 10(5), 731–744.

Eva, H.D. et al. (2012) Forest cover changes in tropical south and Central America from 1990 to 2005 and related carbon emissions and removals. *Remote Sensing*, 4(5), 1369–1391.

FAO (2015) *Global Forest Resources Assessment 2015 Desk reference. Food and Agriculture Organization of the United Nations, Rome.*

FAO (2018) *Food and Agriculture Organization of the United Nations. FAOSTAT Database; FAO: Rome, Italy*. Available at: http://www.fao.org/faostat/en/#data/QC [Accessed: 11 November 2018].

FAO (2020) *FAO, IFAD, UNICEF, WFP and WHO. 2020. The State of Food Security and Nutrition in the World 2020. Transforming food systems for affordable healthy diets. Rome, FAO. https://doi.org/10.4060/ca9692en*.

Feddema, J.J. et al. (2005) The importance of land-cover change in simulating future climates. *Science*, 310(5754), 1674–1678.

Fehlenberg, V. et al. (2017) The role of soybean production as an underlying driver of deforestation in the South American Chaco. *Global Environmental Change*, 45(May), 24–34.

Feng, D. et al. (2016a) Circa 2014 African land-cover maps compatible with FROM-GLC and GLC2000 classification schemes based on multi-seasonal Landsat data. *International Journal of Remote Sensing*, 37(19), 4648–4664.

Feng, D. et al. (2018) A multiple dataset approach for 30-m resolution land cover mapping: a case study of continental Africa. *International Journal of Remote Sensing*, 39(12), 3926–3938.

Feng, M. et al. (2016b) A global, high-resolution (30-m) inland water body dataset for 2000: first results of a topographic–spectral classification algorithm. *International Journal of Digital Earth*, 9(2), 113–133.

Feng, M. et al. (2016c) Earth science data records of global forest cover and change: Assessment of accuracy in 1990, 2000, and 2005 epochs. *Remote Sensing of Environment*,

184, 73–85.

Fensholt, R. et al. (2012) Greenness in semi-arid areas across the globe 1981-2007 - an Earth Observing Satellite based analysis of trends and drivers. *Remote Sensing of Environment*, 121, 144–158.

Fenta, A.A. et al. (2020) Cropland expansion outweighs the monetary effect of declining natural vegetation on ecosystem services in sub-Saharan Africa. *Ecosystem Services*, 45, 101154.

Feranec, J. et al. (2010) Determining changes and flows in European landscapes 1990-2000 using CORINE land cover data. *Applied Geography*, 30(1), 19–35.

Fitzherbert, E.B. et al. (2008) How will oil palm expansion affect biodiversity? *Trends in Ecology and Evolution*, 23(10), 538–545.

Fitzsimmons, M. (2003) Effects of deforestation and reforestation on landscape spatial structure in boreal Saskatchewan, Canada. *Forest Ecology and Management*, 174(1–3), 577–592.

Foley, J.A. et al. (2005) Global consequences of land use. *Science*, 309(5734), 570–574.

Foody, G. (2008) Harshness in image classification accuracy assessment. *International Journal of Remote Sensing*, 29(11), 3137–3158.

Foody, G.M. (2010) Assessing the accuracy of land cover change with imperfect ground reference data. *Remote Sensing of Environment*, 114(10), 2271–2285.

Forget, Y. et al. (2021) Mapping 20 years of urban expansion in 45 urban areas of sub-Saharan Africa. *Remote Sensing*, 13(3), 1–19.

Forkuor, G. et al. (2017) Multiscale remote sensing to map the spatial distribution and extent of cropland in the sudanian savanna of West Africa. *Remote Sensing*, 9(8), 1–24.

Friedl, M.A. et al. (2002) Global land cover mapping from MODIS: Algorithms and early results. *Remote Sensing of Environment*, 83(1–2), 287–302.

Friedl, M.A. et al. (2010) MODIS Collection 5 global land cover: Algorithm refinements and characterization of new datasets. *Remote Sensing of Environment*, 114(1), 168–182.

Fritz, S. et al. (2015) Mapping global cropland and field size. *Global Change Biology*, 21(5), 1980–1992.

Fry, J.A. et al. (2011) Completion of the 2006 national land cover database for the conterminous united states. *Photogrammetric Engineering and Remote Sensing*, 77(9), 858–864.

Fuchs, R. et al. (2018) A global assessment of gross and net land change dynamics for current conditions and future scenarios. *Earth System Dynamics*, 9(2), 441–458.

Furumo, P.R. & Aide, T.M. (2017) Characterizing commercial oil palm expansion in Latin America: Land use change and trade. *Environmental Research Letters*, 12(2), 024008.

Gasparri, N.I. et al. (2013) Linkages between soybean and neotropical deforestation: Coupling and transient decoupling dynamics in a multi-decadal analysis. *Global Environmental Change*, 23(6), 1605–1614.

Gasparri, N.I. et al. (2016) The Emerging Soybean Production Frontier in Southern Africa: Conservation Challenges and the Role of South-South Telecouplings. *Conservation Letters*, 9(1), 21–31.

Gaveau, D.L.A. et al. (2014) Four decades of forest persistence, clearance and logging on Borneo. *PLoS ONE*, 9(7), 1–11.

Geist, H.J. & Lambin, E.F. (2002) Proximate causes and underlying driving forces of tropical deforestation. *BioScience*, 52(2), 143–150.

Gemitzi, A. et al. (2021) Land cover and vegetation carbon stock changes in Greece: A 29-year assessment based on CORINE and Landsat land cover data. *Science of the Total Environment*, 786, 147408.

Geng, B. et al. (2017) Scenario analysis of sustainable intensive land use based on SD model. *Sustainable Cities and Society*, 29, 193–202.

German, L.A. et al. (2020) The environmental effects of sugarcane expansion: A case study of changes in land and water use in southern Africa. *Applied Geography*, 121, 102240.

Gessner, U. et al. (2015) Multi-sensor mapping of West African land cover using MODIS, ASAR and TanDEM-X/TerraSAR-X data. *Remote Sensing of Environment*, 164, 282–297.

Ghar, M.A. et al. (2004) Agricultural land monitoring in the Egyptian Nile Delta using landsat data. *International Journal of Environmental Studies*, 61(6), 651–657.

Gibbs, H.K. et al. (2010) Tropical forests were the primary sources of new agricultural land in the 1980s and 1990s. *Proceedings of the National Academy of Sciences of the United States*

of America, 107(38), 16732–16737.

Gibbs, H.K. et al. (2015) Brazil's Soy Moratorium. *Science*, 347(6220), 377–378.

Gibson, L. et al. (2011) Primary forests are irreplaceable for sustaining tropical biodiversity. *Nature*, 478(7369), 378–381.

Giri, C. & Jenkins, C. (2005) Land cover mapping of Greater Mesoamerica using MODIS data. *Canadian Journal of Remote Sensing*, 31(4), 274–282.

Giri, C. & Long, J. (2014) Land cover characterization and mapping of South America for the year 2010 using landsat 30 m satellite data. *Remote Sensing*, 6(10), 9494–9510.

Gondwe, M.F. et al. (2019) Land use land cover change and the comparative impact of co-management and government-management on the forest cover in Malawi (1999-2018). *Journal of Land Use Science*, 14(4–6), 281–305.

Gong, P. et al. (2013) Finer resolution observation and monitoring of global land cover: First mapping results with Landsat TM and ETM+ data. *International Journal of Remote Sensing*, 34(7), 2607–2654.

Gong, P. et al. (2019) Stable classification with limited sample: transferring a 30-m resolution sample set collected in 2015 to mapping 10-m resolution global land cover in 2017. *Science Bulletin*, 64(6), 370–373.

Gong, P. et al. (2020) Annual maps of global artificial impervious area (GAIA) between 1985 and 2018. *Remote Sensing of Environment*, 236, 111510.

Gorelick, N. et al. (2017) Google Earth Engine: Planetary-scale geospatial analysis for everyone. Remote Sensing of Environment, 202, 18–27.

Graesser, J. et al. (2015) Cropland/pastureland dynamics and the slowdown of deforestation in Latin America. *Environmental Research Letters*, 10(3), 034017.

Di Gregorio, A. (2005) Land Cover Classification System: Classification Concepts and User manual. *FAO, Rome*.

Grekousis, G. et al. (2015) An overview of 21 global and 43 regional land-cover mapping products. *International Journal of Remote Sensing*, 36(21), 5309–5335.

Grigorescu, I. et al. (2021) Modelling land use/cover change to assess future urban sprawl in Romania. *Geocarto International*, 36(7), 721–739.

Guan, D.J. et al. (2011) Modeling urban land use change by the integration of cellular automaton and Markov model. *Ecological Modelling*, 222(20–22), 3761–3772.

Gumma, M.K. et al. (2020) Agricultural cropland extent and areas of South Asia derived using Landsat satellite 30-m time-series big-data using random forest machine learning algorithms on the Google Earth Engine cloud. *GIScience and Remote Sensing*, 57(3), 302–322.

Güneralp, B. et al. (2017) Urbanization in Africa: challenges and opportunities for conservation. *Environmental Research Letters*, 13(1), 15002.

Gutiérrez-Vélez, V.H. et al. (2011) High-yield oil palm expansion spares land at the expense of forests in the Peruvian Amazon. *Environmental Research Letters*, 6(4), 044029.

Halmy, M.W.A. et al. (2015) Land use/land cover change detection and prediction in the north-western coastal desert of Egypt using Markov-CA. *Applied Geography*, 63, 101–112.

Hamad, R. et al. (2018) Predicting land use/land cover changes using a CA-Markov model under two different scenarios. *Sustainability (Switzerland)*, 10(10), 1–23.

Han, H. et al. (2015) Scenario simulation and the prediction of land use and land cover change in Beijing, China. *Sustainability (Switzerland)*, 7(4), 4260–4279.

Hansen, M.C. et al. (2000) Global land cover classification at 1 km spatial resolution using a classification tree approach. *International Journal of Remote Sensing*. 21(6-7), 1331-1364.

Hansen, M.C. et al. (2003) Global Percent Tree Cover at a Spatial Resolution of 500 Meters: First Results of the MODIS Vegetation Continuous Fields Algorithm. *Earth Interactions*, 7(10), 1–15.

Hansen, M.C. et al. (2013) High-resolution global maps of 21st-century forest cover change. *Science*, 342(6160), 850–853.

Hansen, M.C. et al. (2014) Monitoring conterminous United States (CONUS) land cover change with Web-Enabled Landsat Data (WELD). *Remote Sensing of Environment*, 140, 466–484.

Hao, P. et al. (2018) Annual cropland mapping using reference Landsat time series-A case study in Central Asia. *Remote Sensing*, 10(12), 2057.

Hassan, M.M. & Southworth, J. (2017) Analyzing land cover change and urban growth trajectories of the mega-urban region of Dhaka using remotely sensed data and an ensemble classifier. *Sustainability (Switzerland)*, 10(1), 1–24.

He, C. et al. (2019) Detecting global urban expansion over the last three decades using a fully convolutional network. *Environmental Research Letters*, 14(3), 034008.

Helldén, U. & Tottrup, C. (2008) Regional desertification: A global synthesis. *Global and Planetary Change*, 64(3–4), 169–176.

Hennig, E.I. et al. (2015) Multi-scale analysis of urban sprawl in Europe: Towards a European de-sprawling strategy. *Land Use Policy*, 49, 483–498.

Hermosilla, T. et al. (2018) Disturbance-Informed Annual Land Cover Classification Maps of Canada's Forested Ecosystems for a 29-Year Landsat Time Series. *Canadian Journal of Remote Sensing*, 44(1), 67–87.

Herrmann, S.M. et al. (2005) Recent trends in vegetation dynamics in the African Sahel and their relationship to climate. *Global Environmental Change*, 15(4), 394–404.

Hicke, J.A. et al. (2003) Postfire response of North American boreal forest net primary productivity analyzed with satellite observations. *Global Change Biology*, 9(8), 1145–1157.

Hickler, T. et al. (2005) Precipitation controls Sahel greening trend. *Geophysical Research Letters*, 32(21), 1–4.

Higginbottom, T.P. & Symeonakis, E. (2014) Assessing land degradation and desertification using vegetation index data: Current frameworks and future directions. *Remote Sensing*, 6(10), 9552–9575.

Higginbottom, T.P. & Symeonakis, E. (2020) Identifying ecosystem function shifts in Africa using breakpoint analysis of long-term NDVI and RUE data. *Remote Sensing*, 12(11), 1–14.

Hoang, T.T. et al. (2020) New JAXA high-resolution land use/land cover map for Vietnam aiming for natural forest and plantation forest monitoring. *Remote Sensing*, 12(17), 2707.

Homer, C. et al. (2007) Completion of the 2001 National Land Cover Database for the conterminous United States. *Photogrammetric Engineering and Remote Sensing*, 73(4), 337–341.

Homer, C. et al. (2015) Completion of the 2011 national land cover database for the conterminous United States – Representing a decade of land cover change information. *Photogrammetric Engineering and Remote Sensing*, 81(5), 345–354.

Homer, C. et al. (2020) Conterminous United States land cover change patterns 2001–2016 from the 2016 National Land Cover Database. *ISPRS Journal of Photogrammetry and Remote*

Sensing, 162, 184–199.

Hou, H. et al. (2019) Scenario-based modelling for urban sustainability focusing on changes in cropland under rapid urbanization: A case study of Hangzhou from 1990 to 2035. *Science of the Total Environment*, 661, 422–431.

Houet, T. & Hubert-moy, L. (2006) Modelling and Projecting Land-Use and Land-Cover Changes With a Cellular Automaton in Considering Landscape Trajectories : an Improvement for Simulation of Plausible Future States. *EASeL eProceedings*, 63–76.

Hu, Q. et al. (2020) Global cropland intensification surpassed expansion between 2000 and 2010: A spatio-temporal analysis based on GlobeLand30. *Science of the Total Environment*, 746, 141035.

Hu, Y. & Hu, Y. (2019) Land cover changes and their driving mechanisms in Central Asia from 2001 to 2017 supported by Google Earth Engine. *Remote Sensing*, 11(5), 554.

Huang, J. et al. (2020a) Global desertification vulnerability to climate change and human activities. *Land Degradation and Development*, 31(11), 1380–1391.

Huang, Q. et al. (2020b) The occupation of cropland by global urban expansion from 1992 to 2016 and its implications. *Environmental Research Letters*, 15(8), 084037.

Huber, S. et al. (2011) Water availability as the driver of vegetation dynamics in the African Sahel from 1982 to 2007. *Global and Planetary Change*, 76(3–4), 186–195.

Hyandye, C. & Martz, L.W. (2017) A Markovian and cellular automata land-use change predictive model of the Usangu Catchment. *International Journal of Remote Sensing*, 38(1), 64–81.

Ickowitz, A. (2006) Shifting cultivation and deforestation in tropical Africa: Critical reflections. *Development and Change*, 37(3), 599–626.

Jansen, L.J.M. et al. (2008) Analysis of land-cover/use change dynamics in Manica Province in Mozambique in a period of transition (1990-2004). *Forest Ecology and Management*, 254(2), 308–326.

Jew, E.K.K. et al. (2016) Miombo woodland under threat: Consequences for tree diversity and carbon storage. *Forest Ecology and Management*, 361, 144–153.

Jew, E.K.K. et al. (2017) Tobacco cultivation as a driver of land use change and degradation in the miombo woodlands of south-west Tanzania. *Land Degradation and Development*,

28(8), 2636–2645.

Ji, Y. et al. (2020) Unbalanced forest displacement across the coastal urban groups of eastern China in recent decades. *Science of the Total Environment*, 705, 135900.

Jokar Arsanjani, J. et al. (2013) Spatiotemporal simulation of urban growth patterns using agent-based modeling: The case of Tehran. *Cities*, 32, 33–42.

Jokar Arsanjani, J. (2019) Characterizing and monitoring global landscapes using GlobeLand30 datasets: the first decade of the twenty-first century. *International Journal of Digital Earth*, 12(6), 642–660.

Kalaba, F.K. et al. (2013) Contribution of forest provisioning ecosystem services to rural livelihoods in the Miombo woodlands of Zambia. *Population and Environment*, 35(2), 159–182.

Kamusoko, C. et al. (2009) Rural sustainability under threat in Zimbabwe - Simulation of future land use/cover changes in the Bindura district based on the Markov-cellular automata model. *Applied Geography*, 29(3), 435–447.

Kaplan, S. et al. (2014) Land-use change and land degradation in Turkmenistan in the post-Soviet era. *Journal of Arid Environments*, 103, 96–106.

Kastens, J.H. et al. (2017) Soy moratorium impacts on soybean and deforestation dynamics in Mato Grosso, Brazil. *PLoS ONE*, 12(4), 1–21.

Kehoe, L. et al. (2017) Biodiversity at risk under future cropland expansion and intensification. *Nature Ecology and Evolution*, 1(8), 1129–1135.

Kennedy, R.E. et al. (2010) Detecting trends in forest disturbance and recovery using yearly Landsat time series: 1. LandTrendr - Temporal segmentation algorithms. *Remote Sensing of Environment*, 114(12), 2897–2910.

Khuc, Q. Van et al. (2018) Drivers of deforestation and forest degradation in Vietnam: An exploratory analysis at the national level. *Forest Policy and Economics*, 90, 128–141.

Killeen, T.J. et al. (2007) Thirty years of land-cover change in Bolivia. *Ambio*, 36(7), 600–606.

Kim, D.H. et al. (2014) Global, Landsat-based forest-cover change from 1990 to 2000. *Remote Sensing of Environment*, 155, 178–193.

Kityuttachai, K. et al. (2013) CA-Markov analysis of constrained coastal urban growth

modeling: Hua hin Seaside City, Thailand. *Sustainability (Switzerland)*, 5(4), 1480–1500.

Klein, I. et al. (2012) Regional land cover mapping and change detection in Central Asia using MODIS time-series. *Applied Geography*, 35(1–2), 219–234.

Kleinschroth, F. et al. (2019) Road expansion and persistence in forests of the Congo Basin. *Nature Sustainability*, 2(7), 628–634.

Knauer, K. et al. (2017) Monitoring agricultural expansion in Burkina Faso over 14 years with 30 m resolution time series: The role of population growth and implications for the environment. *Remote Sensing*, 9(2), 132.

Kong, R. et al. (2019) Understanding the drivers of deforestation and agricultural transformations in the Northwestern uplands of Cambodia. *Applied Geography*, 102, 84–98.

Kranz, O. et al. (2018) Earth observation based multi-scale assessment of logging activities in the Democratic Republic of the Congo. *ISPRS Journal of Photogrammetry and Remote Sensing*, 144, 254–267.

Kukavskaya, E.A. et al. (2013) Influence of logging on the effects of wildfire in Siberia. *Environmental Research Letters*, 8(4), 045034.

Lambin, E.F. et al. (2001) The causes of land-use and land-cover change : Moving beyond the myths. *Global Environmental Change*, 11(4), 261–269.

Latifovic, R. et al. (2004) Land cover mapping of North and Central America - Global Land Cover 2000. *Remote Sensing of Environment*, 89(1), 116–127.

Latifovic, R. et al. (2017) Circa 2010 land cover of Canada: Local optimization methodology and product development. *Remote Sensing*, 9(11), 1–18.

Latifovic, R. & Pouliot, D. (2005) Multitemporal land cover mapping for Canada: methodology and products. *Canadian Journal of Remote Sensing*, 31(5), 347–363.

Laurance, W.F. et al. (2014) Agricultural expansion and its impacts on tropical nature. *Trends in Ecology and Evolution*, 29(2), 107–116.

Lehmann, E.A. et al. (2013) Forest cover trends from time series Landsat data for the Australian continent. *International Journal of Applied Earth Observation and Geoinformation*, 21(1), 453–462.

Li, C. et al. (2014) A circa 2010 thirty meter resolution forest map for China. *Remote Sensing*,

6(6), 5325–5343.

Li, C. et al. (2017) The first all-season sample set for mapping global land cover with Landsat-8 data. *Science Bulletin*, 62(7), 508–515.

Li, K. et al. (2020) Driving factors and future prediction of land use and cover change based on satellite remote sensing data by the LCM model: A case study from gansu province, China. *Sensors (Switzerland)*, 20(10), 2757.

Li, W. et al. (2016) Major forest changes and land cover transitions based on plant functional types derived from the ESA CCI Land Cover product. *International Journal of Applied Earth Observation and Geoinformation*, 47, 30–39.

Li, W. et al. (2018) Gross and net land cover changes based on plant functional types derived from the annual ESA CCI land cover maps. *Earth System Science Data*, 10, 219–234.

Linder, H.P. et al. (2012) The partitioning of Africa: Statistically defined biogeographical regions in sub-Saharan Africa. *Journal of Biogeography*, 39(7), 1189–1205.

Liu, H. et al. (2020a) Annual dynamics of global land cover and its long-term changes from 1982 to 2015. *Earth System Science Data*, 12(2), 1217–1243.

Liu, H. et al. (2021) Production of global daily seamless data cubes and quantification of global land cover change from 1985 to 2020 - iMap World 1.0. *Remote Sensing of Environment*, 258, 112364.

Liu, X. et al. (2017) A future land use simulation model (FLUS) for simulating multiple land use scenarios by coupling human and natural effects. *Landscape and Urban Planning*, 168, 94–116.

Liu, X. et al. (2018a) High-resolution multi-temporal mapping of global urban land using Landsat images based on the Google Earth Engine Platform. *Remote Sensing of Environment*, 209, 227–239.

Liu, X. et al. (2018b) Identifying patterns and hotspots of global land cover transitions using the ESA CCI land cover dataset. *Remote Sensing Letters*, 9(10), 972–981.

Liu, X. et al. (2020b) High-spatiotemporal-resolution mapping of global urban change from 1985 to 2015. *Nature Sustainability*, 3, 564-570.

Long, X. et al. (2019) Response of vegetation cover to climate variability in protected and grazed arid rangelands of South Australia. *Journal of Arid Environments*, 161, 64–71.

van Loon, M.P. et al. (2019) Impacts of intensifying or expanding cereal cropping in sub-Saharan Africa on greenhouse gas emissions and food security. *Global Change Biology*, 25(11), 3720–3730.

Losiri, C. et al. (2016) Modeling urban expansion in Bangkok Metropolitan region using demographic-economic data through cellular Automata-Markov Chain and Multi-Layer Perceptron-Markov Chain models. *Sustainability (Switzerland)*, 8(7), 686.

Loveland, T.R. et al. (2000) Development of a global land cover characteristics database and IGBP DISCover from 1 km AVHRR data. *International Journal of Remote Sensing*, 21(6–7), 1303–1330.

Lu, D. et al. (2013) Spatiotemporal analysis of land-use and land-cover change in the Brazilian Amazon. *International Journal of Remote Sensing*, 34(16), 5953–5978.

Lymburner, L., Tan, P., McIntyre, A., Thankappan, M., Sixsmith, J. (2015) Dynamic Land Cover Dataset Version 2.1. *Geoscience Australia*.

Ma, Y. et al. (2015) Remote sensing big data computing: Challenges and opportunities. *Future Generation Computer Systems*, 51, 47–60.

Magliocca, N.R. et al. (2020) Direct and indirect land-use change caused by large-scale land acquisitions in Cambodia. *Environmental Research Letters*, 15(2), 024010.

Malhi, Y. et al. (2013) African rainforests: Past, present and future. *Philosophical Transactions of the Royal Society B: Biological Sciences*, 368(1625).

Margono, B.A. et al. (2012) Mapping and monitoring deforestation and forest degradation in Sumatra (Indonesia) using Landsat time series data sets from 1990 to 2010. *Environmental Research Letters*, 7(3), 2000–2010.

Martínez-Fernández, J. et al. (2019) Methodological variations in the production of CORINE land cover and consequences for long-term land cover change studies. The case of Spain. *International Journal of Remote Sensing*, 40(23), 8914–8932.

Masiliūnas, D. et al. (2021) Bfast lite: A lightweight break detection method for time series analysis. *Remote Sensing*, 13(16), 3308.

Mayaux, P. et al. (2004) A new land-cover map of Africa for the year 2000. *Journal of Biogeography*, 31(6), 861–877.

Mayaux, P. et al. (2013) State and evolution of the African rainforests between 1990 and

2010. *Philosophical Transactions of the Royal Society B: Biological Sciences*, 368(1625).

Mayes, M.T. et al. (2015) Forest cover change in Miombo Woodlands: Modeling land cover of African dry tropical forests with linear spectral mixture analysis. *Remote Sensing of Environment*, 165, 203–215.

McNicol, I.M. et al. (2015) How resilient are African woodlands to disturbance from shifting cultivation? *Ecological Applications*, 25(8), 2330–2336.

McNicol, I.M. et al. (2018) Carbon losses from deforestation and widespread degradation offset by extensive growth in African woodlands. *Nature Communications*, 9(1), 1-11.

McRoberts, R.E. et al. (2018) The effects of imperfect reference data on remote sensing-assisted estimators of land cover class proportions. *ISPRS Journal of Photogrammetry and Remote Sensing*, 142, 292–300.

McSweeney, K. et al. (2014) Drug policy as conservation policy: Narco-deforestation. *Science*, 343(6170), 489–490.

Megahed, Y. et al. (2015) Land cover mapping analysis and urban growth modelling using remote sensing techniques in greater Cairo region-Egypt. *ISPRS International Journal of Geo-Information*, 4(3), 1750–1769.

Memarian, H. et al. (2012) Validation of CA-Markov for Simulation of Land Use and Cover Change in the Langat Basin , Malaysia. *Journal of Geographic Information System*, 4, 542–554.

Mertes, C.M. et al. (2015) Detecting change in urban areas at continental scales with MODIS data. *Remote Sensing of Environment*, 158, 331–347.

Meyfroidt, P. et al. (2013) Trajectories of deforestation, coffee expansion and displacement of shifting cultivation in the Central Highlands of Vietnam. *Global Environmental Change*, 23(5), 1187–1198.

Meyfroidt, P. et al. (2016) Drivers, constraints and trade-offs associated with recultivating abandoned cropland in Russia, Ukraine and Kazakhstan. *Global Environmental Change*, 37, 1–15.

Midekisa, A. et al. (2017) Mapping land cover change over continental Africa using Landsat and Google Earth Engine cloud computing. *PLoS ONE*, 12(9), 1–15.

Midgley, G.F. & Bond, W.J. (2015) Future of African terrestrial biodiversity and ecosystems under anthropogenic climate change. *Nature Climate Change*, 5(9), 823–829.

Miettinen, J. et al. (2011) Deforestation rates in insular Southeast Asia between 2000 and 2010. *Global Change Biology*, 17(7), 2261–2270.

Miettinen, J. et al. (2012) 2010 land cover map of insular Southeast Asia in 250-m spatial resolution. *Remote Sensing Letters*, 3(1), 11–20.

Miettinen, J. et al. (2016) 2015 Land cover map of Southeast Asia at 250 m spatial resolution. *Remote Sensing Letters*, 7(7), 701–710.

Mishra, V.N. & Rai, P.K. (2016) A remote sensing aided multi-layer perceptron-Markov chain analysis for land use and land cover change prediction in Patna district (Bihar), India. *Arabian Journal of Geosciences*, 9(4), 249.

Mitchard, E.T.A. & Flintrop, C.M. (2013) Woody encroachment and forest degradation in sub-Saharan Africa's woodlands and savannas 1982-2006. *Philosophical Transactions of the Royal Society B: Biological Sciences*, 368(1625), 1–7.

Monteiro, F. et al. (2017) Cashew as a high agricultural commodity in West Africa: Insights towards sustainable production in Guinea-Bissau. *Sustainability (Switzerland)*, 9(9), 1–14.

Morton, D. et al. (2020) Land Cover Map 2019. *Centre for Ecology and Hydrology, Wallingford*.

Morton, D.C. et al. (2006) Cropland expansion changes deforestation dynamics in the southern Brazilian Amazon. *Proceedings of the National Academy of Sciences of the United States of America*, 103(39), 14637–14641.

Mousivand, A. & Arsanjani, J.J. (2019) Insights on the historical and emerging global land cover changes: The case of ESA-CCI-LC datasets. *Applied Geography*, 106, 82–92.

Muller, M.R. & Middleton, J. (1994) A Markov model of land-use change dynamics in the Niagara Region, Ontario, Canada. *Landscape Ecology*, 9(2), 151–157.

Mundia, C.N. & Aniya, M. (2005) Analysis of land use/cover changes and urban expansion of Nairobi city using remote sensing and GIS. *International Journal of Remote Sensing*, 26(13), 2831–2849.

Nackoney, J. et al. (2014) Impacts of civil conflict on primary forest habitat in northern Democratic Republic of the Congo, 1990-2010. *Biological Conservation*, 170, 321–328.

Negm, A.M. et al. (2016) Nile Delta Biography: Challenges and Opportunities. In: *The Nile Delta; The Handbook of Environmental Chemistry; Springer: Cham, Switzerland*. [Online]. Available at: http://link.springer.com/10.1007/698_2016_62

Nepstad, D. et al. (2014) Slowing Amazon deforestation through public policy and interventions in beef and soy supply chains. *Science*, 344(6188), 1118–1123.

Nguyen, T.A. et al. (2019) Toward a sustainable city of tomorrow: a hybrid Markov–Cellular Automata modeling for urban landscape evolution in the Hanoi city (Vietnam) during 1990–2030. *Environment, Development and Sustainability*, 21(1), 429–446.

Ngwira, S. & Watanabe, T. (2019) An Analysis of the Causes of Deforestation in Malawi: A Case of Mwazisi. *Land*, 8(3), 48.

Nkeki, F.N. (2016) Spatio-temporal analysis of land use transition and urban growth characterization in Benin metropolitan region, Nigeria. *Remote Sensing Applications: Society and Environment*, 4, 119–137.

Nong, D.H. et al. (2018) Quantifying urban growth patterns in Hanoi using landscape expansion modes and time series spatial metrics. *PLoS ONE*, 13(5), 1–18.

Nouri, J. et al. (2014) Predicting Urban Land Use Changes Using a CA-Markov Model. *Arabian Journal for Science and Engineering*, 39(7), 5565–5573.

Nowosad, J. et al. (2019) Global assessment and mapping of changes in mesoscale landscapes: 1992–2015. *International Journal of Applied Earth Observation and Geoinformation*, 78, 332–340.

Nutini, F. et al. (2013) Land-use and land-cover change detection in a semi-arid area of Niger using multi-temporal analysis of Landsat images. *International Journal of Remote Sensing*, 34(13), 4769–4790.

Nzunda, E.F. & Midtgaard, F. (2019) Deforestation and loss of bushland and grassland primarily due to expansion of cultivation in mainland Tanzania (1995–2010). *Journal of Sustainable Forestry*, 38(6), 509–525.

O'Connor, T.G. et al. (2014) Bush encroachment in southern Africa: Changes and causes. *African Journal of Range and Forage Science*, 31(2), 67–88.

Ogutu, B.O. et al. (2021) Impact of vegetation greening on carbon and water cycle in the African Sahel-Sudano-Guinean region. *Global and Planetary Change*, 202, 103524.

Oliphant, A.J. et al. (2019) Mapping cropland extent of Southeast and Northeast Asia using multi-year time-series Landsat 30-m data using a random forest classifier on the Google Earth Engine Cloud. *International Journal of Applied Earth Observation and Geoinformation*,

81, 110–124.

Ollenburger, M.H. et al. (2016) Waking the Sleeping Giant: Agricultural intensification, extensification or stagnation in Mali's Guinea Savannah. *Agricultural Systems*, 148, 58–70.

Olofsson, P. et al. (2013) Making better use of accuracy data in land change studies: Estimating accuracy and area and quantifying uncertainty using stratified estimation. *Remote Sensing of Environment*, 129, 122–131.

Olson, D.M. et al. (2001) Terrestrial ecoregions of the world: A new map of life on Earth. *BioScience*, 51(11), 933–938.

Olsson, L. et al. (2005) A recent greening of the Sahel - Trends, patterns and potential causes. *Journal of Arid Environments*, 63(3), 556–566.

Olthof, I. et al. (2009) Development of a circa 2000 land cover map of northern canada at 30 m resolution from landsat. *Canadian Journal of Remote Sensing*, 35(2), 152–165.

Ordway, E.M. et al. (2017a) Deforestation risk due to commodity crop expansion in sub-Saharan Africa. *Environmental Research Letters*, 12(4), 044015.

Ordway, E.M. et al. (2017b) Oil palm expansion in Cameroon: Insights into sustainability opportunities and challenges in Africa. *Global Environmental Change*, 47, 190–200.

Ordway, E.M. et al. (2019) Oil palm expansion and deforestation in Southwest Cameroon associated with proliferation of informal mills. *Nature Communications*, 10(1), 1–11.

Ozturk, D. (2015) Urban growth simulation of Atakum (Samsun, Turkey) using cellular automata-Markov chain and Multi-layer Perceptron-Markov chain models. *Remote Sensing*, 7(5), 5918–5950.

Pandey, B. & Seto, K.C. (2015) Urbanization and agricultural land loss in India: Comparing satellite estimates with census data. *Journal of Environmental Management*, 148, 53–66.

Paré, S. et al. (2008) Land use analysis from spatial and field data capture in southern Burkina Faso, West Africa. *Agriculture, Ecosystems and Environment*, 127(3–4), 277–285.

Parr, C.L. et al. (2014) Tropical grassy biomes: Misunderstood, neglected, and under threat. *Trends in Ecology and Evolution*, 29(4), 205–213.

Pedrayes, O.D. et al. (2021) Evaluation of semantic segmentation methods for land use with spectral imaging using sentinel-2 and pnoa imagery. *Remote Sensing*, 13(12), 2292.

Pekel, J.F. et al. (2016) High-resolution mapping of global surface water and its long-term changes. *Nature*, 540(7633), 418–422.

Pérez-Hoyos, A. et al. (2017) Comparison of global land cover datasets for cropland monitoring. *Remote Sensing*, 9(11), 1118.

Perrings, C. & Halkos, G. (2015) Agriculture and the threat to biodiversity in sub-saharan Africa. *Environmental Research Letters*, 10(9), 095015.

Phalan, B. et al. (2013) Crop Expansion and Conservation Priorities in Tropical Countries. *PLoS ONE*, 8(1), e51759.

Phalke, A.R. et al. (2020) Mapping croplands of Europe, Middle East, Russia, and Central Asia using Landsat, Random Forest, and Google Earth Engine. *ISPRS Journal of Photogrammetry and Remote Sensing*, 167, 104–122.

Phiri, D. et al. (2019) Four decades of land cover and forest connectivity study in Zambia—An object-based image analysis approach. *International Journal of Applied Earth Observation and Geoinformation*, 79, 97–109.

Piao, S. et al. (2015) Detection and attribution of vegetation greening trend in China over the last 30 years. *Global Change Biology*, 21(4), 1601–1609.

Pijanowski, B.C. et al. (2002) Using neural networks and GIS to forecast land use changes: A Land Transformation Model. *Computers, Environment and Urban Systems*, 26(6), 553–575.

Piquer-Rodríguez, M. et al. (2015) Effects of past and future land conversions on forest connectivity in the Argentine Chaco. *Landscape Ecology*, 30(5), 817–833.

Pittman, K. et al. (2010) Estimating global cropland extent with multi-year MODIS data. *Remote Sensing*, 2(7), 1844–1863.

Plummer, S. et al. (2017) The ESA Climate Change Initiative (CCI): A European contribution to the generation of the Global Climate Observing System. *Remote Sensing of Environment*, 203, 2–8.

Poffenberger, M. (2009) Cambodia's forests and climate change: Mitigating drivers of deforestation. *Natural Resources Forum*, 33(4), 285–296.

Pontius, G.R. & Malanson, J. (2005) Comparison of the structure and accuracy of two land change models. *International Journal of Geographical Information Science*, 19(2), 243–265.

Potapov, P. et al. (2017) The last frontiers of wilderness: Tracking loss of intact forest landscapes from 2000 to 2013. *Science Advances*, 3(1), 1–14.

Potapov, P. et al. (2020) Landsat analysis ready data for global land cover and land cover change mapping. *Remote Sensing*, 12(3), 426.

Potapov, P. V. et al. (2012) Quantifying forest cover loss in Democratic Republic of the Congo, 2000-2010, with Landsat ETM+ data. *Remote Sensing of Environment*, 122, 106–116.

Pouliot, D. et al. (2014) Development and assessment of a 250m spatial resolution MODIS annual land cover time series (2000-2011) for the forest region of Canada derived from change-based updating. *Remote Sensing of Environment*, 140, 731–743.

Pramanik, M.M.A. & Stathakis, D. (2016) Forecasting urban sprawl in Dhaka city of Bangladesh. *Environment and Planning B: Planning and Design*, 43(4), 756–771.

Puertas, O.L. et al. (2014) Assessing spatial dynamics of urban growth using an integrated land use model. Application in Santiago Metropolitan Area, 2010-2045. *Land Use Policy*, 38, 415–425.

Qin, Y. et al. (2015) Forest cover maps of China in 2010 from multiple approaches and data sources: PALSAR, Landsat, MODIS, FRA, and NFI. *ISPRS Journal of Photogrammetry and Remote Sensing*, 109, 1–16.

Qin, Y. et al. (2017) Annual dynamics of forest areas in South America during 2007–2010 at 50-m spatial resolution. *Remote Sensing of Environment*, 201, 73–87.

Radwan, T.M. et al. (2019) Dramatic loss of agricultural land due to urban expansion threatens food security in the Nile Delta, Egypt. *Remote Sensing*, 11(3), 332.

Radwan, T.M. (2019) Monitoring agricultural expansion in a newly reclaimed area in the western nile delta of Egypt using landsat imageries. *Agriculture (Switzerland)*, 9(7), 137.

Radwan, T.M. et al. (2021) Global land cover trajectories and transitions. *Scientific Reports*, 11(1), 1–16.

Ramankutty, N. et al. (2008) Farming the planet: 1. Geographic distribution of global agricultural lands in the year 2000. *Global Biogeochemical Cycles*, 22(1), 1–19.

Rimal, B. et al. (2018a) Land use/land cover dynamics and modeling of urban land expansion by the integration of cellular automata and markov chain. *ISPRS International Journal of Geo-Information*, 7(4), 154.

Rimal, B. et al. (2018b) Urban expansion occurred at the expense of agricultural lands in the Tarai region of Nepal from 1989 to 2016. *Sustainability (Switzerland)*, 10(5), 1341.

Rindfuss, R.R. et al. (2004) Developing a science of land change: Challenges and methodological issues. *Proceedings of the National Academy of Sciences of the United States of America*, 101(39), 13976–13981.

Rivera, S. et al. (2012) A comparison between cluster busting technique and a classification tree algorithm of a moderate resolution imaging spectrometer (MODIS) land cover map of Honduras. *Geocarto International*, 27(1), 17–29.

Rogan, J. & Chen, D.M. (2004) Remote sensing technology for mapping and monitoring land-cover and land-use change. *Progress in Planning*, 61(4), 301–325.

Roques, K.G. et al. (2001) Dynamics of shrub encroachment in an African savanna: Relative influences of fire, herbivory, rainfall and density dependence. *Journal of Applied Ecology*, 38(2), 268–280.

Rossi, J. et al. (2009) Spatial structures of soil organic carbon in tropical forests-A case study of Southeastern Tanzania. *Catena*, 77(1), 19–27.

Rowland, C.S. et al. (2017) Land Cover Map 2015. *Centre for Ecology and Hydrology, Wallingford*, 44, 1–25.

Roy, D.P. et al. (2014) Landsat-8: Science and product vision for terrestrial global change research. *Remote Sensing of Environment*, 145, 154–172.

Rudel, T.K. et al. (2009) Agricultural intensification and changes in cultivated areas, 1970-2005. *Proceedings of the National Academy of Sciences of the United States of America*, 106(49), 20675–20680.

Rudel, T.K. (2013) The national determinants of deforestation in sub-Saharan Africa. *Philosophical Transactions of the Royal Society B: Biological Sciences*, 368(1625).

Ruelland, D. et al. (2010) Patterns and dynamics of land-cover changes since the 1960s over three experimental areas in Mali. *International Journal of Applied Earth Observation and Geoinformation*, 12, S11-S17.

Ryan, C.M. et al. (2016) Ecosystem services from southern African woodlands and their future under global change. *Philosophical Transactions of the Royal Society B: Biological Sciences*, 371(1703).

Sahana, M. et al. (2018) Analyzing urban spatial patterns and trend of urban growth using urban sprawl matrix: A study on Kolkata urban agglomeration, India. *Science of the Total Environment*, 628–629, 1557–1566.

Salerno, J. et al. (2017) The Consequences of Internal Migration in Sub-Saharan Africa: A Case Study. *BioScience*, 67(7), 664–671.

Salvati, L. et al. (2018) Do spatial patterns of urbanization and land consumption reflect different socioeconomic contexts in Europe? *Science of the Total Environment*, 625, 722–730.

Samasse, K. et al. (2020) A high-resolution cropland map for the West African Sahel based on high-density training data, google earth engine, and locally optimized machine learning. *Remote Sensing*, 12(9), 1436.

Santé, I. et al. (2010) Cellular automata models for the simulation of real-world urban processes: A review and analysis. *Landscape and Urban Planning*, 96(2), 108–122.

Santos, C.A.G. et al. (2020) Analysis of forest cover changes and trends in the Brazilian semiarid region between 2000 and 2018. *Environmental Earth Sciences*, 79(18), 1–20.

Schierhorn, F. et al. (2013) Post-Soviet cropland abandonment and carbon sequestration in European Russia, Ukraine, and Belarus. *Global Biogeochemical Cycles*, 27(4), 1175–1185.

Schmitt-Harsh, M. (2013) Landscape change in Guatemala: Driving forces of forest and coffee agroforest expansion and contraction from 1990 to 2010. *Applied Geography*, 40, 40–50.

Schneibel, A. et al. (2017) Using annual landsat time series for the detection of dry forest degradation processes in south-central Angola. *Remote Sensing*, 9(9), 905.

Schneider, A. et al. (2009) A new map of global urban extent from MODIS satellite data. *Environmental Research Letters*, 4(4), 044003.

Schneider, A. et al. (2010) Mapping global urban areas using MODIS 500-m data: New methods and datasets based on 'urban ecoregions'. *Remote Sensing of Environment*, 114(8), 1733–1746.

Searchinger, T.D. et al. (2015) High carbon and biodiversity costs from converting Africa's wet savannahs to cropland. *Nature Climate Change*, 5(5), 481–486.

Sedano, F. et al. (2020) Monitoring forest degradation from charcoal production with historical Landsat imagery. A case study in southern Mozambique. *Environmental Research Letters*, 15(1), 015001.

Serdeczny, O. et al. (2017) Climate change impacts in Sub-Saharan Africa: from physical changes to their social repercussions. *Regional Environmental Change*, 17(6), 1585–1600.

Sesnie, S.E. et al. (2017) A spatio-temporal analysis of forest loss related to cocaine trafficking in Central America. *Environmental Research Letters*, 12(5), 054015.

Seto, K.C. et al. (2012) Global forecasts of urban expansion to 2030 and direct impacts on biodiversity and carbon pools. *Proceedings of the National Academy of Sciences of the United States of America*, 109(40), 16083–16088.

Shafizadeh Moghadam, H. & Helbich, M. (2013) Spatiotemporal urbanization processes in the megacity of Mumbai, India: A Markov chains-cellular automata urban growth model. *Applied Geography*, 40, 140–149.

Shalaby, A. (2012) Assessment of Urban Sprawl Impact on the Agricultural Land in the Nile Delta of Egypt Using Remote Sensing and Digital Soil Map. *International Journal of Environmental Sciences*, 1(4), 253–262.

Shalaby, A. & Moghanm, F.S. (2015) Assessment of urban sprawl on agricultural soil of northern Nile Delta of Egypt using RS and GIS. *Chinese Geographical Science*, 25(3), 274–282.

Shalaby, A. & Tateishi, R. (2007) Remote sensing and GIS for mapping and monitoring land cover and land-use changes in the Northwestern coastal zone of Egypt. *Applied Geography*, 27(1), 28–41.

Shalaby, A.A. et al. (2012) Urban sprawl impact assessment on the agricultural land in Egypt using remote sensing and GIS: a case study, Qalubiya Governorate. *Journal of Land Use Science*, 7(3), 261–273.

Sharma, R.C. et al. (2016) Production of the Japan 30-m land cover map of 2013-2015 using a random forests-based feature optimization approach. *Remote Sensing*, 8(5), 429.

Shen, H. et al. (2019) Remote sensing-based land surface change identification and prediction in the Aral Sea bed, Central Asia. *International Journal of Environmental Science and Technology*, 16(4), 2031–2046.

Shi, K. et al. (2016) Urban expansion and agricultural land loss in China: A multiscale perspective. *Sustainability (Switzerland)*, 8(8), 1–16.

Silva, J.A. et al. (2019) Charcoal-related forest degradation dynamics in dry African woodlands: Evidence from Mozambique. *Applied Geography*, 107, 72–81.

Sleeter, B.M. et al. (2013) Land-cover change in the conterminous United States from 1973 to 2000. *Global Environmental Change*, 23(4), 733–748.

Sloan, S. et al. (2019) The forest transformation: Planted tree cover and regional dynamics of tree gains and losses. *Global Environmental Change*, 59, 101988.

Smaliychuk, A. et al. (2016) Recultivation of abandoned agricultural lands in Ukraine: Patterns and drivers. *Global Environmental Change*, 38, 70–81.

Van Soesbergen, A. (2016) *A Review of Land-Use Change Models*.

Song, X.P. et al. (2018) Global land change from 1982 to 2016. *Nature*, 560(7720), 639–643.

Song, X.P. et al. (2021) Massive soybean expansion in South America since 2000 and implications for conservation. *Nature Sustainability*, 4(9), 784–792.

De Sousa, C. et al. (2020) Cloud-computing and machine learning in support of country-level land cover and ecosystem extent mapping in Liberia and Gabon. *PLoS ONE*, 15(1), 1–24.

Souverijns, N. et al. (2020) Thirty years of land cover and fraction cover changes over the sudano-sahel using landsat time series. *Remote Sensing*, 12(22), 3817.

Souza, C.M. et al. (2013) Ten-year landsat classification of deforestation and forest degradation in the brazilian amazon. *Remote Sensing*, 5(11), 5493–5513.

Spanhove, T. et al. (2012) Can remote sensing estimate fine-scale quality indicators of natural habitats? *Ecological Indicators*, 18, 403–412.

Spiekermann, R. et al. (2015) Woody vegetation and land cover changes in the Sahel of Mali(1967-2011). *International Journal of Applied Earth Observation and Geoinformation*, 34(1), 113–121.

Stehman, S. V. & Foody, G.M. (2019) Key issues in rigorous accuracy assessment of land cover products. *Remote Sensing of Environment*, 231, 111199.

Stevens, N. et al. (2017) Savanna woody encroachment is widespread across three continents. *Global Change Biology*, 23(1), 235–244.

Stibig, H.J. et al. (2007) A land-cover map for South and Southeast Asia derived from SPOT-VEGETATION data. *Journal of Biogeography*, 34(4), 625–637.

Stibig, H.J. et al. (2014) Change in tropical forest cover of Southeast Asia from 1990 to 2010. *Biogeosciences*, 11(2), 247–258.

Stone, T.A. et al. (1994) A Map of the Vegetation America of South Based lmagery on Satellite. *Photogrammetric Engineering & Remote Sensing*, 60(5), 541–551.

Sulla-Menashe, D. et al. (2019) Hierarchical mapping of annual global land cover 2001 to present: The MODIS Collection 6 Land Cover product. *Remote Sensing of Environment*, 222, 183–194.

De Sy, V. et al. (2015) Land use patterns and related carbon losses following deforestation in South America. *Environmental Research Letters*, 10(12), 124004.

Symeonakis, E. et al. (2018) Optimisation of savannah land cover characterisation with optical and SAR data. *Remote Sensing*, 10(4), 1–18.

Symeonakis, E. & Drake, N. (2004) Monitoring desertification and land degradation over sub-saharan africa. *International Journal of Remote Sensing*, 25(3), 573–592.

Tai, A.P.K. et al. (2014) Threat to future global food security from climate change and ozone air pollution. *Nature Climate Change*, 4(9), 817–821.

Takahashi, R. & Todo, Y. (2013) The impact of a shade coffee certification program on forest conservation: A case study from a wild coffee forest in Ethiopia. *Journal of Environmental Management*, 130, 48–54.

Tamiminia, H. et al. (2020) Google Earth Engine for geo-big data applications: A meta-analysis and systematic review. *ISPRS Journal of Photogrammetry and Remote Sensing*, 164, 152–170.

Tan, M. et al. (2005) Urban land expansion and arable land loss in China - A case study of Beijing-Tianjin-Hebei region. *Land Use Policy*, 22(3), 187–196.

Tang, J. & Di, L. (2019) Past and future trajectories of farmland loss due to rapid urbanization using Landsat imagery and the Markov-CA model: A case study of Delhi, India. *Remote Sensing*, 11(2), 180.

Tateishi, R. et al. (2011) Production of global land cover data - GLCNMO. *International Journal of Digital Earth*, 4(1), 22–49.

Tateishi, R. et al. (2014) Production of Global Land Cover Data – GLCNMO2008. *Journal of Geography and Geology*, 6(3), 99.

Teluguntla, P. et al. (2018) A 30-m landsat-derived cropland extent product of Australia and China using random forest machine learning algorithm on Google Earth Engine cloud

computing platform. *ISPRS Journal of Photogrammetry and Remote Sensing*, 144, 325–340.

Thapa, R.B. & Murayama, Y. (2012) Scenario based urban growth allocation in Kathmandu Valley, Nepal. *Landscape and Urban Planning*, 105(1–2), 140–148.

Tian, F. et al. (2017) Mapping gains and losses in woody vegetation across global tropical drylands. *Global Change Biology*, 23(4), 1748–1760.

Tian, Y. et al. (2014) Examining land use and land cover spatiotemporal change and driving forces in Beijing from 1978 to 2010. *Remote Sensing*, 6(11), 10593–10611.

Tilman, D. et al. (2011) Global food demand and the sustainable intensification of agriculture. *Proceedings of the National Academy of Sciences of the United States of America*, 108(50), 20260–20264.

Tobar-López, D. et al. (2019) Deforestation processes in the livestock territory of La Vía Láctea, Matagalpa, Nicaragua. *Journal of Land Use Science*, 14(3), 225–241.

Townshend, J.R. et al. (1987) Characterization and classification of South American Land cover types using satellite data. *International Journal of Remote Sensing*, 8(8), 1189–1207.

Triantakonstantis, D. & Stathakis, D. (2015) Examining urban sprawl in Europe using spatial metrics. *Geocarto International*, 30(10), 1092–1112.

Truong, Van Thinh, Thanh Tung Hoang, Duong Phan Cao, Masato Hayashi, Takeo Tadono, K.N.N. (2019) JAXA Annual Forest Cover Maps for Vietnam Auxiliary Data. *Remote Sensing*, 11(20), 2412.

Tucker, C.J. et al. (1985) African land-cover classification using satellite data. *Science*, 227(4685), 369–375.

Turner, B.L. et al. (2007) The emergence of land change science for global environmental change and sustainability. *Proceedings of the National Academy of Sciences*, 104(52), 20666–20671.

Turubanova, S. et al. (2018) Ongoing primary forest loss in Brazil, Democratic Republic of the Congo, and Indonesia. *Environmental Research Letters*, 13(7), 074028.

Tyukavina, A. et al. (2017) Types and rates of forest disturbance in Brazilian Legal Amazon, 2000–2013. *Science Advances*, 3(4), 1–16.

Tyukavina, A. et al. (2018) Congo Basin forest loss dominated by increasing smallholder

clearing. *Science Advances*, 4(11), eaat2993.

United Nations (2018) *Human Development Indices and Indicators. Statistical Update*.

United Nations (2019a) *The sustainable development goals report 2019*.

United Nations (2019b) *United Nations, Department of Economic and Social Affairs, Population Division (2019). World Population Prospects 2019: Highlights.*

Vancutsem, C. et al. (2021) Long-term (1990–2019) monitoring of forest cover changes in the humid tropics. *Science Advances*, 7(10), eabe1603.

Veldkamp, A. & Fresco, L.O. (1996) CLUE: A conceptual model to study the conversion of land use and its effects. *Ecological Modelling*, 85(2–3), 253–270.

Venter, Z.S. et al. (2018) Drivers of woody plant encroachment over Africa. *Nature Communications*, 9(1), 1–7.

Venter, Z.S. & Sydenham, M.A.K. (2021) Continental-scale land cover mapping at 10 m resolution over europe (Elc10). *Remote Sensing*, 13(12), 2301.

Verbesselt, J. et al. (2010) Detecting trend and seasonal changes in satellite image time series. *Remote Sensing of Environment*, 114(1), 106–115.

Verbesselt, J. et al. (2012) Near real-time disturbance detection using satellite image time series. *Remote Sensing of Environment*, 123, 98–108.

Verburg, P.H. et al. (2002) Modeling the spatial dynamics of regional land use: The CLUE-S model. *Environmental Management*, 30(3), 391–405.

Verburg, P.H. et al. (2011) Challenges in using land use and land cover data for global change studies. *Global Change Biology*, 17(2), 974–989.

Viera, A.J. & Garrett, J.M. (2005) Understanding interobserver agreement: the kappa statistic. *Family medicine*, 37(5), 360–363.

Vittek, M. et al. (2013) Land cover change monitoring using landsat MSS/TM satellite image data over west Africa between 1975 and 1990. *Remote Sensing*, 6(1), 658–676.

Vizzari, M. et al. (2018) Urban-rural-natural gradient analysis with CORINE data: An application to the metropolitan France. *Landscape and Urban Planning*, 171, 18–29.

van Vliet, J. et al. (2017) A global analysis of land take in cropland areas and production displacement from urbanization. *Global Environmental Change*, 43, 107–115.

van Vliet, J. (2019) Direct and indirect loss of natural area from urban expansion. *Nature Sustainability*, 2(8), 755–763.

Vogelmann, J.E. et al. (2001) Completion of the 1990s National Land Cover Data set for the conterminous United States from Landsat thematic mapper data and ancillary data sources. *Photogrammetric Engineering and Remote Sensing*, 67(6), 650–662.

Vu, T.T. et al. (2018) Multiscale remote sensing of urbanization in Ho Chi Minh city, Vietnam - A focused study of the south. *Applied Geography*, 92, 168–181.

Waldner, F. et al. (2015) Mapping priorities to focus cropland mapping activities: Fitness assessment of existing global, regional and national cropland maps. *Remote Sensing*, 7(6), 7959–7986.

Wang, C. & Myint, S.W. (2016) Environmental concerns of deforestation in myanmar 2001-2010. *Remote Sensing*, 8(9), 728.

Wang, J. et al. (2015) Mapping global land cover in 2001 and 2010 with spatial-temporal consistency at 250m resolution. *ISPRS Journal of Photogrammetry and Remote Sensing*, 103, 38–47.

Wang, J. & Maduako, I.N. (2018) Spatio-temporal urban growth dynamics of Lagos Metropolitan Region of Nigeria based on Hybrid methods for LULC modeling and prediction. *European Journal of Remote Sensing*, 51(1), 251–265.

Wang, R. et al. (2018a) Scenario-based simulation of Tianjin city using a cellular automata-Markov model. *Sustainability (Switzerland)*, 10(8), 2633.

Wang, R. et al. (2018b) Spatiotemporal simulation of future land use/cover change scenarios in the Tokyo metropolitan area. *Sustainability (Switzerland)*, 10(6), 2056.

Wang, S.Q. et al. (2012) Accuracy assessments of land use change simulation based on Markov-cellular automata model. *Procedia Environmental Sciences*, 13(2011), 1238–1245.

Wegenast, T. et al. (2019) At Africa's expense? Disaggregating the employment effects of Chinese mining operations in sub-Saharan Africa. *World Development*, 118, 39–51.

Weng, Q. (2002) Land use change analysis in the Zhujiang Delta of China using satellite remote sensing, GIS and stochastic modelling. *Journal of environmental management*, 64(3), 273–284.

Wickham, J. et al. (2017) Thematic accuracy assessment of the 2011 National Land Cover

Database (NLCD). *Remote Sensing of Environment*, 191, 328–341.

Wingate, V.R. et al. (2019) Mapping precipitation-corrected NDVI trends across Namibia. *Science of the Total Environment*, 684, 96–112.

Worldometers (2018) *Worldometers*. Available at: http://www.worldometers.info/world-population/egypt-population/ [Accessed: 6 June 2018].

WorldPop (2018) *No Title*. Available at: http://www.worldpop.org.uk/data/summary/?doi=10.5258/SOTON/%0AWP00078 [Accessed: 6 June 2018].

Wu, F. (2002) Calibration of stochastic cellular automata: The application to rural-urban land conversions. *International Journal of Geographical Information Science*, 16(8), 795–818.

Wu, K.Y. & Zhang, H. (2012) Land use dynamics, built-up land expansion patterns, and driving forces analysis of the fast-growing Hangzhou metropolitan area, eastern China (1978-2008). *Applied Geography*, 34, 137–145.

Wu, Q. et al. (2006) Monitoring and predicting land use change in Beijing using remote sensing and GIS. *Landscape and Urban Planning*, 78(4), 322–333.

Wu, W. et al. (2015) A comparative study of urban expansion in Beijing, Tianjin and Shijiazhuang over the past three decades. *Landscape and Urban Planning*, 134, 93–106.

Wu, Y. et al. (2016) Monitoring urban expansion and its effects on land use and land cover changes in Guangzhou city, China. *Environmental Monitoring and Assessment*, 188(1), 54.

Wulder, M.A. et al. (2008) Monitoring Canada's forests. Part 1: Completion of the EOSD land cover project. *Canadian Journal of Remote Sensing*, 34(6), 549–562.

Wulder, M.A. et al. (2019) Current status of Landsat program, science, and applications. *Remote Sensing of Environment*, 225, 127–147.

Xiong, J. et al. (2017a) Automated cropland mapping of continental Africa using Google Earth Engine cloud computing. *ISPRS Journal of Photogrammetry and Remote Sensing*, 126, 225–244.

Xiong, J. et al. (2017b) Nominal 30-m cropland extent map of continental Africa by integrating pixel-based and object-based algorithms using Sentinel-2 and Landsat-8 data on google earth engine. *Remote Sensing*, 9(10), 1065.

Xu, X. et al. (2019) Quantifying the biophysical and socioeconomic drivers of changes in forest and agricultural land in South and Southeast Asia. *Global Change Biology*, 25(6), 2137–2151.

Xu, Y. et al. (2020) Annual oil palm plantation maps in Malaysia and Indonesia from 2001 to 2016. *Earth System Science Data*, 12(2), 847–867.

Yamazaki, D. et al. (2015) Development of a global ~90m water body map using multi-temporal Landsat images. *Remote Sensing of Environment*, 171, 337–351.

Yan, J. et al. (2020) Spatial-temporal changes of forests and agricultural lands in Malaysia from 1990 to 2017. *Environmental Monitoring and Assessment*, 192(12), 1-16.

Yang, R. et al. (2019) Analysis of forest deforestation and its driving factors in Myanmar from 1988 to 2017. *Sustainability (Switzerland)*, 11(11), 3047.

Yang, X. et al. (2012) A spatiotemporal model of land use change based on ant colony optimization, Markov chain and cellular automata. *Ecological Modelling*, 233, 11–19.

Yin, J. et al. (2011) Monitoring urban expansion and land use/land cover changes of Shanghai metropolitan area during the transitional economy (1979-2009) in China. *Environmental Monitoring and Assessment*, 177(1), 609–621.

Yu, L. et al. (2013) FROM-GC: 30 m global cropland extent derived through multisource data integration. *International Journal of Digital Earth*, 6(6), 521–533.

Yulianto, F. et al. (2019) Analysis of the dynamics of land use change and its prediction based on the integration of remotely sensed data and CA-Markov model, in the upstream Citarum Watershed, West Java, Indonesia. *International Journal of Digital Earth*, 12(10), 1151–1176.

Zabel, F. et al. (2019) Global impacts of future cropland expansion and intensification on agricultural markets and biodiversity. *Nature Communications*, 10(1), 1–10.

Zaehringer, J. et al. (2015) Revealing Regional Deforestation Dynamics in North-Eastern Madagascar—Insights from Multi-Temporal Land Cover Change Analysis. *Land*, 4(2), 454–474.

Zeng, Z. et al. (2018) Highland cropland expansion and forest loss in Southeast Asia in the twenty-first century. *Nature Geoscience*, 11(8), 556–562.

Zhang, C. et al. (2012) Impacts of urbanization on carbon balance in terrestrial ecosystems of the Southern United States. *Environmental Pollution*, 164, 89–101.

Zhang, H.K. & Roy, D.P. (2017) Using the 500 m MODIS land cover product to derive a consistent continental scale 30 m Landsat land cover classification. *Remote Sensing of Environment*, 197, 15–34.

Zhang, X. et al. (2020) Development of a global 30-m impervious surface map using multi-source and multi-temporal remote sensing datasets with the Google Earth Engine platform. *Earth System Science Data Discussions*, 12(3), 1625-1648.

Zhang, X. et al. (2021) GLC_FCS30: Global land-cover product with fine classification system at 30 m using time-series Landsat imagery. *Earth System Science Data*, 13(6), 2753–2776.

Zhao, Y. et al. (2016) Detailed dynamic land cover mapping of Chile: Accuracy improvement by integrating multi-temporal data. *Remote Sensing of Environment*, 183, 170–185.

Zhu, Z. & Woodcock, C.E. (2014) Continuous change detection and classification of land cover using all available Landsat data. *Remote Sensing of Environment*, 144, 152–171.

Zhuravleva, I. et al. (2013) Satellite-based primary forest degradation assessment in the Democratic Republic of the Congo, 2000-2010. *Environmental Research Letters*, 8(2), 024034.

Zoungrana, B.J.B. et al. (2018) MODIS NDVI trends and fractional land cover change for improved assessments of vegetation degradation in Burkina Faso, West Africa. *Journal of Arid Environments*, 153, 66–75.